

University of Warwick institutional repository: <http://go.warwick.ac.uk/wrap>

A Thesis Submitted for the Degree of PhD at the University of Warwick

<http://go.warwick.ac.uk/wrap/3170>

This thesis is made available online and is protected by original copyright.

Please scroll down to view the document itself.

Please refer to the repository record for this item for information to help you to cite it. Our policy information is available from the repository home page.

**CARBON NANOTUBES AND OTHER HIGHLY CURVED
SURFACES FOR FIELD EMISSION AND FIELD-
PROMOTED IONISATION.**

Lewis Paul Mark

Submitted for the qualification of Doctor of Philosophy.

University of Warwick

Department of Chemistry

July 2009

1.2.2 Time-of-flight mass analysers.....	14
1.2.2.1 Linear time-of-flight mass analysers.....	14
1.2.2.2 Ion reflectron in time-of-flight mass spectrometry.....	18
1.2.2.3 Orthogonal acceleration in time-of-flight mass spectrometry.....	20
1.2.2.4 The BioTOF instrument.....	21
1.2.2.4.1 Introduction.....	21
1.2.2.4.2 The ion conveyor.....	24
1.2.2.4.3 The orthogonal accelerator and detector.....	27
1.2.2.4.5 The vacuum system.....	28
1.2.3 Fourier transform ion cyclotron resonance (FTICR) mass analysers.....	29
1.2.3.1 Principle of ion cyclotron resonance.....	29
1.2.3.2 The Bruker Bio APEX - 9.4 T FT-ICR mass spectrometer.....	33
1.2.3.2.1 Introduction.....	33
1.2.3.2.2 Electrospray and Nano-electrospray ionisation sources.....	35
1.2.3.2.3 Transfer optics.....	37
1.2.3.2.4 The ICR cell.....	39
1.2.3.2.5 The vacuum system.....	39
1.3 Ionisation techniques.....	41
1.3.1 Field Ionisation.....	42
1.3.2 Field Desorption.....	45
1.3.2.1 Field-induced electron tunnelling.....	46
1.3.2.2 Field induced extraction: desolvation and ion evaporation.....	49
1.3.2.3 Thermally induced ionization.....	52

1.3.2.4 Discussion of field desorption.....	53
1.3.3 Electrospray Ionisation.....	55
1.3.4 Nano-electrospray ionisation.....	59
1.4 Simion 8 ion optic simulations.....	60
1.4.1 Introduction.....	60
1.4.2 Creation of array and geometry files.....	62
1.4.3 Field and ion trajectory simulations.....	65
1.5 Objectives of the thesis.....	68
1.6 References.....	69
2. Chapter two - A dual-channelled nano-electrospray source for mass spectrometry.....	73
2.1 Introduction.....	73
2.2 Nano-electrospray emitter fabrication.....	76
2.3 Investigation of the performance of the nano-electrospray emitters.....	79
2.3.1 Confocal microscopy.....	79
2.3.2 Characterisation of the dual-channelled emitter.....	82
2.3.3 Mixing experiments.....	88
2.3.3.1 Vancomycin –KAA.....	88
2.3.3.2 Vancomycin – deuterated vancomycin.....	92
2.4 Conclusion.....	96
2.5 References.....	97
3. Chapter three - Carbon nanotubes as field emitters	99
3.1 Introduction.....	99

3.2 Conventional field emitters.....	101
3.2.1 Overview.....	101
3.2.2 TEM interrogation of field-emitter carbon dendrites.....	103
3.3 Arrays of carbon nanotubes as field emitters.....	107
3.3.1 Overview.....	107
3.3.2 Synthesis of carbon nanotubes.....	109
3.3.2.1 Dense arrays of vertically aligned carbon nanotubes.....	110
3.3.2.2 Patterned arrays of vertically aligned carbon nanotubes...	112
3.3.3 The type of arrays to be used in field ionisation/ desorption experiments.....	113
3.3.3.1 Arrays of carbon nanotubes used in field ionisation experiments.....	113
3.3.3.2 Arrays of Carbon nanotubes used in liquid-injection experiments.....	119
3.3.4 Field emitter simulations.....	123
3.3.4.1 Dense arrays.....	123
3.3.4.2 Patterned arrays.....	125
3.3.4.3 The effect of introducing holes into the CNT substrate.....	130
4. Chapter four - Field Ionisation of Gases using Carbon Nanotubes.....	134
4.1 Introduction.....	134
4.2 The first-generation of field ionisation source.....	134
4.2.1 Design.....	134
4.2.2 Results with the first-generation source.....	138
4.2.2.1 Field emission experiments.....	138
4.2.2.2 Field ionisation experiments - proof of concept.....	143
4.3 The Second generation of CNT FI ion source.....	147

4.3.1 Design.....	147
4.3.2 Results with the second generation source.....	157
4.4 Conclusion.....	165
4.5 References.....	165
5. Chapter Five - Direct Introduction of Liquids into the Carbon Nanotube Source.....	166
5.1 Introduction.....	166
5.2 Development of the CNT FD ion source.....	167
5.2.1 Design.....	167
5.2.2 Carbon-nanotube emitters: design and production.....	172
5.2.3 Simulations and flow considerations.....	177
5.3 Source Characterisation: Experiments Results and Discussion.....	185
5.3.1 Method.....	182
5.3.2 Results.....	186
5.3.3 Discussion.....	188
5.4 References.....	192
6. Chapter six - Conclusion.....	193
7. Chapter seven – Appendix.....	197

List of Figures

Chapter One - Introduction to mass spectrometry

Figure 1.1.	Spatial focusing in A) a magnetic sector and B) an electric sector.....	9
Figure 1.2.	Combination of magnetic and electric sectors. The energy dispersion from the first sector is noted as qV_s and $q(V_s+\Delta V_s)$. This is corrected upon exiting the second sector at a focal point X.....	11
Figure 1.3.	Schematic of the magTOF instrument.....	13
Figure 1.4.	Modifications to the electrostatic analyser to allow linear time-of-flight measurements	15
Figure 1.5.	Double-stage reflectron TOF showing the focusing of 3 ions with the same mass but different kinetic energies.....	19
Figure 1.6.	a) Schematic and b) photograph of the bioTOF I mass spectrometer	23
Figure 1.7.	Photo of an ion conveyor, a 1 pence coin is included for size comparison	24
Figure 1.8.	Schematic illustrating the position of the ion conveyors in the bioTOFs source	26
Figure 1.9.	Schematic of the orthogonal accelerator installed in the BioTOF instruments.....	27
Figure 1.10.	Schematic of A) a cylindrical FTICR cell and B) The ICR process where green represents ions just entering the cell, red the ions as they are excited by an RF pulse and blue the ions at a stable orbit.....	32
Figure 1.11.	Photograph (a) and schematic (b) of the Bruker BioAPEX 9.4 T FT-ICR.....	34
Figure 1.12.	Photograph showing the nano-electrospray ionisation source.....	36
Figure 1.13.	Transfer optics used in the 9.4 T FT-ICR	38
Figure 1.14.	Potential energy diagrams showing a valence electron from an analyte atom in A) the absence of an electric field and B) the presence of a high electric field.....	44

Figure 1.15.	Potential energy diagrams for A) a surface atom, B) a surface ion and C) a surface ion in the presence of a high electric field.....	46
Figure 1.16.	Three possible evaporation models. A) Simple ionic bounding, B) evaporation over the image hump after transition from the atomic to ionic state and C) ionization followed by immediate evaporation.....	48
Figure 1.17.	Schematic showing the charge separation in the desolvation model of field desorption.....	50
Figure 1.18.	Schematic showing the protuberance growth in field-assisted evaporation.....	51
Figure 1.19.	Schematic showing the effect of potential on the meniscus at the tip of an electrospray needle. A) The case where there is either a small or no potential applied. B) What occurs when a higher potential is applied where there is a balance between the charge repulsion and surface tension of the meniscus. C) The onset of a spray of droplets created when the potential is increased further.....	57
Figure 1.20.	Simion 8 simulation showing the potential energy surface in three dimensions of a simple Einzel lens. Electrodes 1 and 3 have zero potential, a voltage of 1500 V is applied to the second electrode.....	61
Figure 1.21.	Simion 8 simulations showing examples of the simulation conducted in order to a) model the fields generated by applying a potential to the CNTs and b) model the trajectories of ions through the source and transfer optics.....	67
Chapter two - A dual-channelled nano-electrospray source for mass spectrometry		
Figure 2.1.	Theta-shaped profile of glass capillary, (a) sketch of the distal end and (b) electron micrograph of the very tip (c) electron micrograph of the side of the emitter.....	74
Figure 2.2.	Electron micrographs of the tip of theta shaped needle coated using (a) hand painted method and (b) magnetron sputtering.....	78
Figure 2.3.	Confocal microscope images (provided by Matthew Gill) of a dual- channelled nanospray needle loaded with dyes of different wavelength fluorescence under a potential difference of a) 0 V, b) 750 V and c) 750 V (enhanced view).....	81

Figure 2.4.	Mass spectra of vancomycin [V] = 135 $\mu\text{mol/L}$ for (a) a hand painted dual-channelled emitter (one side loaded) and (b) a conventional single-channelled emitter.....	83
Figure 2.5.	Mass spectra of vancomycin [V] = 135 $\mu\text{mol/L}$ using a sputtered dual-channelled emitter (one side loaded).....	84
Figure 2.6.	Mass spectra of vancomycin [V] = 135 $\mu\text{mol/L}$ recorded at 30 minute intervals using the same dual-channelled emitter.....	87
Figure 2.7.	Mass spectra of vancomycin (a) [V] = 135 $\mu\text{mol/L}$ and [KAA] = 135 $\mu\text{mol/L}$ loaded on either side of a dual-channelled emitter and (b) a premixed solution of [V] = [KAA] = 135 $\mu\text{mol/L}$ sprayed down both sides of a dual-channelled emitter.....	90
Figure 2.8.	Mass spectra of (a) deuterated vancomycin [V- D_x] = 135 $\mu\text{mol/L}$ down one side of a dual-channelled emitter and (b) isotopically normal vancomycin [V] = 135 $\mu\text{mol/L}$ down one side of a dual-channelled emitter and (c) deuterated vancomycin [V- d_x] = 135 $\mu\text{mol/L}$ on the one side and on the other side isotopically normal vancomycin [V] = 135 $\mu\text{mol/L}$ of a dual-channelled emitter.....	93
Figure 2.9.	Mass spectra of (a) isotopically normal normal vancomycin [V] on one side = 135 $\mu\text{mol/L}$, (b) deuterated vancomycin [V- D_x] = 135 $\mu\text{mol/L}$ on the one side and on the other side isotopically normal vancomycin [V] = 135 $\mu\text{mol/L}$ of a dual-channelled emitter and (c) deuterated vancomycin [V- D_x] = 135 $\mu\text{mol/L}$ down one side of a dual-channelled emitter.....	95
Chapter three - Carbon nanotubes as field emitters		
Figure 3.1.	Scanning electron micrograph of the multipoint emitter of Aberth et al.....	99
Figure 3.2.	Scanning electron microscope image of an activated tungsten wire obtained using a ZEISS SUPRA 55VP-23-99.....	102
Figure 3.3.	Transmission electron microscope images of: A) A typical branched carbon needle. B) An example of the structure of the side growths. C) An example of the irregular 'hollows' found at the centre of some structures.....	106

Figure 3.4.	SEM pictures displaying both the side (A) and top view (B) of the dense array of vertically aligned carbon nanotubes.....	114
Figure 3.5.	Transmission electron micrographs showing A) the bamboo like structure of the CNTs. B) the encapsulated catalyst particle.....	116
Figure 3.6.	SEM pictures displaying both the side (A) and top view (B) of the patterned array of vertically aligned carbon nanotubes.....	118
Figure 3.7.	SEM micrographs showing (A) a large area of a typical Dense FD emitter (B) a close up of one of the holes and surrounding nanotubes.....	120
Figure 3.8.	SEM micrographs showing (A) a large portion of a typical ordered array (B) a close up of one of the holes and surrounding nanotubes.....	122
Figure 3.9.	Simion 8 simulation showing the equipotential distribution For a cross-section slice of vertically aligned carbon nanotubes.....	124
Figure 3.10.	Simion 8 simulation depicting the equipotential distribution for a patterned array where each nanotube is separated by a distance equal to one half its length.....	126
Figure 3.11.	The relationship between the length of an isolated nanotube and the simulated local field strength	128
Figure 3.12.	Plots showing the calculated relationship between A) the diameter of a nanotube and the local field strength and B) the tip sharpness of a nanotube and the local field strength.....	129
Figure. 3.13.	Equipotential distribution calculated to determine the effect of introducing holes into an array of CNTs.....	131
 Chapter four - Field Ionisation of Gases using Carbon Nanotubes		
Figure 4.1.	Schematic of the first generation source (arrangement used in field ionisation experiments).....	135
Figure 4.2.	Plot showing an example of the Field emission results obtained at base pressure.....	139
Figure 4.3.	Fowler-Nordheim plot derived from A, the data in figure 4.2 and B the average of 6 sets of data.....	141

Figure 4.4.	Average FI current-voltage characteristic (from 3 experiments with the same CNT emitter) of the first generation FI source for acetone. Note that an error bar is not included for the last data point measured with a acetone at a concentration of 1.09×10^{-5} because in several cases the measurement exceeded the scale of the electrometer used.....	144
Figure 4.5.	Schematic of a second source. Electrode 6 was used to measure current at the end of the lens stack and was removed for experiments in which the object was to transfer charge species beyond the source chamber.....	148
Figure 4.6.	Photograph of source optics used during research with the second-generation source.....	149
Figure 4.7.	Micrographs recorded using a Zeiss SUPRA 55-VP FEG scanning electron microscope showing A) an array of nanotubes cut using laser machining and B) an enlarged region of the array showing the destruction wrought on CNTs near the edge of the array by the machining process.....	150
Figure 4.8a.	Simion 8 simulation of second generation CNT FI ion source (Figure 4.5) showing the trajectory of ions (in green) emitted from a 1 mm diameter wafer of carbon nanotubes. Ions with a red trajectory are emitted from the centre of the array over a diameter of 0.5 mm.....	155
Figure 4.8b.	Simion 8 simulation showing the trajectory of ions emitted from a 1mm diameter wafer optimised to focus and collimate the ions emitted from the centre of the array over a diameter of 0.5 mm.....	156
Figure 4.9.	Graph showing the stability of the emission from carbon nanotube emitter over time.....	159
Figure 4.10.	Comparison between the current obtained using A) a sample of the patterned array of CNTs and B) a sample of the dense array of CNTs.....	161
Figure 4.11.	Simion 8 simulations showing the trajectory of ions emitted from the edge (up to 0.1 mm from the edge) of a 1 mm diameter wafer of carbon nanotubes when an aperture of a) 6 mm and b) 8 mm is present in electrodes 3 and 4.....	163

Chapter five - Direct Introduction of Liquids into the Carbon Nanotube Source

- Figure 5.1** Schematic of the field desorption/field ionisation ion source (adapted with permission from the mechanical drawing by Dr Alex Colburn).....**168**
- Figure 5.2.** Photograph of the emitter mount, with a used carbon-nanotube emitter attached.....**169**
- Figure 5.3.** Photograph of the carbon nanotube emitter assembly and the supporting cylinder.....**171**
- Figure 5.4.** Micrographs showing A) the array of holes from the drilled side prior to sonication and B) one of the holes on the side on which CNTs were to be grown.....**174**
- Figure 5.5.** Photos showing A) a machined wafer and B) a tool fabricated to help remove each emitter disc from the wafer..**176**
- Figure 5.6.** Calculated trajectories of ions emitted from a carbon-nanotube emitter through the counter electrode region (in black) and ion conveyor region (in red). Applied potential had been adjusted to optimise transmission.....**179**
- Figure 5.7.** Calculated trajectories of ions emitted from a carbon nanotube emitter through the counter electrode region (in black) and ion conveyor region (in red) with a potential of -2.5 kV on the counter electrode. (molecular gas velocity 110 mm per second).....**181**
- Figure 5.8.** Spectra recorded using in each case a fresh emitter of A), vancomycin with a counter-electrode potential (5 kV), B) vancomycin without a counter-electrode potential, and C) xylene with a counter-electrode potential of 5 kV.....**187**
- Figure 5.9.** Micrographs showing A, a large region of a used emitter and B, enhanced region showing a carbon nanotube clump..**189**

List of Tables

Table 3.1.	Lattice spacings for carbon nanostructures.....	104
Table 3.2.	Simulated field strengths illustrating the change in local field strength when portions of the CNT array are removed..	125
Table 3.3.	Simulated field strengths illustrating the change in local field strength when the distance between neighbouring nanotubes is altered.....	127
Table 3.4.	Calculated field strengths illustrating the change in local field strength when a hole is present.....	130
Table 4 1.	Average counter electrode current measured (from 5 sets of data) for a number of different gasses under field ionisation conditions.....	144
Table 4.2.	Summary of the relationship between the current recorded at electrode 3 and different samples of CNT array under comparable FI conditions.....	158
Table 4.3.	Current measured at several stages within the optics of the second-generation source. A potential difference between CNTs and counter electrode of 7.5 kV was used during these experiments.....	162
Table 5.1.	Relative field strengths generated by the different morphologies as predicted by Simion 8.....	190

Acknowledgements

Over the course of my Ph.D., many people have given me support and assistance towards achieving my goals; in particular I would like to thank:

My academic supervisor Professor Peter Derrick who I feel I have come to know well towards the latter part of my Ph.D. Peter has never wavered in providing guidance and support through some quite difficult times.

Dr Alex Colburn for his help in solving numerous experimental problems, his help designing parts of instrumentation as well as his friendship and the interesting conversations that we have had over coffee.

Dr Tom Drewello for introducing me into mass spectrometry and his continuing support and friendship

Dr Mark Barrow, Dr Stephanie Geoffroy and Dr Anastasios Giannakopoulos for their mass spectrometry tuition and for staying patient when I bombarded them with endless questions about mass spectrometry.

Dr Gary Lau and Matthew Gill for their numerous acts of assistance in helping me push my projects forwards and for their friendship.

Dr Raff Da Campo, Kym wells, Marek Mahut, Leanne Nye, Jannice Chung and Dr Petr Man have been good friends and colleagues throughout this work, stimulating helpful discussion and offering practical aid.

Dr Aunshih Teh and Dr Mark Mann from the University of Cambridge for providing the arrays of carbon nanotubes crucial to my work.

The other academics and employees of the University of Warwick and the University of Massey who have helped me including Professor Julie McPherson, Dr Steve York, Dr Susan Burrows, Marcus grant, Lee Butcher, Peter Lewis, Dr Henning Klank, David Lloyd, Steve Denby and Keith Whitehead.

I would like to acknowledge the financial support of the EPSRC and sponsorship by Bruker Daltonics.

Finally I would like to thank my family for their help and support and in particular my partner Catherine Tate for her love and support through difficult times.

Declaration

I hereby declare that this thesis is my own work and that, to the best of my knowledge and belief, it contains no material previously published or written by another person, nor material which to a substantial extent has been accepted for the award of any other degree or diploma of a university or institute of higher education, except where due acknowledgement is made in the text. I particularly acknowledge the contributions of Matthew Gill in the characterisation of the dual-channelled nano-electrospray emitters featured in chapter 2 and Dr Alex Colburn in the design of the carbon nanotube source presented in chapter 5 of this thesis.

Lewis Paul Mark

Abbreviations

α	Angle of ion spread entering a single magnetic or electrostatic sector
γ	Enhancement factor
ΔP	Pressure differential
ΔV_s	Energy spread
Λ	Depth of the atomic potential well
μ	The Fermi level
μ	Dynamic viscosity
π	Pi = 3.14159265
ρ_s	Surface resistivity
ΣI_n	The energy required to ionise an atom already removed from the surface
Φ	The work function
ω_c	Angular velocity of an ion
$^{\circ}\text{C}$	Degrees centigrade
K	Kelvin
\AA	Angstrom
a	Gas transmission probability
A	Amps
B	Force of a magnetic field
BioTOF	Bruker Time-of-flight instrument
C	Coulomb
CE	Counter electrode
CI	Chemical ionisation
CID	Collision induced dissociation
CNT	Carbon Nanotube
CRM	Charge residue model
CVD	Chemical vapour deposition
d	Diameter
d_{ft}	length of flight tube in a time-of-flight instrument
D_i	Width of an insulating material
d_{ie}	Inter-electrode distance
d_0	Molecular diameter of a gas
DART	Direct analysis in real time
DESI	Desorption electrospray ionisation
E	Electric field
E_k	Kinetic energy
EI	Electron impact ionisation
EDX	Energy-dispersive X-ray
ESI	Electrospray ionisation
eV	Electron volt
F	Lorentz Force observed by an ion when entering a magnetic field
F'	Centrifugal force
f_c	Induced cyclotron frequency
F_g	Global field
F_l	Local field
F_M	Force that an ion encounters upon entering a magnetic sector

FD	Field desorption
FDI	Field desorption ionisation
FI	Field ionisation
FID	Fourier induction decay
FN	Fowler Nordheim
FOCL 1	Source transfer optic in the Bruker 9.4 T FT-ICR instrument
FOCL 2	Source transfer optic in the Bruker 9.4 T FT-ICR instrument
FTMS	Fourier transform mass spectrometry
FT-ICR	Fourier transform ion cyclotron resonance
Hz	Hertz
hr	Hour
HPLC	High pressure liquid chromatography
I	Current
I_n	n th ionisation energy
I_p	Ionisation potential required to remove a valence electron from an atom
ICR	ion cyclotron resonance
I.D.	Inside Diameter
IEM	Ion evaporation model
J	Joule
K_n	Knudsen number
KAA	Tripeptide di-N-acetyl-l-Lys-d-Ala-d-Ala
L	Litres
L_i	Thickness of an insulator
L_t	Length of tubing
l	Length
LIFDI	Liquid injection field desorption ionisation
m	Meter
m	Mass of an ion
M	Molecular weight
m_r	Molecular mass
MS	Mass spectrometry
m/z	Ratio of mass to charge of an ion
magTOF	Home-made magnetic sector time-of-flight instrument
MALDI	Matrix assisted laser desorption ionisation
MWCNT	Multi-walled carbon nanotubes
N_A	Avogadro's number
nanoESI	Nano-electrospray ionisation
oa-TOF	Orthogonal acceleration time-of-flight
NdYAG	Neodymium doped Yttrium Aluminium garnate
NMR	Nuclear magnetic resonance
O.D.	Outside Diameter
P	Pressure
P_b	Native or base pressure
P_i	Pressure given by an ion gauge
P_w	Power
Pa	Pascal
pH	Measure of the acidity or basicity of a solution
PE-CVD	plasma-enhanced chemical vapour deposition
PEEK	Polyetheretherketone

PEEKsil	Fused silica capillary clad in polyetheretherketone
PID	Proportional–integral–derivative
PL1	Source transfer optic in the Bruker 9.4 T FT-ICR instrument
PL2	Source transfer optic in the Bruker 9.4 T FT-ICR instrument
PL4	Source transfer optic in the Bruker 9.4 T FT-ICR instrument
PL9	Source transfer optic in the Bruker 9.4 T FT-ICR instrument
PTFE	Polytetrafluoroethylene
psi	Pounds per square inch
q	Number of charges that an ion possesses
Q	Flow rate
QBSD	Quadrant Back Scattering Detector
QEA	Quadrupolar excitation axialisation
r	Radius
R	Universal gas constant
R_e	Resistance
r_{ig}	Relative sensitivity of an ion gauge to a particular gas
RAM	Rapid access memory
RF	Radio frequency
s	Second
S	Pumping speed
SEM	Scanning electron microscope
SWCNT	Single-walled carbon nanotubes
t	time
T	Tesla
T	Absolute temperature
t_r	Total time an ion spends in a single stage reflectron
TEM	Transmission electron microscope
TOF	Time-of-flight
v	Velocity
V	Volt
V	Potential
V_a	Potential energy of an atom
V_i	Potential energy of an ion
V_i	Potential difference across an insulator
v_{ix}	Velocity at which an ion enters the first stage of a reflectron
V_s	Accelerating potential of an ion source
W	Watt
X	Point at which an ion beam focuses upon exit of a double sector instrument
x	Reflectron depth
x	Distance from a metal surface
XDFL	X-axis deflectors
YDFL	Y-axis deflectors
z	Unit of charge

Abstract

The thesis describes the development of various novel emitters for the production of gaseous ions from solutions of non-volatile, thermally labile samples for the purposes of mass spectrometry.

Nano-electrospray emitters each containing two separated channels running throughout the length of the emitter were fabricated and evaluated. These emitters were made from “theta-shaped” borosilicate capillaries, employing a number of different coating procedures. Loading of different solutions into the channels demonstrated the possibility of studying solute interactions on ultra-short timescales. It is proposed that interactions took place in a shared Taylor cone. The formation of specific adducts from vancomycin and diacetyl-l-lysyl-d-alanyl-d-alanine was observed by mass spectrometry. From consideration of the extent of H/D exchange between vancomycin and deuterated vancomycin, it was concluded that the interaction times were of the order of 10^{-5} s.

Underlying theoretical considerations, design and fabrication from carbon nanotubes (CNTs) of emitters for field desorption and field ionization ion sources are described and discussed. The emitters fabricated made use of arrays of vertically aligned multi-walled CNTs with in most cases an average length and radius of 15 μm and 35 nm respectively. Emitters using dense coverings of nanotubes and emitters with nanotubes selectively grown so that the height of each nanotube was twice its separation from its nearest neighbour were

investigated. Characterisation of the CNTs by field electron-emission confirmed their effectiveness as field emitters. Fowler-Nordheim plots indicated fields of $6.14 \times 10^9 \pm 0.72 \times 10^9$ V/m at a potential of 700 V. Field ionization of He, Ar, Xe, methane and acetone was achieved with these same CNTs; neither the inert gases nor methane have been field ionised with conventional activated-wire emitters. The fields generally accepted to be required for field ionisation of He and Ar are of the order of several 10^{10} V/m.

To create emitters which would not need to be removed from vacuum between experiments, a means of injecting both liquids and gaseous samples directly to the bottom of the CNTs was devised. This involved drilling 20 μm diameter holes through the silicon substrate between intended sites of nanotube growth, but before actually growing the CNTs. It was discovered that the presence of the holes led to surface migration of the nickel catalysts initiating CNT growth. Experiments undertaken to achieve mass spectrometric measurements with the arrays of CNTs as emitters are described and discussed.

1. Introduction to Mass Spectrometry

1.1 Early mass spectrometry. – From the electron to the atom bomb

The origin of mass spectrometry can be traced back to the late 19th century, a time at which the present-day image of atoms and molecules did not exist.

Scientists of the day were fascinated by the question of what was occurring inside a discharge tube. Slightly earlier in the century, Sir William Robert Grove had brought to the attention of scientific communities the fact that a gas at a certain pressure would produce a light or discharge when an electric potential was applied across it ¹. The solution to this phenomenon was pursued by a number of scientists and these endeavours would eventually lead to the discovery of both the electron and ionised species.

In 1886 a German physicist called Eugene Goldstein coined the term ‘cathode rays’ to represent the emissions from the cathode within a discharge tube. From his own studies with discharge tubes he discovered the existence of a second type of ray, travelling in the opposite direction within the discharge tube. He named these rays kanalstrahlen or canal rays after the way he discovered them emerging through channels at the back of a perforated cathode ². A positive step towards determining the nature of cathode rays was made by Jean Perrin when he identified that cathode rays consisted of negatively charged particles, by using a magnetic field to bend the rays into a faraday cup ³. The English physicist J.J. Thomson repeated the experiments conducted by Perrin and went on to prove that at low pressure cathode rays could also be bent by electric

fields. J.J. Thomson also conducted experiments designed to quantify how much a cathode ray would be bent in a magnetic field and how much energy this ray would carry. From this data he found that the mass-to-charge ratio of a species was directly related to the amount the species was deflected by a magnetic field. He was therefore able to calculate roughly the *ratio* of the mass of a particle to its electric charge (m/z). From these experiments Thomson concluded that the cathode rays consisted of negatively charged particles (which he called corpuscles) and that these particles are constituents of the atom⁴. With these experiments Thomson had discovered the negative particle now known as the electron.

Experiments to determine the nature of canal rays were reported by Wilhelm Wien in 1898⁵. He discovered that in comparison to cathode rays a much larger magnetic field was required to deflect them. The deflections, however, were opposite in nature to cathode rays, and so Wien concluded that these rays consisted of positively charged particles. To investigate these rays further he constructed a device that utilised both electric and magnetic fields to separate the positive rays according to their mass-to-charge ratio. Using this apparatus he was able to find that the mass-to-charge ratio depended on the gas in the discharge tube.

During the first decade of the 20th Century, J. J Thomson also turned his attention to the nature of positive rays^{5,6}. The experiment constructed by Wein can be accredited with laying the first foundations for mass spectrometry for it is on his equipment that J.J. Thomson based his first experiments. Thomson's

phenomenological development culminated in 1913 when he reported the first example of a mass spectrometry experiment in action – the determination of two isotopes of neon⁷. In Thomson's experiment a channelled stream of ionized neon was introduced through a magnetic and an electric field and the deflection measured by placing a photographic plate in the beam's path. Two patches of light could be observed and on the basis of mathematical treatment of this and the fields involved Thomson was able to determine the atomic mass of the ions. This led to the conclusion that neon gas was composed of atoms of two different atomic masses (neon-20 and neon-22). Thomson saw the potential of this technique and with the publication of his book in 1913 he issued a challenge to his peers to investigate the technique further:

'I have described at some length the application of Positive Rays to chemical analysis; one of the main reasons for writing this book was the hope that it might induce others, and especially chemists, to try this method of analysis. I feel sure that there are many problems in chemistry, which could be solved with far greater ease by this than any other method. The method is surprisingly sensitive — more so than even that of spectrum analysis, requires an infinitesimal amount of material, and does not require this to be specially purified; the technique is not difficult if appliances for producing high vacua are available.'

Several of Thomson's peers took up his challenge including in particular F.W. Aston in the UK and A.J. Dempster in the USA. Aston worked with J.J. Thompson as an assistant during his early career so had an insight into the

intricacies of the technique. Shortly after World War I Aston built the first of several mass spectrographs⁸. This instrument consisted of a discharge bulb (ion source), magnet and ion optics to create both velocity and directional focusing of ions. With this apparatus Aston was able to confirm Thomson's experiments regarding the existence of two isotopes of neon⁹ and went on to investigate the isotopic composition of other elements including chlorine and mercury¹⁰.

During the same period Dempster had also built a mass spectrograph instrument¹¹ that utilised a slightly different ionisation method. A sample was heated on a metallic plate and then bombarded with electrons from a hot metal filament. With this Dempster had devised the first electron impact ion source. Dempster used his mass spectrographs to determine the isotopic abundances of elements such as magnesium and his research eventually led him to the discovery of the uranium isotope ^{235}U in 1936¹².

The field of isotopic separation held much of interest to the general chemist at the time of the first mass spectrographs. It is therefore not surprising that once mass spectrographs were found to be capable of the precision mass analysis of an element's isotopes, this interest sustained the new technique's development through the early 1930s. The ability to separate isotopes using electromagnetic fields took a significant twist in the early 1940s when mass spectrographs called Calutrons played a key part in the Manhattan Project. Calutrons, which consisted of an ion source, magnetic sector and collection cup, were used in the production of industrial amounts of the ^{235}U isotope, destined for use in the Atomic bomb 'Little Boy' which was dropped on Hiroshima¹³.

While some mass spectrometry pioneers believed that once the elemental composition of all known elements were identified the technique would have run its course, others believed that there was scope to improve the accuracy and expand the technique beyond isotopic analysis. In hindsight, this line of thought has subsequently opened the door to the development of the analytical tool that is now crucial for most scientific research and industry. ^{2, 14}

1.2 Mass analysers

1.2.1 Sector mass-analysers

1.2.1.1 Magnetic sectors

The early mass spectrometers or spectrographs constructed by Aston and Dempster relied on a magnetic field to deflect a beam of ions by different amounts according to their masses. Ions created in the source of a mass spectrograph will have an inherent kinetic energy E_k at the source exit, (equation 1.1)

$$E_k = \frac{mv^2}{2} = qV_s \quad \text{Equation. 1.1}$$

An ion has a mass m and charge q , and is accelerated through a potential difference V_s to a velocity v . Ions entering the magnetic sector will experience a

force F_M perpendicular to the velocity, as defined by equation 1.2, and in a direction according with Fleming's left-hand rule.

$$F_M = qvB \quad \text{Equation. 1.2}$$

B is the magnetic field. This force F_M causes the ions to enter a circular trajectory with a radius r so that the centrifugal force equilibrates with the magnetic force as shown in equation 1.3

$$qvB = \frac{mv^2}{r} \quad \text{or} \quad mv = qBr \quad \text{Equation 1.3}$$

Combining equations 1.2 and 1.3 shows that when B and V_s are held constant, the ion trajectory radius is directly proportional to the square root of the mass-to-charge ratio (see equations 1.4 and 1.5).

$$\frac{m}{q} = \frac{B^2 r^2}{2V_s} \quad \text{Equation 1.4}$$

$$r = \frac{1}{B} \sqrt{2V_s \frac{m}{q}} \quad \text{Equation 1.5}$$

Ions of different masses but the same charge in the same ion beam will therefore have different radii as they pass through the magnetic field, and will therefore have different positions as they exit the magnetic field. In the case of Thomson and Aston's instruments, ions would hit a photographic plate and the ion's

position on this plate would then be assigned a mass according to the amount of deflection. A second method of operation that is used in most modern magnetic-sector mass analysers is to change the magnetic field as a function of time. If the magnetic sector flight tube is defined to allow only a small range of ion radii (in effect fixing r) then, as can be seen in equation 1.4, for a given value of B only a corresponding mass over charge m/q ratio will go through the analyser.

Changing the magnetic field over time allows successive scans over the entire mass-to-charge range of the ions present.

1.2.1.2 Electric sectors

Electric fields can be used to deflect ions by different amounts according to their kinetic energy. Electric sectors typically consist of a radial electric field applied across two parallel curved plates. As ions enter the field they experience a force causing them to adopt a curved trajectory with a radius of r as defined by equation 1.6,

$$r = \frac{2E_k}{qE} \quad \text{Equation 1.6}$$

E is the electric field strength, q the charge of the ion and E_k the ion's kinetic energy. The equation shows that the radius of the circular trajectory that the ion adopts through the sector is proportional to the kinetic energy that the ion has as it enters the sector. This means that ions with a large kinetic energy will be deflected less by the electric field than ions with low kinetic energies and

therefore ions of the same mass but different energies will be separated by the electric sector.

Electric sectors are normally used in conjunction with a magnetic sector to correct for kinetic energy aberrations of same-mass ions. Aston's mass spectrograph from 1919 is an early example of an electric field being used in this way. In Aston's instrument an electrostatic condenser (analogous to an electric sector) was placed just ahead of a magnetic field. The purpose of the condenser was to separate ions with different velocities so that ions with large velocities would experience less of the following magnetic field than those with lower velocities. This would create a focal point beyond the magnetic field at which ions with the same mass and a range of different velocities could be measured at the same point on a photographic plate. This focusing effect is called velocity focusing.

1.2.1.3 Double focusing analysers - combinations of magnetic and electric sectors

Both magnetic and electric sectors focus ions spatially, i.e. ions entering the field perpendicular to the field edge and at an angle α to the perpendicular ion will converge as they exit the sectors as shown in figure 1.1.

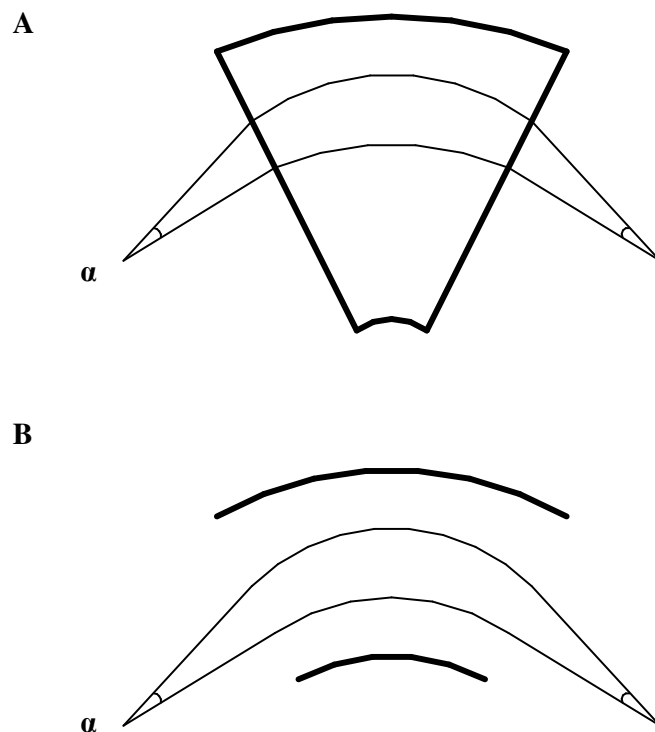


Figure 1.1. Spatial focusing in A) a magnetic sector and B) an electric sector

The ideal operation of magnetic sectors assumes that ions of the same mass will have the same kinetic energy. In reality this is rarely the case, and the resolution that a single magnetic sector can achieve is typically limited by the energy spread of the ions.

Aston's early attempt at velocity focusing proved to be the key to solving this problem: combining a magnetic sector with an electric sector in which the kinetic energy dispersion of one sector compensates for that of the other. Placed in series, the energy dispersion of the first sector should be corrected by a convergence effect of the second sector (figure 1.2). The combination of sectors with matching kinetic energy distributions gives rise to the term "double focusing", because ions are focused both spatially and by their velocity.

Herzog was the first to find a solution for the paths of charged particles through electric and magnetic fields, which allowed the first double-focusing mass spectrometer that could account for kinetic energy aberrations to be constructed by Herzog and Mattauch in 1934¹⁵. Later in 1953 Nier and Johnson developed a double-focusing sector mass spectrometer that could account for both first and second-order spatial aberrations¹⁶.

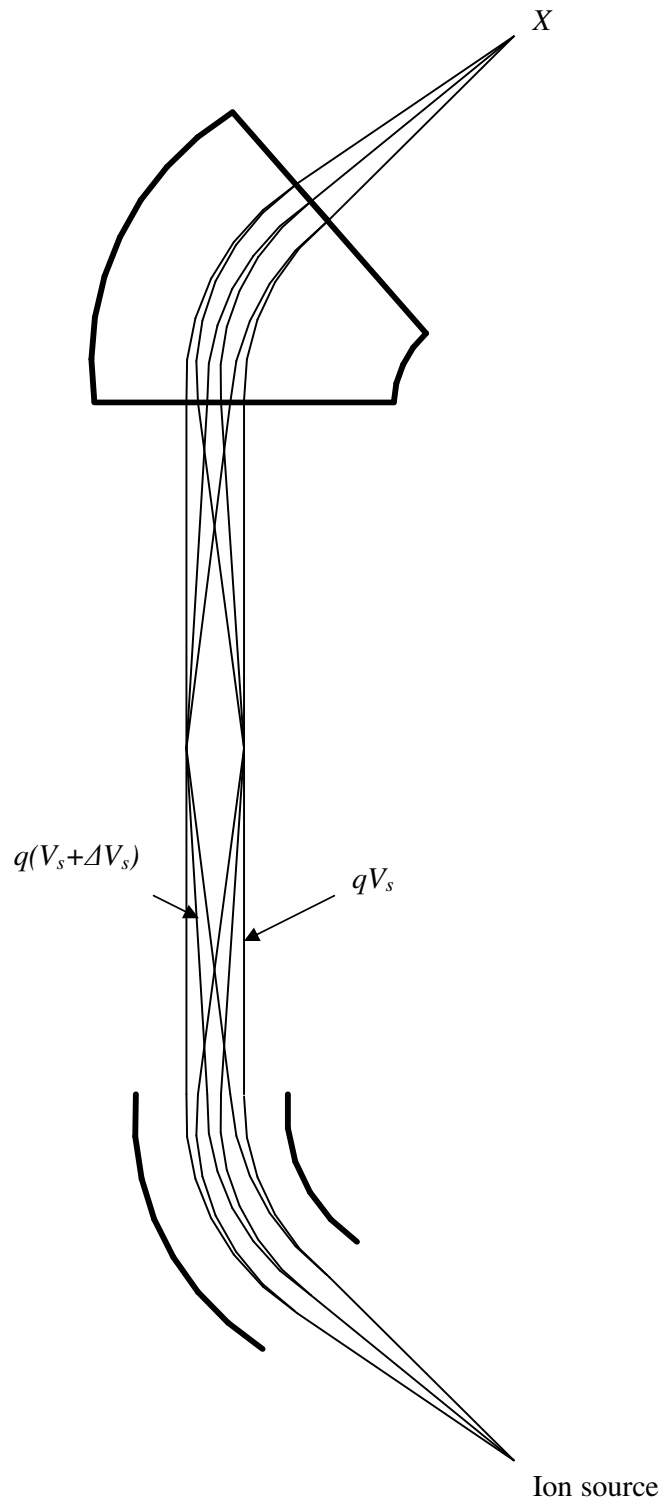


Figure 1.2 Combination of magnetic and electric sectors. The energy dispersion from the first sector is noted as qV_s and $q(V_s + \Delta V_s)$. This is corrected upon exiting the second sector at a focal point X

1.2.1.4 The magnetic-sector time-of-flight (magTOF) instrument.

1.2.1.4.1 Introduction.

The combination of two mass analysers, or tandem mass spectrometry, is used to analyse fragment ions created by processes such as collision-induced dissociation (CID). Scanning mass-analysis techniques such as a magnetic sector are very useful when selecting a precursor ion, however, they are not ideally suited to the role of the second mass-analyser due to the technique's inherent low sensitivity. The combination of a magnetic-sector with a time-of-flight analyser as the second stage aims to resolve these sensitivity issues.

The magTOF, a double-focusing time-of-flight mass spectrometer used in these studies, was built and designed with these considerations in mind ¹⁷. The instrument consisted of a double- focusing mass spectrometer with Nier-Johnson type geometry as the first stage of mass analysis and a quadratic-field ion mirror as the second stage. An ion buncher and collision cell were installed between the two analysers. A schematic of the instrument is shown in figure 1.3. Experiments in this study conducted with the magTOF utilised only the source and linear time-of-flight analyser, so only these aspects of the instrument are discussed in any detail.

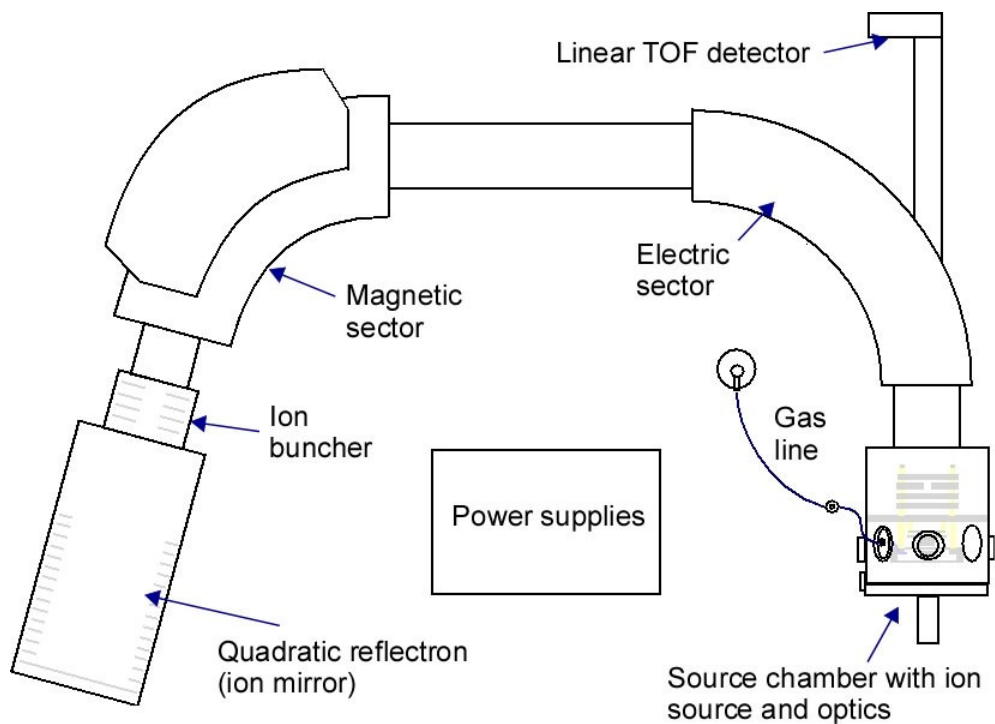


Figure 1.3 Schematic of the magTOF instrument

1.2.1.4.2 Ion source and the linear time-of-flight analyser

The source assembly was mounted on a grounded stainless-steel cradle, fixed to the inside of the source housing using two stainless-steel screws. This cradle was designed to support all the source components and to define the ion-optical axis. Source components were attached to the cradle using either metal or insulating PEEK spacers depending on their electrical requirements. To allow transmission through the cradle a 12 mm hole was drilled in line with the source exit. The source exit was an adjustable slit with a height of about 7 mm and a width which could be adjusted from 0-250 μm . For measurements with the linear TOF detector, this adjustable slit was usually removed to leave a 12 mm source exit hole. Access to the source was via a hinged door at the front of the

source. A Viton O-ring set into the door provided the vacuum seal. Potentials could be applied to the source components via three electrical feedthroughs situated on both sides and the top of the source housing, There was an ion gauge on the side of the source housing.

The original source housing had been designed with adaptability in mind¹⁷ and there were a number of redundant feedthroughs on the side of the source chamber. One of these was adapted to allow a supply of gas into the source. A PTFE tube was used to deliver gas inside the source in front of the cradle; the tube was connected to the feedthrough using a swagelok fitting. A pin valve (Negretti valve division) was connected using swagelok fittings to the exterior of the feedthrough to allow control of the amount of gas bleed into the source system.

The electric sector had been modified to allow linear time-of-flight measurements when the sector was grounded. The field-free region of the linear TOF had been achieved by drilling holes in the larger radius plate and the vacuum chamber of the electric sector in line with the ion optical axis of the source, and welding a stainless-steel tube onto the outside of the analyser's vacuum chamber. These modifications created a field-free region from source exit to detector of approximately 65 cm. To detect the TOF resolved ions an electron multiplier (ETP, Australia) with a multiplication factor of approximately 10^6 was used. A custom-made power supply was used to supply the high voltage required to operate the multiplier. A photograph of the modifications to the electric sector are shown in figure 1.4

The MagTOF instrument^{17, 18} was used in these studies to characterise carbon nanotube emitters.

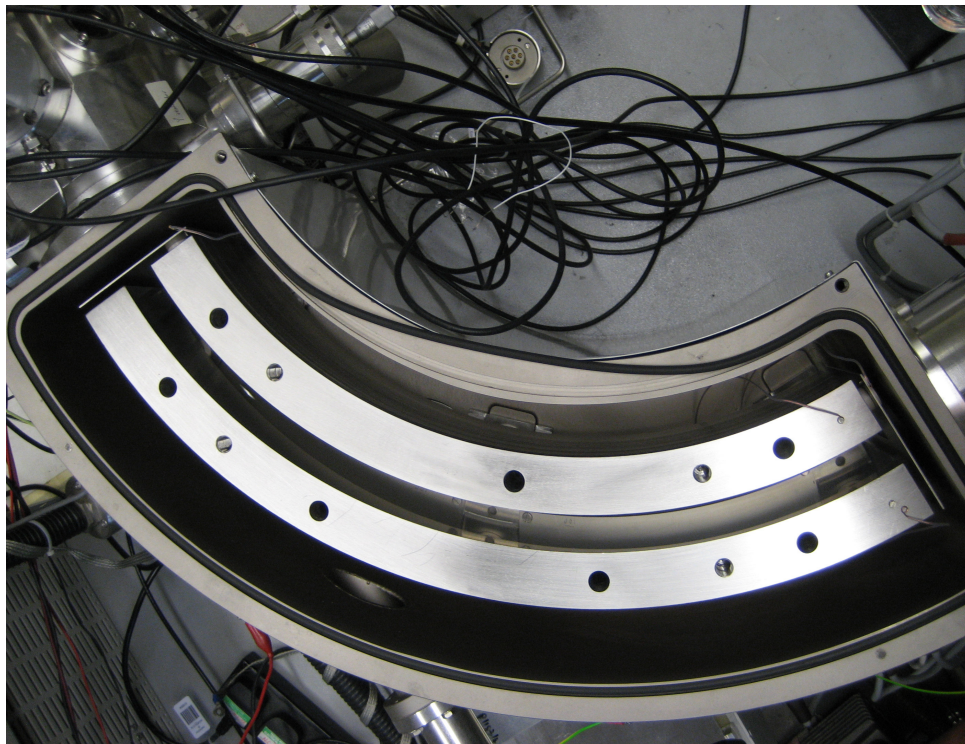


Figure 1.4. Modifications to the electrostatic analyser to allow linear time-of-flight measurements.

1.2.2 Time-of-flight mass analysers

1.2.2.1 Linear time-of-flight mass analysers

Time-of-flight (TOF) mass spectrometry was first described in 1946 by W.E. Stephens¹⁹. He believed that the technique would offer many advantages over the sector instruments used at the time, including, increased speed at which a

mass spectrum could be collected, removal of the need for bulky magnets and for stabilisation equipment and a resolution that did not depend on limiting factors such as slit size. Linear time-of-flight (TOF) is based on a fairly simple principle: the velocity-induced separation of mono-energetic ions as they travel through a field-free region. A continuous beam of ions from an ion source is stored and then, as ion pulses, accelerated by a potential V_s down a flight tube for a distance d_{ft} before reaching a detector. Ions of different masses but the same total charge $q = ze$ have the same kinetic energy (E_k) and therefore different velocities (v), (see equation 1.7).

$$\frac{mv^2}{2} = qV_s = zeV_s = E_k \quad \text{Equation 1.7}$$

The mass-to-charge ratio is determined by measuring the time an ion takes to move through the field-free region between source and detector. Combining equations 1.8 and 1.7 gives equation 1.9 for the flight time.

$$t = \frac{d_{ft}}{v} \quad \text{Equation 1.8}$$

$$t^2 = \frac{m}{z} \left(\frac{d_{ft}^2}{2V_s e} \right) \quad \text{Equation 1.9}$$

Equation 1.9 shows that, assuming all factors such as the kinetic energy and charge are equal; ions of smaller mass will travel faster and reach the detector first. There are several problems with factors limiting the performance of a linear TOF. Firstly, ions in an ion packet will travel very slightly different distances. Some will be closer to the detector at the front of the packet, and ions at the rear of the ion packet will travel slightly longer distances. This is a spatial error. Secondly there is no guarantee that ions with the same mass and charge will have exactly the same initial kinetic energy, and there is an energy dispersion aberration.

In 1955, Wiley and McLaren²⁰ proposed a focusing technique, called time-lag focusing, that would reduce the magnitude of each aberration. Time-lag focusing employs a time delay between the formation of ions and their extraction. During the time lag the ions experience a field-free region located just after the ion source. Ions of the same mass- to-charge with kinetic energy differences, such as different initial velocities or the same kinetic energy but travelling along different trajectories, travel different distances within the field-free region. Once the time lag period ends, an accelerating potential is applied across the previously field-free region. Ions experience different magnitudes of field at different places within the former field-free region. Ions that had larger initial velocities will be closer to the exit of the region and experience less of a potential drop than those ions with a smaller initial velocity have not penetrated through the region as far. The ions that experience more of the potential drop catch up with the initially faster ions at a focal point. By tailoring the potential

gradient it is possible to create a focal point at the detector for same mass-to-charge ratio ions that is independent of their initial kinetic energy. Time-lag focusing, later known as ‘delayed pulse extraction’ was found to increase substantially the resolution of the linear time-of-flight mass analysers. Wiley and McLaren’s prototype mass spectrometer design was later developed into the first commercially available TOF mass spectrometer marketed by the Bendix corporation ².

1.2.2.2 Ion reflectron in time-of-flight mass spectrometry

In the first few decades of commercial TOF, mass resolution proved to be a sticking point that restricted applications. While delayed extraction increased resolution, it was not until the development of the reflectron in 1973²¹ when the attainable resolution was sufficiently high to attract a wider field of interest. The concept of what the reflectron is and what it is able to achieve is fairly simple. Normally comprised of a number of shaped ring- electrodes, the reflectron creates a field that slows and eventually rebounds the ions that enter it back down the flight tube. In a comparison with a linear TOF analyser, the reflectron would be placed just before the position of the linear TOF detector and so ions that reach the reflectron would have already undergone a degree of TOF separation. The degree to which each ion penetrates the field of the reflectron is related to its kinetic energy. Ions with more energy will penetrate the field further and spend more time in the reflectron compared to ions of lower energy. This delay causes ions of the same mass but different energies to focus after

they exit the reflectron as shown in figure 1.5. In order to move this focal point to a reflectron detector, the correct flight length, reflectron electric field and source acceleration potential must be chosen.

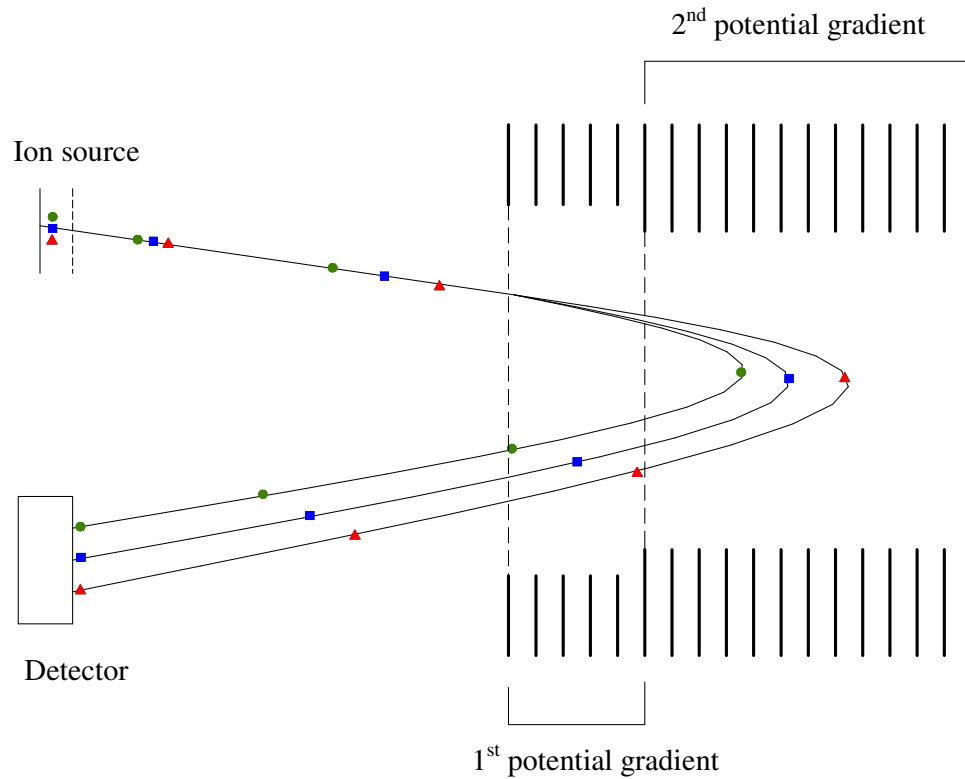


Figure 1.5. Double-stage reflectron TOF showing the focusing of 3 ions with the same mass but different kinetic energies.

Single-stage reflectrons have a uniform field and allow first-order velocity focusing. Double-stage reflectrons introduce a second potential gradient, which allows a further order of velocity focusing. This reasoning can be taken further: a reflectron with an infinite number of potential gradients should eliminate all orders of aberration. This would completely remove an ion's dependence on initial velocity and so the TOF would depend only on the mass-to-charge ratio.

Quadratic reflectrons¹⁸ can achieve this effect by utilising a field in which the field strength varies in the axial direction of the reflectron and there is a quadratic dependence of potential with distance.

1.2.2.3 Orthogonal acceleration in time-of-flight mass spectrometry

Pulsed ionisation techniques can be coupled directly with a TOF mass analyser. Continuous beam ionisation techniques, however, require an intermediate stage where the beam can be stored and ejected as ion packets. One approach to creating ion packets is to pulse part of the source ion optics such as a deflector. The ion beam is deflected away from the source exit until, at set time intervals, the deflection voltage is relaxed and a pulse of ions is allowed through. Although beam modulation has some advantages²², this method is not an ideal way of creating ion packets as most of the ions from the ion source are lost.

A slightly more sophisticated method of creating ion packets involves introducing a storage stage to the source ion optics. This storage device might be a multipole (hexapole, quadrupole) capped at both ends with trapping electrodes and operated in the following way. Ions would flow into the multipole, become trapped and are stored for a defined amount of time while more ions fill the multipole. Once Ions have been collected for the desired amount of time, a potential is applied to the multipole in order to eject all the ions as one ion packet, this process is repeated in order to mimic a pulsed

source. In principle an ion storage device as outlined ensures that a large percentage of the ions produced in the source are used.

Orthogonal acceleration time-of-flight (oa-TOF) mass spectrometry takes the method of ion storage one step further with significant advantages. In oa-TOF, ions are ejected in a direction orthogonal to the ion beam axis. The separation of the TOF and source axes leads to a number of advantages: The average initial velocity component in the TOF direction is reduced to zero and the spread of velocity components is reduced. Spatial errors created by a large ion packet are almost eliminated as the ions are ejected perpendicular to the length of the packet. These advantages lead to a significant increase in resolution to around 25000²³, which is a far cry from the several 100 obtained by the first time-of-flight mass spectrometers.

1.2.2.4 The BioTOF instrument

1.2.2.4.1 Introduction

Instruments that use a combination of time-of-flight (TOF) mass analysis and electrospray ionisation have become very popular for biochemical analysis. This can be attributed to several factors, most instruments are compatible with techniques such as liquid chromatography, the technique is suitable for a large percentage of the mass spectrometry species of interest, the time it takes to

produce a mass spectrum is relatively short and the resolution achieved is normally reasonable. While much larger, the BioTOF instrument can perhaps be considered as an early forerunner to the TOF bench-top instruments that are a common site in laboratories today.

The Bruker BioTOF I mass spectrometer used in these studies (Bruker Daltonics, Billerica USA) consisted of a 120 cm long flight chamber equipped with a double-stage reflectron coupled with an electrospray ion source (Analytica, Branford CT USA) and orthogonal accelerator. The original source optics had been replaced with a homemade ion-focusing device called the ion conveyor²⁴. Figure 1.6 shows a schematic and picture of the instrument.

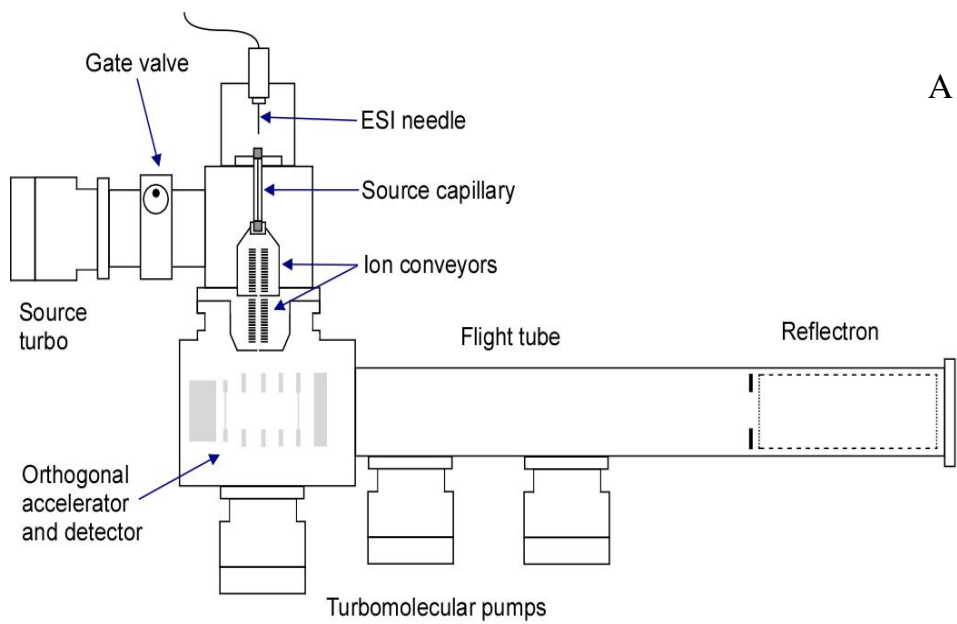


Figure 1.6. a) Schematic and b) photograph of the bioTOF I mass spectrometer.

1.2.2.4.2 The Ion conveyor

The ion conveyor is a home-built ion-focusing device designed to replace the transfer optics and multipoles common in most electrospray sources.²⁴ The transfer optics and multipoles in an electrospray source are typically located in several vacuum regions, which are necessary to create a pressure differential between the electrospray needle and flight tube. A large proportion of the available ionisation current is normally lost in these regions due to the necessity to restrict the conductance between different vacuum regions by including electrodes, otherwise known as skimmers, with small apertures. The primary function of the ion conveyor in the BioTOF was to provide a method of focusing and collimating an ion beam so that the passage through the conductance restrictions did not lead to such losses in ion current.

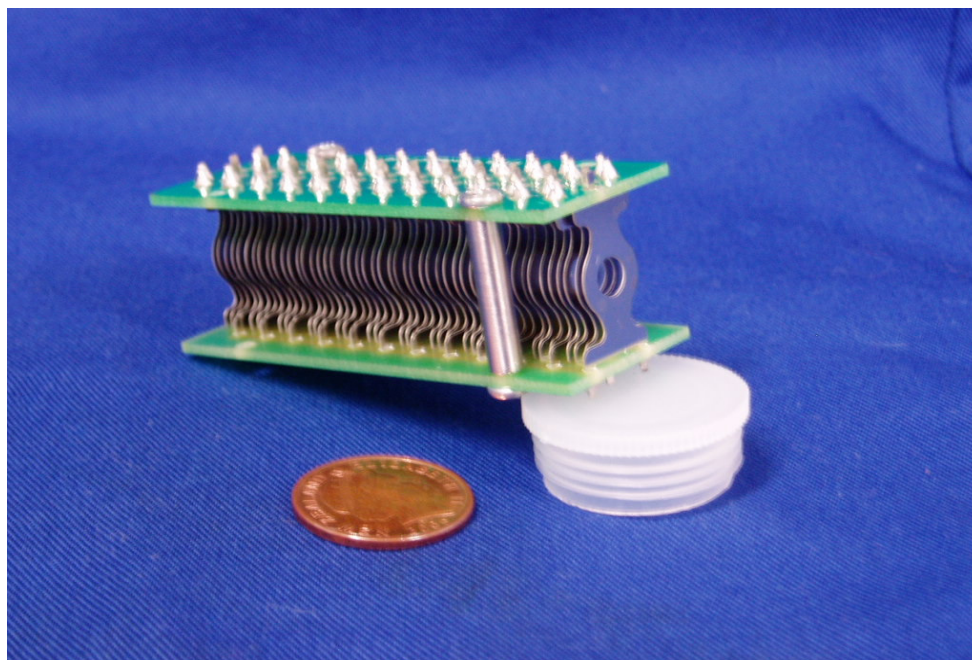


Figure 1.7. Photo of an ion conveyor, a 1 pence coin is included for size comparison.

Each ion conveyor in the BioTOF consisted of a series of ring electrodes (see figure 1.7) which were supplied with a series of 4 sinusoid potentials phase-shifted 90 ° with respect to each other. The combination of the four waveforms could be thought of as creating a travelling wave reproduced in the electric field within the electrode structure. This would create a series of interlinked ‘Paul’ traps²⁵ that, in essence, would trap and focus (with the essential involvement of ion-neutral collisions) the ions in a series of pseudo potential wells that propagated along the axis of the conveyor. Ion-neutral collisions which take place frequently in high-pressure regions are thought to play a vital role in the operation of the conveyor by cooling the ions. Cooler ions have less energy to escape from the pseudo potential wells. A more in-depth explanation of the principle of operation can be found in ion conveyor papers by Colburn et al²⁴,²⁶.

The BioTOF’s source consisted of two neighbouring vacuum regions isolated by an electrode with a 1 mm aperture. The ion conveyor had been installed on the ion optical axis in each vacuum chamber so that the two devices operated in sequence. The first conveyor was located directly after the electrospray source glass capillary in this region of relatively high pressure (of the order of 1 mbar). The second conveyor utilised the dividing plate between the two vacuum regions as its entry electrode and was aligned with the 1 mm hole. Typically the vacuum in the second region was of the order of 1×10^{-3} mbar. The second conveyor was used to accumulate ions before ejecting them into the orthogonal accelerator. The waveforms and other potentials used in each conveyor were controlled using a home-built power supply and a TG 550 function generator

(Thurlby Thandar Instruments Ltd, Huntingdon, Cambridgeshire, UK). The extract potential used to pulse ion packets out of the second conveyor was controlled using the BioTOF-lite acquisition and control software. A schematic of the source and ion conveyors is shown in figure 1.8.

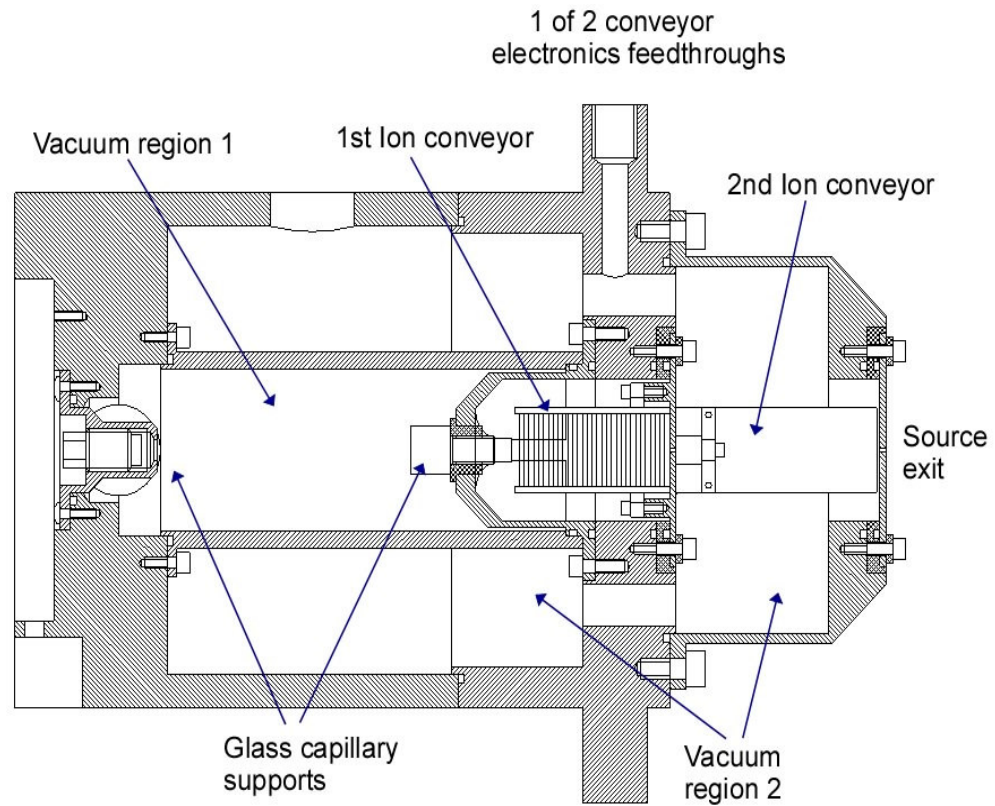


Figure 1.8. Schematic illustrating the position of the ion conveyors in the BioTOF's source

1.2.2.4.3 The orthogonal accelerator and detector

The orthogonal accelerator consisted of an extraction region, repeller and multideflector. A schematic of these components along with the location of the TOF detector is shown in figure 1.9. Upon extraction from the ion conveyor, a packet of ions was transferred to the acceleration region of the orthogonal accelerator. When the packet filled the region, and after a pre-determined transfer delay, a high voltage pulse was applied to the repeller. The high potential accelerated the ion packet out of the extraction region orthogonally and at the same time prevented any more ions from entering the extraction region. The multideflector was used to correct the sideways velocity component from the ions' original motion and thus ensure that the trajectory of ions leaving the accelerator matched the axis of the flight tube.

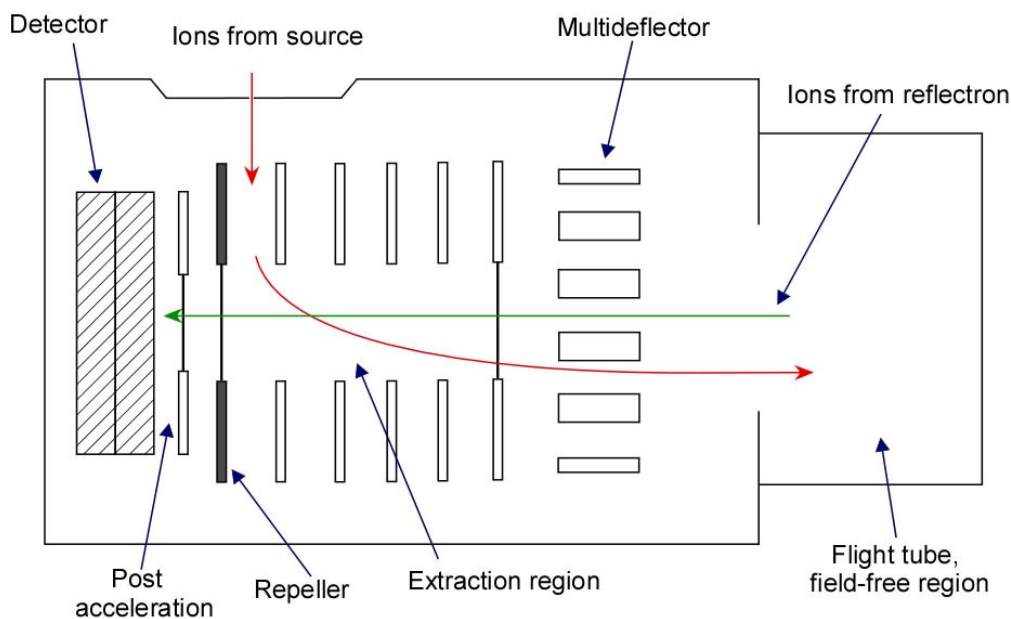


Figure 1.9. Schematic of the orthogonal accelerator installed in the BioTOF instruments.

The BioTOF's double-stage reflectron was coupled with a reflectron lens, which was used for ion collimation. Ions emitted from the reflectron travelled back down the flight tube and entered the orthogonal acceleration region. The steering potential and acceleration potential applied by the multideflector and repeller respectively were switched off according to a timed delay to allow the passage of ions through to a detector. The potentials applied to the orthogonal accelerator and reflectron arrangement were controlled using the BioTOF-lite acquisition and control software.

1.2.2.4.5 The vacuum system

The BioTOF Instrument was pumped by two rotary backing pumps and three turbomolecular pumps (Edwards, Crawley, West Sussex, UK). A vacuum of 1×10^{-9} mbar as indicated by an Edwards metal-sealed active inverted magnetron gauge and controller was normally achieved in the flight tube. A pressure in the flight tube of no higher than 5×10^{-7} mbar was required in order to engage a pressure interlock fitted to the high-voltage supplies for the orthogonal accelerator and reflectron. The pressure in the source of the BioTOF was maintained by a backing ($18 \text{ m}^3/\text{hr}$) and turbomolecular pump (250 L s^{-1}). The first conveyor operated at a pressure of roughly 1mbar, which was sustained by the backing pump. The second conveyor required a lower pressure, which was maintained by the turbomolecular pump. A gate valve was fitted to the source turbomolecular pump in order that the pressure in the second vacuum-region could be varied. The pressures in the first and second regions were measured by

a thermovac and ionivac vacuum gauge (Leybold GmbH, Alzenau, Germany) respectively.

1.2.3 Fourier transform ion cyclotron resonance (FTICR) mass analysers

1.2.3.1 Principle of ion cyclotron resonance

The principle of ion cyclotron resonance (ICR) was first used to achieve mass spectrometric measurements by the omegatron mass spectrometer reported in 1951 by Sommer, Thomas, and Hipple²⁷. An ICR mass spectrometer was later commercially produced by Varian in 1968²⁸. It was not until 1974 that Fourier transform methods were applied to the principle of ICR, creating the technique Fourier transform ion cyclotron resonance mass spectrometry²⁹.

In Fourier transform mass spectrometry (FTMS), ions are injected into an ICR cell, which is located under high vacuum in a very strong magnetic field. When injected the ions experience ion cyclotron resonance which arises from interactions with the magnetic field. Ions are bent into a circular motion in a plane perpendicular to the field by the Lorentz or centripetal force given by the following equation 1.10:

$$F = qvB \qquad \text{Equation 1.10}$$

F is the Lorentz force experienced by the ion in the magnetic field B ; v is the velocity of the ion and q is the ion's charge. The trajectory that the ion takes is defined by a balance of the centripetal force with the centrifugal force that the ion experiences, (equations 1.11 and 1.12)

$$F' = \frac{mv^2}{r} \quad \text{Equation 1.11}$$

$$F = F' = qB = \frac{mv}{r} \quad \text{Equation 1.12}$$

F' is the centrifugal force, r the radius of the trajectory and m the mass of the ion. The ions inside the cell are confined by two trapping plates, which have a low potential applied to them to help prevent ions from proceeding out of the cell along the ion optical axis. Two excitation plates and two detector plates complete the ICR cell. The frequency of rotation (cyclotron frequency) of the ions is related to their m/z ratio as shown in Equation 1.13.

$$f_c = \frac{qB}{2\pi m} = \frac{v}{2\pi r} \quad \text{Equation 1.13}$$

Equation 1.13 can be rearranged to give equation 1.14:

$$\frac{m}{q} = \frac{B}{f_c 2\pi} \quad \text{Equation 1.14}$$

f_c is the induced cyclotron frequency and m is the mass of the ion. The induced cyclotron frequency is related to the angular velocity (ω_c) of the ion by a factor of 2π . The angular velocity therefore depends on the ratio $(q/m) B$ and is independent of the ion's velocity. The radius of trajectory taken by a given ion increases proportionally to the velocity as defined by equation 1.15:

$$\omega_c = 2\pi f_c = \frac{v}{r} = \frac{q}{m} B \quad \text{Equation 1.15}$$

Initially the radius of motion is too small to be detected and so no signal is observed. An RF pulse is swept across the excitation plates in order to excite the ions into larger radii of rotation (each individual ion has its own excitation frequency). Once in a higher orbit, the ions induce an alternating current between the detector plates. This process is illustrated in figure 1.10 The frequency of this current is the same as the cyclotron frequency of the ions and the intensity is proportional to the number of ions. The RF pulse can be considered as exciting all of the ions at the same time, and so all of the different ions (including isotopomers) will induce a different current simultaneously. This results in the measurement of all the ions in one go producing a complex current vs. time spectrum containing all the signals called the transient or Fourier induction decay (FID) signal. The transient can be unravelled by applying Fourier transform methods producing a frequency vs. intensity spectrum, which is then converted to the mass/charge vs. intensity spectrum according to equation 1.14.

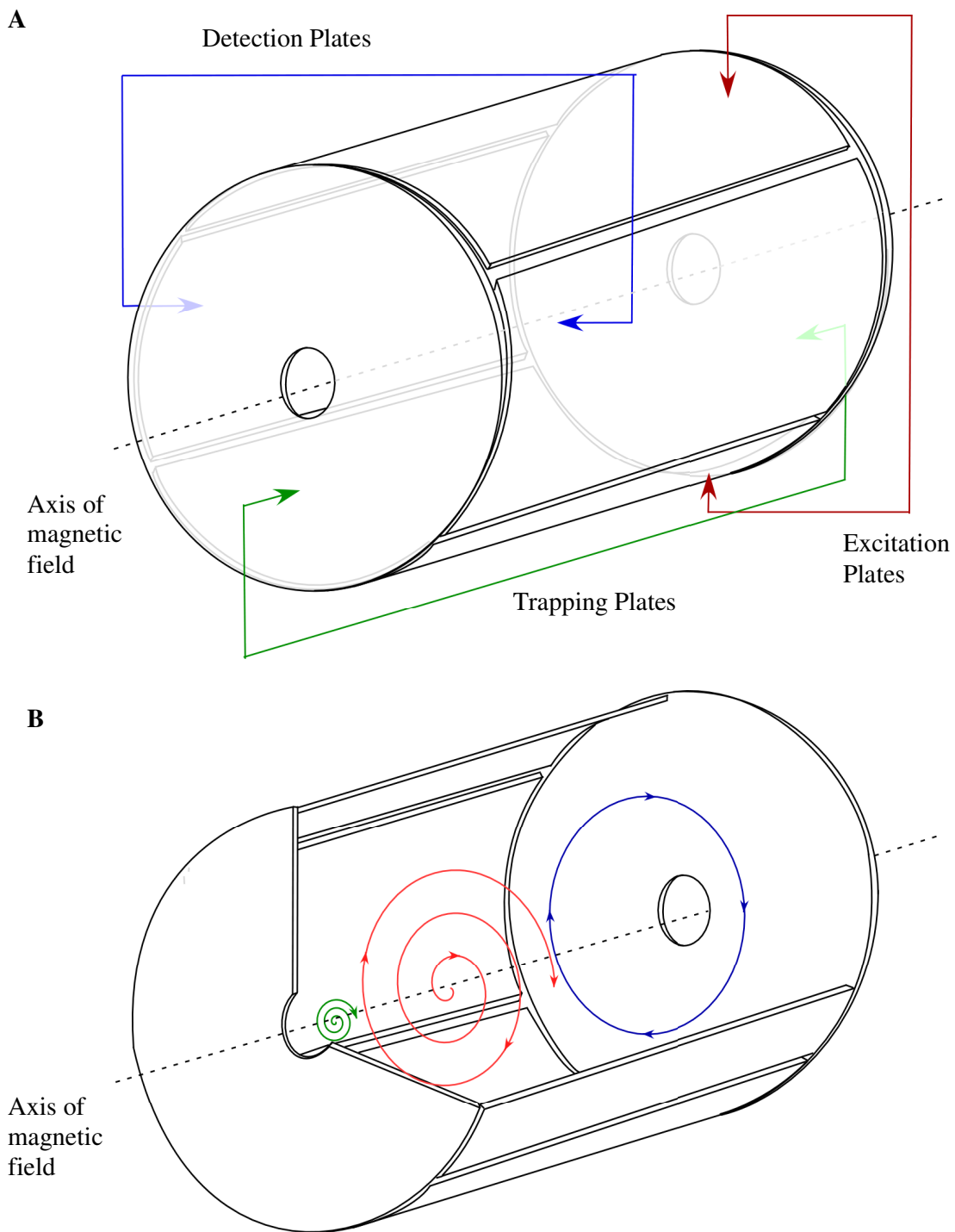


Figure 1.10. Schematic of A) a cylindrical FTICR cell and B) The ICR process where green represents ions just entering the cell, red the ions as they are excited by an RF pulse and blue the ions at a stable orbit.

1.2.3.2 The Bruker Bio APEX - 9.4 T FT-ICR mass spectrometer

1.2.3.2.1 Introduction

The Bruker BioAPEX – 94e FT-ICR³⁰ mass spectrometer used in these studies (Bruker Daltonics, Billerica USA) consisted of a passively shielded 9.4 T central field Nb₃Sn superconducting magnet (Magnex Ltd, Yarnton, Oxfordshire, UK) coupled with a 6 cm diameter, 6 cm long cylindrical INFINITY ICR cell³¹ and interchangeable electrospray and nano-electrospray ion sources (Analytica, Branford CT USA). Figures 1.11a and b show respectively a photograph and general schematic of the instrument, applications of which have been described³²⁻³⁴.

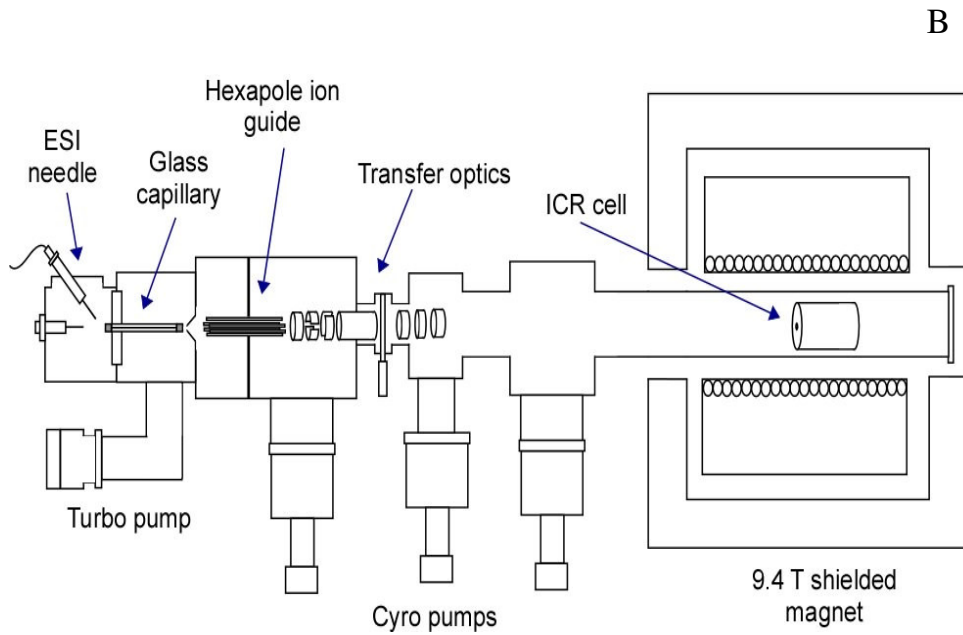
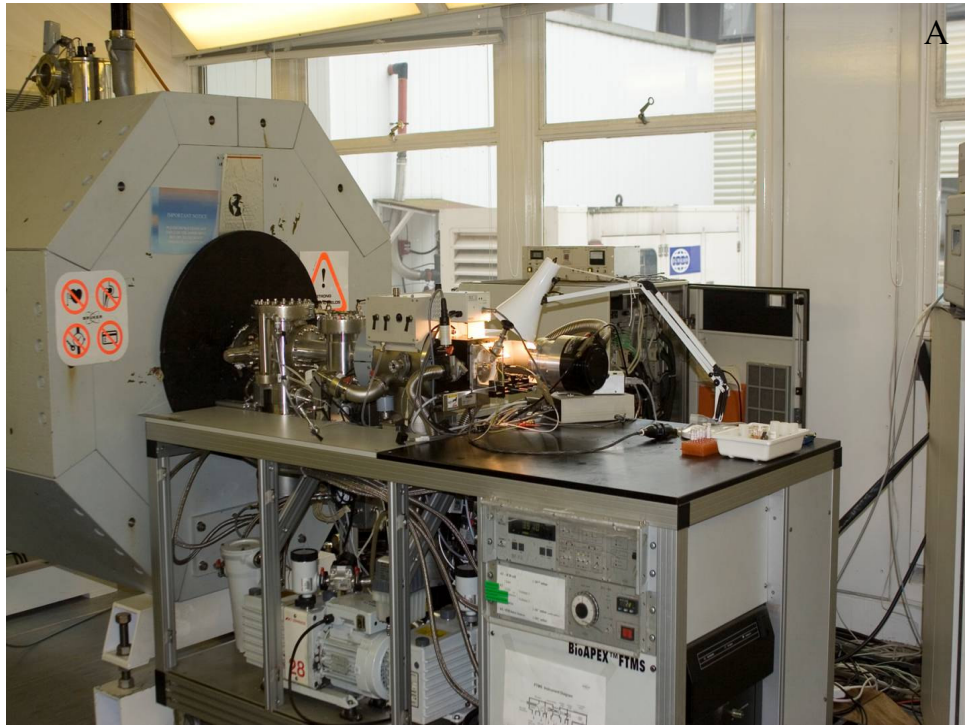


Figure 1.11. Photo (a) and schematic (b) of the Bruker BioAPEX 9.4 T FT-ICR.

1.2.3.2.2 Electrospray and Nano-electrospray ionisation sources

The electrospray source consisted of a metal spray needle connected to a syringe pump to supply a constant flow of sample at a desired rate and an inlet glass-capillary that hosts the first pressure-differential from atmosphere to about 10^{-2} Torr. This region at about 10^{-2} Torr was limited by a skimmer situated directly after the exit end of the inlet capillary. An RF hexapole was located partially after the skimmer in a separate vacuum chamber. The length of the hexapole extended beyond the hexapole chamber and into a third vacuum chamber kept at a pressure of 10^{-7} Torr. Ions could be trapped and stored in the hexapole using a trapping potential. The skimmer acted as one of the trapping plates and a plate immediately after the hexapole as the second. After a desired time ions could be ejected from the hexapole into the transfer optics by applying an extraction potential.

To swap between sources, the front end of the electrospray source (including the metal capillary and syringe pump), was replaced with a nanospray metal coated glass capillary and holder. A good alignment between nanospray needle and inlet capillary was found to be a very important factor in achieving good spectra and so the needle holder had been designed to be adjustable in the x,y and z axis. To help achieve fine alignments a microscope was mounted at a slight angle above the inlet hole. Due to the close proximity of the nano-electrospray source to the inlet capillary, a small-aperture stainless steel cap was placed over the inlet capillary in order to protect it from accidental damage. Figure 1.12 shows a photograph of the ionisation source with the nanospray front-end fitted.

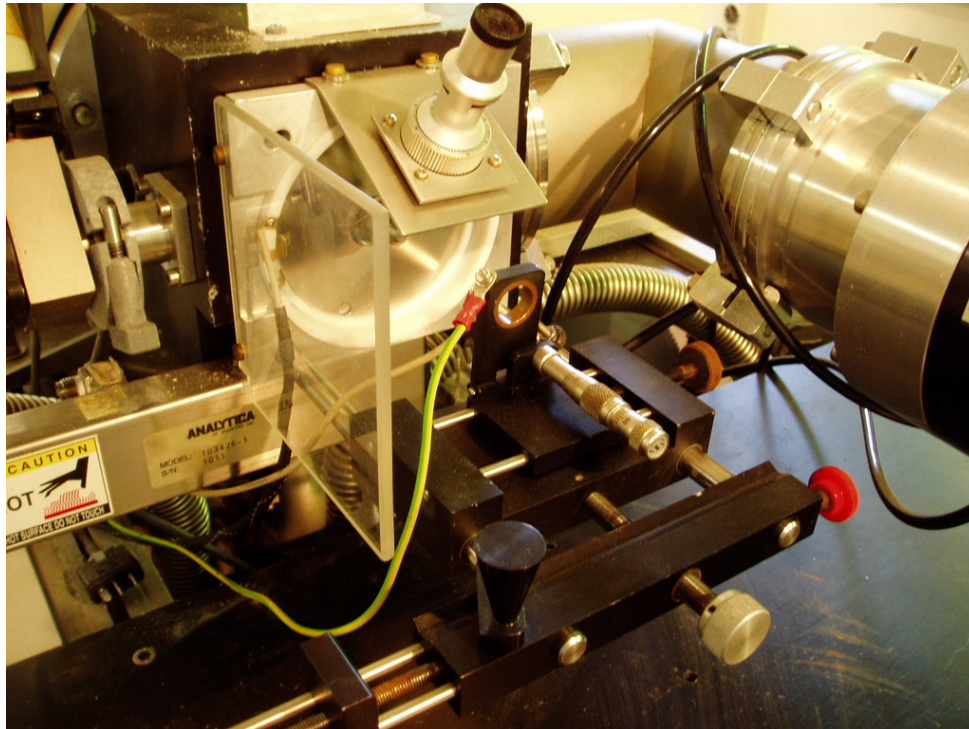


Figure 1.12 Photograph showing the nano-electrospray ionisation source.

Sample was loaded into the metal-coated glass needle prior to securing in the holder and aligning with the capillary inlet. Once positioned and grounded, the spray process from open-ended nanospray emitters (home-made metal-coated glass needles) would be initiated by applying a potential to the inlet capillary end cap. No other modification to the ESI source was required. If the sample was found not to spray easily, a flow of nitrogen gas would be supplied to the rear of the glass needle in order to encourage a spray. The gas was supplied at a pressure between 5-10 psi. Commercial nanospray needles produced by Proxeon Biosystems were supplied with sealed tips and need to be broken before use. Once placed in the nanospray holder the needle tip was carefully broken against the inlet capillary end cap, using the microscope to aid accuracy.

1.2.3.2.3 Transfer optics

Once a sufficient number of ions were accumulated within the trapping hexapole they would be ejected into a series of ion transfer optics by an accelerating potential. These transfer optics consist of a series of lenses and deflectors, designed to optimise the ion beam before it entered the ICR cell. Collimating the ion beam along the instrument's axis and preserving the kinetic energy of the ions is considered to be important due to the magnetic mirror effect that the ions encounter before entering the ICR cell.³⁵ The magnetic mirror effect can be explained in the following simple terms: a beam of ions that is not in line with the field lines created by the 9.4 T magnet will experience a slight deflection according to Fleming's left hand rule. This in turn creates a self-replicating effect where a slight deflection causes the ions to deflect even further and eventually be completely repulsed. Ions that are not in line with the field lines and have larger kinetic energies travel further into the field before the magnetic mirror effect will significantly alter their trajectory.

A schematic of the ion transfer optics is shown in figure 1.13 The optics consist of several ring and tube electrodes (PL1, FOCL 1, PL9 and FOCL 2) in series with deflectors (XDFL and YDFL) and electrodes that could be used to add an element of focusing with deflection (PL2 and PL4).

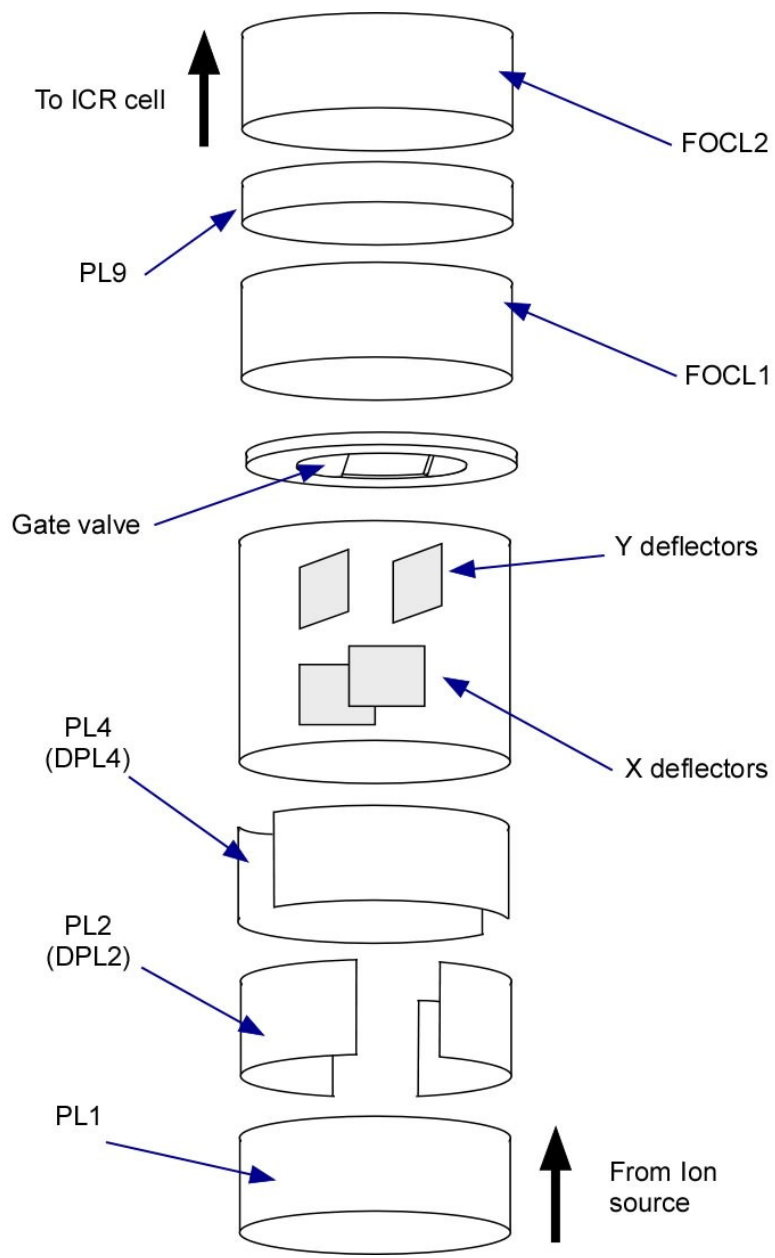


Figure 1.13. Transfer optics used in the 9.4 T FT-ICR.

1.2.3.2.4 The ICR cell

The INFINITY cell³¹ was a cylindrical geometry ICR cell that consisted of a pair of curved plates used for detection and, offset by 90 °, a second pair was used to introduce the radio frequency excitation pulses. Two plates with small central circular apertures capped either end of the cell; during experiments small potentials were typically applied to these plates to complete the trap. To increase trapping efficiency the cell was equipped with the SIDEKICK ion accumulation system.³⁶ This works by giving the ions in the ICR cell a small radial velocity, and the resulting magnetron motion deflects the ions from following an optical axis and so therefore prevents them from exiting out of holes in the trapping plates.³⁶

The instrument was controlled using a Silicon Graphics Indy workstation running XMASS 5.0.10 (Bruker Daltonics, Billerica, MA). Data from the ICR cell was acquired using a digitiser and then transferred to the Indy workstation using a dedicated Ethernet cable.

1.2.3.2.5 The vacuum system

The vacuum system of the 9.4T FT-ICR consisted of three cryogenic pumps, a turbomolecular pump and 2 rotary pumps all supplied by Edwards (Crawley, West Sussex, UK). As mentioned before, the pressure within the ESI/nano-ESI source at the capillary-skimmer region was around $\sim 10^{-2}$ Torr. A rotary pump, pumping at 10 L/s maintained this pressure. The vacuum chamber containing

the front end of the hexapole was backed by the same rotary pump but to achieve a pressure of about 10^{-6} Torr the turbomolecular pump was required (220 L/s). The first cryogenic (800 L/s) pumped the region at the rear of the hexapole and maintained a pressure of $\sim 10^{-7}$ Torr. Both the tube containing the transfer optics and the ICR cell had their own dedicated cryogenic pumps, pumping at 220 L/s and 800 L/s respectively. The pressure above these pumps was typically of the order of 10^{-9} Torr.

A gate valve was located in the ion-transfer optics, in-between the deflectors and FOCL1-FOCL 2 lens region. This allowed access to the source region and transfer optics without having to vent the ICR cell. A vacuum valve was also fitted to the source cryogenic pump in order to prevent overloading the charcoal plates, within the pump, by exposing them to atmosphere. The cryogenic pumps were periodically baked by wrapping heating cable around the exterior of the pump. This removed the build-up of species on the charcoal plates and restored their pumping efficiency.

1.3 Ionisation techniques

In order to analyse a sample it must first be transferred into the gas phase and ionised before its mass can be measured by any of the techniques mentioned above. The development of ionisation techniques is perhaps almost as important as the development of mass analysis techniques, because it has opened the door to an ever increasing range of subject compounds that can be analysed using mass spectrometry. A number of problems have driven the development of ionisation sources since discharge tubes and Dempster's electron impact ionisation were utilised in the first mass spectrometers. The first and most important problem is applicability of the ionisation technique. A mass spectrometer is limited in what it can analyse by what the ionisation source can ionise. The first ionisation techniques such as electron impact ionisation (EI) and its successor chemical ionisation (CI)³⁷ were only capable of analysing volatile low-molecular-mass compounds. A further problem is preserving the compound through its transfer into the gas phase and ionisation. Charging a sample can create unstable sample ions that may undergo fragmentation processes. While some fragmentation can be useful if the identity of the analyte is unknown, too much can lead to the molecule-ion peak disappearing completely.

The development of "soft" ionisation techniques such as field desorption decreased the degree of fragmentation by reducing the amount of energy conveyed into the analyte. This was coupled with an increase in the range of compounds that could be ionised. Techniques such as electrospray ionisation

and matrix-assisted laser desorption ionisation³⁸ further expanded the range of compounds that could be analysed. A perfect ionisation process would be able to preserve a compound from solution into the gas phase and while “soft” ionisation techniques will not (unless desired) cause much fragmentation, weakly bound non-covalent complexes that are often of interest in proteomics research may not be preserved into the gas phase. In this way, as the range of compounds that can be analysed is increased, further problems are discovered.

The most recent ionisation source developments such as desorption electrospray ionisation (DESI) and direct analysis in real time (DART)^{39,40} have raised the possibility of almost completely eliminating the sample preparation stage in mass spectrometry. Despite these developments no current ionisation technique can ionise every class of analyte and yield consistently good mass spectra.

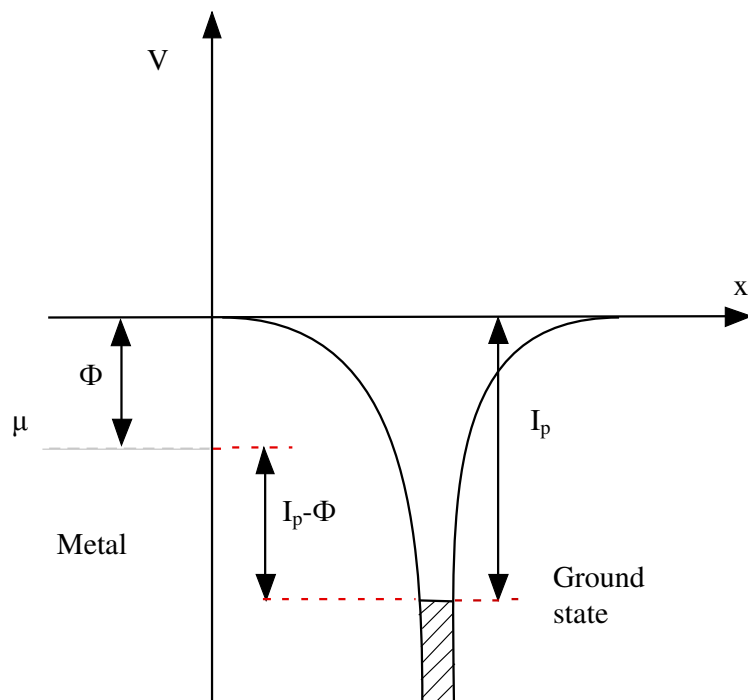
1.3.1 Field Ionisation

Field ionisation (FI) is the process by which atoms and molecules are ionized when they are subjected to a high electric field generated at a field emitter, and it can be traced back to the discovery of the field ion microscope by Erwin Muller in 1951⁴¹. Muller was working with field emission microscopy and made his discovery when he found that if the polarity of the field was reversed and applied to a metal tip, gaseous atoms introduced into the vacuum chamber of the microscope would be ionized. These ions would be repelled away from the surface of the tip in a direction related to the surface curvature thus allowing an image of the tip to be collected. It was not until 1954 that a field ion

microscope was adapted so that it could be used as an ion source for mass spectrometry⁴².

Theoretical treatment of the mechanism of field ionization has been given by Inghram and Gomer⁴², Muller and Bahadur⁴³ and by Beckey⁴⁴ to name but a few. The theory developed by these authors, ionization by electron tunnelling, can be discussed with the aid of the potential energy diagrams shown in figure 1.14. The diagram uses an ideally smooth metal surface to represent a field emitter. The potential energy of a valence electron of an atom is drawn as a function of the distance from this surface with and without a potential applied to the emitter. Electrons in the metal surface are filled up to the Fermi level (μ , the highest occupied energy level). Valence electrons of a gaseous atom a distance x away from the metal surface are assumed to reside in the electronic ground state as shown in figure 1.5a. Φ is the work function of the emitter and I_p is the ionisation potential of the atom. In the case where there is not a strong field applied to the emitter, the atom's valence electron can not escape its potential well. When a field is applied to the emitter the potential of a ground state electron is effectively shifted up relative to the metal and the potential well distorted so that at a minimum distance from the surface, the energy of the valence electron differs very little from the Fermi level of the metal surface (figure 1.14b). This process is not due to electronic excitation of the electron⁴⁵ rather the ground state is in a sense shifted up. When this occurs there exists a probability that the valence electron will quantum mechanically tunnel through the walls of its potential well to the matched Fermi level of the emitter, thus ionising the atom.

A



B

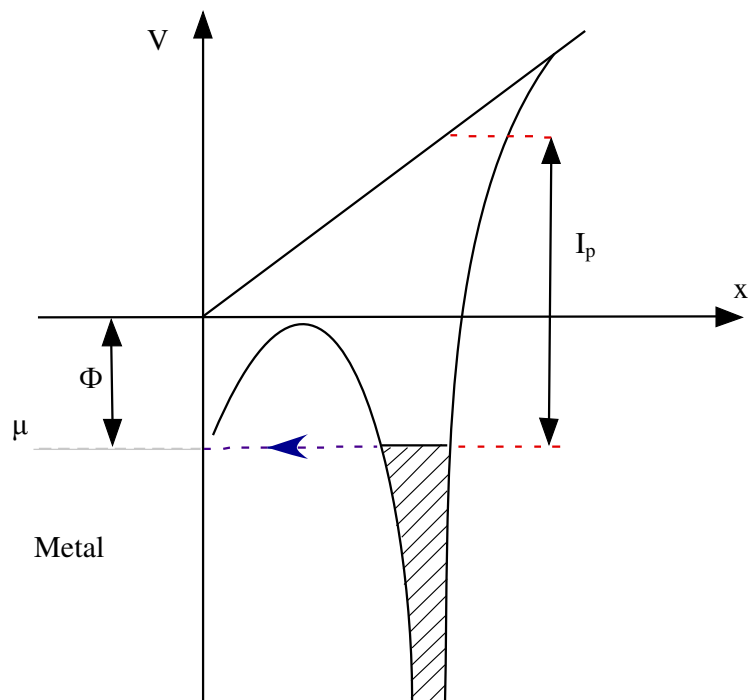


Figure 1.14. Potential energy diagrams showing a valence electron from an analyte atom in A) the absence of an electric field and B) the presence of a high electric field.

Field ionisation is a relatively soft ionization technique and was therefore an appealing technique at the time of its development as it would provide complimentary results to the more energetically harsh electron impact ionization method ⁴⁶. The technique suffered from several major disadvantages: The sample compound used in FI must be thermally volatile enough to be transferred into the gas phase before it is field ionized and during this process the sample must be stable enough to withstand thermal decomposition. This coupled with the problem that the field generated by the field emitters was not strong enough to ionize every range of compound, restricted the number of compounds that could be ionized to the low mass range. Improvements in field emitter technology such as changing the emitter shape or introducing emitters with field-enhancing carbon microstructures (see chapter 3) increased field strength and therefore the range of compounds that could be ionized. It was not until field desorption was applied to mass spectrometry in 1969 ⁴⁷ that some of the thermal problems were solved.

1.3.2 Field Desorption

Field Ionization is considered to be the precursor of field desorption (FD), with the distinguishing feature that in field desorption a liquid sample directly coats the field emitter. The theoretical treatment of field desorption is somewhat more complicated than that of field ionisation. Several different theories have been put forward to explain the mechanism of field desorption. There is not one set mechanism that explains the ionisation and evaporation of every field

desorption analyte. There are three different descriptions of ion production in field desorption generally discussed.

1.3.2.1 Field-induced electron tunnelling

One model of ionization in field desorption involves a natural theoretical progression from the method of ionization used in field ionization: electron tunnelling. The mathematical treatment considered by Muller⁴⁸ and then Gomer⁴⁹ considers atoms on a clean metal surface. The potential energy diagrams as shown by McKinstry⁵⁰ (reproduced in figure 1.15) show the curve for an atom on the metal surface (atomic) and also the case for an ion on a metal surface with and without the presence of an external electric field (ionic).

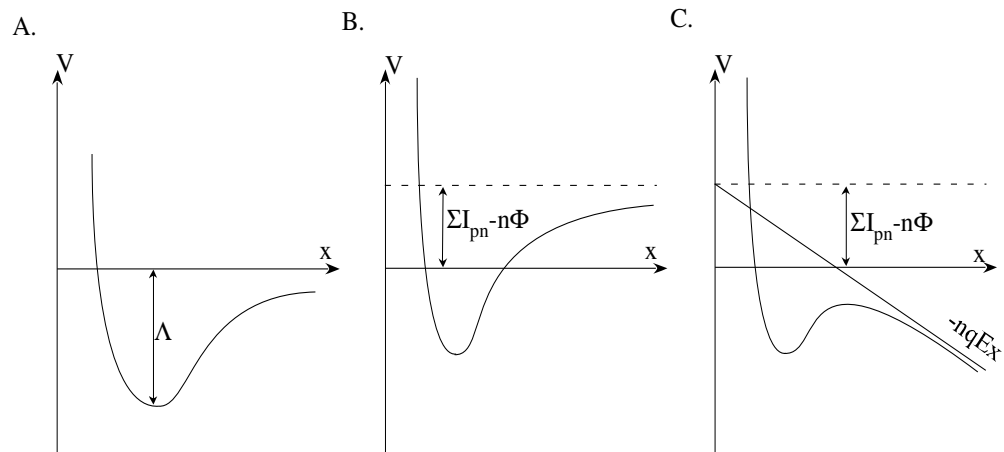


Figure 1.15. Potential energy diagrams for A) a surface atom, B) a surface ion and C) a surface ion in the presence of a high electric field.

The energy required to remove the atom from the surface, the desorption energy, is given by the depth of the atomic potential well (Λ). The energy required to ionise an atom already removed from the surface is given by the term ΣI_{pn} where the charge of the ion is given by nq and I_{pn} is the n th ionisation energy. The difference between the zero level of the ionic curve and the zero level of the atomic curve is given by $\Sigma I_{pn} - n\Phi$. Applying a positive electric field (E) causes the ion to experience a repelling force (nqE). Superimposing the atomic and ionic curves gives rise to several different situations describing ionization and evaporation. This can be measured in terms of the magnitude of ionisation energy and the metal's work function $\Sigma I_{pn} - n\Phi$. Figure 1.16 shows the potential energy diagrams (McKinstry) of three different cases. Part (a) depicts the case when the terms ΣI_{pn} and $n\Phi$ are of a similar magnitude. The difference is small enough that no intersection between the atomic and ionic curves takes place.

Fig 1.16 Parts (b) and (c) both depict the case where $\Sigma I_{pn} - n\Phi$ is large and the field causes an intersection between the atomic and ionic curve. When there is an intersection, it is expected that ionization can occur⁵⁰. Two competing theories have been put forward to explain the sequence of ionization and evaporation in terms of the magnitude of the field applied and distance from the surface. The image hump model⁴⁸ shown in (b) describes the case when intersection occurs in the potential well of the ionic curve. The removal of an electron causes forces to draw the ion into the interior of the metal. The ion must therefore have enough energy to overcome the hump (image hump or schottky saddle) in the ionic curve before evaporation can follow ionisation –

evaporation is the rate determining step. The second theory (shown by part c) called the intersection model ⁴⁹ assumes that intersection occurs past the image hump of the ionic curve. Forces acting on a newly formed ion will repel it from the metal surface and so desorption immediately follows ionisation. In this case overcoming the ionisation energy is the rate determining step of the process. McKinsty presents in his paper arguments as to when each model should be used.

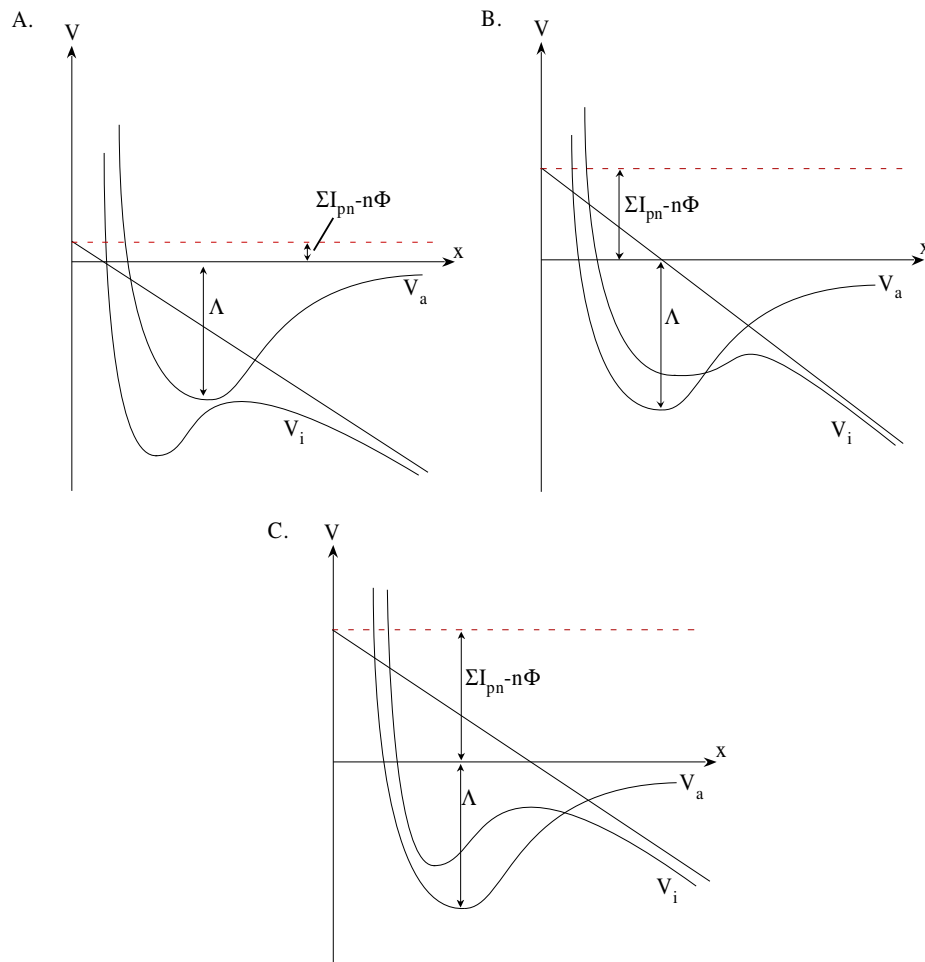


Figure 1.16. Three possible evaporation models. (A) Simple ionic bonding, (B) evaporation over the image hump after transition from the atomic to ionic state and (C) ionization followed by immediate evaporation.

In general, electron tunnelling will produce ions of the form M^{n+} and upon subsequent reaction their protonated equivalents. Although in theory multiply charged ions can be produced according to the above models, a postionization mechanism has been introduced⁵¹ to try and account for the production of more highly charged ions. In simple terms the model predicts that ions that are accelerated away from the surface can be further ionised by electron tunnelling.

1.3.2.2 Field-induced extraction: desolvation and ion evaporation

A second mechanism of ion formation and desorption considers the field-induced extraction of preformed sample ions from salt-containing solutions or electrolytes⁵². Ionisation is considered to occur via proton or cation attachment in the solution phase. Applying a field to the FD emitter causes the ions to charge separate: In the case of a positive emitter, negative ions would be attracted towards the emitter surface and be neutralised. Positive ions on the other hand are repelled away from the emitter surface and accumulate at the sample surface. This charge separation causes the sample to bulge outwards and form fine protrusions of sample with high surface-to-volume ratios. Evaporation of solvent from these projections can cause the formation of a condensed glass-like phase at the surface layer of the projections (figure 1.17)⁵². It is thought that the field strength at the tips of these protrusions will become high enough to cause the rearrangement of the ions at the surface and cause extraction of ions by rupture of intermolecular bonds. Geissmann et al have studied this desolvation process using optical microscopy⁵³ for several analytes. Wong et al took this one step further and have put forward a schematic representation of the

extraction and desolvation process⁵⁴. The same authors also postulate that in the presence of activated emitters the field may be strong enough to cause extraction without the formation of sample protrusions.

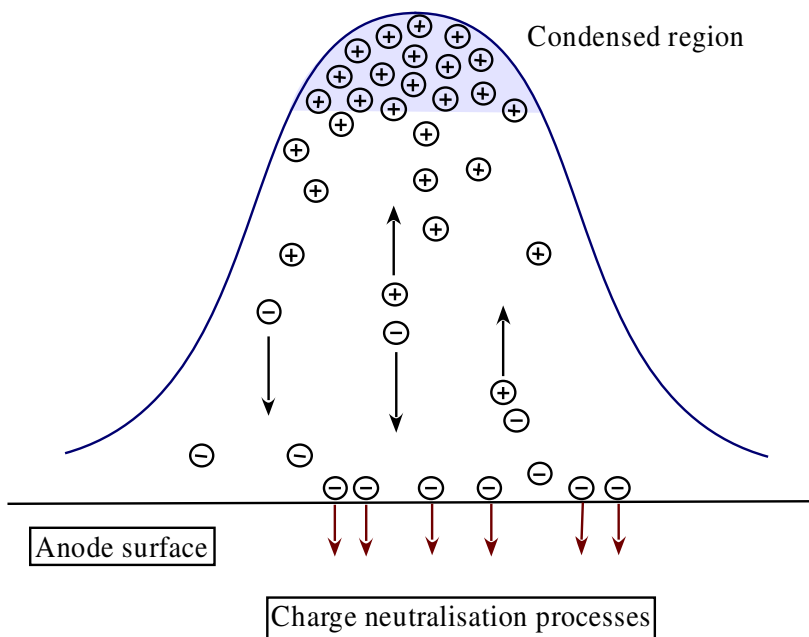


Figure 1.17. Schematic showing the charge separation in the desolvation model of field desorption

A model of field-assisted evaporation introduced to explain the field desorption process shares many similarities with the desolvation method outlined above. In ion evaporation, ionisation and desorption are once again considered separately. The theoretical model supposes that ionization occurs by cation attachment, creating an ion comprising of the original cation and at least one sample molecule. The evaporation process is envisaged as follows. The repulsion between neighbouring cations would normally be in balance with the attractive force between neutral molecules that restrains evaporation. The application of a

high potential and heating shifts this balance by causing the interactions between analyte molecules to weaken while not affecting the repulsive cation-cation forces. Due to ascendancy of the repulsive force, an ion (cation, attached sample molecules and solvation shell) may start to bulge out of the surface and form a protuberance containing the ion. As the repulsive force increases it will eventually overcome the surface tension of the protuberance and the cation and attached molecule will be expelled. This process is examined quantitatively and the mechanism illustrated by Davis et al ⁵⁵ and Colburn et al ⁵⁶. Figure 1.18 illustrates the model for protuberance growth as presented in these papers. The obvious difference between the field-assisted evaporation and desolvation model is the scale of protuberance formed. The former deals with single-ion protuberances, while with the latter the protuberances contain many ions. It may be the case that the production of large protuberances is associated with lower field strengths and the evaporation from these protuberances may be described by the field-assisted evaporation model ⁵².

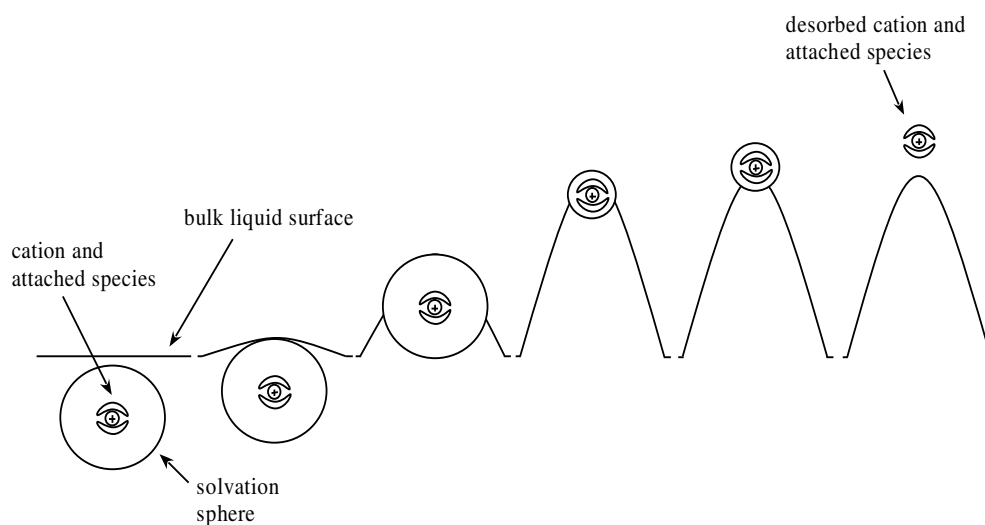


Figure 1.18. Schematic showing the protuberance growth in field-assisted evaporation.

1.3.2.3 Thermally induced ionization

Thermal energy plays an important role in the models of field desorption mentioned. Experimentally it is hard to achieve field desorption mass spectra without an element of heating. The possibility of a purely thermal field desorption process has garnered much debate and controversy. A thermal ionisation mechanism was outlined in 1976 by Holland et al⁵⁷, however, some flaws in the experimentation designed to support this theory were pointed out and the mechanism was not generally accepted by their peers. In 1978 the thermionic emission of metal ions was reported with little dependence on field strength at temperatures greater than 800 K⁵⁸. In a review of mass spectrometry in 1980⁵⁹, the authors stated that in their opinions ‘the electric field is not merely essential but the dominating factor in FD’. Cotter et al⁶⁰ designed experiments to prove that cationized molecules and stable cations from non-volatile organic salts could be formed in a “field desorption process” that was entirely thermally induced. They were successful in producing a number of thermal desorption spectra and concluded that the role of thermally induced mechanisms could not be dismissed. It seems likely that for most compounds of a large masses there is no role for a thermal mechanism. This would be particularly true in the case of larger mass molecules where the increase in thermal energy could cause the molecule to undergo thermal degradation. In the case of low-mass inorganic and organic salts, however, desorption may be possible without a dependence on electric field⁵².

1.3.2.4 Discussion of Field Desorption

Identifying which mechanism to adopt to describe a given field-desorption (FD) experiment can be difficult. According to Giessmann⁵³ it is possible to differentiate between low-field and high-field processes. At high fields ($>10^9 \text{ V m}^{-1}$) it is proposed that field ionisation processes will take place and so electron tunnelling is the appropriate mechanism of ionisation. In order to generate the high fields required for this type of ionisation the emitter must be activated by the growth of micro needles (see chapter 3); Ionisation is likely to occur at the tips of these micro needles. This raises the point that the tips of the micro needles make up a very small percentage of an activated emitter and so there must be supply processes in action to provide sample to the tips. The most probable method of supply appears to be either a particle gas-phase process⁶¹ or a surface-diffusion process⁵². At lower field strengths $10^7 - 10^9 \text{ V m}^{-1}$ it is thought that the ion- extraction methods of desorption would apply. Due to the lower field strengths required it is possible to achieve this kind of desorption using unactivated emitters⁶². In addition to the strength of field, distinctions between the different methods of FD can be achieved by looking at what form of molecule ion is present in the mass spectrum. For example, field ionisation is the obvious process to form a molecular ion M^+ , while ions of the form $[\text{M} + \text{alkali}]^+$ are likely to be produced by desolvation and/or ion evaporation. A table showing a list of different ions and possible mechanisms of formation is shown in appendix 1a

Field desorption (FD) was introduced at a time when electron impact and chemical ionization were the prevalent mass-spectrometry ionisation-

techniques. It became a key technique in providing mass spectrometric data of involatile and thermally unstable compounds. While the technique was perhaps not as easy to operate as other second-generation techniques such as fast atom bombardment and secondary ion mass spectrometry, FD was the first ionization technique really to open the door for the analysis of larger mass biological samples^{63, 64}.

Compared to ESI and MALDI, FD has several major disadvantages. FD is not continuous: emitters must be removed from vacuum and coated with sample between runs. This is not only labour intensive but also a time-consuming process and so unlike ESI, FD can not be readily coupled with high-performance liquid chromatography for high through-put analysis. Secondly, FD has not had as great a success in analysing some of the much larger proteins that are now routinely studied with ESI and MALDI. This may be due to currently available emitters not producing the strength of field necessary for ionisation by electron tunnelling. The introduction of a liquid-injection field-desorption technique that delivers a continuous flow of sample directly to the emitter has been a good step towards reducing the time and labour required to run field desorption experiments^{65, 66}. The problems associated with applying FD to larger biological compounds remain unsolved, however.

1.3.3 Electrospray Ionisation

Electrospray ionisation (ESI) appears deceptively to be a very different method of ionising and transferring sample into the gas phase compared to FDI. Malcolm Dole and colleagues first recognised the possibility of using an electrospray to create gaseous ions and in their 1968 paper⁶⁷ he and his colleagues describe an electrospray technique used to ionise and transfer large polystyrene molecules intact into the gas phase. While subsequent research has suggested that their ions were still heavily solvated⁶⁸, this experiment provided the inspiration for John Fenn and colleagues to develop electrospray into the technique which is familiar today. Dole et al's work on electrospray first came to Fenn et al's attention when they were working on the effect of leaks in vacuum systems and the supersonic jets created by the flow of gas into these leaks⁶⁸. This work enabled Fenn to see a way of improving Dole's ideas by introducing a jet of warm gas in the counter direction to the electrospray which would encourage full desolvation of the subject ions. Fenn et al took electrospray a step further by then interfacing the technique with a mass analyser, which enabled them to record the first accurate mass spectra as a result of electrospray^{69, 70}. Fenn and his colleagues went on to use electrospray to look at peptides and polymers where they observed a tendency for electrospray to produce multiply charged ions. This would become one of the main facets of electrospray allowing users of the technique to analyse molecules that exceed the upper limits of their mass analyser for singly charged ions. This work culminated with the publication in 1989 of the mass spectra of large biomolecules obtained using electrospray⁷¹.

In electrospray ionization a liquid sample is pushed through a small metal needle/capillary held at a high potential by atmospheric pressure. The liquid sample will normally contain the analyte of interest, as well as solvent, and for biological samples possibly aqueous buffer. The sample delivered to the tip of the electrospray capillary will experience a strong electric field. Ionisation of the sample occurs when charged species such as H^+ (created through the oxidation of water) or Na^+ , K^+ or Cl^- (that originate from salts) stabilise by adding onto the sample. The field causes the charged sample to accumulate at the liquid surface at the end of the capillary tip. If the potential applied to the needle is positive, it is the positive ions that will accumulate towards the liquid surface due to charge repulsion. Any negative ions present in the sample will be attracted towards the walls of the capillary. At low potentials this charge accumulation causes the liquid meniscus to bulge outwards. Slightly larger potentials can cause the meniscus to adopt a conical shape that reflects a perfect balance between the electrostatic force created by the accumulation of charged particles and the surface tension of the liquid. This meniscus is normally referred to as a Taylor cone. If the potential is increased even further, the Taylor cone will be drawn to a filament and droplet emission from this filament will occur when the electrostatic force exceeds the surface tension. It is in this process that similarities with FD can be strongly drawn – the effect of the strong electric field on the liquid sample at the tip of the capillary is reminiscent of the effect of the strong field generated at the tips of field emitters in field desorption. A schematic illustrating the effect of potential on the liquid surface at the tip of an ESI capillary is shown in figure 1.19.

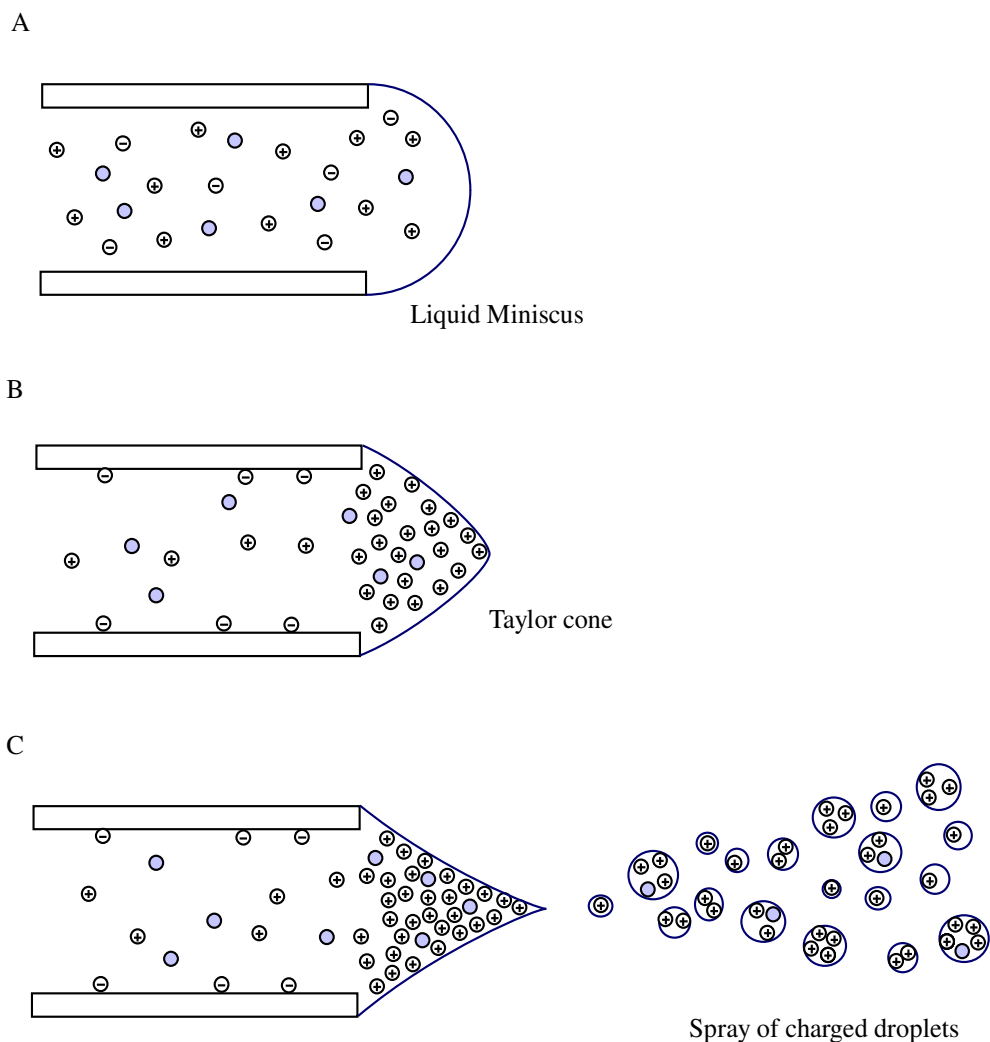


Figure 1.19. Schematic showing the effect of potential on the meniscus at the tip of an electrospray needle. A) The case where there is either a small or no potential applied. B) What occurs when a higher potential is applied where there is a balance between the charge repulsion and surface tension of the meniscus. C) The onset of a spray of droplets created when the potential is increased further.

The fine spray emitted from the Taylor cone is desolvated to produce gaseous ions often with the help of a neutral drying gas. There are two competing descriptions of how this is achieved. The droplets emitted from the Taylor cone contain a high density of charged molecules. Evaporation of solvent from the

initially formed droplets will occur as they traverse a pressure gradient towards the analyser of the mass spectrometer. This evaporation will cause the droplet to shrink and bring the charges held within closer together. In the charge residue model (CRM) ⁶⁷, as evaporation of the droplet continues there are a point at which the repelling Coulombic force between the charges are large enough to destabilise and overcome the surface tension holding the droplet together. The point at which a charged droplet becomes unstable is known as the Rayleigh limit. Fission of the droplet produces several smaller charge-containing droplets. It is envisaged that the evaporation and fission process continue until the ions are completely desolvated. The ion evaporation model (IEM) ⁷² differs from the CRM in what occurs when the droplet evaporates and the density of charge increases. In the IEM, as the droplet shrinks, the coulombic repulsion increases causing an ion to be ejected from the droplet. This occurs because the repulsive force acting on an ion at the droplet edge exceeds the ion's adhesion to the droplet surface. The ejection of the ion will stabilise the droplet by temporarily reducing the electrostatic force counteracting the surface tension of the droplet. In this model the solvent from the droplet continues to evaporate causing more and more ions to be ejected. Which of the two models best describes the ion's transition into the gas phase is a point of debate, but it seems likely that both models may have their place in describing the electrospray process fully. It is also worth taking note that the formation of the Taylor cone has certain mechanistic parallels to the ion extraction methods of field desorption. The field-desorption ion evaporation process in particular seems near-identical to how ions are evaporated in the IEM model. There are many different reviews outlining the electrospray process. ^{68, 73, 74}.

ESI, like field desorption, is characteristically a “soft” ionization process and so consequently very little fragmentation is produced. Large as well as small molecules can be transferred into the gas phase intact and weak interactions from the solution phase can be preserved. The production of multiply charged ions has already been mentioned. These characteristics coupled with a very high sensitivity (high femtomole to low picomole) and the ability to couple with high-pressure liquid chromatography (HPLC) equipment has driven ESI to become a crucial tool in the analysis of biological samples^{75,76}.

1.3.4 Nanoelectrospray ionisation

Nanoelectrospray ionization (nanoESI) is a variant of the conventional electrospray ionization technique described above⁷⁷. NanoESI operates in the same way as normal ESI, except on a much smaller scale. Typical nanoESI tip apertures range from 1-5 μm in diameter, with 2 μm being the size reported to give the most reproducible results⁷⁸. As a consequence of the smaller needles, smaller sample flow rates are used. Droplets produced from a nanospray tip are often an order of magnitude smaller than those produced with ESI. The time required to desolvate completely the droplets is reduced in comparison to ESI, which allows the nanospray needles to be placed much closer to the capillary or other inlet of the mass spectrometer. This in turn reduces the number of ions that hit the counter electrode and surface entrance of the capillary and so using nanospray a larger percentage of ions are transmitted through the source. Nanospray has been found to have a much lower sample consumption and to be more sensitive than ESI. These are factors that are important, particularly in

proteomics where often only small amounts of samples are available ⁷⁹. NanoESI has also been found to have a higher tolerance toward salt contamination and analyte suppression effects when compared to conventional ESI ⁸⁰.

1.4 Simion 8 ion optic simulations

1.4.1 Introduction

The ability to simulate the behaviour of ions in electric and magnetic fields under vacuum is very important when constructing instrumentation for mass spectrometry. Simulation programs such as Simion⁸¹ (Scientific instrument services, Ringoes, New Jersey, USA) allow an insight into how charged species would behave in a piece of instrumentation before it is built and can be used to guide the development of the piece of instrumentation from the initial design²⁴. Complete instruments have been designed and optimised using Simion prior to fabrication ^{82, 83}.

Simion uses potential arrays to define the geometry of electrodes as well as the potentials both on the electrodes and in the empty space between the electrodes. A potential array consists of a number of equally spaced grid points (the number can be defined by the user). Each grid point is defined either as an electrode or as no electrode. The groups of electrode points make up the electrode that the user wants to simulate and groups of non-electrode points make up the empty spaces between electrodes. The potentials applied to each electrode are defined

by the user and the potentials between electrodes are calculated by Simion by solving the Laplace equation with the electrodes acting as boundary conditions. The solution of the Laplace equation can be thought of in a physical sense as being similar to the surface of a rubber sheet stretched between electrodes, where the height of the electrode corresponds to the electrostatic potential. The behaviour of a marble on this sheet yields a reasonable approximation to that of an ion in an electrostatic field. In a similar way, Simion uses potential energy surfaces to make the behaviour of ions in an electrostatic field more intuitive. Figure 1.20 shows an example of the potential energy surface of a simple Einzel lens.

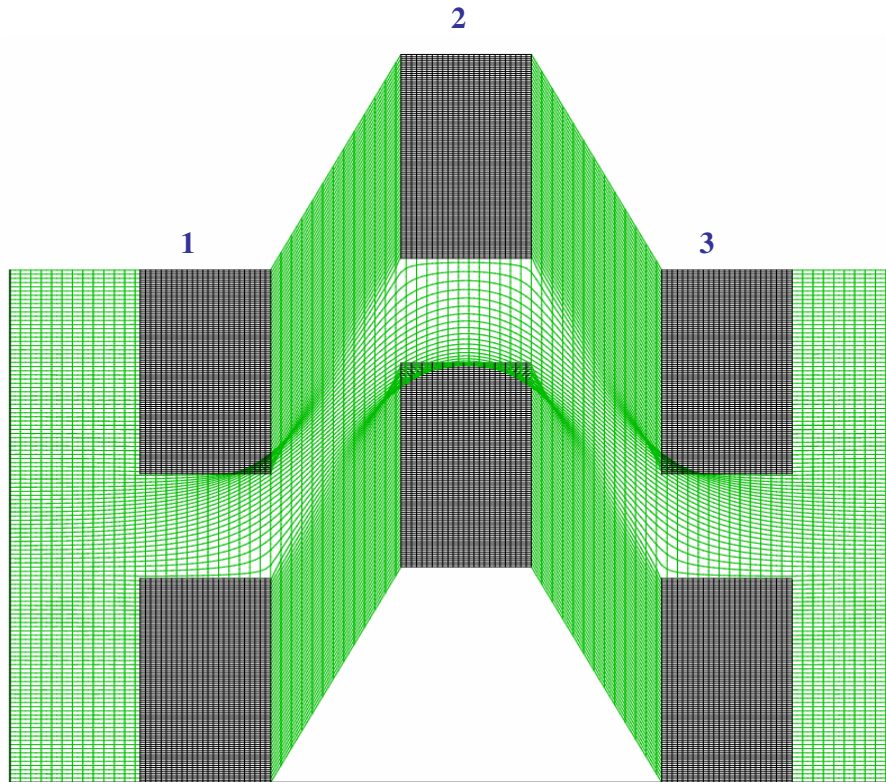


Figure 1.20. Simion 8 simulation showing the potential energy surface in three dimensions of a simple Einzel lens. Electrodes 1 and 3 have zero potential, a voltage of 1500 V is applied to the second electrode.

1.4.2 Creation of array and geometry files

There are two approaches a user can take to tackle the problem of building a piece of instrumentation with the help of Simion. The first approach, which is usually only useful for simple arrays, involves manually filling in the grid points on a potential array to create the desired electrode structure. This would create a two-dimensional (2D) array that could be expanded depending on whether it had cylindrical or planar geometry. If the array has the former it could be projected to create a volume of revolution about an axis. In contrast, 2D-planar geometry assumes that the array itself is one layer of an infinite number of layers in the z axis. In addition to this, each type of array can be mirrored to create a symmetrical electrode structure, which allows a much smaller array to be used to model a larger area (cylindrical geometry arrays already mirror). This is particularly important when the processing power of the computer used to simulate the instrumentation is taken into account. Each point in the array requires 10 bytes of RAM, so a very small array consisting of 100 by 100 by 100 would use 10 megabytes of RAM. Large arrays therefore, may require anything up to several gigabytes of RAM. This is a size which unless upgraded many commercially available computers would not be able to offer, and so if the design permits, the value of mirroring the array is clear.

The second approach, which can be used as a stand-alone method or in conjunction with the manual modify method mentioned above, involves geometry files. Geometry files are typically used for building complex three-dimensional (3D) geometries and incorporate the planar and cylindrical

geometries as well as mirroring. A geometry file is an ASCII file with a .GEM extension that uses a 3D solid-geometry modelling-language to define the desired electrode array geometry via a series of fill coordinates and other instructions. Simion reads the selected geometry file and constructs the geometry in a user-defined potential array. An example of a geometry file used to build a simple Einzel lens is shown in Appendix 1b. Simion uses a variety of different geometry instructions to build the shape of a piece of instrumentation. A list of the different instructions can be found in the Simion version 8 user manual (pages I10- I28). Potentially this would allow a designer to build the entire piece of instrumentation in 3D in the array. Because of the problems with available RAM, however, it is sensible to use mirroring where possible. It is also possible to match two different geometry files together in Simion's workbench. This allows less complicated areas of instrumentation to be simulated using the minimum array size (mirroring, cylindrical geometry), while still maintaining the option to have complicated 3D areas. However, this is only advisable if the files are matched at a well-defined grounded area (as field-free as possible). Due to the change between different geometries or unit sizes, ions may not be simulated accurately if the files are matched in a region of high field.

Before a simulation can be conducted, the potential array (whether created by the modify or gem-file method) must be refined. Refining uses the potentials of electrode array points to estimate the potentials of the non-electrode array points. This is achieved using Simion's finite difference technique to solve the Laplace equation. In simple terms, Simion uses the average potential of the

nearest neighbour points to estimate the potential of each non-electrode point in the array. The entire array is scanned point-by-point and the estimated potential of each non-electrode point is updated using the average of its nearest points. One scan through the array is called an iteration. Simion will continue to scan through the array (multiple iterations) until the array comes into an equilibrium where no point in the array changes by more than a user-set potential. Once this convergence limit is reached, Simion will have estimations for the potentials at all non-electrode points. The accuracy of this estimation depends on several factors including the convergence limit potential and the number of points in the array.

A process called fast adjusting is necessary before the potentials applied to the electrodes in a refined file can be adjusted. Simion fast adjusts by proportional scaling. Each point in the array is multiplied by a scaling factor related to the new potential applied to the electrode. Fast adjusting must be completed each time a potential is changed. For simulations involving ions, an ion definition file must also be created. This involves defining an ion's mass, charge, starting kinetic energy, time of birth, starting location and initial angle, as well as defining whether the ion is flown in a group or individually. Simion computes an ions trajectory by assessing how the ion interacts with the potential estimated for each non-electrode grid point.

1.4.3 Field and ion trajectory simulations

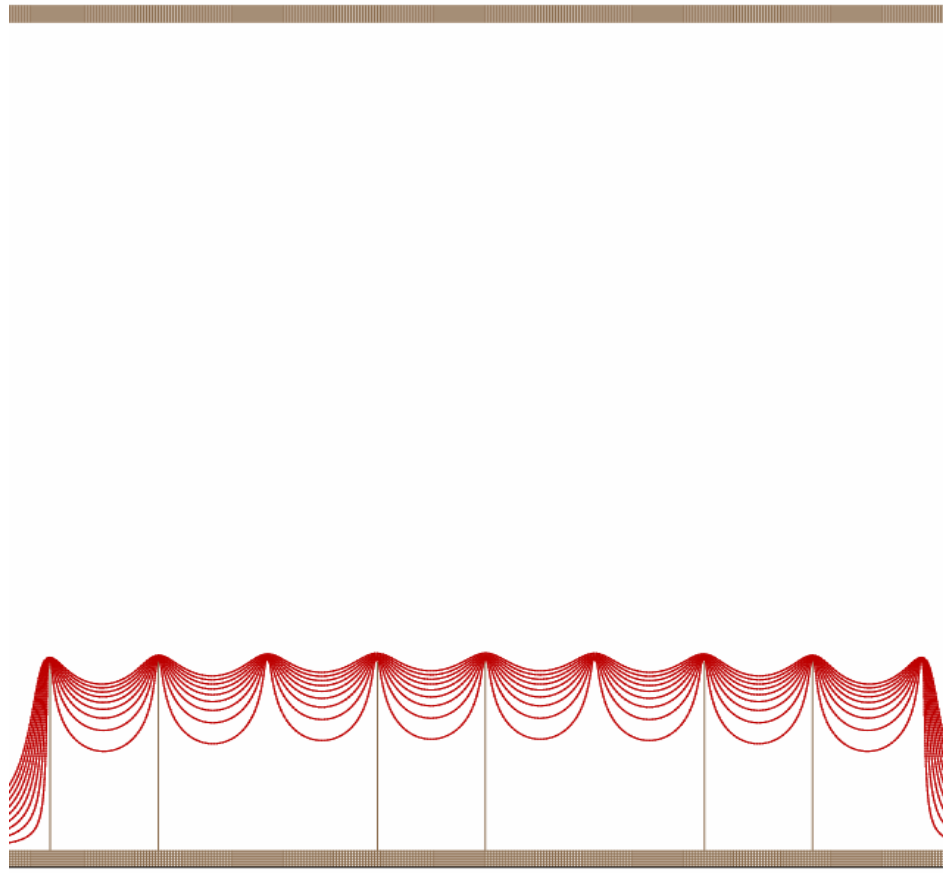
Simulation packages like Simion are capable of achieving quite complicated goals. In terms of this project Simion was used in two main ways to further development:

Simion was firstly used to simulate the fields generated at the tips of field ionisation/desorption field emitters in an effort to aid the understanding of what properties would be desirable to create a strong field. This helped identify the likely locations of ionisation sites on an emitter. Similar simulations were also used to compare different arrangements of field emitters in order to ascertain which would be the most suitable for achieving mass spectrometric measurements. These simulations were conducted using geometry files to define a 2D slice of the emitter. Once refined and fast-adjusted the simulated local field strengths were recorded at a small potential difference away from the tip (0.1 V). With the exception of difficulties in exceeding the maximum workable size of potential array, these simulations were fairly simple to create as no ions were required in the simulation. An example of the simulations conducted, which are discussed in much more detail in chapter 4, is shown in figure 1.21a.

Simion was also put to a more conventional use, namely to aid the development of ion transfer optics via ion trajectory simulations. The potential arrays used in these simulations were also built using geometry files, however, 3D simulations were required. In order to build the entire set of transfer optics, both cylindrical and planar geometries were put into use and in some cases combined to

minimise the total size of potential arrays used. Once refined, the effect of each electrode could be investigated and the optics could be optimised to give a rough idea of the potentials required to yield a collimated beam and/or maximum transmission. Simulations of this nature were conducted at nearly every stage of instrumentation development to test modifications and to help infer what was required to move the design forward. An example of an ion trajectory simulation is shown in figure 1.21b.

A



B

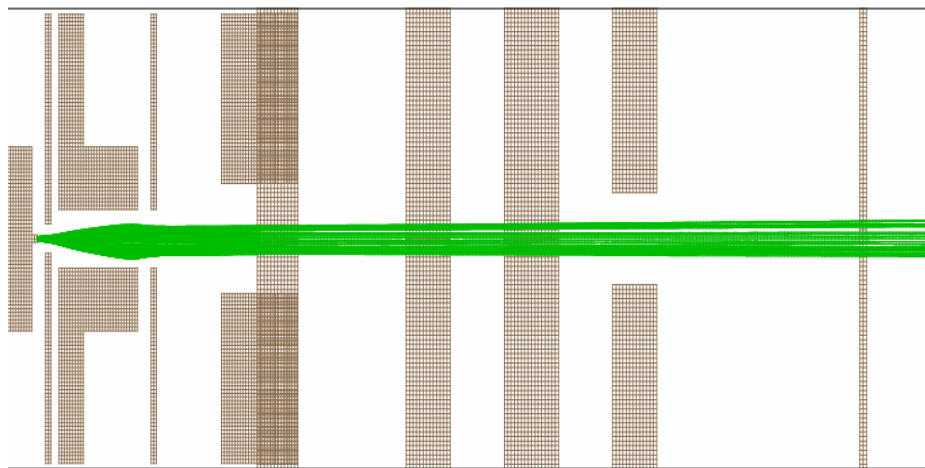


Figure 1.21 Simion 8 simulations showing examples of the simulation conducted in order to a) model the fields generated by applying a potential to the CNTs and b) model the trajectories of ions through the source and transfer optics.

1.5 Objectives of the thesis

The development of new mass spectrometry ionisation and analysis techniques continues. For analysis techniques it is desirable to be sensitive to very small amounts of material, produce spectra with high-mass resolution over short periods of time and keep the instrument fairly simple with a small laboratory footprint. FT-ICR mass spectrometry boasts the highest obtainable mass resolution but also has a fairly slow turn-around speed, requires large amounts of space and a reasonably high level of competence to operate. The development of recent instrumentation such as Thermoelectron's orbitrap⁸⁴ and Bruker's maXis⁸⁵ take significant steps towards achieving FTICR-like resolution without its main disadvantages.

For ionisation techniques the goals are varied: automation and higher levels of integration with the mass spectrometer and micro-fluidic technology has shown to be desirable with the advent of the robotic "nanomate"⁸⁶. The fundamental processes behind some of the ionisation techniques, however, are still not well understood. New techniques such as DESI⁴⁰ and DART³⁹ enhance the possibility of using mass spectrometry in places of public security to detect trace samples of dangerous chemicals such as explosives on the clothes and luggage of the general public. In the laboratory an ionisation source that can softly ionise any class of analyte remains a very desirable goal. This would open the door to a very flexible instrument that could be combined with both gas and liquid chromatography systems.

The work in this thesis describes studies of ion source instrumentation that aim to contribute towards some of the goals mentioned above. The development of a continuous-flow field desorption/ionisation source which uses arrays of vertically aligned carbon nanotubes as field emitters is discussed and explored. The structures of the vertically aligned carbon nanotubes have been characterised and their properties as field emitters of electrons investigated. A source has been constructed potentially to allow ionisation of samples in both gas and liquid phases and also theoretically any type of sample. A dual channelled nanospray emitter is described, which has the potential to yield further information on the nanospray process and hence on field-desorption processes in liquids. It is demonstrated that the dual channelled emitter makes possible the study of biological reactions over a fast time scale.

1.6 References

- (1) Grove, W. R. *Abstracts of the Papers Communicated to the Royal Society of London (1843-1854)* **1852**, 6, 168-169.
- (2) Svec, H. J. *International Journal of Mass Spectrometry and Ion Processes* **1985**, 66, 3-29.
- (3) Perrin, J. *Comptes rendus de l'Academie des sciences* **1895**, 121, 1130-1134.
- (4) Thomson, J. J. *Philosophical Magazine*, 44, 293 (1897) **1897**, 44, 293.
- (5) Thomson, J. J. *Philosophical Magazine Series 6* **1907**, 13, 561-575.
- (6) Thomson, J. J. *Philosophical Magazine Series 6* **1910**, 20, 752-767.
- (7) Thomson, J. J. *Rays of Positive Electricity and their Application to Chemical Analysis*; Longmans, Green and Co. Ltd.: London, 1913.
- (8) Aston, F. W. *Philosophical Magazine* **1919**, 38.
- (9) Aston, F. W. *Nature* **1919**, 104, 334.
- (10) Aston, F. W. *Nature* **1920**, 105, 617-619.
- (11) Dempster, A. J. *Physics Review* **1918**, 11, 316-325.
- (12) Dempster, A. J. *Nature* **1936**, 138, 120.
- (13) Parkins, W. E. *Physics Today* **2005**, 58, 45-51.
- (14) Bauer, S. H. *Journal of the American Society of Mass Spectrometry* **2001**, 12, 975-988.
- (15) Mattauch, J.; Herzog, R. *Zeitschrift fur Physik*, **1934**, 89, 786-795.
- (16) Johnson, E. G.; Nier, A. O. *Physics Review* **1953**, 91, 10-17.

- (17) Andersen, U. N.; Colburn, A. W.; Makarov, A. A.; Raptakis, E. N.; Reynolds, D. J.; Derrick, P. J.; Davis, S. C.; Hoffman, A. D.; Thomson, S. *Review of Scientific Instruments*. **1998**, *69*, 1650-1660.
- (18) Colburn, A. W.; Giannakopoulos, A. E.; Derrick, P. J.; Von Raumer, M. *European Journal of Mass Spectrometry* **2000**, *6*, 523-530.
- (19) Stephens, W. E. *Physical Review* **1946**, *69*, 691.
- (20) Wiley, W. C.; McLaren, I. H. *The Review of Scientific Instruments* **1955**, *26*, 1150-1157.
- (21) Mamyrin, B. A.; Karataev, V. I.; Shmikk, D. V.; Zagulin, V. A. *Sov. Phys. JETP*, **1973**, *37*, 45
- (22) Yefchak, G. E.; Schultz, G. A.; Allison, J.; Enke, C. G.; Holland, J. F. *Journal of the American Society of Mass Spectrometry*. **1990**, *1*, 440-447.
- (23) Boyle, J. G.; Whitehouse, C. M. *Anal. Chem.* **1992**, *64*, 2084-2089.
- (24) Colburn, A. W.; Giannakopoulos, A. E.; Derrick, P. J. *European Journal of Mass Spectrometry* **2004**, *10*, 149-154.
- (25) Paul, W. *Review of Modern Physics* **1990**, *62*, 531-540.
- (26) Colburn, A. W.; Barrow, M. P.; Gill, M. C.; Giannakopoulos, A. E.; Derrick, P. J. *Physics Procedia* **2008**, *1*, 51-60.
- (27) Sommer, H.; Thomas, H. A.; Hipple, J. A. *Physical Review* **1951**, *82*, 697-702.
- (28) Baldeschwieler, J. D. *Science* **1968**, *159*, 263 - 273.
- (29) Comisarow, M. B.; Marshall, A. G. *Chemical Physics Letters* **1974**, *25*, 282-283.
- (30) Palmblad, M.; Håkansson, K.; Håkansson, P.; Feng, X.; Cooper, H. J.; Giannakopoulos, A. E.; Green, P. S.; Derrick, P. J. *European Journal of Mass Spectrometry* **2000**, *6*, 267-275.
- (31) P. Caravatti, M. A. *Organic Mass Spectrometry* **1991**, *26*, 514-518.
- (32) Barrow, M. P.; McDonnell, L. A.; Feng, X.; Walker, J.; Derrick, P. J. *Anal. Chem.* **2003**, *75*, 860-866.
- (33) Barrow, M. P.; Feng, X.; Wallace, J. I.; Boltalina, O. V.; Taylor, R.; Derrick, P. J.; Drewello, T. *Chemical Physics Letters* **2000**, *330*, 267-274.
- (34) Hill, T. J.; Lafitte, D.; Wallace, J. I.; Cooper, H. J.; Tsvetkov, P. O.; Derrick, P. J. *Biochemistry* **2000**, *39*, 7284-7290.
- (35) Marshall, A. G.; Schweikhard, L. *International Journal of Mass Spectrometry and Ion Processes* **1992**, *118*, 37-70.
- (36) Caravatti, P.; Patent., U. S., Ed., 1990.; Vol. 4,924,089.
- (37) Munson, M. S. B.; Field, F. H. *Journal of the American Chemical Society* **1966**, *88*, 2621-2630.
- (38) Karas, M.; Bachmann, D.; Hillenkamp, F. *Analytical Chemistry* **1985**, *57*, 2935-2939.
- (39) Cody, R. B.; Laramée, J. A.; Durst, H. D. *Analytical Chemistry* **2005**, *77*, 2297-2302.
- (40) Takats, Z.; Wiseman, J. M.; Gologan, B.; Cooks, R. G. *Science* **2004**, *306*, 471-473.
- (41) Muller, E. W. *Annual Review of Physical Chemistry* **1967**, *18*, 35-56.
- (42) Inghram, M.; Gomer, R. *Journal of Chemical Physics* **1954**, *22*, 1279-1281.
- (43) Muller, E. W.; Bahadur, K. *Physical Review* **1956**, *102*, 624-631.
- (44) Beckey, H. D. *Principles of Field Ionization and Field Desorption Mass Spectrometry*, First ed.; Pergamon Press: Oxford, 1977.
- (45) Beckey, H. D.; Hey, H.; Heising, H.; Metzinger, H. G. *Advances in Mass Spectrometry* **1968**, *4*, 817-831.

- (46) Beckey, H. D. *Research/Development* **1969**, *20*, 26-29.
- (47) Beckey, H. D. *Journal of Mass Spectrometry and Ion Physics* **1969**, *2*, 495-500.
- (48) Muller, E. W. *Physical Review* **1956**, *102*, 618-624.
- (49) Gomer, R. *Journal of Chemical Physics* **1959**, *31*, 341-345.
- (50) Mckinstry, D. *Surface Science* **1972**, *29*, 37-59.
- (51) Haydock, R.; Kingham, D. R. *Physical Review Letters* **1980.**, *44*, 1520-1523.
- (52) Prokai, L. *Field Desorption Mass Spectrometry*; Marcel Dekker INC: New York, 1990.
- (53) Giessmann, U.; Rollgen, F. W. *International Journal of Mass Spectrometry and Ion Physics* **1981**, *38*, 267-279.
- (54) Wong, S. S.; Giessmann, U.; Karas, M.; Rollgen, F. W. *International Journal of Mass Spectrometry and Ion Processes*, **1984**, *56*, 139-150.
- (55) Davis, S. C.; Natoli, V.; Neumann, G. M.; Derrick, P. J. *International Journal of Mass Spectrometry and Ion Processes*, *78 (1987) 17-35* **1987**, *78*, 17-35.
- (56) Colburn, A. W.; Davis, S. C.; Derrick, P. J., Lovanger, Sweden. 1989; John Wiley and Sons; 145-155.
- (57) Holland, J. F.; Soltmann, B.; Sweeley, C. C. *Biomedical Mass Spectrometry* **1976**, *3*, 340-345.
- (58) Rollgen, F. W.; Giessmann, U.; Heinen, H. J.; Beckey, H. D. *Ultramicroscopy* **1979**, *4*, 375-376.
- (59) Burlingame, A. L.; Baillie, T. A.; Derrick, P. J.; Chizhov, O. S. *Analytical Chemistry* **1980**, *52*, 214R-258R.
- (60) Cotter, R. J.; Yergey, A. L. *Analytical chemistry* **1982**, *53*, 1306-1307.
- (61) Okuyama, F.; Shen, G. H. *International Journal of Mass Spectrometry and Ion Physics* **1981**, *39*, 327-337
- (62) Rollgen, F. W.; Giessmann, U.; Heinen, H. J.; Reddy, S. J. *International Journal of Mass Spectrometry and Ion Physics* **1977**, *24*, 235-238.
- (63) Winkler, H. U.; Beckey, H. D. *Biochemical and Biophysical Research Communications* **1972**, *46*, 391-398.
- (64) Beckey, H. D.; Schulten, H. R. *Angewandte Chemie International Edition in English* **1975**, *14*, 403-415.
- (65) Linden, H. B. *European Journal of Mass Spectrometry* **2004**, *10*, 459-468.
- (66) Schaub, T. B.; Linden, H. B.; Hendrickson, C. L.; Marshal, A. G. *Rapid communications in Mass Spectrometry* **2004**, *18*, 1641-1644.
- (67) Dole, M.; Mack, L. L.; Hines, R. L.; Mobley, R. C.; Ferguson, L. D.; Alice, M. B. *Journal of Chemical Physics* **1968**, *49*, 2240-2249.
- (68) Fenn, J. B. *Journal of Biomolecular Techniques*, **2002**, *13*, 101-118.
- (69) Yamashita, M.; Fenn, J. B. *Journal of Physical chemistry* **1984**, *88*, 4451-4459.
- (70) Yamashita, M.; Fenn, J. B. *Journal of Physical Chemistry* **1984**, *88*, 4671-4675.
- (71) Fenn, J. B.; Mann, M.; Meng, C. K.; Wong, S. F.; Whitehouse, C. M. *Science* **1989**, *246*, 64.
- (72) Iribarne, J. V.; Thomson, B. A. *J. Chem. Phys.* **1976**, *64*, 2287-2294.
- (73) Rohner, T. C.; Lion, N.; Girault, H. H. *Physical Chemistry Chemical Physics* **2004**, *6*, 3056 – 3068.
- (74) Gaskell, S. J. *Journal of Mass spectrometry* **1997**, *32*, 677-688.
- (75) Yates III, J. R. *Journal of mass spectrometry* **1998**, *33*, 1-19.
- (76) Mano, N.; Goto, J. *Analytical Sciences* **2003**, *19*, 3-14.

- (77) Wilm, M. S.; Mann, M. *International Journal of Mass Spectrometry and Ion Processes*. **1994**, *136*, 167-180.
- (78) Zampronio, C. G.; Giannakopoulos, A. E.; Zeller, M.; Bitziou, E.; Macpherson, J. V.; J., D. P. *Analytical Chemistry* **2004**, *76*, 5172-5179.
- (79) Wilm, M.; Mann, M. *Analytical Chemistry* **1996**, *68*, 1-8.
- (80) Schmidt, A.; Karas, M.; Dulcks, T. *Journal of the American Society of Mass Spectrometry* **2003**, *14*, 492-500.
- (81) Dahl, D. A.; Delmore, J. E.; Appelhans, A. D. *Review of Scientific Instruments*. **1990**, *61*, 607-609.
- (82) Austin, D. E.; Cruz, D.; Blain, M. G. *Journal of the American Society for Mass Spectrometry* **2006**, *17*, 430-441.
- (83) Sun, W.; May, J. C.; Russell, D. H. *International Journal of Mass Spectrometry* **2007**, *259*, 79-86.
- (84) Hu, Q.; Noll, R. J.; Li, H.; Makarov, A.; Hardmanc, M.; Cooks, R. G. *Journal of Mass Spectrometry* **2005**, *40*, 430-443.
- (85) Bruker In *Conference of the British Mass spectrometry Socceity*: York, 2008.
- (86) Kim, S.; Rodgers, R. P.; Blakney, G. T.; Hendrickson, C. L.; Marshall, A. G. *Journal of the American Society for Mass Spectrometry* **2009**, *20*, 263-268.

2. A dual-channelled nano-electrospray source for mass spectrometry

2.1 Introduction.

The development of electrospray ionization (ESI)¹ and nano-electrospray (nano-ESI)² has permitted the study of many biological and biochemical problems using mass spectrometry. One important example is the characterization of non-covalent complexes involving proteins or peptides. ESI and nano-ESI are capable of releasing a non-covalent complex from its native solution state into the gas phase in the form of multiply charged ions and has allowed the detection of complexes for a number of protein-protein³ and protein-ligand⁴ interactions. Since such interactions are essential for an orderly function of a cell, their study is of crucial importance.

Despite the large amount of research concerning ESI and nano-ESI, fundamental details at the molecular level are not well understood. The two competing theories proposed for the mechanism of ESI each explain some ESI characteristics, but neither accounts for all experimental observations. Salient questions which remain unanswered are the influence of temperature, pressure and extraneous substances such as salts and detergents. The continuation of research concerning the nature of ESI and nano-ESI is important in order to allow a greater understanding of the analyte interactions studied using these ionisation techniques. In this chapter the fabrication and testing of nano-electrospray emitters that have two channels running throughout the length of

the emitters is described. Such a dual-channelled emitter is illustrated in Figure 2.1

Dual-channelled emitters could provide insight into the details of the electro spray process as well as fundamental information on physical and chemical processes occurring within the solutions while spraying. This study deals with the fabrication of dual-channelled emitters, and evaluation of their suitability as electro spray emitters. Some of the capabilities of these emitters have been investigated by spraying two different solutions one from each channel.

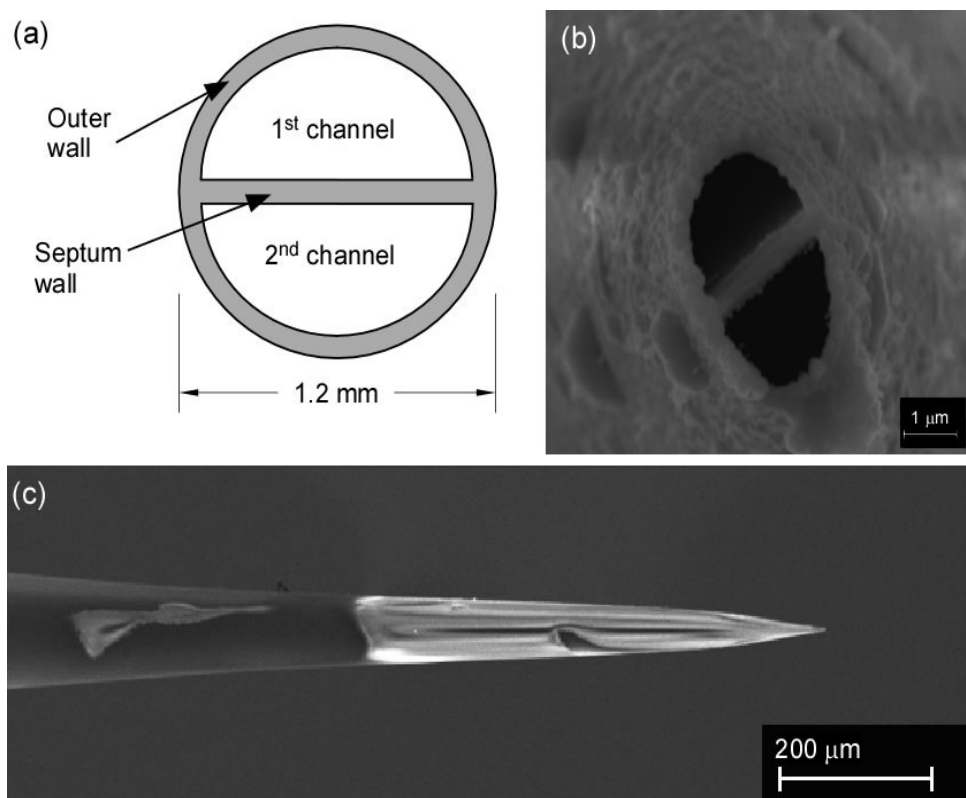


Figure 2.1. Theta-shaped profile of glass capillary, (a) sketch of the distal end and (b) electron micrograph of the very tip (c) electron micrograph of the side of the emitter.

The dual-channelled emitters could be regarded as electrospray-coupled microfluidic devices^{5,6} in which the mixing volume has been reduced to zero. Both channels run the length of a dual-channelled emitter and mixing of the contents of the two channels would be expected to be restricted to the shared Taylor cone. Results with vancomycin are presented for the dual-channelled emitters. Vancomycin belongs to the glycopeptide group of antibiotics, which are characterised by a macrocyclic backbone with sugar moieties attached at various sites. Its usefulness as an antibiotic comes from its ability to inhibit bacterial biosynthesis by binding to peptidoglycan precursors terminating in the sequence *d-Ala-d-Ala* on the immature cell wall of gram positive bacteria.^{7,8} Vancomycin is often referred to as the “antibiotic of last resort”, because bacteria have become resistant to so many other drugs.⁹ With reports of vancomycin resistant strains of bacteria, investigating how vancomycin interacts with cell wall mimics such as *di-N-acetyl-L-Lys-d-Ala-d-Ala* (KAA) has become of even greater interest.

Glycopeptide antibiotics such as vancomycin were observed many years ago to aggregate in aqueous solution.¹⁰ NMR-experiments with similar peptidoglycan antibiotics, ristocetin and eremomycin, showed that their complexes with their corresponding cell-wall precursor mimics form hydrogen-bonded dimers.^{11,12} The hydrogen bond interactions are said to be formed between the ‘back’ faces of two antibiotic molecules, meaning, the faces not directly involved in ligand binding. It has been proposed that the dimerization plays an important role in the effectiveness of the antibiotic and thus is implicated in the physiological mode of action of these antibiotics.¹³

2.2 Nano-electrospray emitter fabrication.

Dual-channelled nano-ESI emitters (needles) were produced in the laboratory from theta-shaped borosilicate glass capillaries (Hilgenberg GmbH, 1.20 mm O.D., 0.96 mm. I.D., Prod.No. 1402415) using a microcapillary puller (Sutter Instrument Co., Model P-2000). The microcapillary puller operated by using a carbon dioxide laser to heat the centre of the borosilicate capillary, each end of the capillary was secured in the instrument and attached to weights. As the glass was heated it becomes soft and started to flow. The force applied by the weights caused the liquid glass to draw out until a limit was reached, at which point the two ends were separated. The puller would therefore produce two smaller capillaries each with a fine tip. The theta nature of the capillary was preserved to the tips of nearly all of the capillaries produced

An optical microscope equipped with a calibration grid (Olympus BH2-HLSH) with accuracy $\pm 0.5 \mu\text{m}$ was used to check the tip size. A tip diameter of $2 \mu\text{m}$ per channel was produced very consistently, while the whole emitter tip had a diameter of $4.5 \mu\text{m}$. The diameter produced could be varied depending on the settings used by the puller. Programs designed to produce tip diameters below $4.5 \mu\text{m}$ were found to be less consistent. It is worth noting that a diameter of $2 \mu\text{m}$ has been shown to lead to the most reproducible spectra in the analysis of non-covalent complexes when using conventional single-channelled nano-ESI needles.¹⁴

A platinum coating was prepared using organometallic paint 'bright platinum' (PBV00158), diluted with a paint thinner (OIL 00058). Both were purchased from Johnson Matthey Noble Metals (Stoke-on-Trent, UK). Each emitter was manually painted using a rotating device and heated in an oven at 600 °C for 30 minutes in order to remove excess solvent. A flow of air was used to purge the capillaries while the needles were being painted, thus preventing paint from blocking the capillary opening. It was necessary to recheck each emitter with the optical microscope to make sure that the emitter was not damaged during the preparation process.

For comparison purposes the noble metal coating was also produced by sputtering in a magnetron (Moorfield, Knutsford, UK). Sputtering was performed in two steps. In Step 1, the needles were coated with a thin (~15 nm) titanium layer, while a thicker (~100 nm) gold layer was attached in Step 2.¹⁵ Both steps were time consuming due to the small number of emitters that could be sputtered at the same time. After sputtering the needles were ready for use. The effect of sputtering ensured that the metal particles were coated all the way to the edge and even inside the emitter tip. This can be seen in a comparison between the tips of emitters coated using both methods shown in Figure 2.2

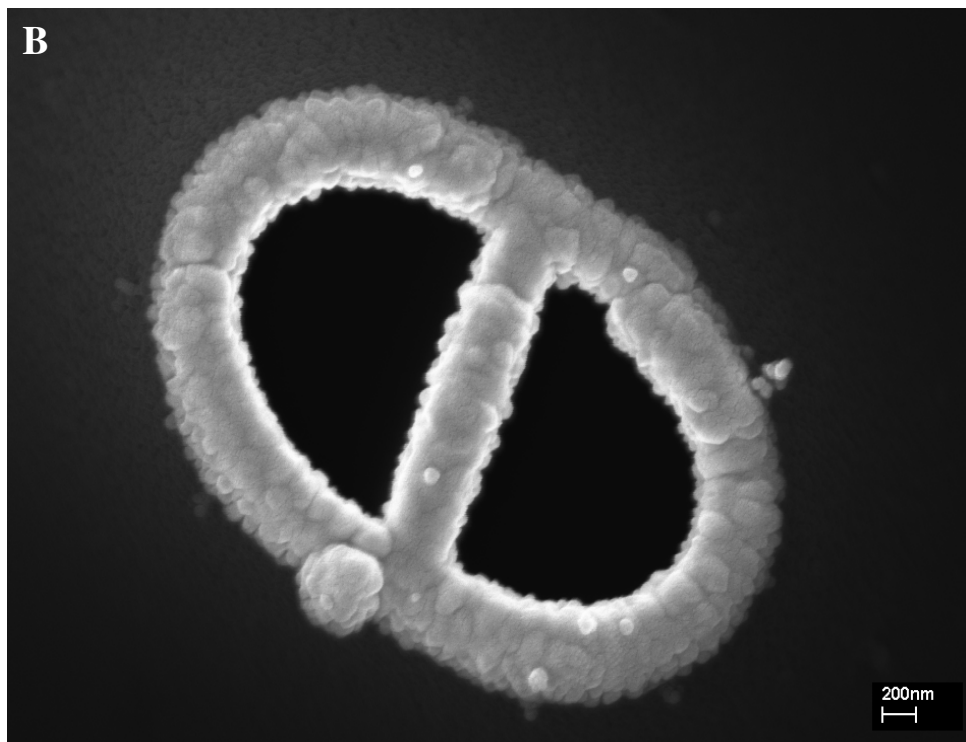
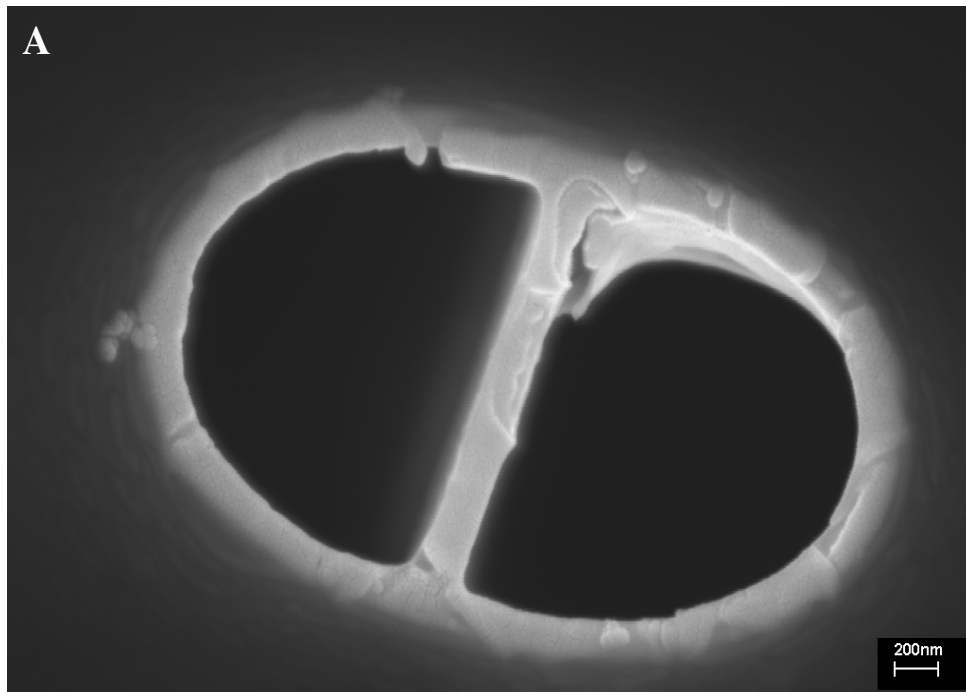


Figure 2.2. Electron micrographs of the tip of theta-shaped needle coated using (a) hand-painted method and (b) magnetron sputtering.

2.3 Investigation of the performance of the nano-electrospray emitters.

2.3.1 Confocal microscopy

Confocal microscopy was used to investigate whether the dual-channelled emitters would form an electrospray and if so whether there would be a shared Taylor cone when samples were loaded down both channels. The confocal microscope works in a similar fashion to a fluorescence microscope, in so far as a laser is used to excite a sample and the fluorescence produced as the sample returns to its ground state is observed. The confocal microscope differs however because it allows a defined depth of field to be viewed rather than a composite of the fluorescence produced from all depths. Higher resolution is obtained by removing the blur produced by a composite.¹⁶

In order to simulate nanospray conditions in the confocal microscope, a holder was constructed to allow a nanospray emitter to be placed close to a counter electrode. The counter electrode represented the capillary entrance of a normal source and a variable potential could be applied to it. The Taylor cone(s) and any mixing between the two channels was imaged using two dyes (rhodamine B (red) and fluorescein yellow/green) which fluoresced at different wavelengths. Using two lasers to excite independently each dye at the same time, the fluorescence produced from each channel could be monitored. Overlapping the images produced by the lasers gave an image which provided information on the extent of the mixing.

Images of an emitter loaded with the two dyes were recorded as the potential applied to the counter electrode was increased to 750 V. The potential difference between the electrode and emitter could not be increased further than 750 V due to safety reasons. Figure 2.3 shows the images recorded at potential differences of a) 0 V and b) 750 V (provided by Matthew Gill). The formation of what was taken to be a Taylor cone was observed at a potential slightly below 750 V. The image (figure 2.3) suggests that a single Taylor cone was formed, although it should be noted that the rounded shape of the protuberance is unusual. Enhancing the image (figure 2.3 c) a yellow colour can be seen in the volume where the dyes would mix. The yellow colour was attributed to the combination of the fluorescence from the two dyes and was taken as a clear indication of mixing of the two dyes from the two channels.

The results from the confocal microscope suggested that in a real nano-electrospray experiment a single Taylor cone would be formed and that mixing would occur within that shared Taylor cone. The rounded Taylor cone may indicate that no electrospray was formed and so mixing within the Taylor cone may not have occurred over a short timescale. There were a few differences between the parameters of this approximation and a real nano-electrospray experiment. The emitter in a real nano-electrospray experiment would be closer to the capillary entrance and the emitter would therefore experience a stronger field. This difference might explain the rounded Taylor cone observed in the confocal microscope at a potential difference which would produce an elongated Taylor cone in electrospray experiments on a mass spectrometer.

It seems likely that, if the potential difference in the confocal microscope could have been increased beyond 750 V, an elongated Taylor cone would have been observed.

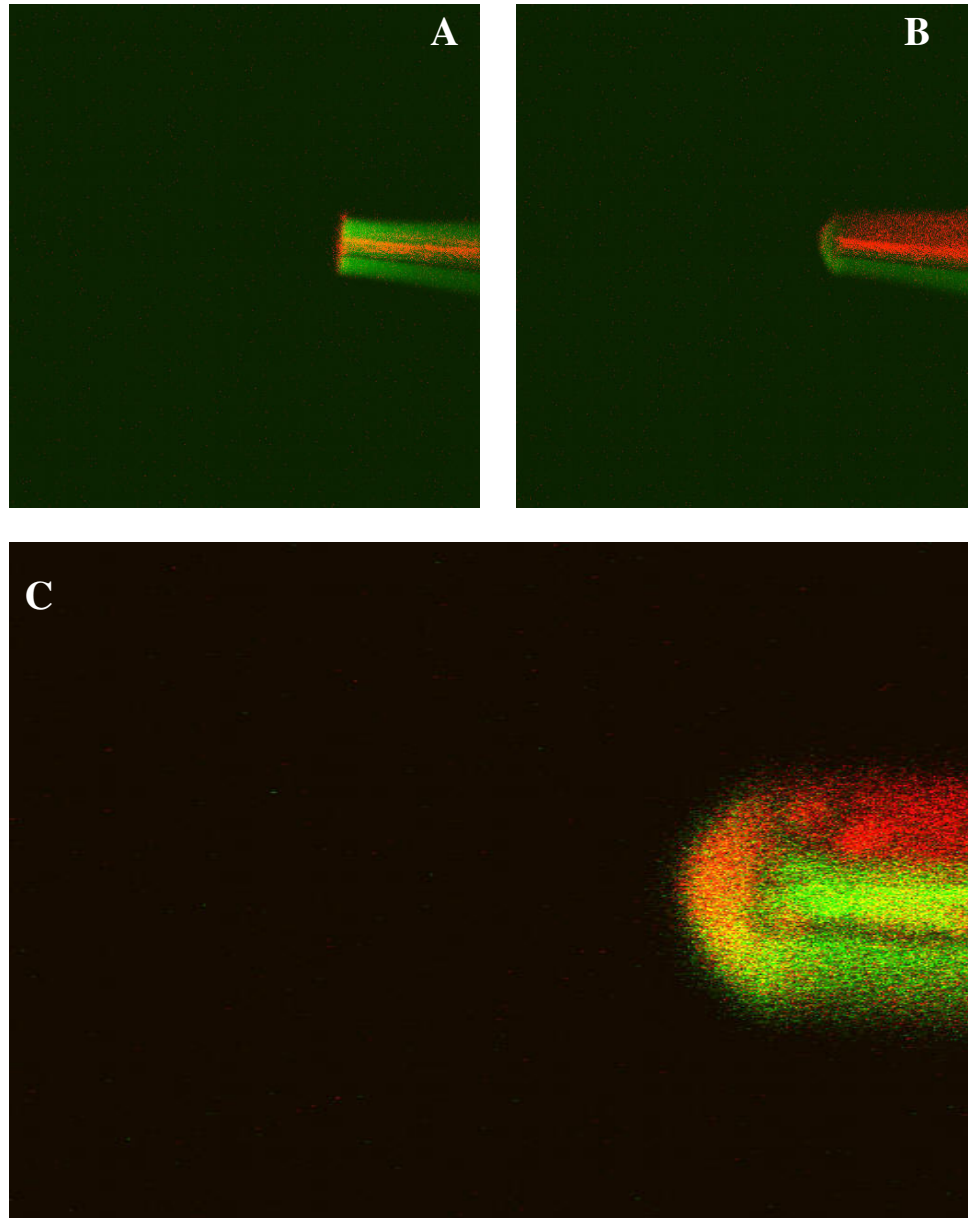


Figure 2.3. Confocal microscope images (provided by Matthew Gill) of a dual channelled nanospray needle loaded with dyes of different wavelength fluorescence under a potential difference of a) 0 V, b) 750 V and c) 750 V (enhanced view).

2.3.2 Characterisation of the dual-channelled emitter

Positive nano-ESI FT-ICR was used to investigate whether viable mass spectrometric measurements could be made with dual-channelled emitters coated by the hand-painting procedure. A solution of vancomycin (Sigma chemical co.) was prepared using ammonium acetate buffer (0.05 M, pH 5.2) and shaken mechanically for 1 minute in order to promote dissolution.

Nanospray emitters were loaded with approximately 10 μ l of sample solution using a GELoader pipette tip (Eppendorf AG, Hamburg). In all experiments, the emitter was positioned at a distance of 2 mm from the counter electrode, and a voltage of between -400 to -900 V was applied while the needle was grounded. Carbon dioxide was used as a backing gas at 10 psi. The capillary-exit voltage, the offset, the residence time in the hexapole (4 s) and the ion injection time in the cell (4400 μ s) were maintained constant throughout. The ion source was operated without desolvation gas at a temperature of 25 $^{\circ}$ C. Spectra were acquired as a sum of 64 scans, and each scan was digitized to 512 K data points.

Figures 2.4(a) and (b) show mass spectra recorded with a dual-channelled emitter and a conventional emitter purchased from Proxeon (Odense, DK), respectively. Mass spectra were obtained with dual-channelled emitters when one side was loaded with vancomycin solution. There was little difference in the mass spectra regardless of whether the vancomycin solution was sprayed from both or just one channel. Comparing the two spectra in Figure 2.4 there are no significant differences. It is concluded that dual-channelled emitters are well suited for producing electrospray.

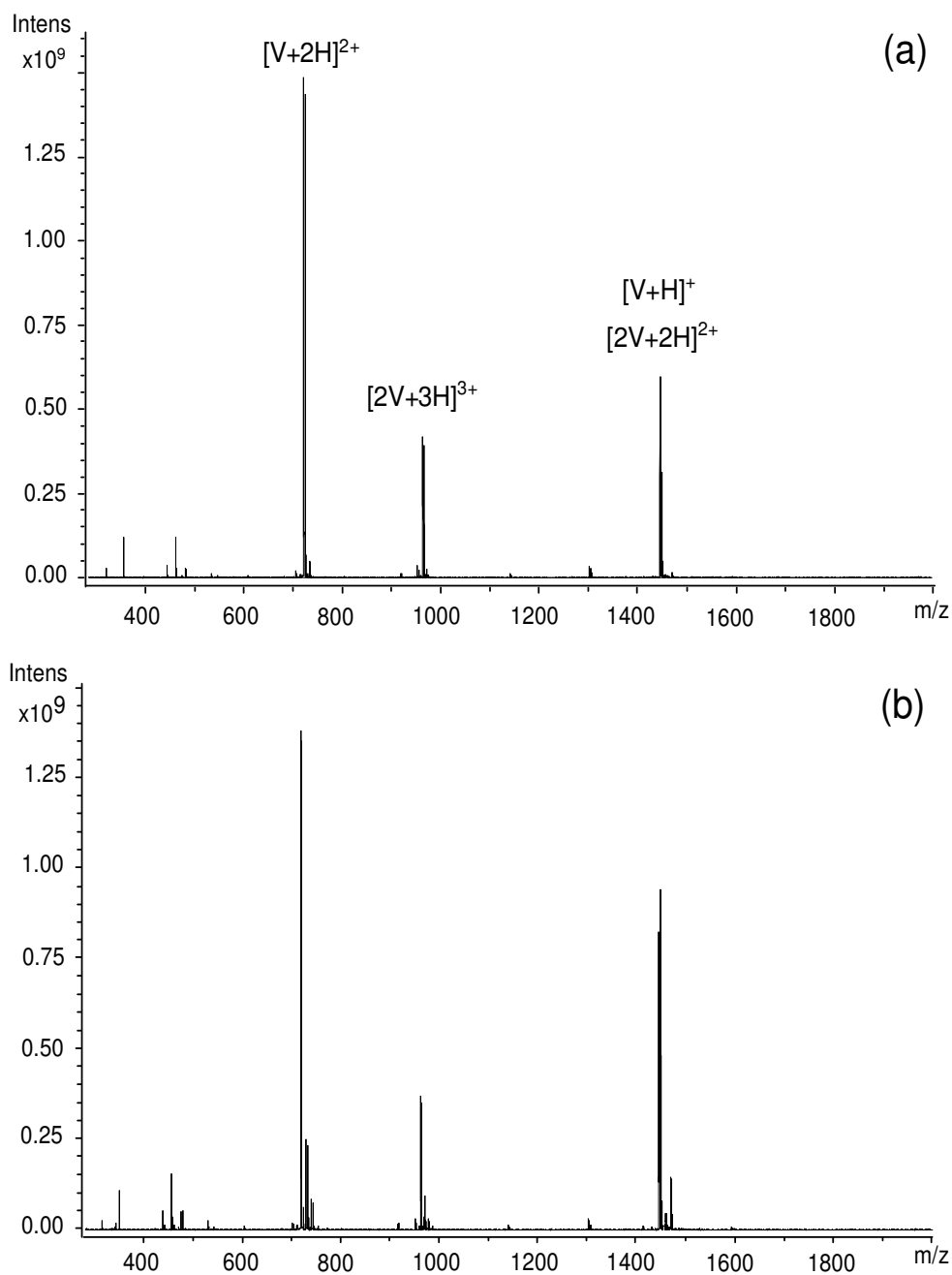


Figure 2.4. Mass spectra of vancomycin $[V] = 135 \mu\text{mol/L}$ for (a) a hand-painted dual-channelled emitter (one side loaded) and (b) a conventional single-channelled emitter.

The characteristics of dual-channelled emitters coated by magnetron sputtering were similar. A spectrum obtained using identical instrument parameters as above but with a fresh 135 μm solution of vancomycin is shown in Figure 2.5. However, in this case, slightly lower voltages on the counter electrode ~300 to 500 V were necessary in order to produce a stable electrospray. It was assumed that lower voltages were required because sputtered emitters were coated to the very tip of the emitter.

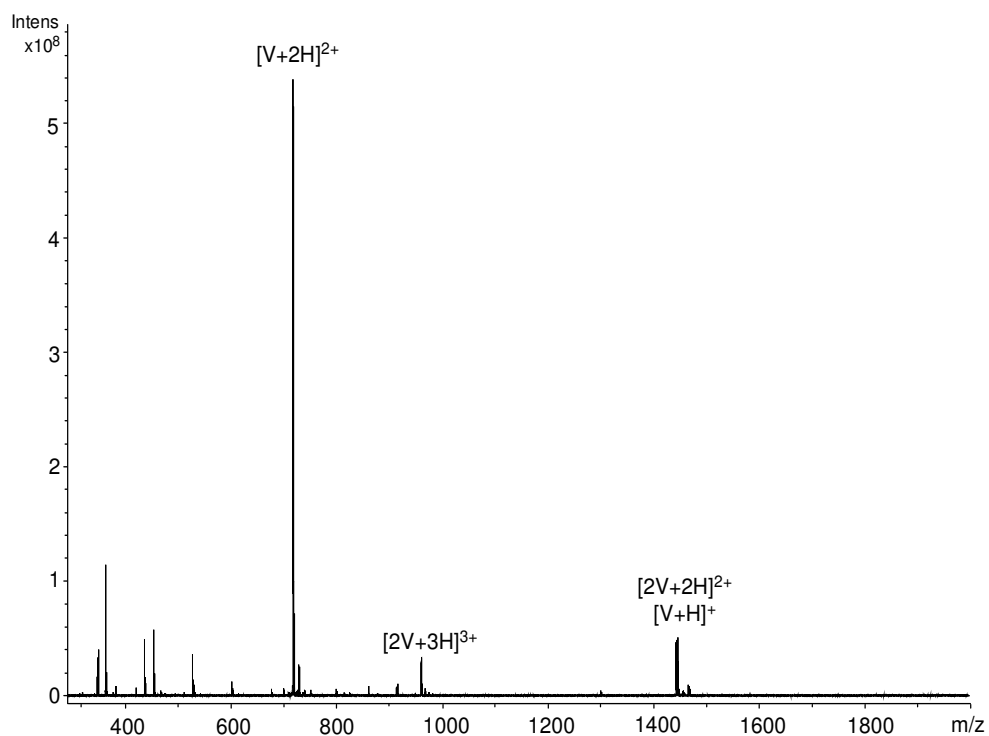


Figure 2.5. Mass spectra of vancomycin $[V] = 135 \mu\text{mol/L}$ using a sputtered dual-channelled emitter (one side loaded)

When compared with a hand-painted needle the spectra appear differed, in particular at the low-mass range and in the relative intensities of the major peaks. These differences were attributed to:

- ❖ the lower voltage used with the sputtered needles,
- ❖ different Taylor cone formation due to the sputtered metal coating at the end of the emitter.

Aside from these differences, sputtering of the noble metal coating provided no noticeable improvement in the mass spectrometric performance. Considering the times required to produce the coated emitters, hand-painted emitters were used to investigate further the characteristics of the dual-channelled emitters.

The performance achieved with nano-electrospray emitters, whether commercially bought or home-made, was not reproducible. Commercially bought nano-electrospray emitters were found sometimes to have high levels of salt contaminate and when these faulty emitters were used for to form an electrospray the contamination could be such that the mass spectrometric measurements were rendered useless. Very high levels of reproducibility were not always guaranteed with uncontaminated or 'good' nano-electrospray emitters: Experiments conducted using the same instrumental parameters but with different emitters could yield slightly different peak intensities. This was found to be true also of dual channelled emitters. It is possible that differences in Taylor cone formation may be responsible for such differences. It was that there was not any significant difference found between spraying down one channel as compared to spraying down both channels.

The durability of dual-channelled nanospray emitters was investigated. A solution of vancomycin prepared as above was loaded into an emitter and using the same needle parameters sprayed into the FTICR. By refilling the needle when the loaded sample ran out, it was possible to record mass spectrometric measurements with the same needle over large periods of time. Figure 2.6 compares the mass spectra recorded every 30 minutes over a period of 1.5 hours. As can be seen a stable signal was achieved for up to 1.5 hours. A signal could be achieved beyond this limit, however, it was not envisaged that a nanospray measurements would require longer than 1.5 hours to complete and so the experiment was curtailed. Over the time-scale of the experiment there was little variation among the relative intensities of peaks in each spectrum. There was a slight drop in absolute intensity as the experiments progressed. Note that the ion injection time into the cell used for the durability experiment was slightly larger than previous experiments (4800 μs) and so ions of larger m/z were more prominent in the mass spectra.

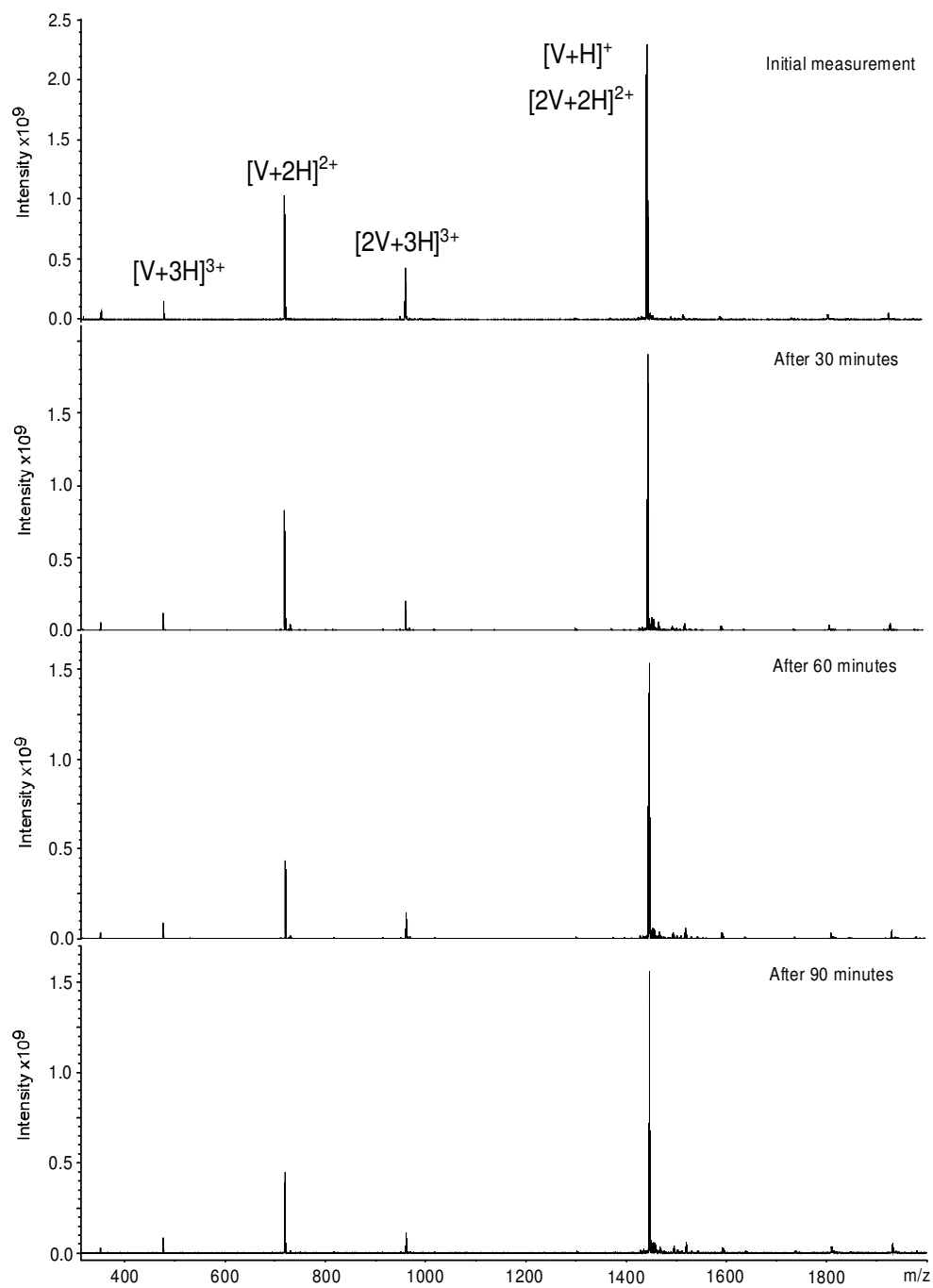


Figure 2.6. Mass spectra of vancomycin [V] = 135 $\mu\text{mol/L}$ recorded at 30 minute intervals using the same dual-channeled emitter.

2.3.3 Mixing experiments

The dual-channelled emitters were designed with the expectation that different samples loaded down the two channels would mix in a shared Taylor cone. The study of their reaction kinetics over a short timescale might then be accessible. The above experiments gave insight into some of the emitter's properties but they did not answer questions such as whether two different samples would spray at the same time, whether different samples might form a shared Taylor cone or whether two individual cones would ever be seen. The interaction between vancomycin and KAA was investigated using the dual-channelled emitters to begin to address these questions

2.3.3.1 Vancomycin –KAA

Vancomycin solution was loaded down one channel, and a solution of KAA (prepared using the same method as for vancomycin) was loaded down the other channel of a dual-channelled emitter. The emitter was used to form an electrospray using the same experimental conditions as were used for the first proof of concept experiment in subchapter 2.3.2.

In the spectrum (Figure 2.7a), a peak at m/z 910.82 can be seen which is attributed to the vancomycin/KAA complex. This observation strongly suggests that a shared Taylor cone was formed by the two channels and that mixing between samples from the two channels took place within the cone. Different species of complex were also seen, such as a vancomycin molecule with two KAA ligands or a vancomycin dimer with two and one KAA, respectively,

many in various charge states. Other ion signals were attributed to fragments of vancomycin. It is noteworthy, considering the proposed physiological mode of action of vancomycin, that the intensity of the monomer-bound complex far outweighed that of the dimer-bound complex. Previous mass spectrometry based studies of the vancomycin-KAA bonding however, have also failed to show the levels of dimerization suggested by the NMR studies of vancomycin.¹⁷

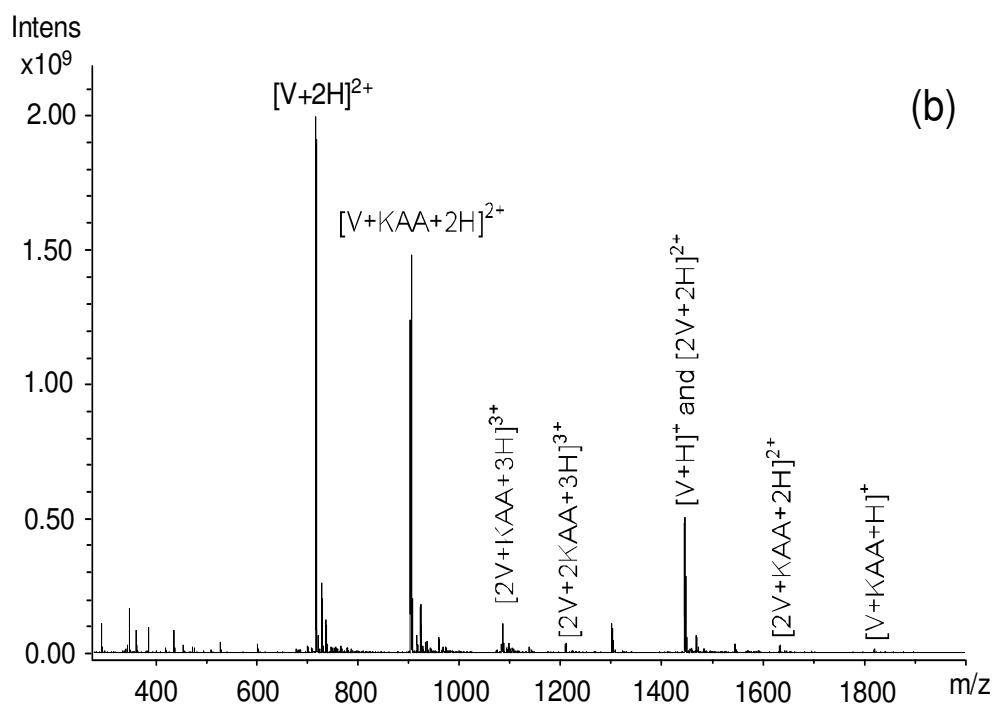
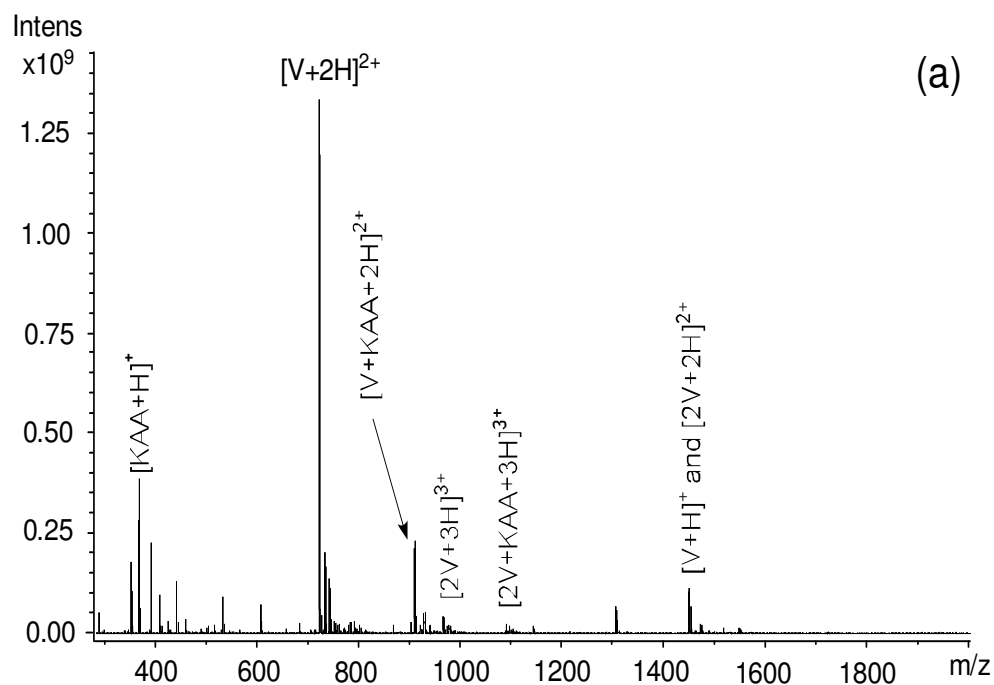


Figure 2.7. Mass spectra of vancomycin (a) $[V] = 135 \mu\text{mol/L}$ and $[KAA] = 135 \mu\text{mol/L}$ loaded on either side of a dual-channelled emitter and (b) a premixed solution of $[V] = [KAA] = 135 \mu\text{mol/L}$ sprayed down both sides of a dual-channelled emitter

In order to estimate the mixing time, the amount of bound vancomycin (to the peptide ligand) was taken from mass spectra and related to the time required to form this amount on the basis of the kinetic parameters in the literature ($k_{on} = 3.4 \times 10^7$).¹⁸ The ratio of bound vancomycin was estimated from the relative peak intensities as given by Equation 6.1. As in FTICR the signal increases linearly with ion charge, the sensitivity for the double-charge state was considered to be twice that of the single-charge state.¹⁹ To correct for this influence, the intensities of doubly charged species were divided by 2.

$$\frac{[V + KAA]}{[V]_0} = \frac{\frac{I_{[V+KAA+2H]^+}}{2}}{I_{[V+H]^+} + \frac{I_{[V+2H]^{2+}}}{2} + \frac{I_{[V+H+Na]^{2+}}}{2} + \frac{I_{[V+KAA+2H]^{2+}}}{2}} \quad \text{Equation 6.1}$$

$$t = \frac{\frac{1}{[V]_0 \left(1 - \frac{[V + KAA]}{[V]_0}\right)} - \frac{1}{[V]_0}}{k_{on}} \quad \text{Equation 6.2}$$

Following Equation 6.2 a mixing time (t) of $77 \pm 20.3 \mu\text{s}$ is calculated. The initial concentration of vancomycin $[V]_0$ in the Taylor cone where mixing occurred is $67.5 \mu\text{mol/L}$. The uncertainty in the mixing time reflects changes from one needle to another as their dimensions were not absolutely the same and the effect of the applied electrospray voltage. The effect of vancomycin dimer on the intensity of free Vancomycin was neglected because of its small

contribution in these experiments. The possibility of further mixing in shared droplets was not accounted for.

Comparing the spectrum from the mixing experiment to the spectrum of a pre-mixed solution prepared four hours prior to mass spectrometric measurements (Figure 2.7 b), the main difference was the dramatic rise of the doubly charged complex peak $[V+KAA+2H]^{2+}$. Complex species involving two vancomycin molecules were also more intense. These variations in intensity were bigger than the normal variations found when using nanoESI. It was considered that for the vancomycin/KAA binding, complete mixing of the two solutions was not achieved in the timescale available in the shared Taylor cone of the dual-channel emitter.

2.3.3.2 Vancomycin – deuterated vancomycin

The principle of mixing in a shared Taylor cone was tested further using a sample of isotopically normal vancomycin loaded down one side of a dual-channeled emitter and a sample of deuterated vancomycin down the other. Mass spectra were collected on the FTICR as above except that the cell injection-period was 4000 μ s. Deuterated vancomycin (V-Dx) was prepared through H/D exchange by dissolving normal vancomycin in heavy water, and as such did not have a defined isotopic composition. Despite this fact, the mass shift, evident in Figure 2.8 a/b, was more than sufficient to distinguish the two forms of vancomycin. At least 6 hydrogen atoms had been exchanged in all cases, the average being 12 hydrogen atoms. Due to the high resolution of the FT-ICR

mass spectrometer, peaks from deuterated vancomycin and those from the non-deuterated sodium adducts could be assigned unambiguously.

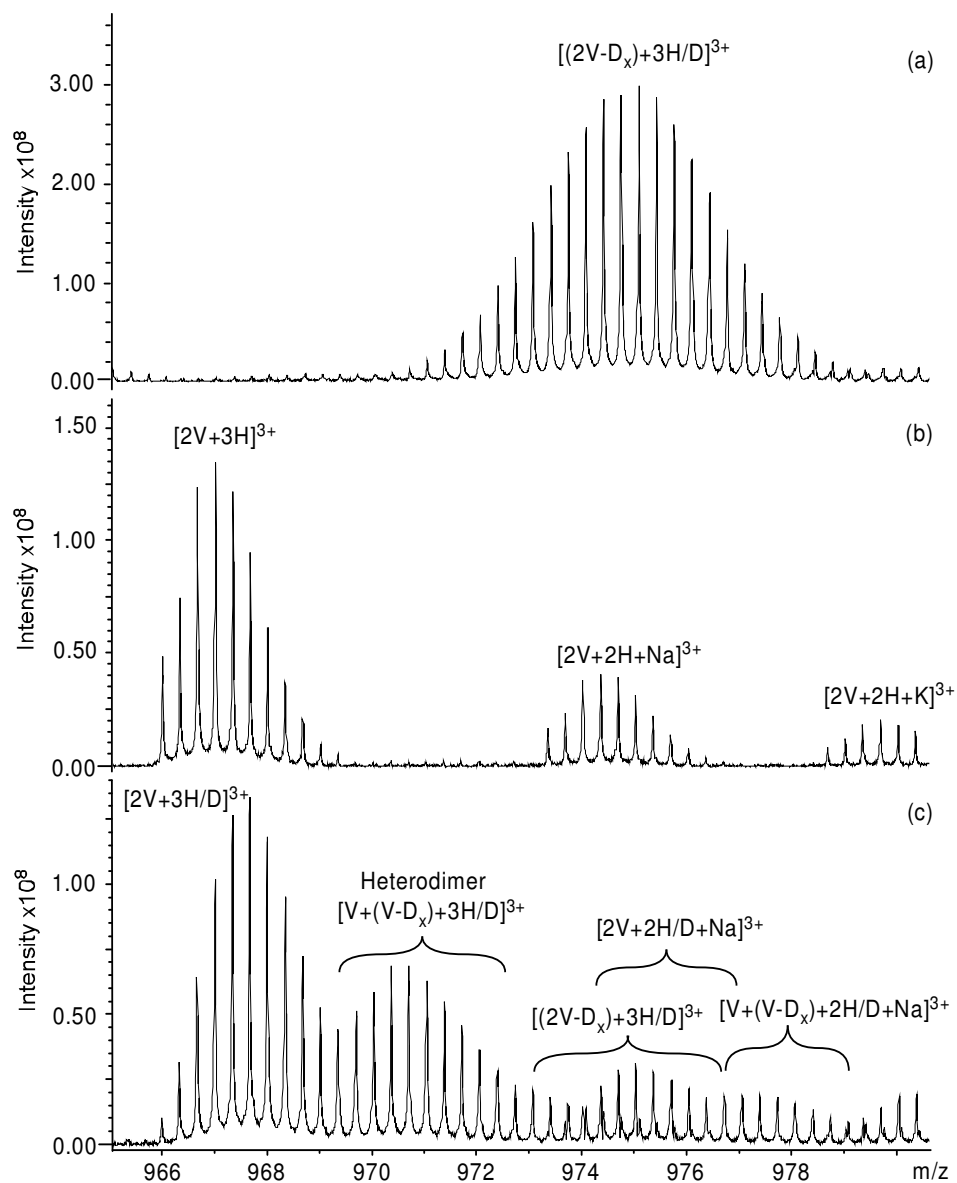


Figure 2.8. Mass spectra of (a) deuterated vancomycin $[V-D_x] = 135 \mu\text{mol/L}$ down one side of a dual-channelled emitter and (b) isotopically normal vancomycin $[V] = 135 \mu\text{mol/L}$ down one side of a dual-channelled emitter and (c) deuterated vancomycin $[V-d_x] = 135 \mu\text{mol/L}$ on the one side and on the other side isotopically normal vancomycin $[V] = 135 \mu\text{mol/L}$ of a dual-channelled emitter

The dimer region of mass spectra, where non-deuterated has been loaded on one side and deuterated vancomycin on the other side of the dual-channelled emitter, showed an isotopic envelope between the envelopes of normal and deuterated vancomycin dimer, respectively. This envelope could only be caused by a heterodimer, formed from one molecule of normal vancomycin and a second, deuterated vancomycin molecule. To illustrate this, the triply-charged dimer regions with both deuterated and non-deuterated vancomycin are shown in comparison to spectra with one species only (Figure 2.8). Additionally, the monosodiated triply-charged dimer species show the same envelope shape as the triply protonated ones which is another evidence of mixing in the Taylor cone. No mass spectrum with the theoretical intensity ratio of 1 : 2 : 1 (light homodimer : heterodimer : heavy homodimer) was obtained, which was attributed to spraying discrimination, i.e. one channel was spraying more than the other.

While for the main part, the mixing effect described above was reproducible, in certain experiments some cases extreme channel discrimination was observed. In this event no hetero dimer was observed and either the vancomycin or the heavily deuterated vancomycin was absent from the spectrum. For example Figure 2.9 shows the mass spectrum obtained using one such needle with a heavy channel imbalance.

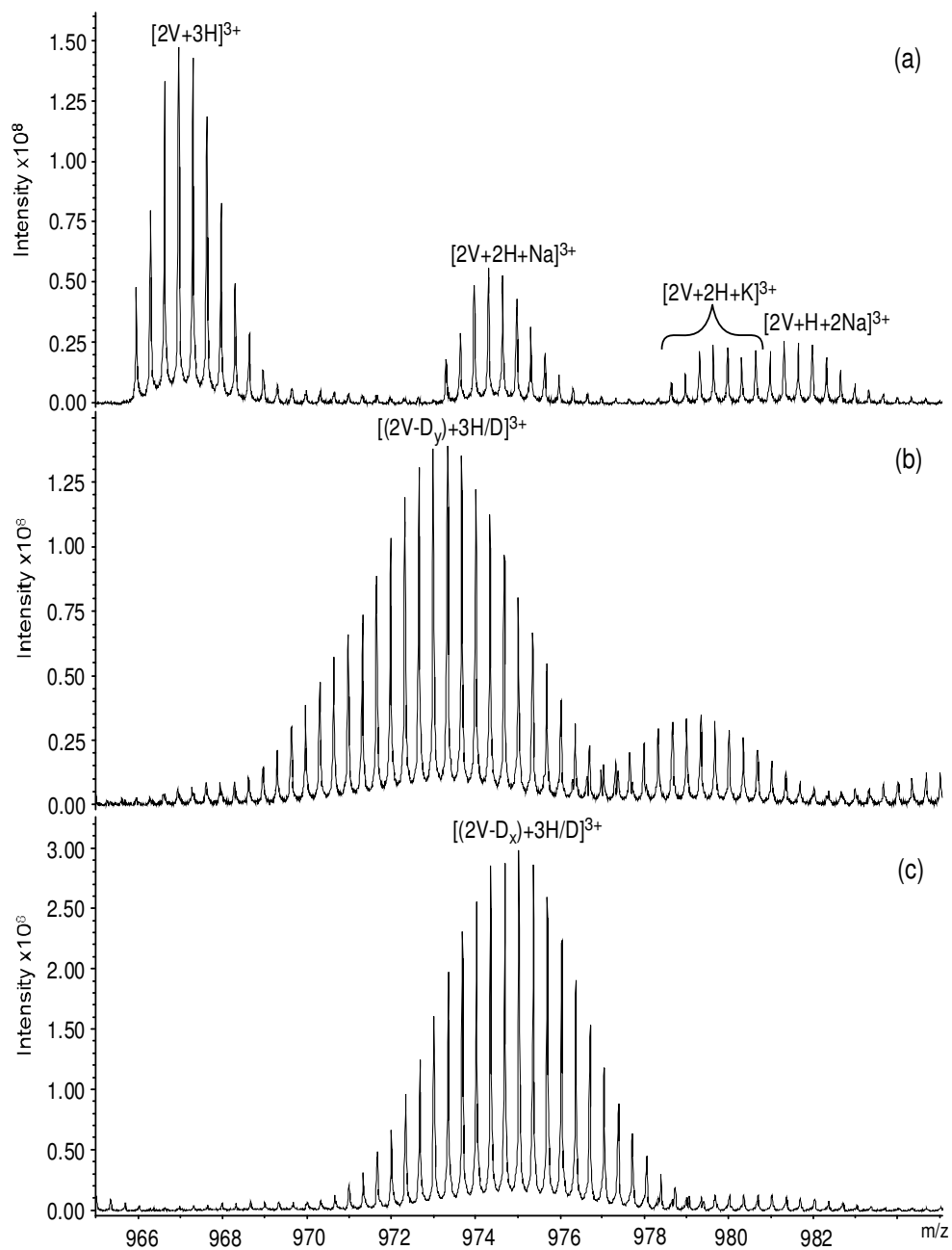


Figure 2.9. Mass spectra of (a) isotopically normal vancomycin [V] on one side = 135 $\mu\text{mol/L}$, (b) deuterated vancomycin $[V-D_x] = 135 \mu\text{mol/L}$ on the one side and on the other side isotopically normal vancomycin [V] = 135 $\mu\text{mol/L}$ of a dual-channelled emitter and (c) deuterated vancomycin $[V-D_x] = 135 \mu\text{mol/L}$ down one side of a dual-channelled emitter.

The spectrum (figure 2.9b) shows a broad distribution of what appears to be deuterated vancomycin, however, on average only eight hydrogens had been exchanged for deuteriums which was considerably lower than with deuterated vancomycin alone (figure 2.9c). This shows further evidence of mixing in a shared Taylor cone even when the supply from one channel of the dual channelled emitter was severely limited.

2.4 Conclusion

Nano-ESI FT-ICR experiments with theta-shaped dual-channelled emitters established their suitability as electrospray emitters. Mass spectra of a single solution were reproducible and similar to mass spectra obtained with conventional single-channelled nano-ESI emitters. Mixing experiments where each of the channels of a dual-channelled emitter was loaded with a different solution showed that mixing took place. In experiments with vancomycin and diacetyl-l-Lys-d-Ala-d-Ala a 1:1 complex was formed. The conclusion drawn is that the complex was formed as a result of mixing in the Taylor cone. From the results of these experiments it was possible to calculate a mixing time which was of the order of several tens of microseconds. Experiments with vancomycin and deuterated vancomycin provided further evidence of mixing through formation of a heterodimer when spraying in dual-channelled emitters.

The experiments that have been carried out here all involve vancomycin and it would be of interest to investigate other systems using the emitters. The emitter fabrication process was fairly simple and flexible and it might be possible to

fabricate capillaries with further channels. Further channels might complicate the sample-loading process. The concept of two channels combined in a single nano-ESI emitter looks very promising in relation to studying liquid interactions occurring on fast time-scales.

2.5 References

- (1) Fenn, J. B.; Mann, M.; Meng, C. K.; Wong, S. F.; Whitehouse, C. M. *Science* **1989**, *246*, 64.
- (2) Wilm, M.; Mann, M. *Analytical Chemistry* **1996**, *68*, 1-8.
- (3) Sobott, F.; Robinson, C. V. *Current Opinion Structural Biology* **2002**, *12*, 729-734.
- (4) Hill, T. J.; Lafitte, D.; Wallace, J. I.; Cooper, H. J.; Tsvetkov, P. O.; Derrick, P. J. *Biochemistry* **2000**, *39*, 7284-7290.
- (5) Rob, T.; Wilson, D. J. *Journal of the American Society for Mass Spectrometry* **2009**, *20*, 124-130.
- (6) Wilson, D. J.; Konermann, L. *Analytical chemistry* **2003**, *75*, 6408-6414.
- (7) Gale, E. F.; Cundliffe, E.; Reynolds, P.; Richmond, M. H.; Waring, M. J. *The Molecular Basis of Antibiotic Action*, Second Edition ed.; Wiley-Interscience: New York, 1981.
- (8) Kannan, R.; Harris, C. M.; Harris, T. M.; Waltho, J. P.; Skelton, N. J.; Williams, D. H. *Journal of the American Chemical Society* **1988**, *110*, 2946-2953.
- (9) Cohen, M. L. *Science* **1992**, *257*, 1050-1055.
- (10) Nieto, M.; Perkins, H. R. *Biochem. J.* **1971**, *123*, 773-787.
- (11) Waltho, J. P.; Williams, D. H. *Journal of the American Chemical Society* **1989**, *111*, 2475-2480.
- (12) Batta, G.; Sztaricskai, F.; Kover, K. E.; Ruedel, C.; Berdnikova, T. F. *Journal of Antibiotics* **1991**, *44*, 1208-1221.
- (13) Mackay, J. P.; Gerhard, U.; Beauregard, D. A.; Williams, D. H.; Westwell, M. S.; Searle, M. S. *Journal of the American Chemical Society* **1994**, *116*, 4581-4590.
- (14) Zampronio, C. G.; Giannakopoulos, A. E.; Zeller, M.; Bitziou, E.; Macpherson, J. V.; J., D. P. *Analytical Chemistry* **2004**, *76*, 5172-5179.
- (15) Kelly, J. F.; Ramaley, L.; Thibault, P. *Analytical chemistry* **1997**, *69*, 51-60.
- (16) Prasad, V.; Semwogerere, D.; Weeks, E. R. *Journal of Physics: Condensed Matter* **2007**, *19*, 113102 (113125pp).
- (17) Heck, A. J. R.; Jørgensen, T. J. D.; O'Sullivan, M.; von Raumer, M.; Derrick, P. J. *Journal of the American Society of Mass Spectrometry* **1998**, *9*, 1255-1266.
- (18) Popieniek, P. H.; Pratt, R. F. *Journal of the American Chemical Society* **1991**, *113*, 2264-2210.

- (19) Marshall, A. G.; Hendrickson, C. L.; Jackson, G. S. *Mass Spectrometry Reviews* **1998**, *17*, 1-35.
- (20) Atkins, P. W. *Physical Chemistry*, Sixth ed.; Oxford University Press: Oxford, 1998.

3. Carbon nanotubes as field emitters

3.1 Introduction

An aim of this study was to investigate how arrays of carbon nanotubes could be used as field emitters which would enhance the applicability of mass spectrometry. Examples of field emitters are discussed here. Of particular relevance to this project is the multipoint ion source developed by Aberth et al ¹. This multipoint source (Fig 3.1) consisted of thousands of 40 μm tall cone shaped metal tips with a typical tip radius of curvature of $1 \times 10^{-1} \mu\text{m}$ on a 2 mm^2 area of gold-plated copper grid. The multipoint source allowed a flow of gaseous sample to be fed between the tips.

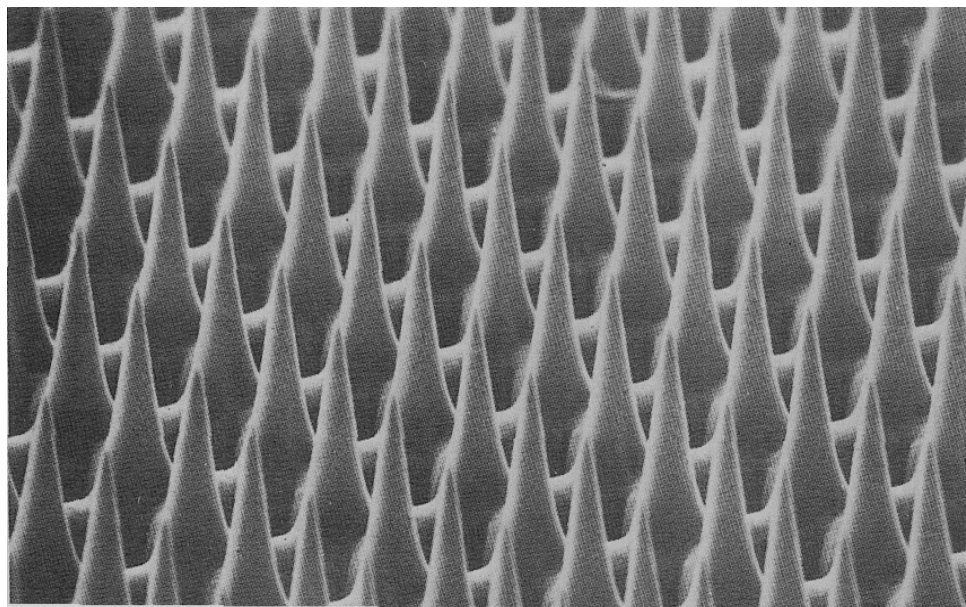


Figure 3.1 Scanning electron micrograph of a section of the multipoint emitter of Aberth et al ¹.

Compared to the tips in the multipoint source, carbon nanotubes should be superior field emitters. The carbon nanotubes used in this study had smaller radii of curvature (on average $3.5 \times 10^{-2} \mu\text{m}$), could be grown to chosen and longer lengths and retained a more uniform thickness along the length of a protrusion. In combination, these factors should mean that a nanotube would produce a higher field when compared to a single cone-shaped tip. It has been shown that nanotubes have favourable electron emission characteristics (15 mA/cm^2 at an applied field of $14 \text{ V}/\mu\text{m}$)³. The field ionization of helium has also been reported⁴. Ionisation of helium has typically not been possible with the types of emitters used to date in field ionisation mass spectrometry.

Improving the field that can be generated by an emitter is perhaps only half the battle in terms of bringing field desorption back onto a par with the current ionisation techniques of ESI and MALDI. FD will be a poor choice, whilst it is necessary to go through the time-consuming steps of removing an emitter from vacuum in order to apply a sample. This problem has been tackled with conventional field emitters, in the LIFDI ion source introduced by H. B. Linden^{5,6}. An aim of the present study was to develop a means of continuously supplying sample to the nanotubes. An analyte was to be loaded into a syringe pump and fed directly to the nanotubes via holes drilled through the substrate. This would happen without the need to remove anything from vacuum. This aspect of the study is discussed in much more detail in chapter 5. It is worth noting that a continuous method of sample supply would open up possibilities for high-throughput applications.

3.2 Conventional field emitters

3.2.1 Overview

Field ionisation (FI) emitters have been through many stages of development. In the early years, close ties existed with FI microscopy and thin metal tips (tip radius of 1 μm) were used as field emitters for both techniques ⁷. A natural progression from the single-tip emitter was to combine several of these wire tips together to make a bundle or multi-tip emitter. This had the advantage of increasing the ion-emission area of the emitter.

Types of emitters developed slightly later were foils, razor blades and thin wires ^{8,9}. The use of foils and razor blades proved to be a more robust solution compared to the first platinum-wire emitters, which were fragile and prone to rupture when handled. This advantage became less relevant with the introduction of emitter-activation processes where thicker more robust tungsten wires could be used to produce even stronger fields. The base field strength of these FI emitters prior to activation was insufficient to be really useful for mass spectrometry. The emitter could be 'activated' by the growth of micro-needles on the emitter surface, which enhanced the field strength.

The high-temperature activation process as described by Beckey ¹⁰ was the most widely used method of activation. In this activation process a 10 μm tungsten wire was spot welded to two supports spaced 6 mm apart and this was inserted into a vacuum chamber filled with benzonitrile gas to a pressure of

approximately 10^{-2} Torr. The wire was heated to about 1500 K by increasing a heating current passed through the wire. At about 1500 K an increase in resistance and voltage across the wire would be observed, which corresponded to an exothermic chemical reaction between the tungsten and benzonitrile. When a high potential was applied to the wire, 30- 60 μm long needle-like structures grew on the wire over a period of 7 – 12 hours (Fig 3.2). Other significant methods of activation and improvements have since been developed by Derrick et al ¹¹ and Linden et al ¹².

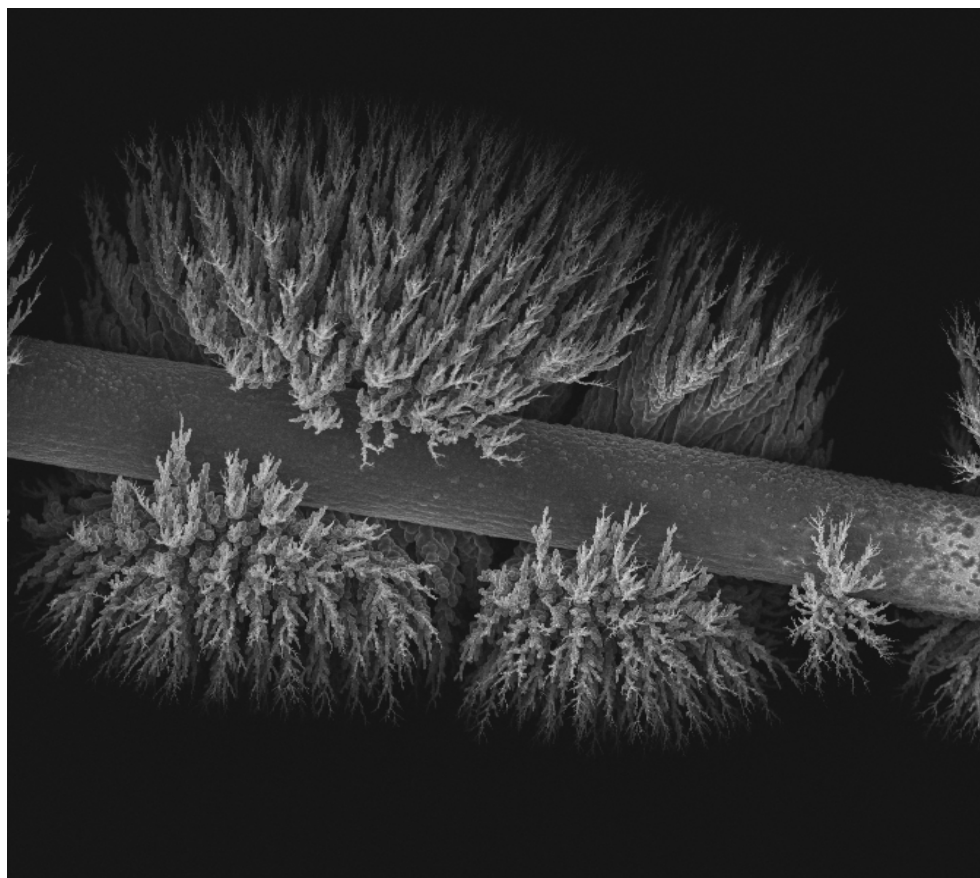


Figure 3.2 Scanning electron microscope image of an activated tungsten wire obtained using a ZEISS SUPRA 55VP-23-99.

3.2.2 TEM interrogation of field-emitter carbon dendrites

The composition and structure of micro needles of the type shown in figure 3.2 was not known initially. Field ion microscopy used to probe the surface of the micro needles indicated a layered structure similar to that of graphite¹³. Ajeian et al¹⁴ concluded from electron microscopy that the structure corresponded to a concentric layering of graphite-like domains around the axes of the micro needles. They found using electron diffraction that the lattice spacings of the micro needles matched that found for graphite 3.35 Å. Derrick et al¹⁵ used auger spectroscopy, X-ray diffraction and electron microscopy to study the micro needles. They concluded that the needles were composed solely of carbon. X-ray diffraction of the micro needles yielded two lattice spacings 3.44 and 2.36 Å, which they could not immediately identify and so, in contrast to the previous reports, they concluded that the structure was not that of graphite but instead a more ordered form of pyrolytic carbon.

A boom in carbon-based nanotechnology has taken place since these studies were conducted, and as a result, the exact nature of the carbon micro needles may be easier to identify. The lattice spacings of some established carbon nanostructures are given in Table 3.1.

Carbon species	Multiwalled carbon nanotube	Diesel soot	Carbon black	Pyrolytic carbon
Interlayer spacing (Å)	3.4-3.9 ¹⁶	3.58-4.08 ¹⁷	3.36-3.60 ¹⁷	3.49-3.62 ¹⁸
Carbon species	Carbon nanoonion	Glass-like carbon	Carbon nanoloop	Graphite
Interlayer species (Å)	3.4 ¹⁹	3.5 ²⁰	3.7-4.4 ¹⁹	3.35 ²¹

Table 3.1 Lattice spacings for carbon nanostructures.

Several carbon structures match the lattice spacing of 3.44 Å found by Derrick et al, including ordered multi-walled carbon nanotubes. The second weak lattice spacing of 2.36 Å is not evident in any of the candidate structures. Certain tungsten carbides such as W₂C exhibit a lattice spacing of 2.36 Å (Appendix 3a), however, spacings representing the complete powder diffraction file were not reported. In order to try and determine whether the structure of the micro needles was similar to those of established carbon structures, high-resolution TEM was used to probe needles scraped directly from a thin-wire field emitter.

Examination of the TEM images (Figure 3.3) suggests that the structure of the needles is not uniform. Spherical growths appear on the sides of the needles (Figure 3.3b), these seem to have a more-ordered structure than that of pyrolytic carbon in the form of carbon black and soot, and a less-ordered structure than

those of multi-walled fullerenes or nanooxions. The fine order is disrupted where the growth attaches to the main body of the needle. Instead of whole nanooxion-like structures or the multi-walled nano buds reported by Nasibulin et al ²², it seems likely that the growths are highly ordered proto-stages of the branching seen throughout the micro needles. The images also suggest that small nanotube-like hollows may exist at the centre of some of the needles (Figure 3.3c), however, the total disorder of the structure is such that these could not be counted as nanotubes.

In conclusion, the evidence is that carbon micro needles grown on field emitters have a non-uniform structure that has some areas of high order, analogous to other ordered carbon structures, but also areas of disorder similar to that found in pyrolytic carbon. It is possible, that if the parameters of activation were changed, more ordered structures and perhaps even nanotubes might be produced.

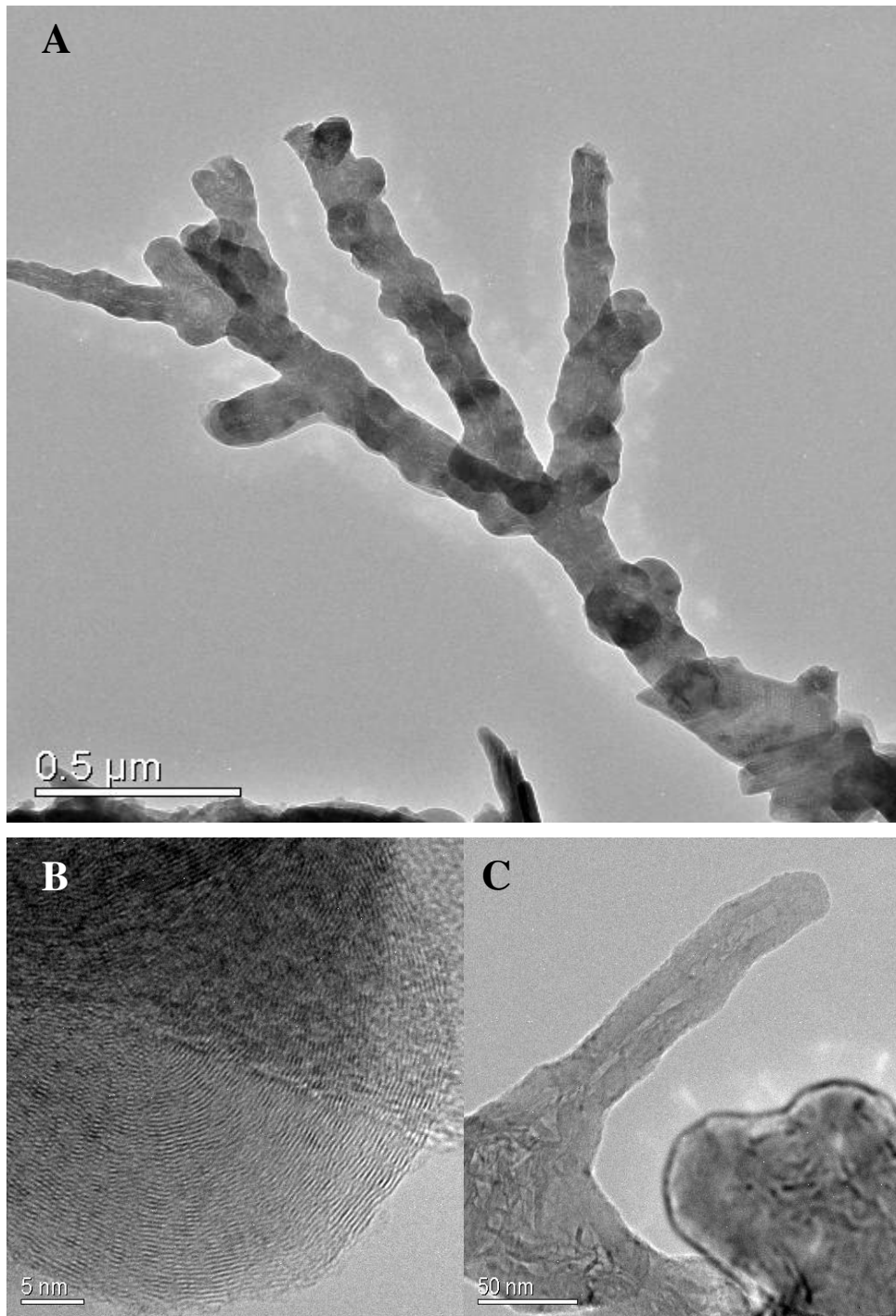


Figure 3.3 Transmission electron microscope images of: A) A typical branched carbon needle. B) An example of the structure of the side growths. C) An example of the irregular 'hollows' found at the centre of some structures.

3.3 Arrays of carbon nanotubes as field emitters

3.3.1 Overview

It is not surprising that the carbon micro needles grown to activate field emitters share some structural similarities with carbon nanotubes. Perhaps more surprising is the fact that carbon nanotubes were not identified before Sumio Iijima's paper in 1991²³. A wealth of research into carbon fibers took place before the discovery of nanotubes²⁴. It is quite possible that nanotubes were produced but not identified in processes such as those used by Smalley, Kroto and others in the discovery of C₆₀²⁵.

In simple terms, a perfect single-walled carbon nanotube can be thought of as a single graphite sheet rolled into a tube with half a fullerene capping the tube at either end. Multi-walled carbon nanotubes (MWCNT) consist of more than one rolled sheet capped in a similar way. In terms of size, nanotubes usually have a diameter of between 1 (single-wall carbon nanotubes SWCNTS) and 100 nm and a length of several hundred nanometers to a few millimetres. Their aspect ratios tend, therefore, to be very high. Nanotubes are known to have remarkable properties including a tensile strength and Young's modulus of 40-50 GPa and 1.25 TPa respectively^{26,27}; both of which far exceed those measured for steel. The observed thermal conductivity of a MWNT is more than 3000 W/mK at room temperature, which is double that observed for diamond²⁸. It was, however, a nanotube's electrical properties that made them particularly interesting in the context of the aims of this study.

Single-walled carbon nanotubes have been shown to exhibit both metallic and semi-conducting behaviour, depending on the nanotubes' structure and chirality. Considering the graphite sheet, differences in structure arises because there is more than one way in which the sheet can be rolled²⁹. In the case of multi-walled nanotubes, each wall of a multi-walled tube can have either a metallic or a semi-conducting nature. Theoretically, it would be possible to have tubes of each type and some that are mixed. In theory, if metallic layers were present in the multi-walled tube the tube might be expected to take on metallic behaviour, except that there would be interactions between tube layers. In the case of double-layered tubes, Satio et al³⁰ calculated that interactions between walls were too weak to affect the electrical properties of a metallic tube. Other research³¹ has indicated that for some double-walled carbon nanotubes, interactions can change the nature of the tube from conducting to semi-conducting. Experiments to determine the nature of MWCNTs were, until recently, difficult because only the outside wall of the tube could be easily characterised. Methods to connect more than the outside wall so that each shell of a MWCNT would contribute to the measured current carrying capacity have since been developed.³²

Because of the good electrical-conductance properties combined with the high aspect-ratio, electric fields around the tips of CNTs are enhanced when potentials are applied to them³³. The growth of carbon nanotubes on conducting substrates over a large area is essential for uniform electron-emission required for most applications of field electron-emission. The production of forest-like arrays of carbon nanotubes with densities of tubes of 10^9 nanotubes/cm² was a

first step towards fulfilling this requirement³⁴. It is, however, the ability to pattern arrays of nanotubes, so that the position of each vertically aligned nanotube can be controlled, that has been shown to produce arrays with the most desirable field electron-emission characteristics³.

The fields generated at the tips of carbon nanotubes have been shown to be sufficiently high to strip an electron from helium, which of course is the element with the highest ionisation energy⁴. In light of the fact that the field strengths of currently used activated-wire emitters are not sufficient to ionise helium, arrays of carbon nanotubes might prove to be very effective field emitters for field desorption/ionisation mass spectrometry. The much higher field strengths might facilitate quantum tunnelling of electrons from proteins and polymers. The amalgamation of carbon nanotube technology and mass spectrometry has already had some success³⁵, but the hope was there might be potential to pave the way for much more significant applications of CNTs and field ionisation/desorption mass spectrometry.

3.3.2 Synthesis of carbon nanotubes

The synthesis of carbon nanotubes has been demonstrated using at least three different methods: a) arc discharge between carbon rods, b) laser ablation of a carbon substrate and c) chemical vapour deposition (CVD). Of these three techniques, CVD³⁶ including plasma-enhanced chemical vapour deposition (PECVD) has been used in this study to grow arrays of carbon nanotubes.

In CVD, a carrier gas such as CO or Argon is used to aid the transport of a gaseous carbon feedstock such as ethylene over a silicon substrate treated with a (normally iron or nickel) catalyst at a temperature around 750 °C. The catalyst is fundamental to the growth of any carbon nanostructures, being essential for the dissociation of the hydrocarbon molecules. Liberated carbon atoms diffuse through the metal particles and precipitate at the opposite end, hence metal nanoparticles can often be found incorporated at the tip of a nanotube. A nanotube array produced using this method is often quite irregular, in that the nanotubes in the array are not uniform in size. The electron-emission characteristics of a vertically aligned CNT array grown by CVD can also be quite uneven, and this is generally accepted to be due to enhanced emission from tubes that are much longer than the average length. These tubes stretch out along the field lines towards the anode and thus experience a much higher local field than the rest of the array³⁷.

3.3.2.1 Dense arrays of vertically aligned carbon nanotubes

For the majority of applications of field electron-emission, an aligned homogenous nanotube array is attractive³⁸. Plasma-enhanced chemical vapour deposition (PECVD) has been used to grow homogeneous arrays of aligned nanotubes with specific lengths. PECVD differs only slightly from CVD in that the feedstock gas is introduced with a plasma. This has the effect of enhancing the reaction between feedstock and metal catalyst, allowing lower temperatures to be employed and offering a degree of control over the nanotube growth. Morjan et al³⁹ have described a PECVD method. Iron catalyst particles were

deposited on a silicon wafer by evaporating a 1nm thick film of iron. Substrates were attached to a grounded cathode that contained a heater. The film separated into small iron catalytic islands, once heated to the growth temperature of 700 °C in a low vacuum. After heating, a C₂H₂/H₂ feedstock gas was introduced into the chamber at the same time as a voltage (400 V) was applied to the anode. The height of the nanotube array grown could be controlled by varying the deposition time. A deposition time of about 30 seconds gave nanotubes of length around 5 μm, where as a deposition time of 45 minutes afforded a growth of up to 170 μm. It was reported that for growth times of 5 minutes and above (corresponding to nanotube lengths of 40 μm and above) secondary thorn-like structures formed at the tips. This is thought to be due to the reaction with C₂ and C₂H radicals in the plasma. The growth of secondary structures on the longer nanotubes was advantageous, further field enhancement being observed as a result ⁴⁰.

Iron is not the only metal used as a catalyst in PECVD growth of carbon nanotubes. Nickel has been put to arguably more effective use in this role. Carpet-like arrays of aligned, wide multi-walled carbon nanotubes (150 nm outside diameter and 20 μm length), which are often called nanofibers due to the axial defects observed along the length of the tube, have been grown using a nickel film catalyst ³⁴. The method utilised magnetron sputtering to coat a thin nickel layer onto a glass substrate. A second gaseous catalyst (NH₃) was introduced before the ethylene feedstock gas (C₂H₂), at temperatures below 666 °C. It was found that the outside diameter of the CNTs produced was dependent on the thickness of the Ni layer used. Plasma etching using NH₃ for 20 minutes

prior to acetylene introduction, reduced the diameter greatly to ~65 nm, and so NH₃ not only has the role of a catalyst but also of an etching agent in this process.

3.3.2.2 Patterned arrays of vertically aligned carbon nanotubes

Further development of the Ni catalysed methods led to the patterned growth of freestanding carbon nanotubes, in which a nickel layer could be photolithographically patterned onto the substrate to form a design of small nickel 'nanodots'. CNTs grew only where the catalyst was placed and so a patterned array of CNTs could be grown^{41,42}. Merkulov et al [41] have shown that depending on the size of the nickel nanodot, either a single or several nanotubes will grow. This was rationalised by the finding that when the catalyst nanodots were heated to about 700 °C, the dots would split up into several smaller droplets and seed the growth of several nanotubes. It was found that for a dot of size less than 350 nm only one droplet was formed and so only one nanotube was grown.⁴³

With this patterned growth, the exact position of each nanotube can be chosen through the photolithographic patterning. The CNT's width can be kept uniform by keeping the Ni dots uniform and the height can be controlled through the deposition time. For field electron-emission, it has been shown that the shielding from closely packed arrays of nanotubes has adverse effects on the field emission properties³⁸. An array in which the individual CNTs are spaced apart at twice their height has been found to be an ideal field emitter³.

3.3.3 Arrays of carbon nanotubes used in field ionisation/desorption experiments

Both densely spaced and the more sparse arrays of carbon nanotubes were used in this study. All of the arrays were produced using the Ni-catalyst based methods described above, in the Electronic Devices and Materials Group, Department of Engineering, University of Cambridge.

3.3.3.1 Arrays of carbon nanotubes used in field ionisation experiments

Scanning electron microscopy (SEM) and transmission electron microscopy (TEM) were used to examine arrays. Using a Supra 55vp-23-99 scanning electron microscope, it was determined that the samples used primarily as emitters in the field ionisation experiments consisted of approximately 3.41×10^9 vertically aligned nanotubes per cm^2 . These were considered to be dense arrays of nanotubes. Figure 3.4 shows typical scanning electron micrographs. The density was obtained by counting the number of nanotubes present in a $10 \mu\text{m}^2$ area of an SEM micrograph. The majority of the nanotubes in these dense arrays were found to range between 8-15 μm in length and have diameters between 50-70 nm. Some stunted nanotubes were observed in between the larger tubes. It is unlikely that these would be helpful for field electron-emission or ionisation due to the shielding by the surrounding taller tubes. The nanotubes appear to be localised in clumps, suggesting that the nickel-catalyst particles used in the growth had split up into smaller nickel particles and the growth of more than one nanotube was seeded per original particle. This was not necessarily ideal for

field ionisation experiments, because the tips of comparable-length tubes grown from the same particle are likely to be in close proximity with each other and mutual shielding will reduce the fields generated at the tips.

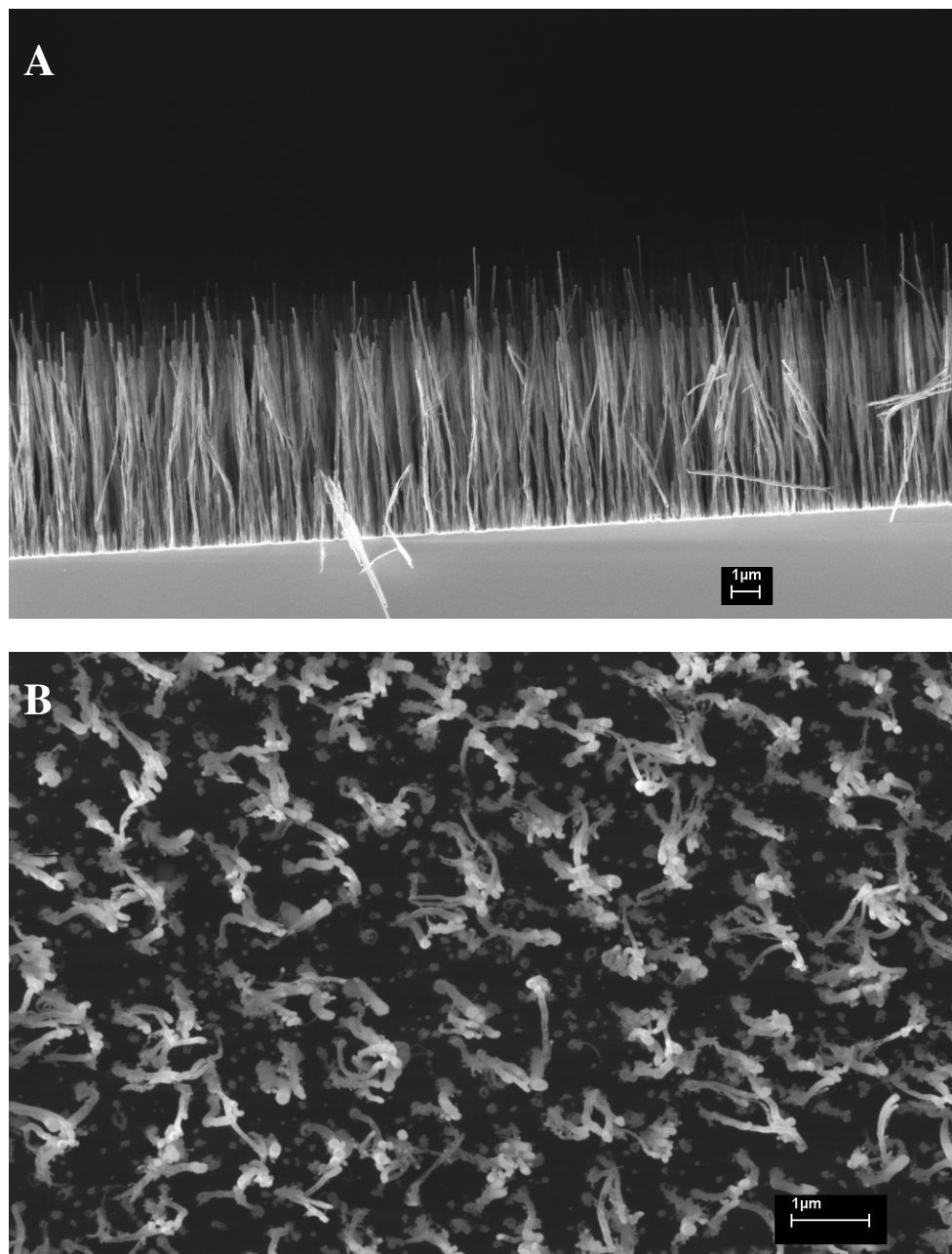


Figure 3.4. SEM pictures displaying both the side (A) and top view (B) of the dense array of vertically aligned carbon nanotubes.

High-resolution TEM electron microscopy of similar nanotubes has been used previously used to show that in some cases nickel becomes totally encapsulated by the growing nanotube⁴³. Nickel particles, if attached to a nanotube, might adversely affect the generation of a high field at the tip. In order to establish whether nickel was still attached to the nanotubes, the array was examined under the electron microscope using a quadrant back-scattering detector (QBSD) (Appendix 3b). The QBSD collects back-scattered electrons, the production of which varies directly with the atomic number of the sample. Higher atomic-number elements appear brighter than lower atomic-number elements. The QBSD electron micrograph of the nanotube array showed a number of bright spots standing out from the darker shade of the nanotubes. When this micrograph was compared with a micrograph of the same area using a secondary electron (SE2) detector, it could be seen that the bright spots were roughly in line with the tips of the nanotubes. The conclusion drawn was that the nickel catalyst was attached to the ends of at least some of the nanotubes.

Transmission electron microscopy (TEM) was used to examine individual nanotubes carefully extracted from the nanotube forest. The axial bamboo-like defects typical of nanotubes grown using this method were observed. Nickel particles appeared to be embedded in the end of every nanotube, and that each nickel particle was encapsulated within a thin layer of carbon (Figure 3.5).

Energy-dispersive X-ray spectroscopy (EDX) was used to analyse the encapsulated particles. It was confirmed that the particles were composed of nickel (Appendix 3c). The EDX spectrum also showed traces of copper and silicon. Copper could originate from the grid used to mount the nanotubes for

TEM analysis. The silicon present might be a consequence of interactions between the nickel catalyst and silicon substrate.

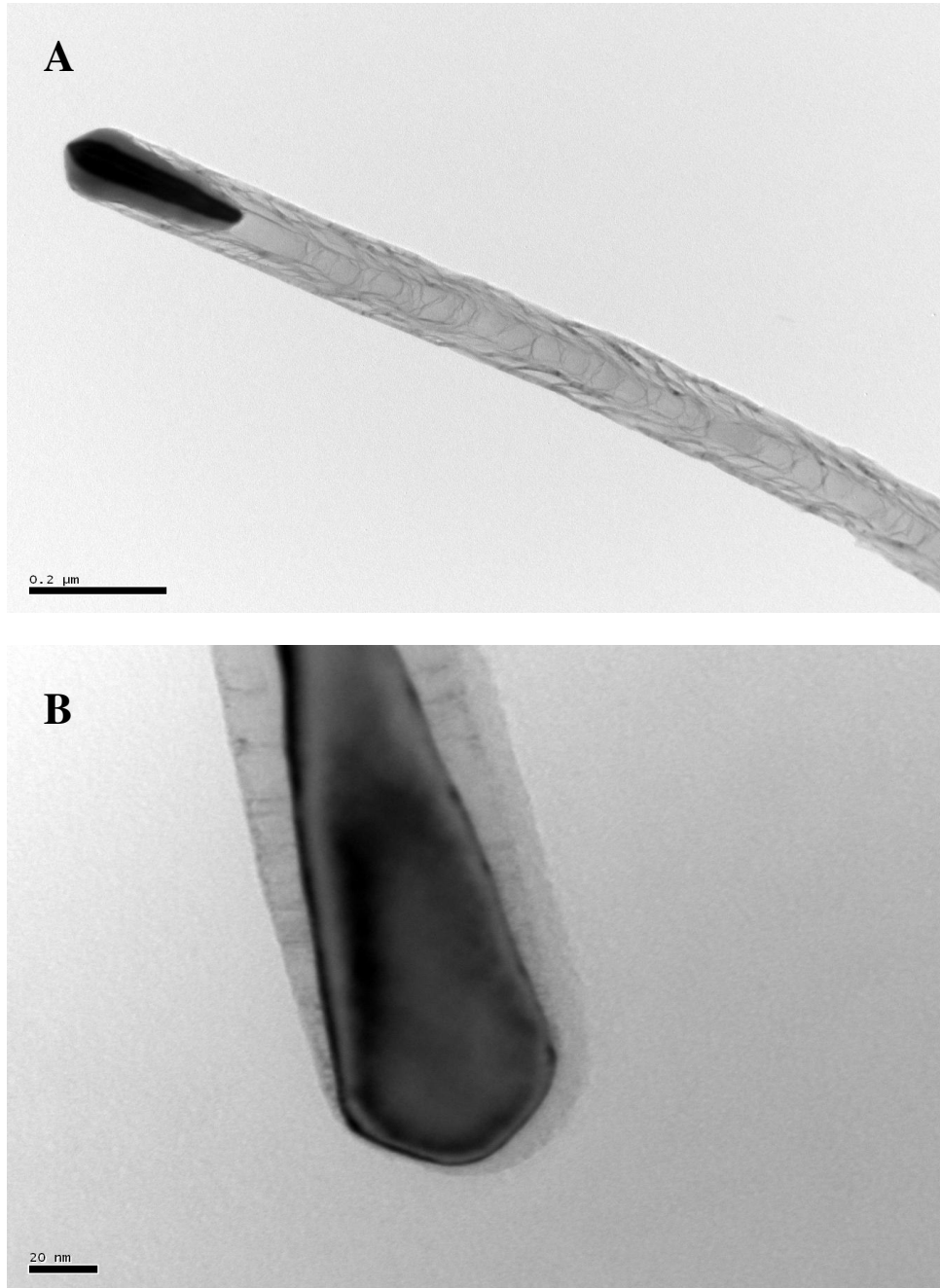


Figure 3.5. Transmission electron micrographs showing A) the bamboo like structure of the CNT. B) the encapsulated particle.

Later in the study samples of the patterned arrays of carbon nanotubes were used for field ionisation. These were characterised using SEM. The majority of the nanotubes in these arrays were between 2 and 5 μm in length and had diameters of about 100 nm. The nanotubes were spaced apart at roughly twice their heights with a distance of approximately 5 μm between each neighbouring carbon nanotubes in the array. An average covering of approximately 6.15×10^6 vertically aligned nanotubes per cm^2 was obtained by counting nanotubes in a smaller area as before. SEM micrograph of both the side and top of a sample is shown in Figure 3.6.

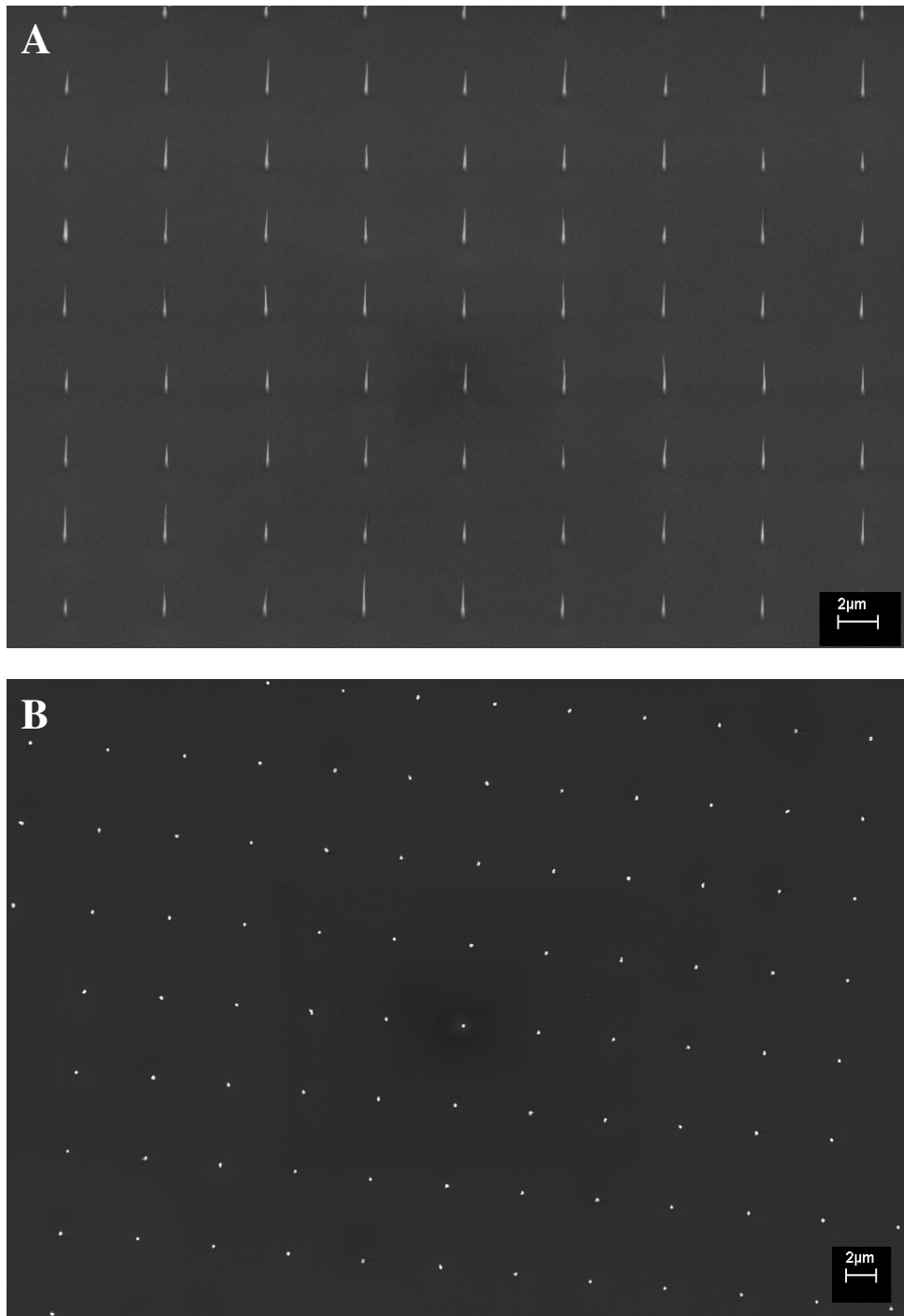


Figure 3.6. SEM pictures displaying both the side (A) and top view (B) of the patterned array of vertically aligned carbon nanotubes.

3.3.3.2 Arrays of Carbon nanotubes used in liquid-injection experiments.

The arrays of carbon nanotubes used in field desorption experiments were distinguished by the presence of arrays of holes as discussed further in Chapter 5. The holes were drilled prior to the growth of the nanotube array, and the CNTs were expected to grow all the way up to the edges of the holes. There was the possibility, however, that strange patterns of growth might occur near the holes as a consequence of the changed morphology. For example, nanotubes might grow in the holes themselves.

Scanning electron microscopy (SEM) was used to characterise the two types of array used in field desorption experiments. Figure 3.7 shows micrographs of a dense array of carbon nanotubes. The CNTs are present right at the edge of each hole. In terms of the nanotube growth, there appear to be no irregularities near or in the holes. The rest of the array appears similar to the samples of dense forest grown in the absence of holes for field ionisation experiments with a similar density of covering. The nanotubes in the dense arrays were found to range between 6 and 10 μm in length (taking into account that the SEM micrograph was taken at an angle of 115 degrees) and had diameters between 50-70 nm. Some stunted nanotubes could be observed in between the larger tubes as was found with the previous samples.

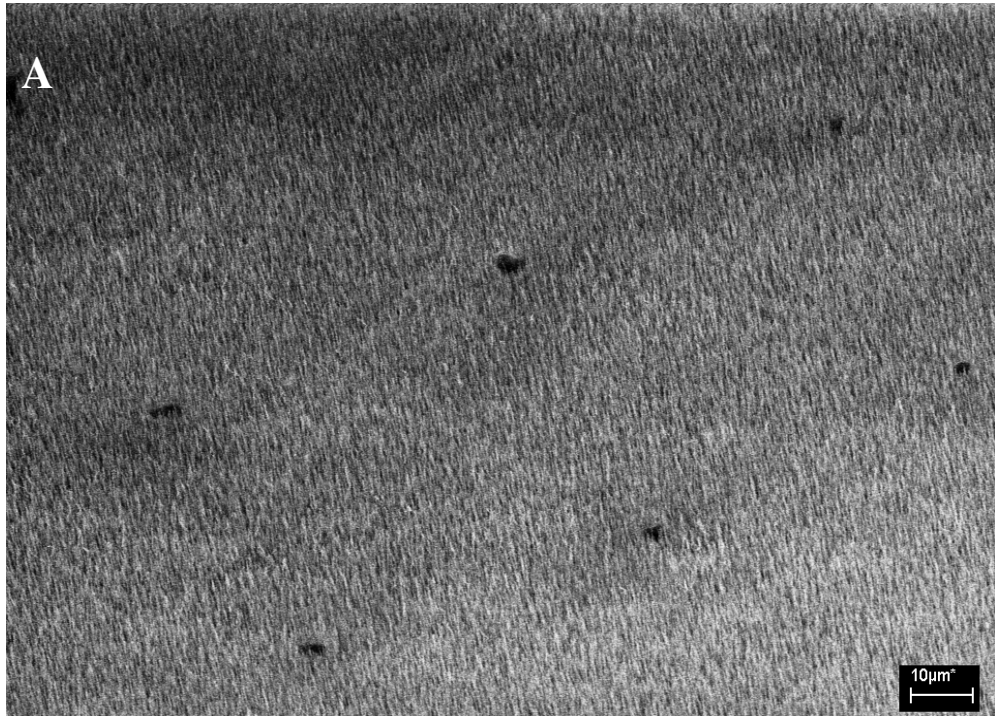


Figure 3.7. SEM micrographs showing (A) a large area of a typical dense array (B) a close-up of one of the holes and surrounding nanotubes.

The intention was that an ordered array would be grown with one nanotube placed equidistantly among every 4 holes. There would therefore also be 4 CNTs around every hole. Given a distance of 60 μm between the centres of adjacent holes in the array, there would be 60 μm between the growth sites of adjacent nanotubes. To maximise fields and minimise shielding, growth time was set to produce nanotubes approximately 30 μm in length. It was found that, presumably during the process of lithographically etching the catalyst layer, the drops of catalyst had migrated towards the holes. The SEM characterisation of the emitters revealed arrays much different from the intended design.

The SEM micrographs in figure 3.8 show that the nanotubes had grown around the rim and partially inside most of the holes, while very little growth was evident at the sites in between the holes. In some cases only a single large nanotube was grown. More often, however, a small clump was grown around each of the holes. The lengths of the nanotubes varied over a large range from about 3 μm up to about 35 μm . Typically at least one sizeable nanotube was present at the edge of each hole. This behaviour can perhaps be attributed to the holes creating potential wells towards which the catalyst particles migrated. Alternatively, considering the difficulty experienced in lithographically etching the catalyst film, it might be that the catalyst was not removed from the edges of the holes. The positions of nanotubes right next to holes would mean that sample introduced via the holes would necessarily pass close to the carbon nanotubes. Having only one tall nanotube at the edge of each hole might minimise shielding. There was therefore reason to evaluate these patterned arrays for field emission.

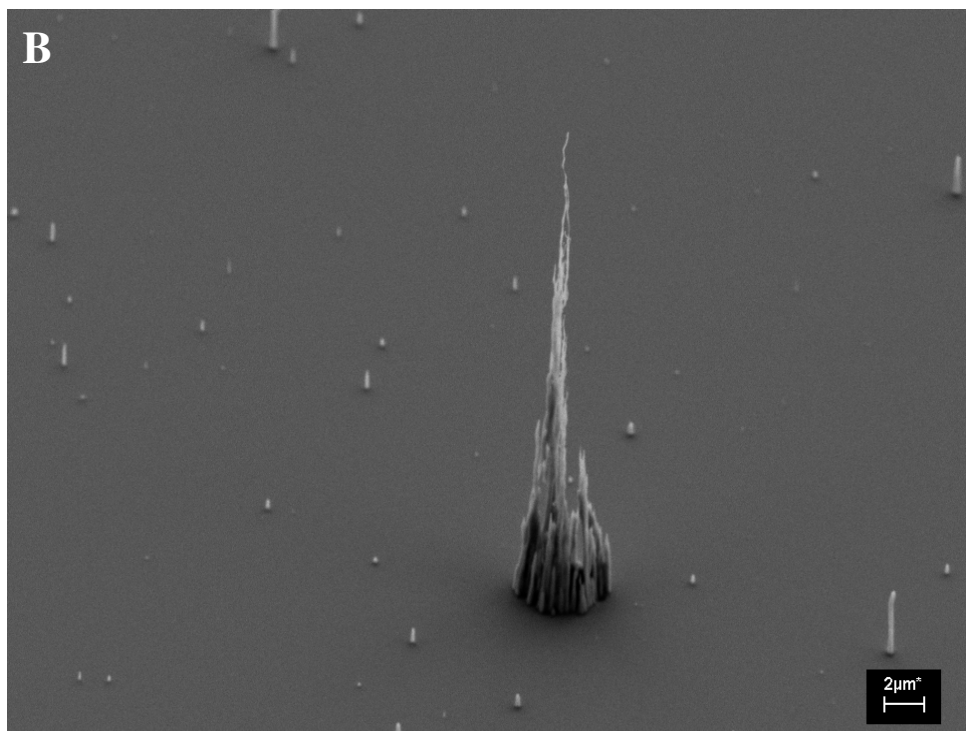
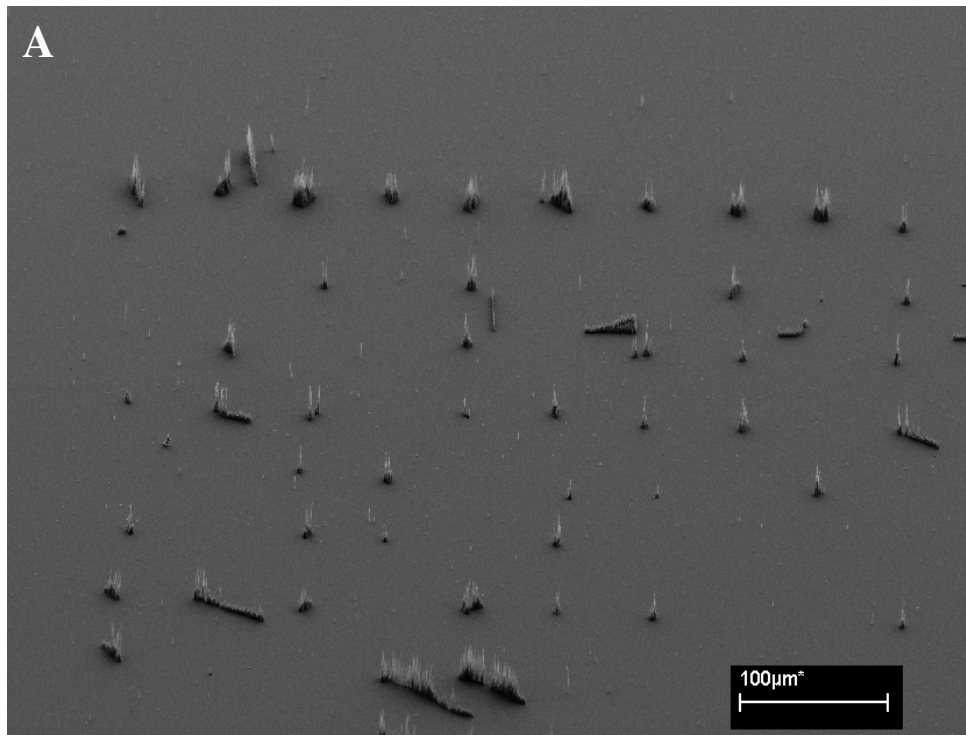


Figure 3.8. SEM micrographs showing (A) a large area of a typical ordered array (B) a close up of one of the holes and surrounding nanotubes.

3.3.4 Field emitter simulations

The fields around the nanotube arrays were simulated using the Simion 8 package. The real scale of the nanotubes was used in the simulations, so that the unit size of the simulation array was too coarse to represent accurately the curvature of the tip of each individual nanotube. As a result, the fields quoted do not represent accurately the field enhancement by the nanotubes, but were considered to be useful for like-for-like comparisons between different arrangements.

3.3.4.1 Dense arrays

The first simulation performed was of a 2D slice of a dense array. Realistic nanotube separations, lengths and diameters collected from SEM images were used. The diameter of the nanotubes were typically 40-120 nm. Given the computer RAM available, simulating the experimental separation between CNTs and the counter electrode was not practical. In order to get around this, the distance between counter electrode and the voltage applied to the nanotubes were both scaled down linearly. For the purpose of comparisons, the field strengths calculated at a potential difference of 0.1 volt from a nanotube were considered. Figure 3.9 shows an example of the calculated equipotential distribution of vertically aligned nanotubes. From the calculated field strengths, several conclusions could be drawn: Taller CNTs reduce the field generated by smaller surrounding CNTs (shielding) and taller nanotubes sticking above the mean are likely sites for ionization.

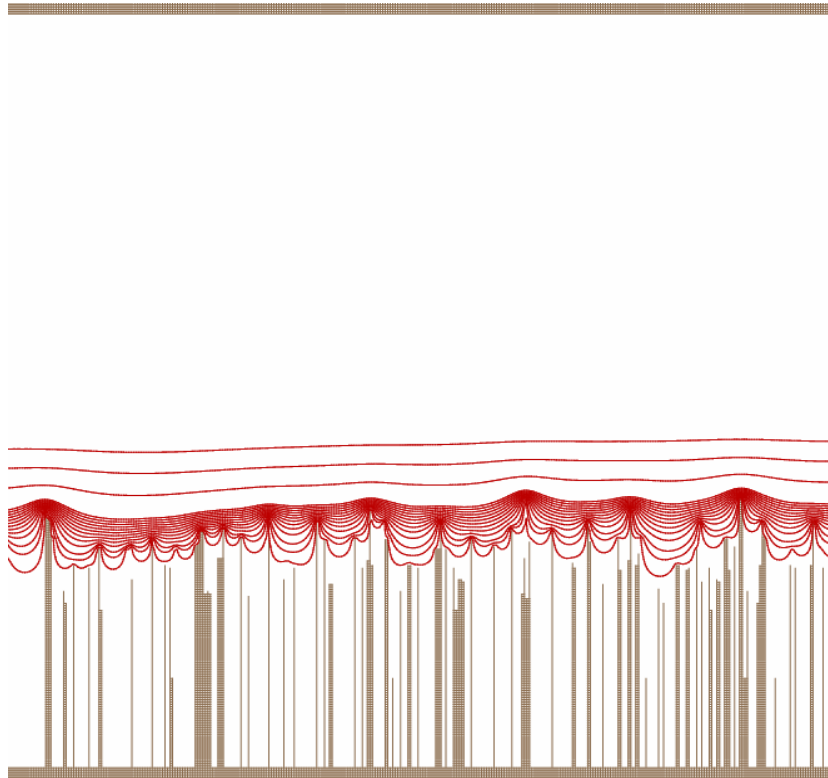


Figure 3.9. Simion 8 simulation showing the equipotential distribution for a cross-section slice of vertically aligned carbon nanotubes

CNTs at the edge of the array would not be expected to experience as much shielding compared to nanotubes within the body of the array. The change in field strength at a selection of nanotubes as half the array was removed was calculated to simulate how nanotubes near an edge enhanced the field. The results in Table 3.2, show that as larger portions of the array were removed an increase in the field strengths at the remaining nanotubes was observed. This was particularly marked in the case of nanotube 5, which provided the strongest field enhancement in the complete array. These results indicated that nanotubes at the edge of the array enhance the field more strongly due to the reduction in

shielding when compared to their forest-locked equivalents. This might suggest that the edge of the forest would be the first place that ionisation would occur.

CNT	Position on x axis (mm)	Field strength $\times 10^4$ (V/mm)			
		Complete slice	CNTs removed between (mm)		
			$0.017 > x < 0.03$	$0.01 > x < 0.03$	$x < 0.03$
1	0.00329	5.2	5.3	5.8	
2	0.0165	4.4	6.0		
3	0.02257	5.0			
4	0.02669	3.1			
5	0.03175	7.8	9.4	10.1	11.4
6	0.03796	4.3	4.4	4.5	4.8
7	0.04452	4.2	4.3	4.3	4.4

Table 3.2. Simulated field strengths illustrating the change in local field strength when portions of the CNT array are removed.

3.3.4.2 Patterned arrays

The patterned array of nanotubes was originally designed to minimise shielding for field emission purposes. Nilsson et al³⁸ reported that to minimize shielding and still maintain a covering, the ideal array of nanotubes would consist of an ordered array with nanotubes separated by a distance equalling twice their height. Simion was used to simulate the difference in the field enhancement at the nanotubes when the distance between nanotubes was changed. The length, diameter and sharpness of each nanotube was kept uniform. An example of the simulations calculated equipotential distribution is shown in Figure 3.10.

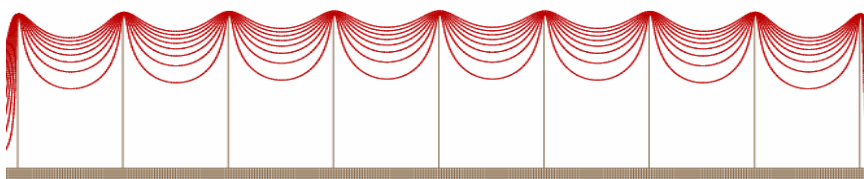


Figure. 3.10. Simion 8 simulation depicting the equipotential distribution for a patterned array where each nanotube is separated by a distance equal to one half its length

The calculations showed a decrease in field enhancement when the distance between nanotubes was reduced, as would be expected if the nanotubes were shielding each other more when brought closer together (Table 3.3). This suggests that, because of the reduced shielding, an array in which the individual CNTs were spaced apart at twice their height would enhance fields more strongly compared to a dense array. The fields generated at such a patterned array should be fairly uniform for all of the nanotubes over the entire sample. This might make the patterned array more suited for application in an ionisation source, as the ionisation sites would be likely to be more quantifiable for ion optical focusing.

CNT length to separation ratio	Separation (μm)	Field strength $\times 10^4$ (V/mm)
1:2	22.00	9.7
1:15	16.50	8.8
1:1	11.00	7.5
1:0.5	5.50	5.5
1:0.25	2.75	4.0
1:0.125	1.38	2.9

Table 3.3. Simulated field strengths illustrating the change in local field strength when the distance between neighbouring nanotubes is altered.

The length of the nanotube affects its enhancement factor. Simulations were conducted to determine how much of an effect changing the length of a single nanotube would have on the field strength (Figure 3.11). The diameter of the nanotube was $70 \mu\text{m}$. The relationship between nanotube length and field strength was linear until the length was reduced below $3 \mu\text{m}$, at which point the field strength decreased more rapidly. The conclusion drawn from this calculation was that shielding from the surface of the substrate affected the field enhancement at the shorter nanotubes.

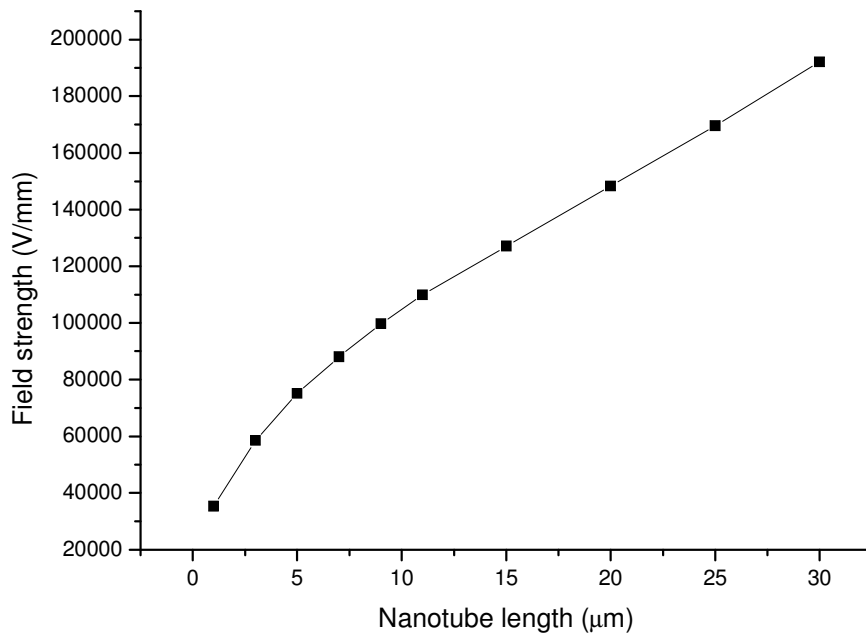


Figure 3.11 The relationship between the length of an isolated nanotube and the simulated local field strength.

The effect of altering the diameter and sharpness of the CNT was also calculated. The difference in field strengths for a lone nanotube of a range of diameters is shown in figure 3.12a. The height of the nanotube was 11 μm. The results indicate that field strength increased with increasing aspect ratio (ratio of height/ diameter). Changing the ‘sharpness’ of a nanotube was achieved by altering the y parameter of the oval that makes up the tip of the nanotube, (normally this is a circle that has a diameter equivalent to that of the nanotube) while keeping the total height of the nanotube the same. As expected, the results showed the field enhancement at the nanotubes increasing with increasing sharpness (Figure 3.12b).

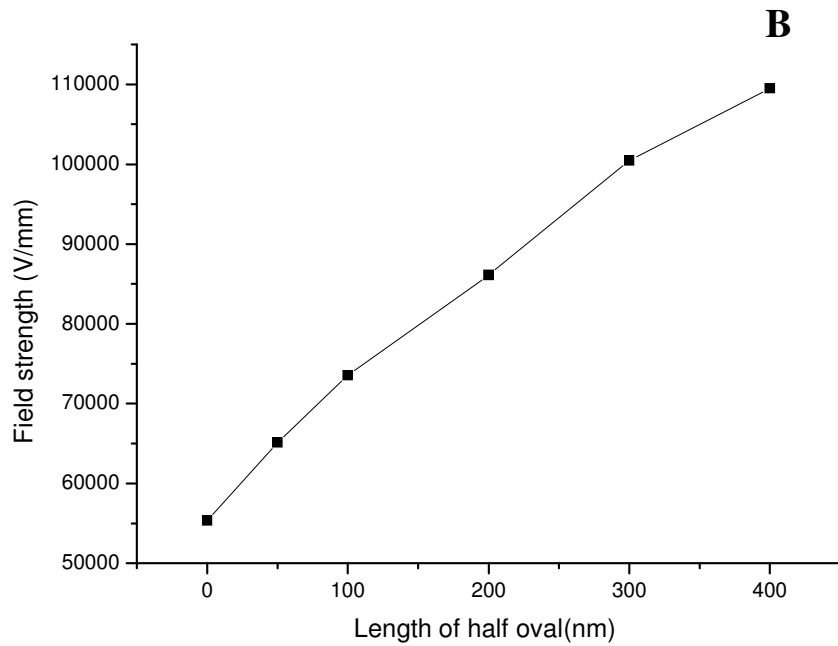
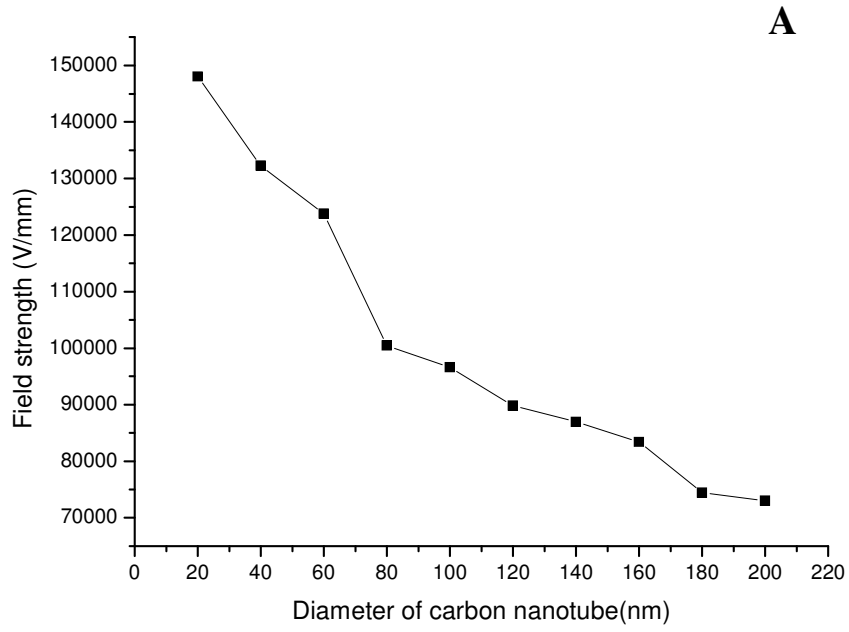


Figure 3.12. Plots showing the calculated relationships between A) the diameter of a nanotube and the local field strength and B) the tip sharpness of a nanotube and the local field strength.

3.3.4.3 The effect of introducing holes into the CNT substrate

The array of holes will affect the morphology of the field generated across the CNT array. An increase in the field enhancement was found for nanotubes at the edge of an array, and the field enhancement at nanotubes near the edges of the holes might also increase. Simulations were conducted to compare a dense array of nanotubes with the same array with a 10 micron hole drilled through the centre. Table 3.4 shows that the CNTs enhance the field to a larger degree when the hole was present in the simulation. Figure 3.13 shows an example of a calculated equipotential distribution.

Nanotube number	position of CNT in 50 micron slice (um)	Field strength without hole $\times 10^4$ (V/mm)	Field strength in presence of 20 micron hole $\times 10^4$ (V/mm)
1	0.79	1.7	1.7
2	3.29	5.2	5.3
3	16.50	4.4	4.9
4	19.42	2.6	3.7
5	31.75	7.8	8.9
6	35.46	2.6	2.8
7	37.96	4.3	4.4
8	41.98	4.2	4.3

Table 3.4. Calculated field strengths illustrating the change in local field strength when a hole is present

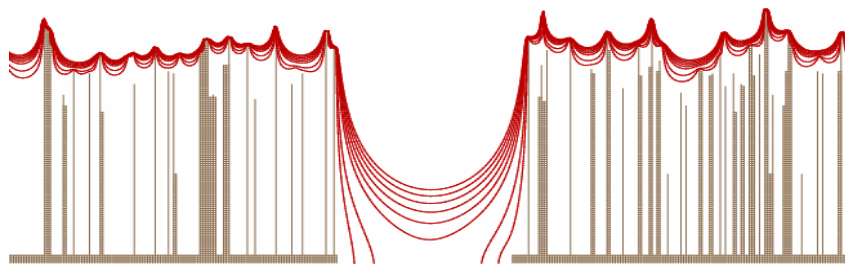


Figure 3.13. Equipotential distribution calculated to determine the effect of introducing holes into an array of CNTs.

The effect of introducing holes into an ordered array of nanotubes was slightly harder to simulate because the holes had a very real effect on where the nanotubes grew. The possibility of more than one tall CNT around each hole would affect the field enhancement at each nanotube as a function of the proximity. By introducing a hole, a small portion of the shielding created by the substrate would be removed. Simulations were conducted using two CNTs 25 μm long and 70 nm in diameter, spaced either side of a 10 micron hole. These calculations indicated that there was little difference in the magnitude of the field enhancement at each nanotube when a hole was introduced into the simulation. It was likely that if shorter nanotubes had been considered the effect would have been more noticeable.

3.4 References

- (1) Anbar, M.; Aberth, W. H. *Analytical chemistry* **1974**, *46*, 59-62A.
- (2) Beckey, H. D. *Journal of Physics E: Scientific Instrumentation* **1979**, *12*, 72-83.
- (3) Teo, K. B. K.; Chhowalla, M.; Amaratunga, G. A. J.; Milne, W. I.; Pirio, G.; Legagneux, P.; Wyczisk, F.; Pribat, D.; Hasko, D. G. *Applied Physics Letters* **2002**, *80*, 2011-2013.
- (4) Riley, D. J.; Mann, M.; MacLaren, D. A.; Dastoor, P. C.; Allison, W.; Teo, K. B. K.; Amaratunga, G. A. J.; Milne, W. I. *Nano Letters* **2003**, *3*, 1455-1458.
- (5) Linden, H. B. *European Journal of Mass Spectrometry* **2004**, *10*, 459-468.
- (6) Schaub, T. B.; Linden, H. B.; Hendrickson, C. L.; Marshal, A. G. *Rapid communications in Mass Spectrometry* **2004**, *18*, 1641-1644.
- (7) Inghram, M.; Gomer, R. *Journal of Chemical Physics* **1954**, *22*, 1279-1281.
- (8) Robertson, A. J. B. *J. Chem. Soc. A*, **1966**, 1843-1849.
- (9) Beckey, H. D. *Fresenius' Zeitschrift fuer Analytische Chemie* **1963**, *197*, 80-82.
- (10) Beckey, H. D.; Hilt, E.; Schulten, H. R. *Journal of Physics E: Scientific Instruments* **1973**, *6*, 1043-1044
- (11) Derrick, P. J.; Chan, T.-W. D.; Colburn, A. W.; Alderice, D. S. *International Journal of Mass Spectrometry and Ion Processes*, **1991**, *107*, 491-501.
- (12) Linden, H. B.; Beckey, H. D.; Hilt, E. *Journal of Physics E: Scientific Instrumentation* **1978**, *11*, 1033-1036.
- (13) Taylor, D. M.; Rollgen, F. W.; Beckey, H. D. *Surface Science* **1973**, *40*, 264-281.
- (14) Ajeian, B.; Beckey, H. J.; Maas, A.; Nitschke, U. *Applied. Physics*. **1975**, *6*, 111-119.
- (15) Derrick, P. J.; Neumann, G. M.; Rogers, D. E.; Paterson, J. K. *Journal of Physics D: Applied Physics* **1980**, *13*, 485-484.
- (16) Kiang, C.-H.; Endo, M.; Ajayan, P. M.; Dresselhaus, G.; Dresselhaus, M. S. *Physical Review Letters* **1998**, *81*, 1869-1872.
- (17) Palotás, Á. B.; Rainey, L. C.; Feldermann, C. J.; Sarofim, A. F.; Vander Sande, J. B.-. *Microscopy Research and Technique* **1996**, *33*, 266-278.
- (18) Machnikowski, J.; Jasienko, S. *Carbon* **1981**, *19*, 205-208.
- (19) Li, C. P.; Teo, B. K.; Sun, X. H.; Wong, N. B.; Lee, S. T. *Chemistry of Materials* **2005**, *17*, 5780-5788.
- (20) Iwashita, N.; Inagaki, M. *Carbon* **1993**, *31*, 1107-1113.
- (21) Ozawa, M.; Goto, H.; Kusunoki, M.; Ozawa, E. *Journal of Physical chemistry B* **2002**, *106*, 7135-7138.
- (22) Nasibulin, A. G.; Pikhitsa, P. V.; Jiang, H.; Brown, D. P.; Krashennikov, A. V.; Anisimov, A. S.; Queipo, P.; Moisala, A.; Gonzalez, D.; Lientsching, G.; Hassanien, A.; Shandakov, S. D.; Lolli, G.; Resasco, D. E.; Choi, M.; Tomanek, D.; Kauppinen, E. I. *Nature* **2007**, *2*, 156-161.
- (23) Iijima, S. *Nature* **1991**, *354*, 56-58.

- (24) Bacon, R. *Journal of Applied Physics* **1960**, *31*.
- (25) Kroto, H. W.; Smalley, R. E.; Heath, J. R.; O'Brien, S. C.; Curl, R. F. *Nature* **1985**, *318*, 162-163.
- (26) Krishnan, A.; Dujardin, E.; Ebbesen, T. W.; Yianilos, P. N.; Treacy, M. M. J. *Physical Review B* **1998**, *58*, 14013-14019.
- (27) Wei, C.; Cho, K.; Srivastava, D. *Physical Review B* **2003**, *67*, 115407-115407.
- (28) Kim, P.; Shi, L.; Majumdar, A.; McEuen, P. L. *Physical Review Letters* **2001**, *87*, 215502-215501-215504.
- (29) Dresselhaus, M. S.; Dresselhaus, G.; Saito, R. *Physical Review B* **1992**, *45*, 6234-6242.
- (30) Dresselhaus, M. S.; Dresselhaus, G.; Saito, R. *Carbon* **1995**, *33*, 883-891.
- (31) Charlier, J.-C. *Journal of Materials Research* **1998**, *13*, 2368-2379.
- (32) Li, H. J.; Lu, W. G.; Li, J. J.; Bai, X. D.; Gu, C. Z. *Physical Review Letters* **2005**, *95*, 086601-086601-086604.
- (33) De Heer, W. A.; Chatelain, A.; Ugarte, D. *Science* **1995**, *270*, 1179-1110.
- (34) Ren, Z. F.; Huang, Z. P.; Xu, J. W.; Wang, J. H.; Bush, P.; Siegal, M. P.; Provencio, P. N. *Science* **1998**, *282*, 1105-1107.
- (35) Bower, C. A.; Gilchrist, K. H.; Piascik, J. R.; Stoner, B. R.; Natarajan, S.; Parker, C. B.; Wolter, S. D.; Glass, J. T. *Applied Physics Letters* **2007**, *90*, 124102-124101-124103.
- (36) Nerushev, O. A.; Sveningsson, M.; Falk, L. K. L.; Rohmund, F. *Journal of Materials Chemistry* **2001**, *11*, 1122-1132.
- (37) Sveningsson, M.; Morjan, R. E.; Nerushev, O.; Campbell, E. E. B. *Carbon* **2004**, *42*, 1165-1168.
- (38) Nilsson, L.; Groening, O.; Emmenegger, C.; Kuettel, O.; Schaller, E.; Schlappach, L.; Kind, H.; Bonard, J. M.; Kern, K. *Applied Physics Letters* **2000**, *76*, 2071-2073.
- (39) Morjan, R. E.; Maltsev, V.; Nerushev, O. A.; Yao, Y.; Falk, L. K. L.; Campbell, E. E. B. *Chemical Physics Letters*. **2004**, *383*, 385-390.
- (40) Sveningsson, M.; Nerushev, O. A.; Morjan, R. E.; Campbell, E. E. B.; Malsch, D.; Schaefer, J. A. *Applied Physics Letters* **2004**, *85*, 4487-4489.
- (41) Ren, Z. F.; Huang, Z. P.; Wang, D. Z.; Wen, J. G.; Xu, J. W.; Wang, J. H.; Calvet, L. E.; Chen, J.; Klemic, J. F.; Reed, M. A. *Applied Physics Letters* **1999**, *75*, 1086-1088.
- (42) Teo, K. B. K.; Chhowalla, M.; Amaratunga, G. A. J.; Milne, W. I.; Hasko, D. G.; Pirio, G.; Legagneux, P.; Wyczisk, F.; Pribat, D. *Applied Physics Letters* **2001**, *79*, 1534-1536.
- (43) Merkulov, V. I.; Lowndes, D. H.; Wei, Y. Y.; Eres, G.; Voelkl, E. *Applied Physics Letters* **2000**, *76*, 3555-3557.

4. Field Ionisation of Gases using Carbon Nanotubes

4.1 Introduction

A simple field ionisation (FI) ion source was designed and constructed for the purpose of investigating whether the use of arrays of carbon nanotubes to field ionise gases was practical.

4.2 The first-generation of field ionisation source.

4.2.1 Design

A field ionisation (FI) source was designed to fit onto the support already installed in the source chamber of the MagTOF instrument. Initially there was no intention of attempting to transfer ions through the instrument to the magTOF's detectors, and so the magTOF's existing optics were not an immediate consideration. Under native conditions, a vacuum of 5×10^{-6} Torr could be achieved in the source chamber using a Edwards backing pump (5 m³hr) and a Leybold–Heraeus turbomolecular pump (460 Ls⁻¹). The source pressure was measured using a cold-cathode ion gauge.

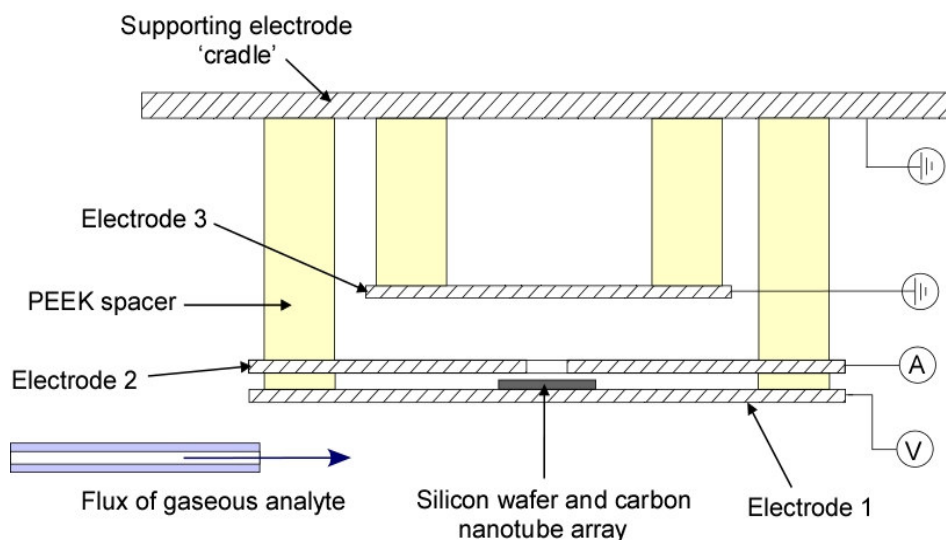


Figure 4.1. Schematic of the first-generation source (arrangement used in field ionisation experiments)

The source consisted of three circular stainless-steel electrodes arranged in series as shown in figure 4.1 (The electrodes were made out of non-magnetic 304 grade stainless steel with a thickness of 1 mm). The first electrode was used as a mount for an 8 mm by 8 mm array of carbon nanotubes (manually broken from the bulk of the CNT sample using a diamond-tipped scorer). The array was stuck directly to the centre of the electrode using a conductive silver-lined epoxy (RS components, Corby, UK). Electrode 2, which would act as a counter electrode to the CNTs, was separated from the first electrode using three insulating PEEK spacers arranged in a tripod. This provided a distance of approximately 300 μm between the tips of the CNTs and the second electrode. An aperture of diameter 3 mm was present in the second electrode in order to allow ions through to a third electrode separated by a further 5 mm. In a typical experiment, potentials of up to 0.9 kV were applied to electrode 1. An

electrometer (Keithley Instruments, Inc, Cleveland, Ohio) was connected to either electrode 2 or 3. If connected to the second electrode a piece of tin foil was fixed to the back of the electrode to ensure that the electrometer would pick up all of the charged species produced. Gaseous sample was introduced into the source chamber via PTFE tubing that was positioned fairly close to the electrodes. The gas was allowed to flood completely the source chamber.

The concentration n of sample gas in the source chamber was calculated from the pressure obtained from the ion gauge using the ideal gas law (equation 4.1):

$$n = \frac{P}{RT} \quad \text{Equation 4.1}$$

Where n is the gas concentration, R is the universal gas constant, T is the absolute temperature (293 ° K in this case), and P is the pressure of the gas. The pressure P was different from the reading of the ion gauge, as the gauge had varying sensitivities depending on the gas used. A correction was made using equation 4.2:

$$P = \frac{P_i - P_b}{r_{ig}} \quad \text{Equation 4.2}$$

P_i (Pa) is the pressure given by the ion gauge, P_b (Pa) is the native or background pressure reading. r_{ig} is defined as the relative sensitivity of the ion gauge to a particular gas, which was obtained from *A Users Guide to Vacuum Technology* by O'Hanlon ¹. Most of the gases were fed into the source

directly from a gas cylinder via the feed-through and pin valve (see chapter 1). In the case of acetone, however, it was necessary to extract acetone gas from a liquid sample. This required a purification process to remove any air in the sample and container which involved freezing the acetone with liquid nitrogen and pumping off any gas in the container.

Care had to be taken to ensure that the source chamber ion gauge was always switched off during experiments. If the ion gauge was left on, false positive currents could be observed at electrodes within the source chamber.

Field ionisation of gases using nanotubes has been achieved previously by Riley et al², however, the design described above differs greatly from the experiment detailed in the literature. This is particularly evident when the emitter and how it was mounted in their experiments was considered: A small array of densely packed vertically aligned nanotubes of typical length 2 μm and radius of 50 nm was grown on the blunt end (by CVD of acetylene) of an inverted T-piece of stainless steel wire over a radius of about 20 – 30 μm . It is very likely that by growing their array on the tip of a thin wire the authors obtained a large field enhancement that would significantly encourage field ionisation when compared to the 8x8 mm array of vertically aligned carbon nanotubes and silicon wafer described above. While a large enhancement is desirable, using the tip of a wire as the mount for the nanotubes restricts the potential for further adaptation of the field emitter, in particular in terms of developing an effective sample delivery mechanism. Conversely the nanotubes grown by Riley et al were likely to be less effective at creating a high field than the nanotubes used

with the first-generation source. The longer length of the nanotubes used with the first generation source (over 10 μm) coupled with the ability to space the nanotubes is likely to yield a stronger and more regular field as shown by the simulations in chapter 3. As a consequence of these differences the experiments conducted by Riley et al can not be used as proof of concept for the first generation source.

4.2.2 Results with the first-generation source

4.2.2.1 Field emission experiments

It is documented that arrays of CNTs are very good field emitters of electrons, as was discussed in chapter 3. While field emission is obviously different from field ionisation, it is likely that if emitters intended to be used in field ionisation experiments were not capable of providing a good field emission current of electrons then they would probably not be very useful for FI. For this reason preliminary field emission experiments were conducted in which potential was applied to the counter electrode (electrode 2) and the electrometer was connected to electrode 1. This allowed the emission of electrons from the CNTs to be investigated by measuring by the positive current at electrode 1. Figure 4.2 shows a typical result obtained. The findings suggest that a current due to field emission was obtained when the potential difference between electrodes was increased to 500 V. When the potential difference was increased beyond 500 V the current was found to increase sharply.

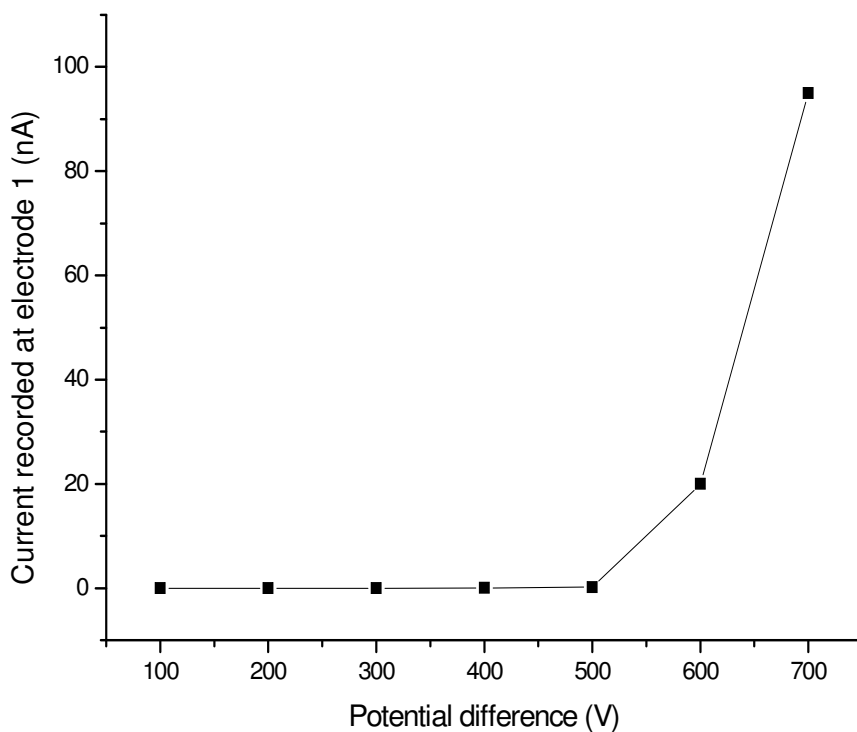


Figure 4.2. Plot showing an example of the Field emission results obtained at base pressure

Fowler-Nordheim (FN) theory applies to field emission³ and was applied to the results in order to probe the field enhancement factors of the array of carbon nanotubes. FN theory has previously been applied in this manor to interpret the field emission results from carbon-nanotube-based emitters⁴. The theory provides a relationship between the emitted current I (A) and the local field F_l at the emitter surface. The local field F_l can be expressed by equation 4.3

$$F_l = \gamma \frac{V}{d_{ie}} \quad \text{Equation 4.3}$$

V is the potential difference, d_{ie} is the inter-electrode distance, and γ is the enhancement factor. The enhancement factor is a measure of the enhancement

of the field which would exist between the electrodes in the absence of fine structure on the surface. The relationship between the local field at the CNTs and the global field F_g (the electric field between CNTs and counter electrode) is given by equation 4.4

$$F_l = F_g \gamma \quad \text{Equation 4.4}$$

According to Fowler-Nordheim theory, the relationship between applied voltage and emitted current is given by equation 4.5⁴

$$I = S \times \frac{1.5 \times 10^{-6}}{\phi} \times \left(\frac{V}{d_{ie}}\right)^2 \times \gamma^2 \times \exp\left(\frac{10.4}{\sqrt{\phi}}\right) \times \exp\left(-\frac{6.44 \times 10^9 \times \phi^{1.5} \times d_{ie}}{\gamma \times V}\right)$$

$$\text{Equation 4.5}$$

Where S has the dimension of an area (m^2) and Φ is the work function of the CNTs (4.9 ± 0.1 eV for carbon-based emitters)⁴. In order to calculate the enhancement factor of the CNTs, equation 4.5 can be rearranged to give equation 4.6

$$\ln\left(\frac{I}{V^2}\right) = \ln S + \ln\left(\frac{1.5 \times 10^{-6}}{\phi}\right) - 2 \ln d_{ie} + 2 \ln \gamma + \frac{10.4}{\sqrt{\phi}} - \frac{6.44 \times 10^9 \times \phi^{1.5} \times d_{ie}}{\gamma} \times \frac{1}{V}$$

$$\text{Equation 4.6}$$

A plot of $\ln(I/V^2)$ against $1/V$ has a gradient of $(6.44 \times 10^9 \times \phi^{1.5} \times d_{ie})/\gamma$ from which the enhancement factor can be calculated knowing the work function and the inter-electrode distance.

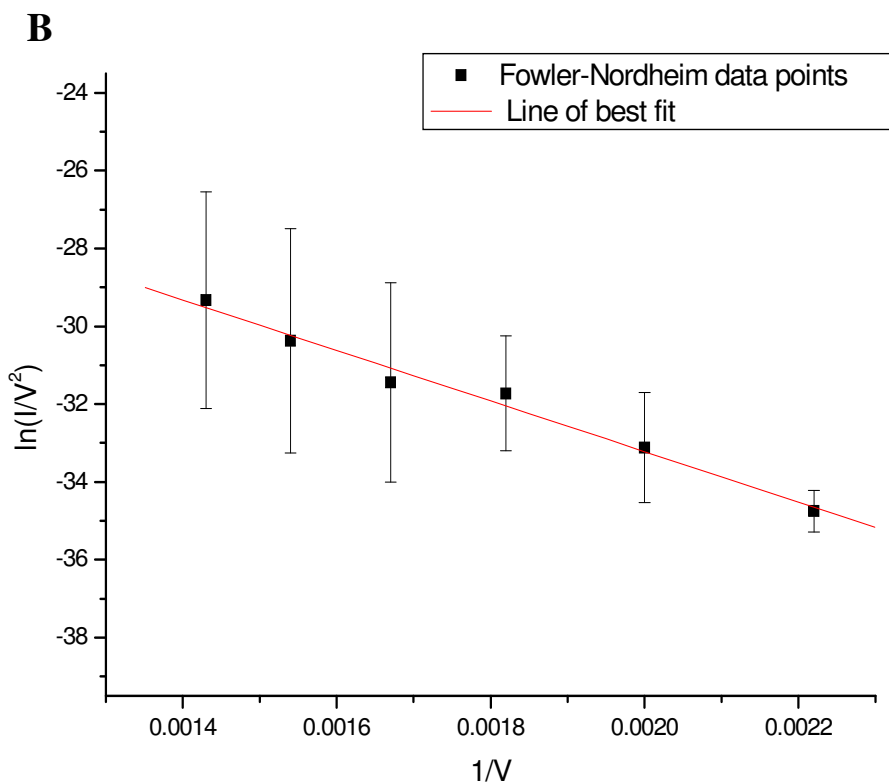
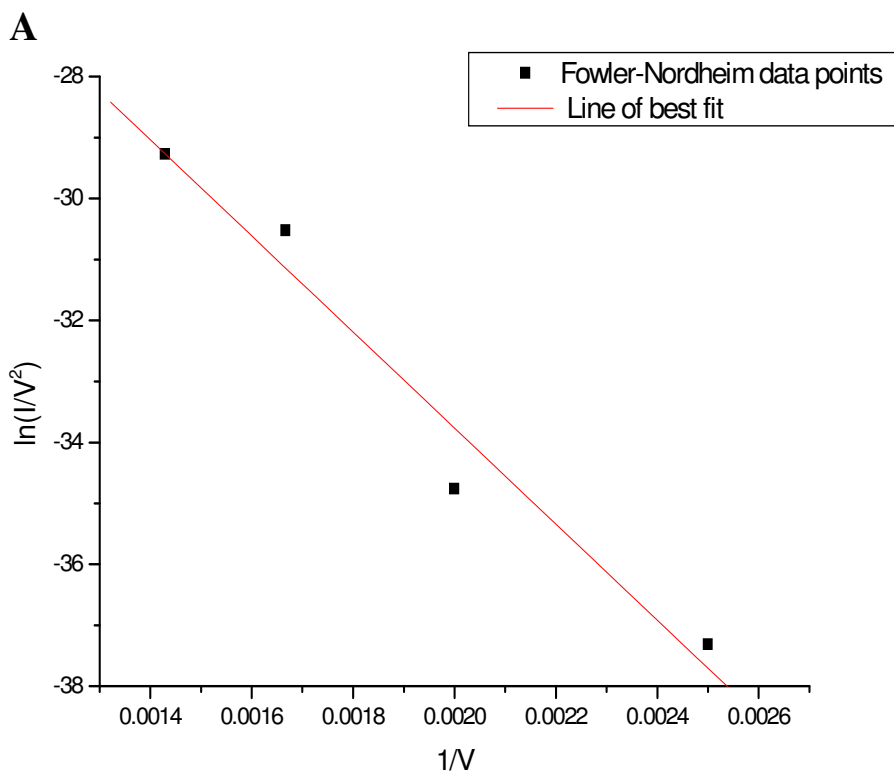


Figure 4.3. Fowler-Nordheim plot derived from A, the data in figure 4.2 and B the average of 6 sets of data

Figure 4.3a shows the Fowler-Nordheim plot derived from the data in figure 4.2. The enhancement factor γ was calculated to be 2698. Bonard et al gave a value of 1800 for a CNT emitter which consisted of a film of irregular carbon nanotubes grown by CVD⁴, γ values of 1081, 1036 and 776 were calculated respectively for a patterned, sparse and dense array of CNTs by Teo et al⁵. Five further FN calculations were conducted using repeat field emission measurements, the average enhancement factor calculated from these and the original value was 2635 +/- 310. The Fowler Nordheim plot derived from the average data including the associated error bars is shown in figure 4.3b. The degree to which these values vary may be indicative of different emission sites on the array which may come about due to damage inflicted by the fields, (the potential difference between electrodes was set to zero between experiments so field emission was initialised in each experiment). It is possible that these variations arise due to a ‘break in period’ as observed by Riley et al², however, this seems slightly less likely because the emitters were used for several experiments prior to these measurements. Alternatively the variations may in part, be due to the comparatively small number of data points used for each FN plot.

The enhancement factor of the average vertically aligned carbon nanotube of length l and radius r within the emitter can be calculated using equation 4.7⁴

$$\gamma = 1.2 \times \left(2.5 + \frac{l}{r} \right)^{0.9} \left[1 + 0.013 \times \left(\frac{d_{ie} - l}{d_{ie}} \right)^{-1} - 0.033 \times \left(\frac{d_{ie} - l}{d_{ie}} \right) \right] \quad \text{Equation 4.7}$$

Assuming the nanotube is 15 μm long and has a radius of 35 nm then an enhancement factor of 277 was arrived, this approximately an order of magnitude less than the value recorded for the entire array from the field emission measurements. In agreement with the results of the field strength simulations in chapter 3 these results suggest that emission does not occur uniformly across the array and that the emitting tubes within the emitter are likely to have a small diameter and be exceptionally long.

The local field strength at the emitter can be calculated from the average enhancement factor using equation 4.3. A value of $6.14 \times 10^9 \pm 0.72 \times 10^9$ V/m was arrived at. This matches well with the value calculated by Bonard et al⁴ (6 V/nm) for a film of carbon nanotubes and compares favourably to the field strength achieved by Riley et al's carbon nanotube emitter (1.7 V/nm).

4.2.2.2 Field ionisation experiments - proof of concept

Characterization of the source for field ionisation began by measuring the current produced with background gas alone in the vacuum chamber (base pressure 5×10^{-6} Torr). The voltage applied to electrode one was increased slowly to a maximum of 1 kV. Acetone was then introduced into the source so that the ion gauge reading increased to 5×10^{-5} Torr, (corresponding to an acetone concentration of 4.92×10^{-7} mol m^{-3}). The experiment was repeated twice (i.e. further fluxes of the analyte gas). Results obtained for acetone gas is shown in Figure 4.4. More ions were produced when the concentration of the analyte was increased.

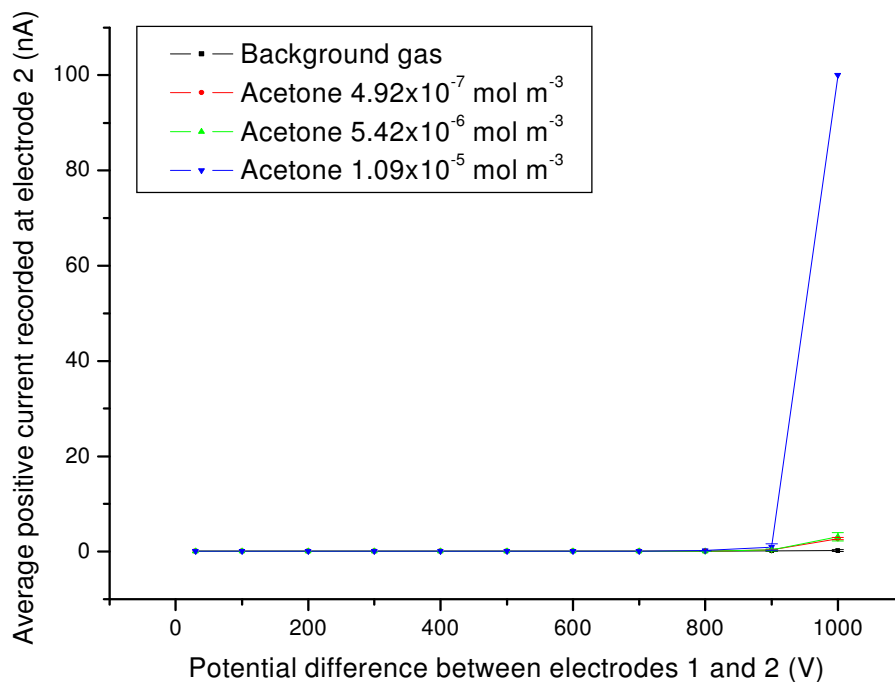


Figure 4.4. Average FI current-voltage characteristic (from 3 experiments with the same CNT emitter) of the first generation FI source for acetone. Note that an error bar is not included for the last data point measured with acetone at a concentration of 1.09×10^{-5} because in several cases the measurement exceeded the scale of the electrometer used.

Gas	Ionization energy (eV)	Concentration (mol/m ³)	Global field strength (V/m)	Average Current (nA)
He	24.58	1.37×10^{-5}	2.5×10^6	0.3
Ar	15.76	2.10×10^{-5}	2.5×10^6	3
Methane	12.62	1.90×10^{-5}	2.6×10^6	60
Xe	12.13	1.93×10^{-5}	2.6×10^6	42
Acetone	9.6	1.09×10^{-5}	2.5×10^6	100

Table 4.1. Average counter electrode current measured (from 5 sets of data) for a number of different gasses under field ionisation conditions.

Using the same method, currents were observed with different gases with a range of ionization energies (see Table 4.1). Under similar conditions (including analyte concentrations and field strengths), more ions were produced for an analyte with a lower ionization energy. The average current measured for acetone may not accurately represent the magnitude of ionised species produced in the presence of acetone. This was because it was later found that, when conducting experiments with the second generation source, there was a leak in the connection between the liquid acetone container and gas line. After this discovery, the connection was replaced with an improved swagelok ultra-torr fitting which was specifically designed to give a good seal with glass. It is hard to quantify the degree of air impurity introduced into the sample; however, it is reasonable to assume that this will have reduced the magnitude of the current observed compared to what would have been observed for pure acetone. The major constituents of air such as nitrogen and oxygen have significantly higher ionisation energies than acetone (14.5 and 13.6 eV respectively compared to 9.6 eV). Measurements were repeated with different samples of the same dense CNT array and some variation was observed, due probably to different morphologies of the samples.

The proximity of electrodes 1 to 2 linked by PEEK spacers makes it possible that the currents (table 4.1) could be due in part to current leaking from electrode 1 to electrode 2. Such a current would most probably travel across the surface of the insulator in which case, an estimation is possible using equation 4.8 with the assumption that the surface of the insulator was clean.

$$\rho_s = \frac{\frac{V_i}{L_i}}{\frac{I}{D_i}} \quad \text{Equation 4.8}$$

ρ_s is the surface resistivity of the insulating material (PEEK has a surface resistivity of $1 \times 10^{-16} \Omega\text{s}^6$), V_i is the potential difference across the insulator, L_i is the length of the insulator, I is the current across the surface and D_i is width of the insulating material. D_i is taken to be the sum of the inner and outer circumferences of the spacer. At a potential difference of 1.1 kV a current of 5.2 pA is calculated. This is several orders of magnitude lower than the current recorded at the same potential difference and therefore it is possible to conclude that these currents can not be accounted for by a leakage current across the insulating spacer assuming that the surface of insulator was kept clean. When the wafer of CNTs used in these experiments was replaced with a blank silicon wafer of equivalent dimensions, no current could be observed regardless of which gas was introduced. This was also found to be the case when a sample of CNTs that previously yielded currents was wiped clean of CNTs.

The observations indicate that the currents measured within the source were due to the presence of the CNTs and that field ionisation using carbon nanotubes had been achieved. A new generation of source was designed and built in order to try and realise mass spectrometric analysis of the currents.

4.3 The Second generation of CNT FI ion source

4.3.1 Design

The design of this second source was directed towards achieving mass spectrometric analysis. Some of the ideas that arose as a result of work with the first generation source were incorporated. Due to the problems associated with achieving this goal the design remained fluid with numerous modifications being made over time. Figures 4.5 and 4.6 show respectively, a schematic of the design used towards the end of this period of research and a photograph of one incarnation of the source optics removed from the source. A detailed drawing which includes dimensions is given in Appendix 4A.

A lens system was required in the second-generation source to focus ions into a tight ion beam and control the deflection of ions to increase transmission. The source chamber slits of the MagTOF were removed to allow a much larger channel through to the linear TOF detector.

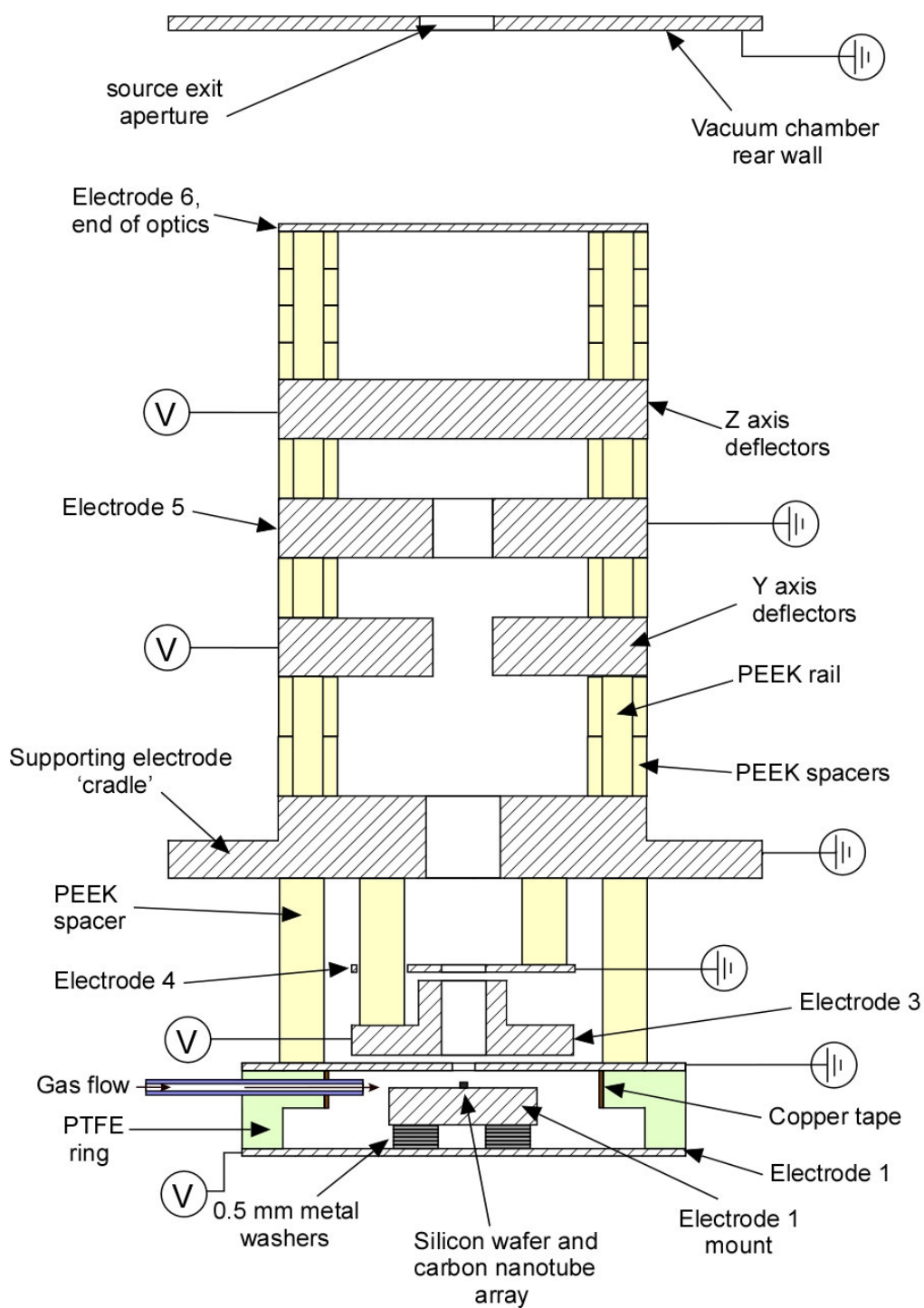


Figure 4.5. Schematic of a second source. Electrode 6 was used to measure current at the end of the lens stack and was removed for experiments in which the object was to transfer charge species beyond the source chamber.

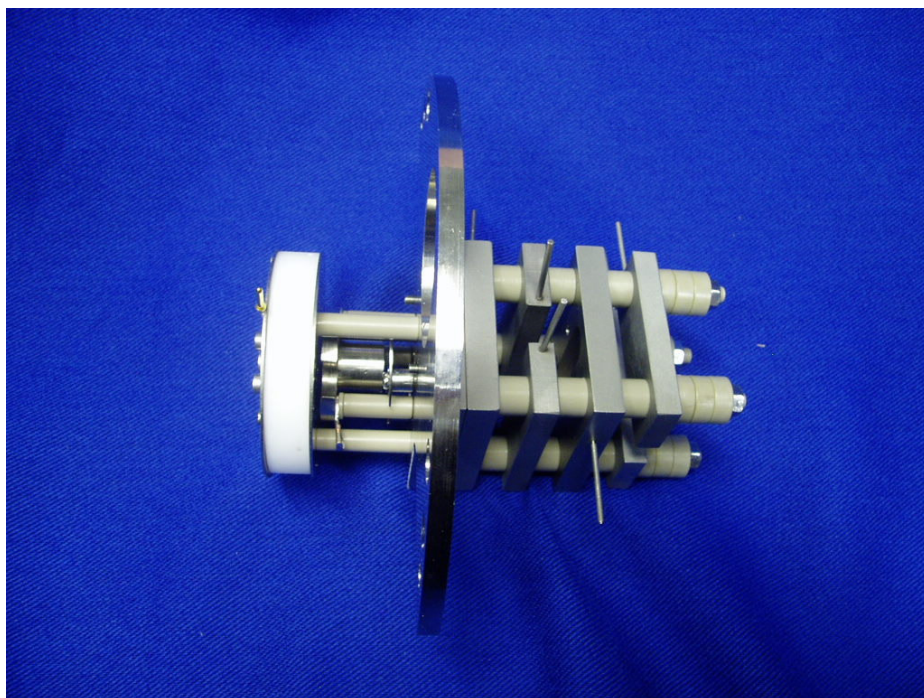


Figure 4.6. Photograph of source optics used during research with the second-generation source

The space between electrodes 1 and 2 was increased and enclosed by an insulating ring of Teflon PTFE. Analyte gas could be introduced into the enclosed space via a small inlet in the side of the PTFE ring. This avoided flooding the entire vacuum chamber with gas. Copper tape was wrapped around the lower step of the PTFE spacer and placed in contact with electrode 2, so as to prevent the surface charging of the spacer. Electrode 1 (where the CNTs were mounted) was made to be adjustable so that the inter-electrode distance could be controlled easily. In most experiments this was set so there was a distance between the CNTs and counter electrode 2 of 1mm. The size of the Si wafer was initially reduced to 1.5 mm × 1.5 mm, which was smaller than the aperture in electrode 2, in order to avoid electric arcing between the CNTs and Electrode

2. This was subsequently altered when laser micromachining was used to cut out smaller discs of carbon nanotubes.

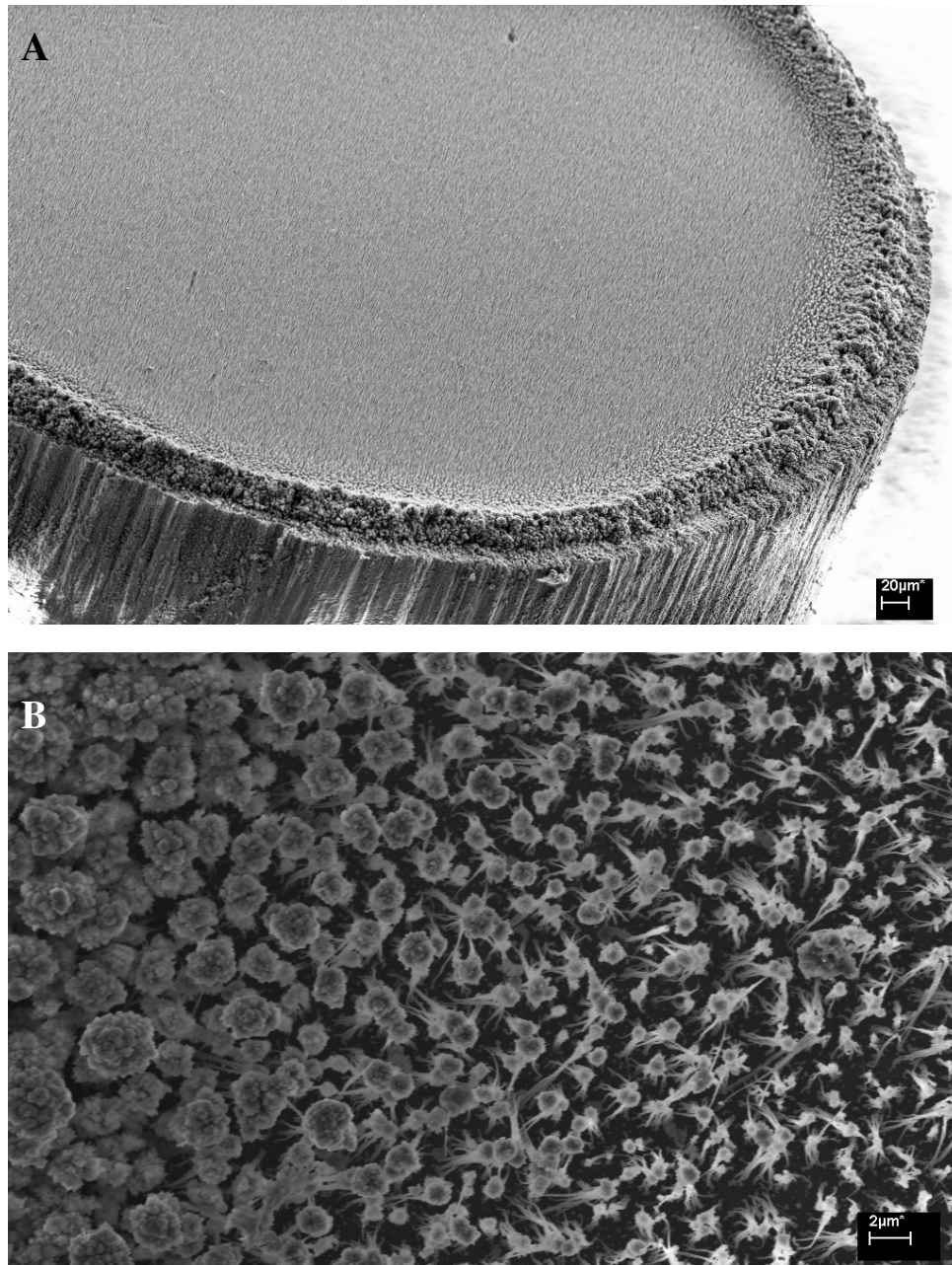


Figure 4.7. Micrographs recorded using a Zeiss SUPRA 55-VP FEG scanning electron microscope showing A) an array of nanotubes cut using laser machining and B) an enlarged region of the array showing the destruction wrought on CNTs near the edge of the array by the machining process.

Figure 4.7 (A) and (B) show micrographs of a 1mm diameter disc of CNTs cut using the DP100-1064 Micromachining System, using a Q-switched NdYAG laser operating at 355 nm (Oxford Lasers Ltd, Oxon, UK). The micrographs show that the fine structure of the CNTs near the cut edge had been destroyed by the machining process. If it is taken into account that these sites were much harder to image and therefore much poorer emitters it seems likely that these cauliflower-like structures consist of amorphous carbon. The ring of amorphous carbon was found to shield the main body of CNTs and so was removed using a fine blade before introduction into the mass spectrometer.

In the second-generation source, the pressure inside the PTFE ring could not be read directly by the ion gauge. There was a pressure differential between the main source chamber and the interior of the ring. It was therefore necessary to model the flow through the hole in electrode 2 and calculate the pressure difference¹. This was complicated further because there are different formulations of fluid dynamics and that which is appropriate depends on the scale of the flow. The Knudsen number, named after Danish physicist Martin Knudsen, is useful for deciding which model of fluid dynamics to use. Normally if the Knudsen number is greater than 1, it is appropriate to use a statistical mechanics model. This situation arises to when the mean free path of a molecule is comparable to the scale of the device. The Knudsen number K_n is given in equation 4.9¹

$$K_n = \frac{RT}{\sqrt{2\pi}d_0^2PN_A d} \quad \text{Equation 4.9}$$

d_0 is the molecular diameter of the gas (0.63 nm for acetone), P is the pressure of the gas, N_A is the Avogadro's number ($6.0221 \times 10^{23} \text{ mol}^{-1}$) and d is the diameter of the aperture in the electrode (3 mm). If acetone is considered it is possible to calculate that the flow would act according to statistical mechanics as long as the pressure is no larger than 6×10^{-3} Torr. Above this pressure the calculation became considerably more difficult as this enters a transition region between the statistical and continuum dynamics ($0.01 < K_n < 1$) where neither describes the situation very accurately. If it is assumed that for these experiments the gas flow remained molecular, equation 4.10 can be used to calculate Q , the flow-rate of gas through the aperture in electrode 2,

$$Q = \frac{ad^2}{4} \sqrt{\frac{\pi RT}{2M}} \cdot \left(P - \frac{P_i - P_b}{r} \right) \quad \text{Equation 4.10}$$

where P is the real pressure of the analyte gas inside the ring, a is the gas transmission probability of the aperture in electrode 2 (0.75 if it is assumed that the diameter of the aperture in electrode 2 is 3 mm and the thickness of the electrode is 1 mm¹), d is the diameter of the aperture in electrode 2, and M is the molecular mass of the analyte. As the pressure inside the main source chamber and the ring were both maintained by the same turbomolecular pump it is possible to relate them with Q as shown in equation 4.11,

$$Q = \frac{P_i - P_b}{r} \cdot S \quad \text{Equation 4.11}$$

S is the pumping speed of the turbomolecular pump (360 L/s for the Edwards turbo pump fitted on the MagTOF's source). By combining the two equations defining Q , it is possible to create an equation (4.12) that can be used to calculate the pressure within the PTFE ring.

$$P = \left(1 + \frac{4S}{ad^2} \sqrt{\frac{2M}{\pi RT}}\right) \cdot \frac{P_i - P_b}{r} \quad \text{Equation 4.12}$$

Simion 8 software was used extensively during the development of the second-generation source to model the trajectory of ions through the source acceleration and transfer optics. The design shown in figure 4.5 was modelled using the following assumptions:

1. Ions are produced uniformly (in terms of emission site spacing and distance away from the counter electrode) across a 1 mm diameter disc of carbon nanotubes.
2. An ion can be emitted in any direction within a hemispherical shell sited at each emission point.
3. Ion-neutral collisions are neglected.

The results (figure 4.8a) suggested that a good percentage of the ions emitted should be transferred through the ion optics and to some extent the ion beam should remain collimated after it exited the source chamber. This was particularly true when a smaller diameter bed of CNTs was considered. For example, if the CNT array was reduced to a diameter of 500 μm , the simulation could be optimised so that all the ions emitted from this area would be transferred and the beam of ions would be nicely collimated (figure 4.8b).

However, due to the relatively large area of potential emission sites, it is difficult to design optics and apply set potentials that will perfectly focus 100% of the ions produced by the emitters.

To achieve mass analysis by TOF a method of splitting the beam into packets with a defined starting time would be required. The simple solution of pulsing the potential applied to electrode 3 (normally used to focus the ion beam) to split a continuous beam into packets was explored. A switch (Behlke power electronics GmbH, Kronberg, Germany) was placed in sequence with the power supply. A pulse generator connected to the switch was used to set how many times a second the switch would activate and for how long. In most experiments the switch was activated 5 times a second for a duration of 1 micro second each time to create ion packets. An oscilloscope was connected to the TOF detector to image any signals from the detector

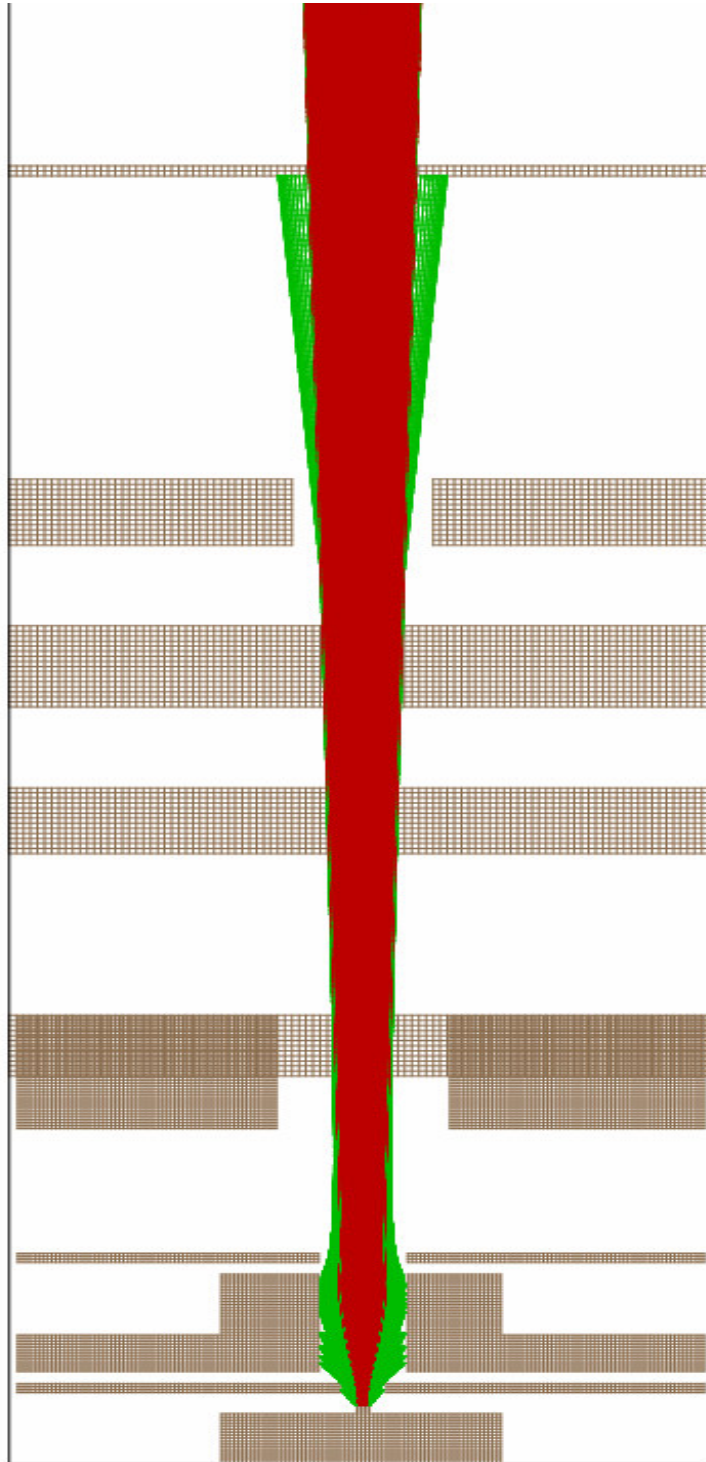


Figure 4.8a. Simion 8 simulation of second-generation ion source (Figure 4.5) showing the trajectory of ions (in green) emitted from a 1mm diameter wafer of carbon nanotubes. Ions with a red trajectory are emitted from the centre of the array over a diameter of 0.5 mm

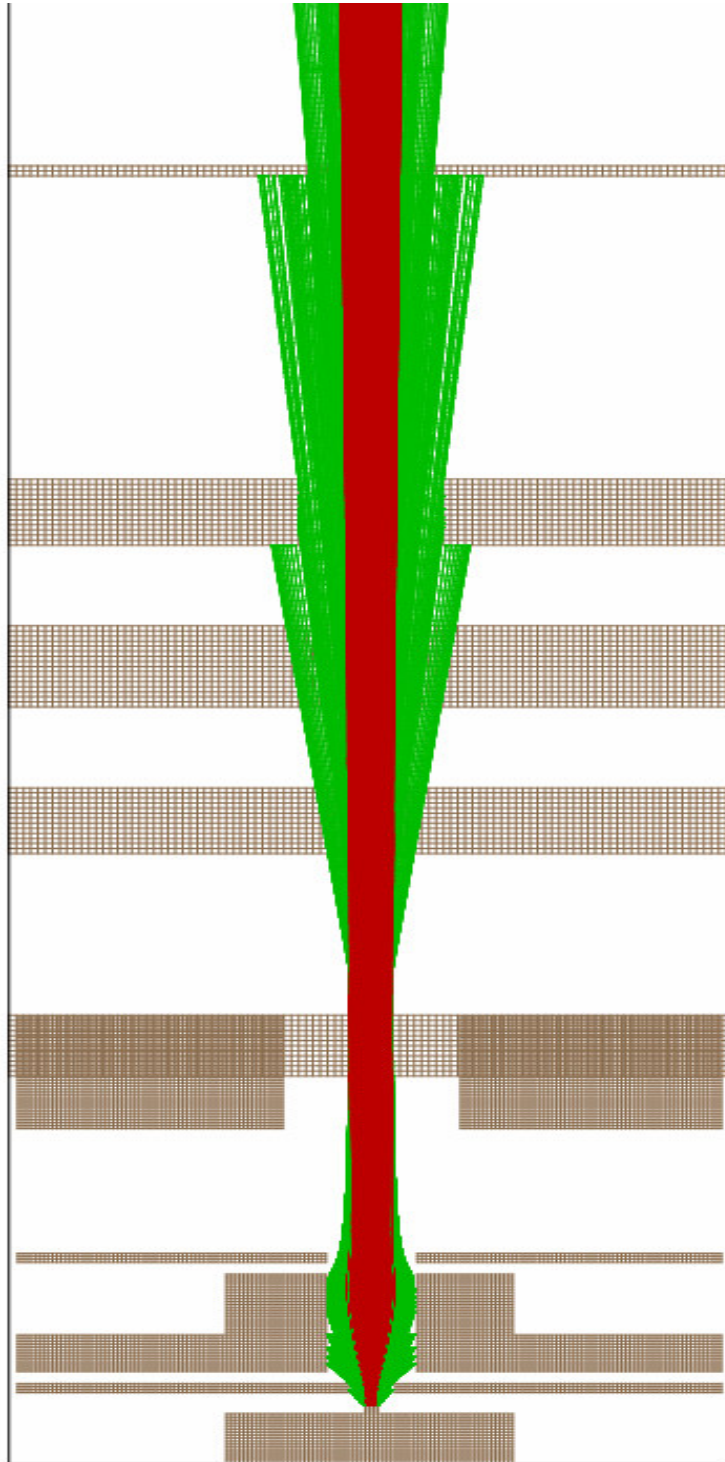


Figure 4.8b. Simion 8 simulation showing the trajectory of ions emitted from a 1 mm diameter wafer optimised to focus and collimate the ions emitted from the centre of the array over a diameter of 0.5 mm

4.3.2 Results with the second generation source

A large number of small modifications were made to the source during the course of experiments. Characterization of the source at each step produced a large number of experimental results and Simion simulations. These results are summarised and discussed here.

The current at electrode 3 (figure 4.5) was measured using acetone gas as the analyte. Acetone was introduced (normally equivalent to a concentration of $1.36 \times 10^{-4} \text{ mol m}^{-3}$ within the PTFE ring) and the potential applied to electrode 1 was increased until the desired level is reached. It is important to note that due to the larger separation between electrodes 1 and 2 (1 mm) in the second source design a larger maximum potential was used to reflect a similar field as experienced with the first source. Dependence of current on concentration of the analyte was observed and the signal scaled with potential as would be expected.

The lifetime, stability and variation among samples of dense CNT emitters under field ionization conditions were investigated. There was a difference between arrays of carbon nanotubes cut to a prescribed size using laser machining and the arrays manually broken into non-uniform pieces.

Experiment date	Wafer number	emitter preparation method	Current measured at electrode 3 (pA) when a potential of 7 kV was applied to the CNT emitter and acetone at concentration of 0.00136 (mol m ⁻³) was fed into the source
07/08/2007	1	Manual	85
15/08/2007	2	Manual	180
17/08/2007	3	Manual	240
26/09/2007	4	Laser	550
28/09/2007	4	Laser	350
01/10/2007	5	Laser	340
12/11/2007	5	Laser	250
19/11/2007	6	Laser	850
10/12/2007	6	Laser	950
03/01/2008	7	Laser	570
18/03/2008	7	Laser	400

Table 4.2. Summary of the relationship between the current recorded at electrode 3 and different samples of CNT array under comparable FI conditions

Table 4.2 summarises results with different samples of CNT array under the same FI conditions. The average current was 433 pA and the standard deviation was 273 pA. If only the laser cut emitters were considered this average increased to 533 pA with a lower standard deviation of 252 pA. This variation was not unexpected as each sample of CNTs would have a different morphology and might be more or less suitable for FI.

The lifetime of a given carbon nanotube emitter was found to be substantial; over 1 month of continuous use was achieved without any noticeable

degradation. In any experiment, the current produced by a sample of CNT array was found to decrease slowly over a period of about an hour while maintaining a constant high potential upon applying the high potential, see figure 4.9 (the power supplies were switched on at least one hour prior to measurements to avoid any 'warming up' issues). This could perhaps be explained if neutral acetone molecules were found to condense on the CNT emitters over the hour, up until an equilibrium point is achieved between the acetone in the gaseous and liquid state.

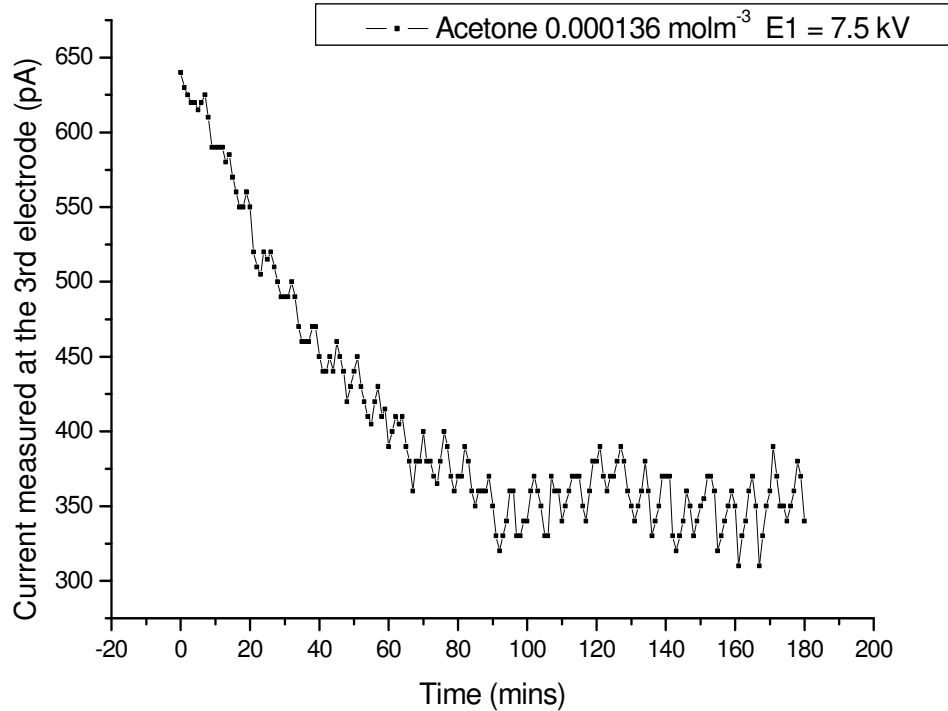


Figure 4.9. Graph showing the stability of the emission from carbon nanotube emitter over time

Measurements with the second-generation source were conducted using samples of dense forest-like carbon nanotubes and acetone. Theoretically this type of array might be expected to create lower maximum fields than a patterned array

of carbon nanotubes. A manually cut sample of the patterned CNT array (discussed in chapter 3) was compared with a sample of dense CNTs under the same experimental conditions. Figure 4.10 shows the comparison between the currents. The ion current was an order of magnitude less with the patterned array than that with the dense array. This result was reproducible. The conclusion drawn is that the fields with the sample of dense CNTs are above the threshold for ionisation. The larger currents are the result of a larger surface area for field ionisation.

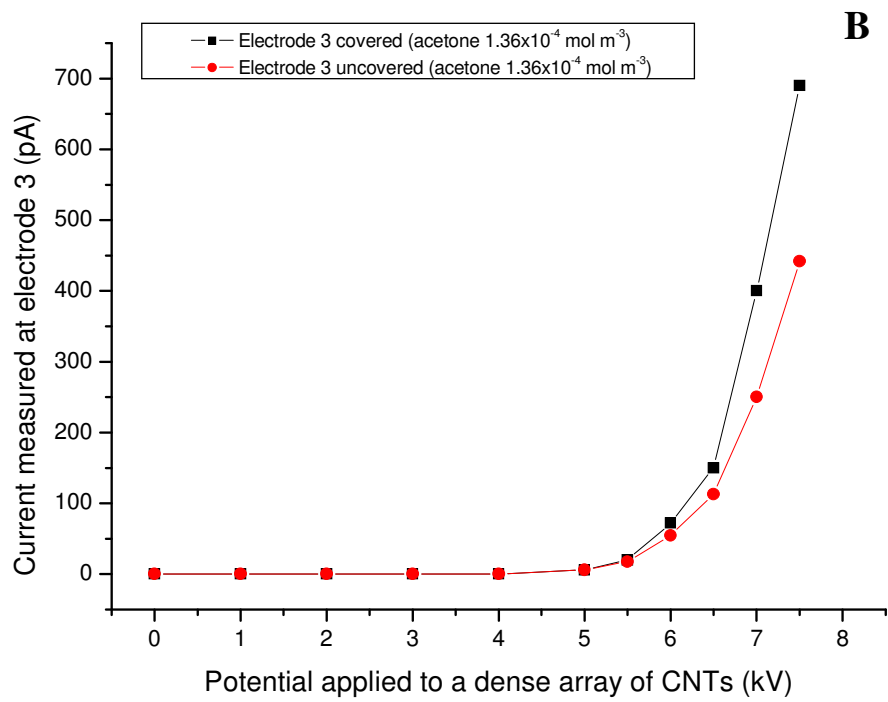
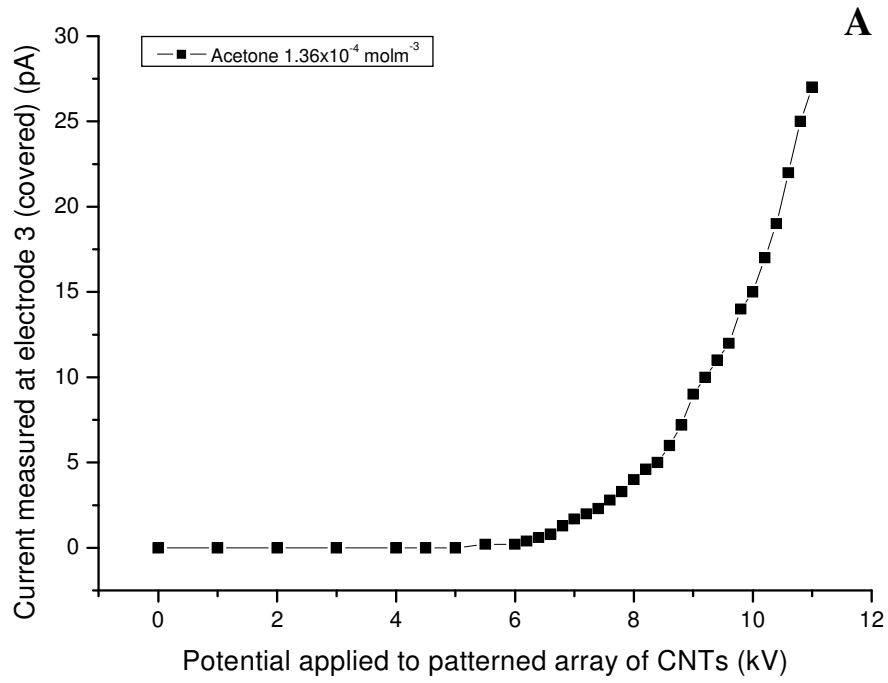


Figure 4.10. Comparison between the currents obtained using A) a sample of the patterned array of CNTs and B) a sample of the dense array of CNTs.

The transmission of the source transfer optics was probed by measuring the current at each individual electrode when covered with metal foil. The difference between the current measured when the electrode was covered and uncovered is exemplified in Figure 4.10B. For the source shown in figures 4.5 and 4.8 the currents recorded, assuming 5 measurements at each electrode, are shown in Table 4.3.

Optic at which the measurement was made	current obtained using an E3 potential of 5.5 kV (pA)	Potential applied to electrode 3 to achieve maximum current (kV)	Maximum current (pA)
Electrode 3	N/A	N/A	442
YDFL	29	6.25	32
Electrode 5	31	6.25	33
ZDFL	35	5.5	35
Electrode 6	20	5.5	20

Table 4.3. Current measured at several stages within the optics of the second-generation source. A potential difference between CNTs and counter electrode of 7.5 kV was used during these experiments.

There was a sharp decrease in the current measured at electrodes after the cradle, what would seem to contradict the predications of the Simion model of the source. One explanation would be that the majority of emission sites were at the edges of the array, since, the modelling indicated that there would be no transmission to the end of the lens stack (figure 4.11 A).

This train of thought would suggest that smaller radii of samples of CNTs would significantly improve transmission. However, experiments conducted with a 0.5 mm diameter array of CNTs yielded only a small improvement. It is concluded that there were some other factor not taken into account by the simulations that was adversely affecting the transmission. It seems likely that there was a fault in the modelling of the nanotubes, i.e. they were not represented correctly in the simulations.

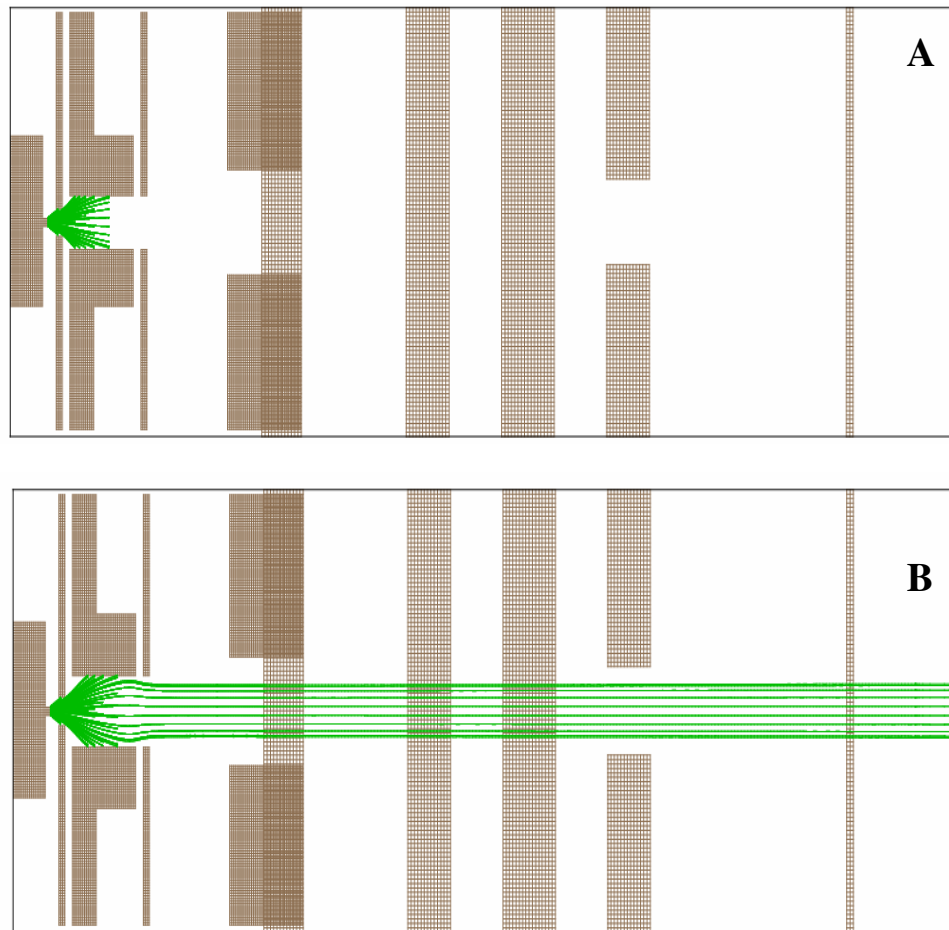


Figure 4.11. Simion 8 simulations showing the trajectory of ions emitted from the edge (up to 0.1 mm from the edge) of a 1 mm diameter wafer of carbon nanotubes when an aperture of a) 6 mm and b) 8 mm is present in electrodes 3 and 4

Experiments were conducted to measure ions at the linear-TOF detector of the MagTOF instrument. Using acetone at a concentration of $1.36 \times 10^{-4} \text{ molm}^{-3}$ a maximum of 200 nA was recorded at the linear-TOF detector. The multi channelled plate detector could have amplified the signal by a factor of as much as 1×10^6 and so the observed current of 200 nA could equal 0.2 pA at the detector. The time required for an ion of acetone to travel between electrode 1 and the multiplier was calculated. The kinetic energy E_k gained by the ions is given by equation 4.12, V (V) is the potential applied to electrode 1 and q is the charge of each ion(C).

$$E_k = Vq \quad \text{Equation 4.12}$$

The velocity, v (ms^{-1}) of an ion can be calculated from equation 4.13 where m is the mass of the ion.

$$E_k = \frac{1}{2}mv^2 \quad \text{Equation 4.13}$$

The time-of-flight is calculated using equation 4.14, where time is defined by t (s) and the distance of the TOF region is determined by d_{ft} (m).

$$t = \frac{d_{ft}}{v} \quad \text{Equation 4.14}$$

A time-of-flight of 7 μs was calculated. Experiments with the parameters E1 7 kV, E3 5.78 kV, YDFL 90 V, MCP -1.8 kV (achieved after tuning for

maximum ion current) failed to yield any consistent signal in the 1-25 μ s region as measured by the oscilloscope. The conclusion is that although detected there was insufficient ions to yield a mass resolving signal after beam modulation.

4.4 Conclusion

The strategy was made to design the FI source for use with the BioTOF instrument. The BioTOF was an orthogonal-acceleration instrument equipped with a hexapole which would allow the accumulation of ions. The BioTOF also contained an ion conveyor⁷ that was specifically designed to collimate, transfer and preserve ions.

4.5 References

- (1) O'Hanlon, J. F. *A User's Guide to Vacuum Technology* Third ed.; John Wiley & Sons, Inc: Hoboken, New Jersey, 2003.
- (2) Riley, D. J.; Mann, M.; MacLaren, D. A.; Dastoor, P. C.; Allison, W.; Teo, K. B. K.; Amaratunga, G. A. J.; Milne, W. I. *Nano Letters* **2003**, *3*, 1455-1458.
- (3) Fowler, R. H.; Nordheim, L. *Proc. R. Soc. Lond. A* **1928**, *119*, 173-181.
- (4) Bonard, J.-M.; Dean, K. A.; Coll, B. F.; Klinke, C. P. R. L., 197602 (2002). *Physics Review Letters* **2002**, *89*, 197602-197606.
- (5) Teo, K. B. K.; Chhowalla, M.; Amaratunga, G. A. J.; Milne, W. I.; Pirio, G.; Legagneux, P.; Wyczisk, F.; Pribat, D.; Hasko, D. G. *Applied Physics Letters* **2002**, *80*, 2011-2013.
- (6) Murari, A.; Barzon, A. *IEEE Transactions on Dielectrics and Electrical Insulation* **2004**, *11*, 613-619.
- (7) Colburn, A. W.; Giannakopoulos, A. E.; Derrick, P. J. *European Journal of Mass Spectrometry* **2004**, *10*, 149-154.

5. Direct Introduction of Liquids into the Carbon Nanotube Source.

5.1 Introduction.

The results of the experiments with the first generation of carbon-nanotube-based ion source (Section 4.2) established that carbon nanotubes could be used to produce charged species from gaseous analytes. These results suggested heavily, by way of the different relative current for each different analyte, that these charged species were in fact ionised forms of the analytes. For reasons discussed it was not possible to support this conclusion by mass spectrometry.

The second-generation source was designed to rectify the shortcomings of the first-generation source and to further the project by way of incorporating the capability to supply continuously liquid sample to the carbon-nanotube emitters. By doing so, a continuous-flow desorption and field ionisation might be accomplished.

5.2 Development of the CNT FD ion source.

5.2.1 Design

The existing instrumentation on the BioTOF allowed a greater degree of freedom for the design of the CNT FD/FI source than had been possible with the MagTOF. It was relatively straightforward to re-design the entire front of the BioTOF's source with optics as desired. In order to be able to carry out a field desorption experiment, a pressure no higher than the order of $\times 10^{-3}$ mbar would be required in the emitter region when a sample was being introduced. The first ion conveyor was designed to operate at a pressure in the order of 5 bar. Due to this mis-match, it was decided that only the second conveyor would be used in the new design.

To keep the new source as simple as possible, the carbon nanotubes were positioned such that any ions produced would enter immediately the second ion conveyor. Only one pressure region therefore was required in the source. The conveyor housing was used as was, but the first ion conveyor was removed. A schematic showing the FD/FI source is shown in Figure 5.1.

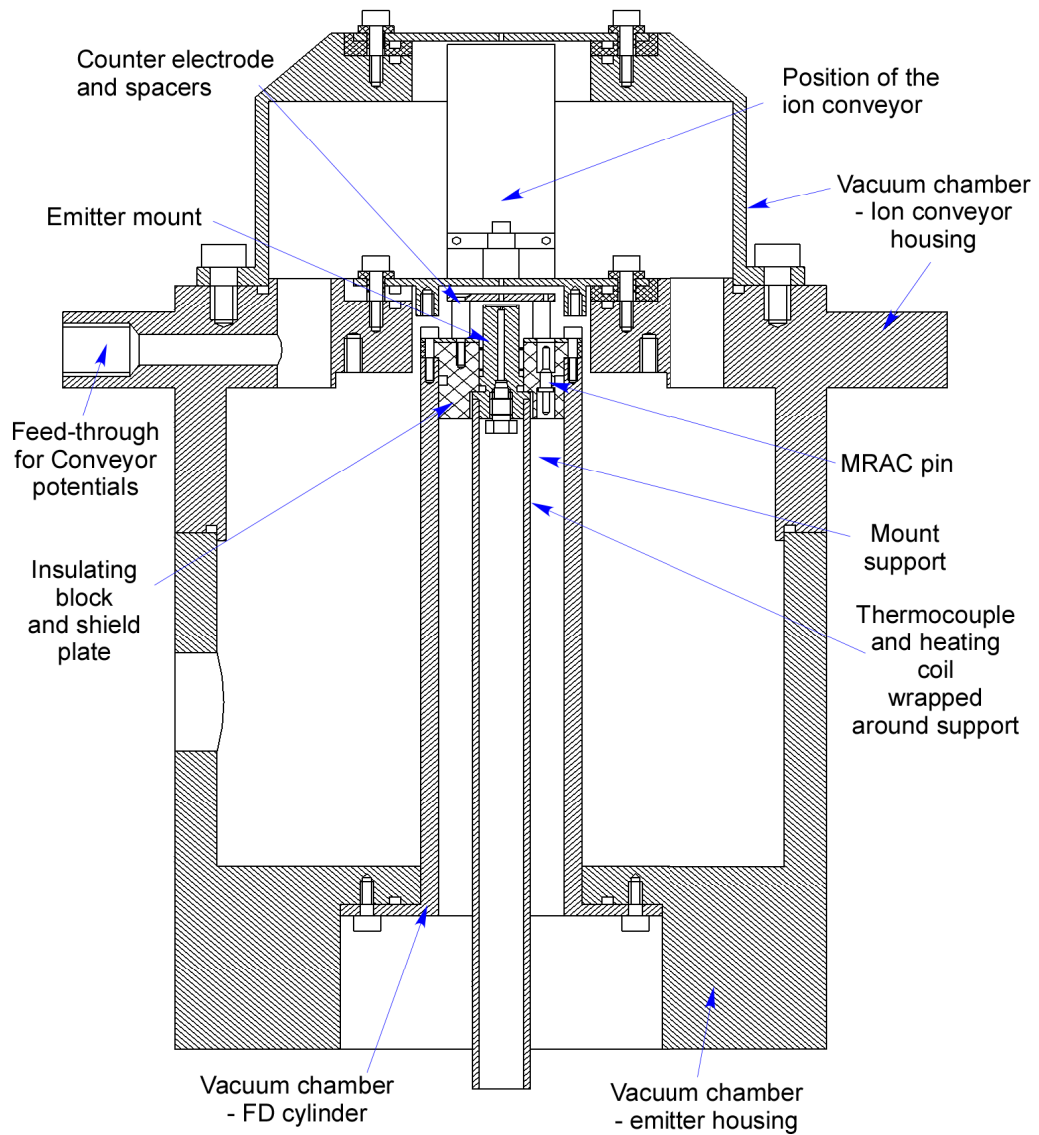


Figure 5.1 Schematic of the field desorption/field ionisation ion source (adapted with permission from the mechanical drawing by Dr Alex Colburn).

The CNT emitter was separated from the ion conveyor by a stainless-steel counter electrode with an aperture of 1 mm diameter. This counter electrode was 2 mm from entrance electrode of the conveyor and 1 mm from the emitter.

The emitter was mounted using conductive epoxy(RS components, Corby, UK) on a stainless steel fitting designed to allow a flow of liquid to the back of the wafer via a short 0.5 mm channel, a length of PEEK tubing (length 0.5 m and I.D of 250 μm) and a chromatography fitting (Supelco, Bellfonte, PA, USA). The rim of the mount was raised slightly to create a shallow recess for the silicon wafer (Figure 5.2).



Figure 5.2. Photograph of the emitter mount, with a used carbon-nanotube emitter attached.

The mount was connected to a stainless steel support to create a probe-like emitter assembly in a similar fashion to conventional FDI probes. If necessary the emitter and mount assembly could be removed from the source. This would however require that the entire source was brought up to atmospheric pressure. A number of mounts were constructed to facilitate preparation of different carbon-nanotube emitters for testing.

The emitter could be heated using RW80 nichrome resistance wire (Resistance Wires Ltd, Glasgow, UK) coiled around the mount support in between layers of insulating glass fibre tape (Farnell, Leeds, UK). The resistance wire was coiled, without touching neighbouring coils, enough times to give a total resistance of 3 ohms. A 12 V power supply would give a heating power of 50 W. A calibrated thermocouple connected to a PID temperature controller (Farnell, Leeds, UK) was incorporated into the system and allowed the temperature to be adjusted and kept at a constant throughout experiments. Temperatures of up to 150 °C could be reached, but temperatures in the range of 100-120 °C were used more routinely.

It was envisaged that the necessary potential difference (several kilovolts) between counter electrode and emitter, would be achieved by applying a large negative potential to the counter electrode and only a small positive potential of the order of about ten volts would be applied to the emitter. By drilling a hole into the end of the mount assembly and connecting to a 12 V battery it was possible to float the emitter and the entire assembly at the required small positive bias.

The emitter and mount assembly were aligned with the ion conveyor and the counter electrode using a block of PEEK. This PEEK block was intended to isolate the emitter from the rest of the source, act as insulation for the feedthrough bringing the large potential to the counter electrode and form vacuum tight seals between both the emitter mount and the cylindrical wall of the vacuum chamber. Viton O rings (Binneys, Coventry, UK) and a thin coating of vacuum grease were used to create the seals.

A metal plate covered the vacuum side of the insulating block to ensure that contact with random charged particles would not charge up its surface. There was sufficient clearance from the feedthrough and the mount assembly to be confident that there would be no current leakage. The counter electrode was mounted on to the PEEK block using 10 mm long PEEK spacers. A gold MRAC pin was used to connect the counter electrode to the electrical feedthrough. The feedthrough consisted of a stainless steel MRAC pin made to fit in the insulating block to form an air tight seal. A photograph showing the mount assembly, insulating block, counter electrode and the supporting cylinder which was part of the vacuum chamber is shown in Figure 5.3.



Figure 5.3. Photograph of the carbon nanotube emitter assembly and the supporting cylinder.

A vacuum-tight seal between the supporting cylinder (Figure 5.1 and figure 5.3) and the rest of the source vacuum-chamber was made with a viton O-ring and

vacuum grease. Six equidistantly-spaced screws between the two pieces to applied pressure to the O-ring. It was necessary to check that the counter electrode was aligned with the conveyor entrance plate each time the supporting cylinder was taken out. According to an ionivac vacuum gauge (Leybold GmbH, Alzenau, Germany) the background pressure of the source was 1×10^{-6} mbar, employing the rotary pumps and the turbomolecular pump and gate valve of the BioTOF.

5.2.2 Carbon-nanotube emitters: design and production

Significant modifications of the carbon-nanotube emitters were made so as to permit a flow of sample (gas or liquid) to be fed through to the foot of the nanotubes. Regular patterns of holes were drilled in the silicon wafers by means of a micromachining device. This device employed a Q-switched NdYAG laser operating at 355 nm. (Oxford lasers, UK) to ablate holes in the emitter. Holes were drilled prior to the growth of the carbon nanotube array because the heat generated would destroy the structure of the carbon nanotubes near the drilled area (even when drilled from the reverse side). This had been established in tests made early on in the studies.

In terms of ion optics a small area of active nanotubes should be advantageous. For this reason the machined holes were drilled within a square of 540×540 μm . An array of 100 holes was drilled in rows of ten with a separation of approximately 60 microns between the centre points of each neighbouring hole. The laser drilling process produced holes with a taper, the extent of the taper

depending on the type and thickness of the material. The holes were drilled through the 5 cm diameter silicon wafer with a thickness of approximately 250 μm . Holes were drilled to a diameter of 20 μm on one side of the wafer, on the other side holes were between a 2 and 6 μm in diameter. It was difficult to make each hole in an array identical in terms of diameter and shape. Scanning electron micrographs of both sides of a silicon wafer are shown in Figure 5.4.

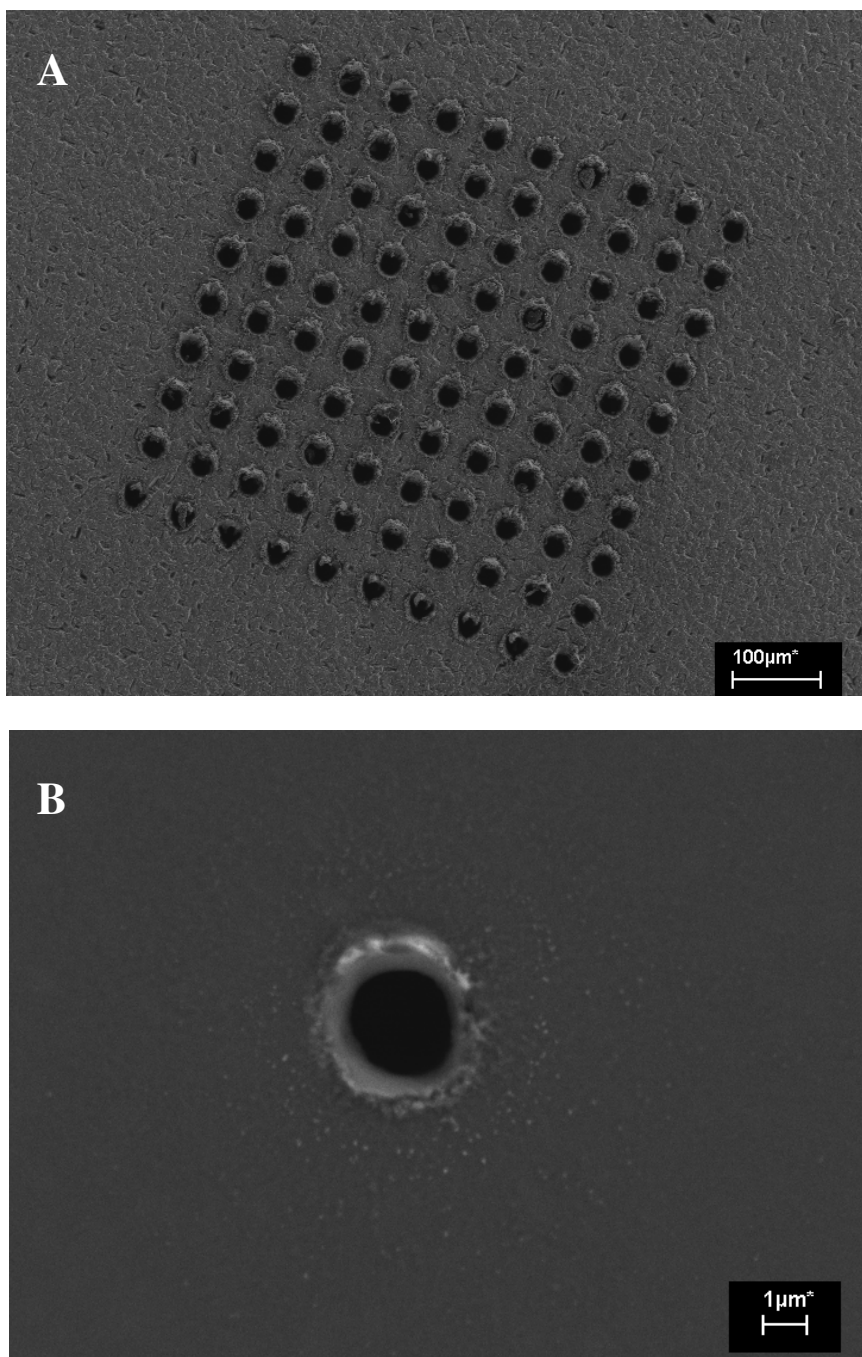


Figure 5.4. Micrographs showing A) the array of holes from the drilled side prior to sonication and B) one of the holes on the side on which CNTs were to be grown.

In order to be able to affix an emitter to the mount pieces using silver-lined epoxy, the diameter of each emitter was larger than the area taken up by the

holes and CNTs. Each emitter had a diameter of 5 mm with holes and CNTs located in the middle. Each 5 mm disc was only partially cut out of the silicon wafer using the laser machining device, which allowed multiple discs to be handled more easily in the CVD process for growing the CNTs. It was possible to get as many as 18 discs from the 5 cm-diameter silicon wafer. Once a wafer had been machined, it was placed in methanol (Fisher Scientific, Loughborough, UK) and sonicated for 5 minutes in order to remove the build up of detritus around each hole. A fine balance was struck between cutting out each emitter disc sufficiently for it to be popped out with the minimum of effort, and keeping making the wafer robust for sonication and CVD processing without discs falling out. Figure 5.5 shows photographs of a machined wafer and of the tool designed and custom-machined made to pop out the discs more easily.

Carbon nanotubes were grown on the wafer using plasma-enhanced chemical vapour deposition (PE-CVD) and characterised, as described (chapter 3). Great care was taken when mounting an emitter to ensure that the epoxy did not block any of the drilled holes but did form a seal all the way round the 5 mm disc. The seal was required to preclude setting up alternative routes for the flow of sample, other than those through the holes in the silicon wafer.

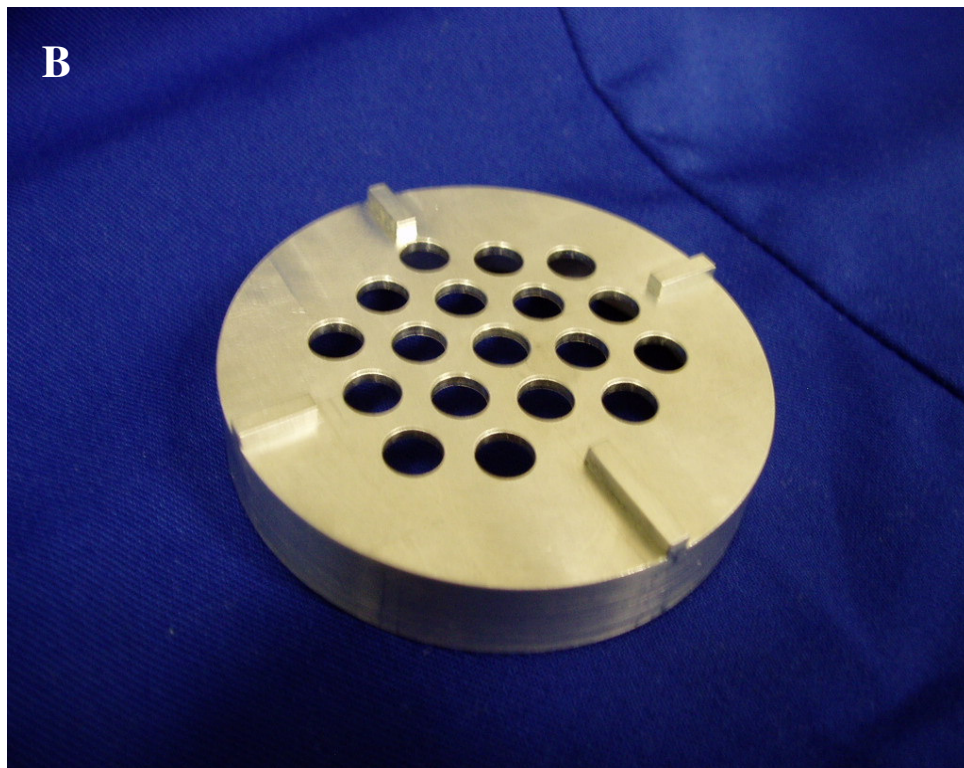
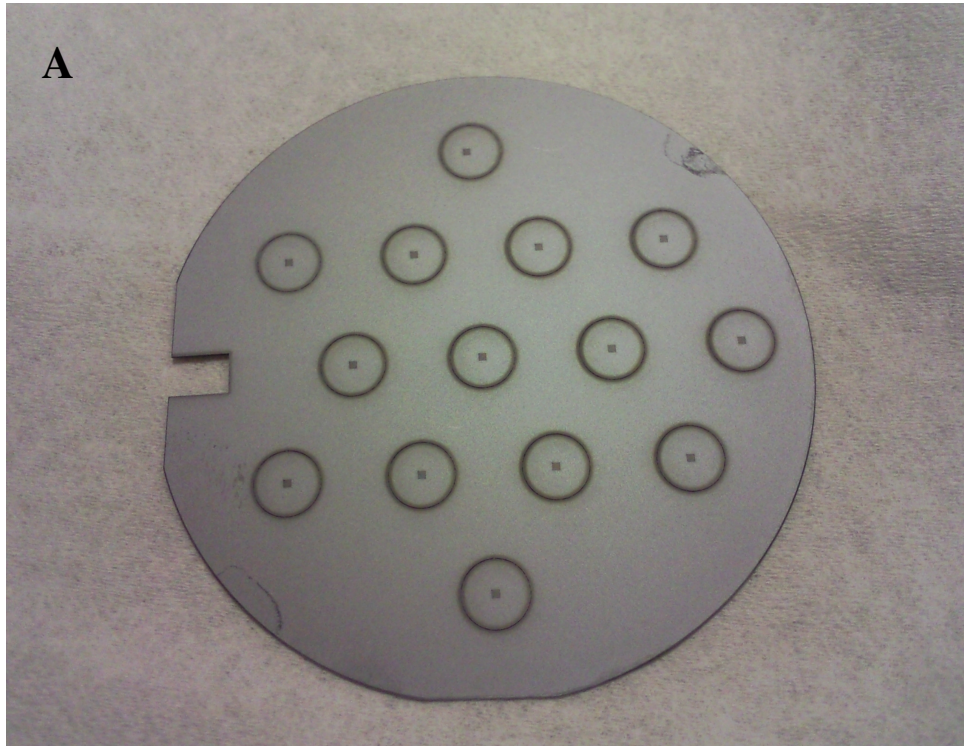


Figure 5.5. Photos showing A) a machined wafer and B) a tool fabricated to help remove each emitter disc from the wafer.

5.2.3 Simulations and flow considerations

Simion 8 software was used to model the trajectories of ions through the source and ion conveyor. The geometry of the mount, counter electrode and ion conveyor is shown in Figure 5.1. In order to model the ion conveyor collisions were treated using the hard-sphere HS1 collision model available from Simion. The HS1 model is based on the classical kinetic theory of gases. The individual collisions between ion and gas particles treated as hard spheres are modelled. The mean free path between collisions, as given by the kinetic theory of gases, is a function of the known pressure, temperature, and collisional cross-sections of colliding particles. Each collision results in the transfer of energy between ion and gas particle as well as deviation in ion trajectory which is plotted in Simion. In general the collisions in the ion conveyor energetically cool ions. More detail and the main assumptions of the HS1 model are available on the Simion website¹. By including an HS1 collision model in the ion conveyor a gas flow perpendicular to the optical axis could be included. In order to simulate the difference in gas flow velocity between the emitter region and ion conveyor, the HS1 model was applied with appropriate parameters to the volume between the emitter and counter electrode. The following assumptions were made:

4. Ions are produced uniformly at emission sites across a 1 mm diameter square section of carbon nanotubes.
5. To gas flowing through has a velocity only in the direction of the ion optical axis both in the counter electrode region and the ion conveyor.

6. The gas was assumed to have the mass of methanol (most of the sample were made up in water/methanol mixes).
7. Any aerodynamic effects that might contribute were not considered.

Figure 5.6 shows the results of the simulation with the following parameters. The emitters, counter electrode, conveyor-entry electrode, conveyor offset and conveyor-exit electrode were set with potentials of 25, 0, 20, 10 and 0 V respectively. The RF frequency and amplitude applied to the conveyor were set to 600 kHz and 21 V peak-to-peak respectively. The pressure was set at 1×10^{-3} mbar in the conveyor region and slightly higher at 1×10^{-2} mbar in the counter-electrode region. The molecular velocity in the counter-electrode region and conveyor region was set to 10 mm per second and 7 mm per second respectively.

The results of this showed that ions entering the ion conveyor were transmitted without loss. The apertures in the counter electrode and entrance electrode constituted restrictions which reduced the overall transmission. If the apertures in these electrodes were made larger more ion were transmitted overall.

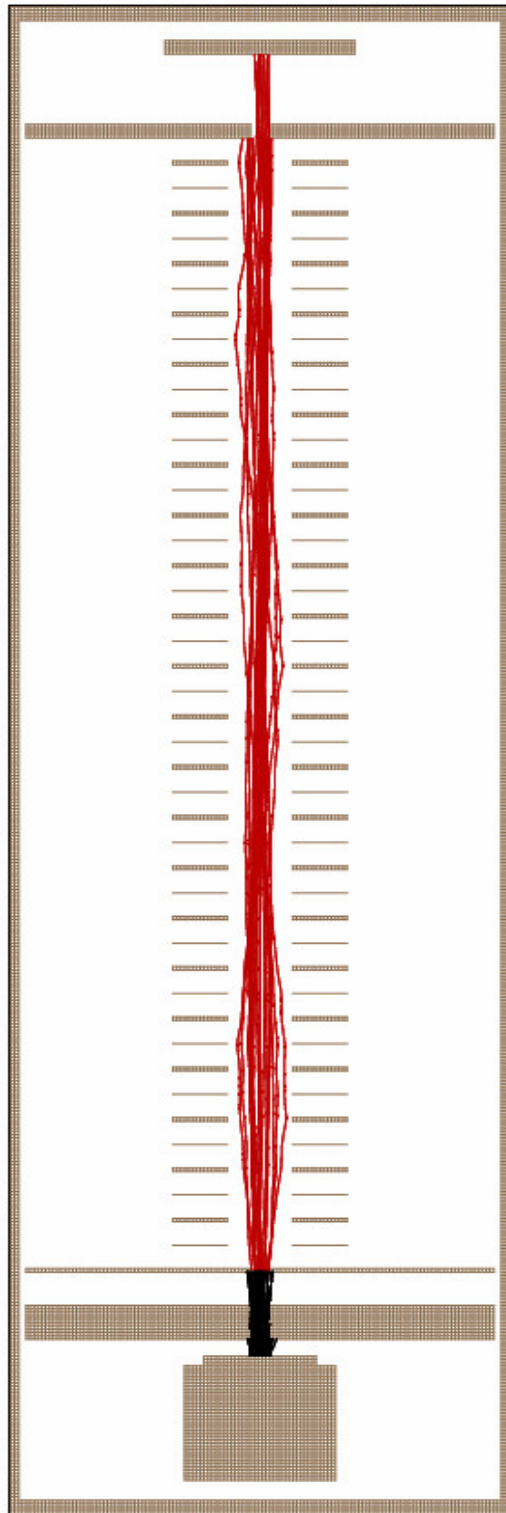


Figure 5.6. Calculated trajectories of ions emitted from a carbon-nanotube emitter through the counter electrode region (in black) and ion conveyor region (in red). Applied potential had been adjusted to optimise transmission

The parameters used in the simulation the results of which are shown in figure 5.6 were ideal in the sense that they gave optimum transmission. The potentials used in the experiments were different, in particular a much larger potential difference between the emitter and counter electrode was used (at least -2.5 kV) in practice. The results of a simulation with a realistic counter-electrode potential are shown in Figure 5.7. One other difference was that the molecular velocity was set at 110 mm per second in both regions. The transmission was poor. The large negative potential applied to the counter electrode caused divergence. Upon entering the ion conveyor, the ions had gained too much energy from the flow of gas and were less effectively confined by the conveyor waveforms. A more realistic model would have gradually reduced the molecular velocity as the ions moved into the ion conveyor

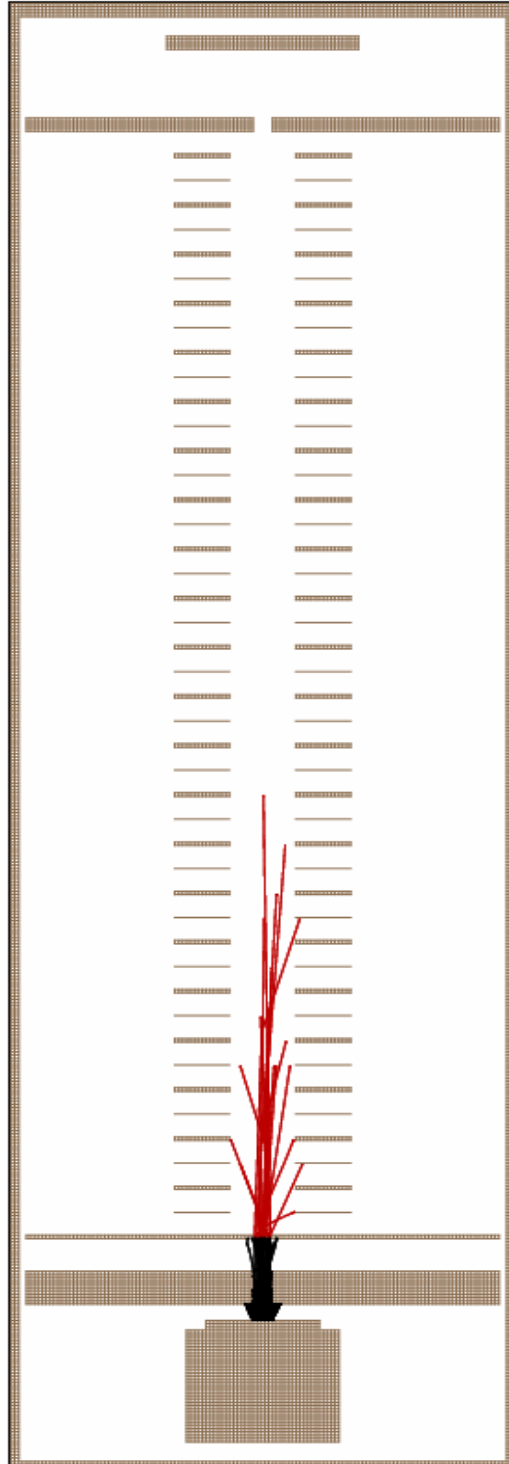


Figure 5.7. Calculated trajectories of ions emitted from a carbon nanotube emitter through the counter electrode region (in black) and ion conveyor region (in red) with a potential of -2.5 kV on the counter electrode. (Molecular gas velocity 110 mm per second).

If the first simulations shown (figure 5.6) represented a best-case scenario, the second simulations (figure 5.7) represented a worst-case scenario. The complexity of the action of the ion conveyor precluded more sophisticated modelling in the time available. The worst-case scenario indicated that over half the ions found their way into the conveyor.

The flow rate at which liquid would be introduced into the source required careful consideration. The intention was to use the syringe pump to maintain a specific and low flow rate of 6-10 μL and hopefully limit the amount of sample on the emitter at any one time. To put this in perspective, with electrospray ionisation flow rates of between 60 and 120 μL per hour were used routinely. From personal experience, flow rates used with nano-electrospray were in the range of 20-30 μL per hour, as calculated from the time a known volume of material takes to spray completely from a nanospray needle. Linden et al have suggested that very small loadings (40 nL) are required to wet completely an activated wire emitter without overloading in their LIFDI source ¹.

When a sample was loaded into the syringe pump, it was found that the high vacuum in the source would “suck” the sample in at a much higher rate than that set by the syringe pump. The “pull” from the vacuum did not have a constant effect on the liquid in the syringe, however on average a 10 μL loading would empty in 10-15 minutes equates to a flow rate of between 40-60 μL per hour. By rearranging the Hagen-Poiseuille law ² in Equations 5.1 to 5.2 it was possible to calculate the theoretical flow rate Q (in $\text{m}^3 \text{s}^{-1}$).

$$\Delta P = \frac{8\mu L_t Q}{\pi r^4} \quad \text{Equation 5.1}$$

$$Q = \frac{\Delta P \pi r^4}{8\mu L_t} \quad \text{Equation 5.2}$$

The Hagen–Poiseuille equations describe slow viscous incompressible flow through a constant circular cross-section. ΔP is the pressure differential between the high vacuum of the source and atmosphere, in this case very near to 1 bar (1×10^5 Pa). μ is the dynamic viscosity of the sample, for this a 50/50 mix of water/methanol was assumed which gave a μ of 1.51×10^{-3} Pa s³. L_t is the length of the tubing that the sample travelled through, and r is its internal radius (m).

A value of $Q = 4.6 \times 10^4$ $\mu\text{l hr}^{-1}$ was arrived at and, this value was way beyond what the experimental data suggested and so it is likely another factor was not considered. This could perhaps be accounted for if the ferrules used to form tight seals with the tubing compress the tubing enough to form severe conductance restrictions to the flow of sample.

To reduce the effect of the pressure differential and gain control of the flow, either the length of the tubing must be increased or its inner diameter decreased. If the inner diameter were kept constant the calculation showed that to achieve a flow rate of 10 μl per hour a length of PEEK tubing over 2280 metres would be required. Reducing the inner diameter however had a much more significant effect on the flow rate. If the diameter were reduced to 25 μm and the length of

tubing was 0.5 m, a flow rate of $4.57 \mu\text{l hr}^{-1}$ was calculated. A desired starting rate of $10 \mu\text{l}$ per hour was arrived at by reducing the length of $25 \mu\text{m}$ I.D tubing to 0.23 meters.

Homemade PEEKsil tubing was used to provide the desired small-bore tubing because normal PEEK tubing was not available at such a small inner diameter. PEEKsil consists of a fused-silica capillary clad in tight-fitting PEEK tubing. The PEEKsil chosen was constructed from $25 \mu\text{m}$ I.D $363 \mu\text{m}$ O.D fused silica capillary (Polymicro technologies, Phoenix, Arizona, USA) and PEEK tubing (Upchurch, Fischer Scientific, Loughborough, Leicestershire, UK). This was selected as it has an outer diameter suitable for the fittings used in the source and an inner diameter that would allow a tight fit to the outside of the silica tubing. The silica tubing in the PEEKsil was not as susceptible to compression as PEEK tubing, which meant that experimental flow rates were less likely to be affected by ferrules. Experiments with the length of PEEKsil tubing installed showed that the time required to empty a full $10 \mu\text{L}$ syringe was almost exactly one hour. The flow rate could then be altered either by reducing/increasing the length of tubing or by putting the fluid under extra pressure by increasing the rate on the syringe pump.

5.3 Source Characterisation: Experiments Results and Discussion

5.3.1 Method

The source was intended to be compatible with both liquid and gas phase samples. Experiments with gases were not straightforward using the BioTOF, because the instrument had a lower mass limit of m/z 100. Liquid samples were therefore used to characterise the new source. Two different types of sample were chosen for the initial measurements. A 25 $\mu\text{mol}/\mu\text{L}$ of vancomycin (Sigma Chemical co.) was prepared in a 50/50 mix of methanol (Fischer Chemical co.) and distilled water. This solution was shaken mechanically for 1 minute in order to ensure complete dissolution. A second solution of xylene was prepared by diluting 100 μl of xylene in 1ml of methanol.

In the initial experiments 10 μL of a solution was loaded into the syringe pump and injected into the source at a flow rate of 10 μl per hour. The source ion gauge showed a pressure increase from 1×10^{-7} mbar up to about 5×10^{-4} mbar. The pressure was increased to 1×10^{-3} mbar as was supposed to be optimum for the ion conveyor by slightly closing the gate valve attached to the source turbomolecular pump ten minutes prior to injecting the sample. A temperature of 120 °C was set on the PID temperature controller.

The source and instrument electronics were switched on one hour before measurements in order to avoid any ‘warming up’ issues with the power supplies. The ion conveyor was set to an operating frequency of 400 kHz for vancomycin and 550 kHz for xylene. A conveyor amplitude of 20 V peak-to-

peak was used for both analytes. The entry plate and offset potentials of the conveyor were tuned over the range -30 and 30 V, always ensuring that the entry plate was slightly the more positive. The emitter was at a positive potential between 0-15 V. A negative potential was slowly applied to the counter electrode in increments of -250 V. The BioTOF's acquisition software was set to a tuning mode which allowed the accumulation of 100 scans before the accumulation cycle was repeated. It was possible to monitor the appearance of the mass spectra as the counter-electrode potential was slowly increased.

5.3.2 Results

An initial goal of these first experiments was to establish a potential difference between the emitter and counter electrode, similar to that used with the first generation source. It proved difficult, however, to achieve this goal because arc discharges between the two electrodes would occur when the counter electrode potential was raised beyond 5 kV (The effect of the discharge on the nanotube array is shown in appendix 5a). No signals were recorded using either vancomycin or the xylene solution prior to the arcing regardless of how the potentials were tuned. Numerous emitters were investigated. Spectra were collected at 5 kV using 10000 scans in order to make sure that no weak signals were missed as a consequence of using the tuning mode. Figure 5.8 A, B and C shows the spectra recorded (using a fresh emitter) of vancomycin with and without a counter-electrode potential and xylene with a counter-electrode potential. No signals could be assigned in any of the spectra; the very low level intensities in all cases indicate that only background noise was recorded.

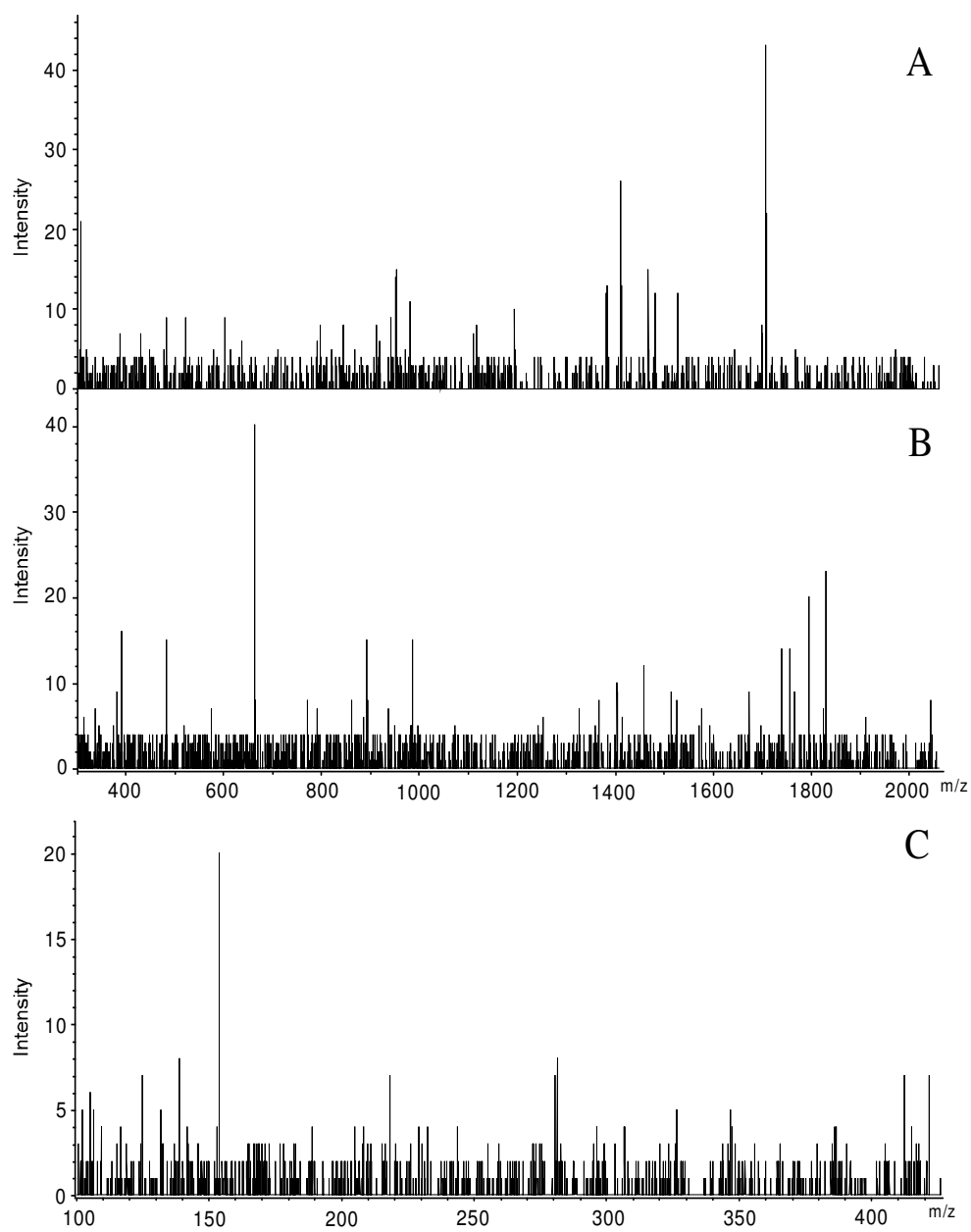


Figure 5.8. Spectra recorded using in each case a fresh emitter of A), vancomycin with a counter-electrode potential (5 kV), B) vancomycin without a counter-electrode potential, and C) xylene with a counter-electrode potential of 5 kV.

Ion currents could be detected at 5 kV in previous experiments with the first-generation source and gaseous samples. Experiments were conducted with the new source in order to confirm that ion currents were being produced. The conveyor electrodes and entry plate were connected to an electrometer, and floated using a battery at a slight negative potential 9 V. The emitters were floated and counter electrode potential applied in increments as normal. The heating temperature was 120 °C as in the previous experiment. No current was detected.

Acetone gas (produced in the same way from liquid as discussed earlier) was also used as an analyte, as there was no requirement to record mass spectra. No current was detected at the ion conveyor at a potential difference of 5 kV when acetone was injected as a liquid. When acetone was introduced as a gas it was not possible to detect any current. It was possible to increase the potential up to at least 6 kV without causing a discharge with gaseous acetone. These results indicate that the FD emitters were not operating as was expected.

5.3.3 Discussion

Scanning electron microscopy was used to investigate an array of carbon nanotubes that had been used in the FD source with liquid-phase samples. The micrographs in Figure 5.9 show that the nanotubes have clumped together into cones. It seems possible that this occurred upon the introduction of a liquid sample. This change in morphology might explain partially why the emitters appear to not have produced any ions. Simion 8 modelling programme was used

to calculate the fields produced by the altered array in comparison to those for the original morphology. The difference in field strength between the two morphologies is illustrated in Table 5.1.

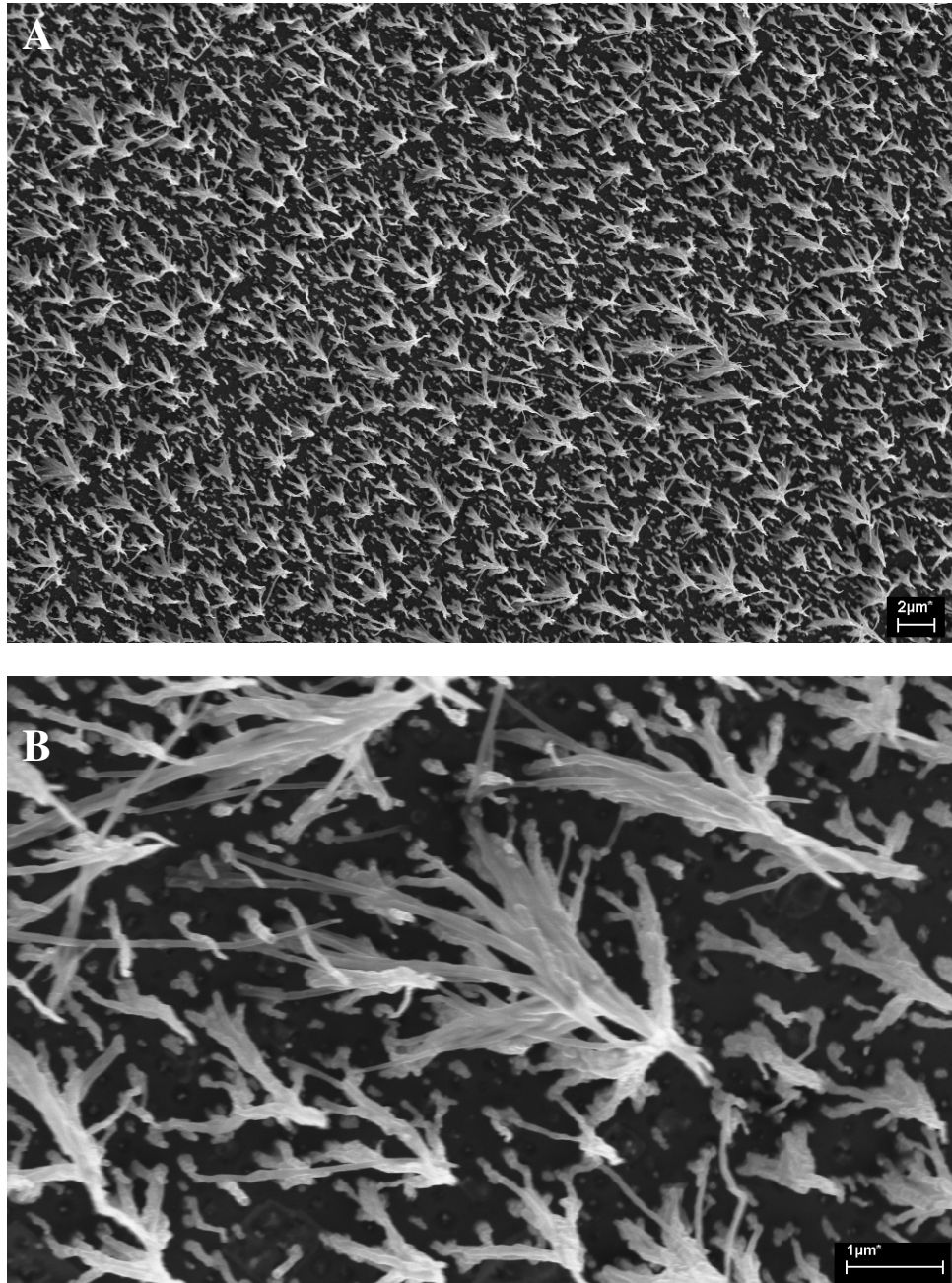


Figure 5.9. Micrographs showing A, a large region of a used emitter and B, enhanced region showing a carbon nanotube clump

The fields generated at similar positions along the simulated slice were much the same. In some cases, the field was actually enhanced by clumping in comparison to those with the original morphology. Appendix 5b shows 2D slices through the two morphologies.

CNT position in simulated slice (μm)	Field strength (V/mm)	Relative position of clump in simulated slice (μm)	Field strength (V/mm)
8.09	31437	7.75	30596
11.04	41015	10.5	37160
17.64	36496	17.15	38425
24.73	32206	23.2	28486
28.01	38068	27.5	39953
31.69	39246	32	37472
38.5	31823	38.4	11121
42.22	37354	42	33819
46.61	39239	46.61	39790

Table 5.1. Relative field strengths generated by the different morphologies as predicted by Simion 8

These results can be explained in terms of shielding. In the normal “forest” array, the field that each nanotube produces at its tip is shielded by its neighbouring nanotubes. By clumping the nanotubes together into pyramids, the shielding from neighbouring nanotubes in the same clump is no longer a factor. In comparison to a nanotube of equal length, a clump will not produce the same magnitude of field due to its poorer aspect ratio and relative size. On the other hand, neighbouring clumps will not shield each other so much due to the

relatively large distance between clumps. These two factors compete and might cancel each other out to yield similar fields regardless of the changed morphology.

The results of the simulation suggest that nanotubes clumping together would not have caused the CNTs to stop emitting. This, coupled with the fact that no current could be recorded from a fresh emitter using a gaseous analyte, seems to suggest that these particular emitters were not suitable for field ionisation. One explanation for this would be that these particular emitters did not generate a strong enough field. In comparison to the 'forest-like' emitters used in the first-generation source, the experiments were carried out using a similar potential difference (4-5 kV) at a similar emitter/counter electrode separation (1 mm).

The nanotubes used in the first-generation source, had a higher aspect ratio than those used with the liquid-introduction source and might have created stronger fields. Yet it is unconvincing given the large difference in ionisation energy, to propose that the earlier array could be used to ionise helium gas while the more recent arrays of a similar sort could not be used to ionise acetone.

Given the lack of success with the dense arrays of carbon nanotubes, a sparse array (discussed in chapter 3) was installed into the source. The nanotubes in the sparse array were much longer and so might be more likely to yield successful measurements. Experiments were repeated using liquid samples of vancomycin and xylene as before. Again arc discharges occurred upon increasing the potential difference between emitter and counter electrode past 5 kV. No current could be detected prior to the discharge when using either of the analytes. As

with the dense arrays, acetone was used. Again no current due to charged species could be detected.

The observation of the arc discharge at relatively low potential differences may point towards the formation of droplets on the emitter surfaces. Depending on the solvent, a droplet might also have frozen on the wafer. The formation of droplets might have created a partial bridge between the two electrodes which in turn might have facilitated an arc discharge. Droplet formation does not, however, explain why no current could be recorded when using a gaseous analyte.

5.4 References

- (1) Linden, H. B. *European Journal of Mass Spectrometry* **2004**, *10*, 459-468.
- (2) O'Hanlon, J. F. *A User's Guide to Vacuum Technology* Third ed.; John Wiley & Sons, Inc: Hoboken, New Jersey, 2003.
- (3) Wensink, E. J. W.; Hoffmann, A. C.; van Maaren, P. J.; van der Spoel, D. *Journal of Chemical Physics* **2003**, *119*, 7308-7317.

6. Conclusion

The objective of this study was, through exploiting the particular properties of carbon nanotubes (CNTs), to achieve a quantum leap forward in the analytical capability of mass spectrometry. CNTs offer the possibility of creating very high and stable electric fields by virtue of their mechanical strength and sharpness of their tips. Electrospray ionisation (ESI) can be thought of as “field desorption from a droplet” where the field is that of the droplet itself. The very broad idea to be explored was that of using the field above a CNT to desorb ions from liquids and to field ionise gases.

Partly as a preliminary exercise in familiarisation with ESI, dual-channelled electrospray needles were created through precisely controlled extension of the near- molten dual-channelled capillaries. These twin-channelled needles have potential for the investigation of the kinetics of biological reactions. There was no evidence that the structures imposed upon the tip of the needle adversely affected ESI. The evidence was that a Taylor cone was formed as in ESI with a single-channel needle, and droplets were emitted in a normal fashion. With CNTs, the liquid was intended to flow around the carbon needle with perhaps formation of Taylor cones and droplet emission. There are, however, properties of the CNTs raised to high potentials which raise fundamental questions.

The arrays of CNTs showed field electron-emission with the sort of qualitative dependence on potential expected. The Fowler-Nordheim treatment of the field emission data yielded an enhancement factor between two and three thousand

which agrees to within an order of magnitude with values reported for CNT arrays in the literature¹⁻³. This is larger by an order of magnitude than the enhancement factor calculated in this study for a single nanotube. Quite obviously this calculation did not consider shielding from neighbouring nanotubes, which would be present in an array and which would reduce the calculated enhancement factor if taken into account. The Field strength for an array of CNT emitters taken from the Fowler-Nordheim plot was $8.78 \times 10^9 \pm 1.03 \times 10^9$ V/m at a potential of 1000 V. This is in line with a literature value being slightly stronger than that reported for a CNT emitter used to ionise helium¹. The conundrum posed by all of this is that the magnitude of field necessary to reach helium's first ionisation energy (24.58 eV) has been placed at 6.33×10^{10} V/m⁴ i.e. an order of magnitude larger.

Field ionisation of a number of different gases with first ionisation energies between 9.6-24.59 eV was achieved in this study with arrays of CNTs. The finding that both helium and argon (onset field strength 2.6×10^{10} V/m⁴) were ionised by the CNT array showed that the CNT array was able to ionise elements which have never been field ionised using conventional activated wire emitters as routinely used for field desorption and field. Experiments to transfer the ions to a linear-TOF mass analyser and measure mass spectra were not successful. The failure to measure mass spectra probably had its origin in the area of ion optics. The emission characteristics of CNT arrays with respect to angle and energy need to be determined.

The source designed to allow the delivery of both liquids and gaseous samples directly to the arrays of CNTs led to unexpected findings about the CNTs. The injection of both liquids and gases directly through the substrate of the CNT arrays was achieved easily enough. No mass spectrometric measurements or currents due to ionised species were recorded however. Could the arrays of CNTs used with the source have been unable to produce the high fields necessary for field ionisation?

An interesting finding was that patterns of CNTs readily achieved with plain silicon wafers could not be created after the holes had been drilled through the wafer. The CNTs grew in the immediate vicinity of the holes despite the fact that the nickel initiators had been deposited far from the holes. The conclusion is that the nickel migrated. There is no justification however, for supposing that the CNTs in the proximity of the holes were associated with lower field strengths than CNTs in the absence of holes. Possibly, the failure to detect ions was essentially ion optical as a result of the distortions in the potential distributions caused by the holes, in turn perturbing initial trajectories of ions adversely. It is not at all obvious, however, why the forest of CNTs would suffer similarly adverse effect on the trajectories as a result of the holes being present.

The results from the field emission and the early field ionisation experiments indicate that, despite possible transmission problems, arrays of CNTs should not be discounted as emitters for field ionisation and field desorption. At the risk of repetition, conventional activated-wire emitters are unable to ionise helium but this has been demonstrated with arrays of CNTs. It is very possible that arrays

of CNTs might have been able to field ionise some of the other species of analyte, such as proteins and polymers, which, like helium, have always been beyond the scope of the conventional activated-wire emitters. With this in mind the prospects for further work with CNTs as emitters are both strong and promising.

- (1) Riley, D. J.; Mann, M.; MacLaren, D. A.; Dastoor, P. C.; Allison, W.; Teo, K. B. K.; Amaratunga, G. A. J.; Milne, W. I. *Nano Letters* **2003**, *3*, 1455-1458.
- (2) Bonard, J.-M.; Dean, K. A.; Coll, B. F.; Klinke, C. P. R. L., 197602 (2002). *Physics Review Letters* **2002**, *89*, 197602-197606.
- (3) Teo, K. B. K.; Chhowalla, M.; Amaratunga, G. A. J.; Milne, W. I.; Pirio, G.; Legagneux, P.; Wyczisk, F.; Pribat, D.; Hasko, D. G. *Applied Physics Letters* **2002**, *80*, 2011-2013.
- (4) Brandon, D. G. *Brit. J. Appl. Phys.* **1963**, *14*, 474-484.

7. Appendix

Chapter 1: Introduction to mass spectrometry

Appendix 1a

Table of frequently observed molecular ions and ions formed upon further reaction in FD mass spectra adapted from Prokai.[1]

Analyte	Ion type	Possible mechanism of formation
M (neutral molecule)	M^+	Field ionisation (electron tunnelling)
	M^{n+}	Field Ionisation (electron tunnelling) or Desolvation and/or ion evaporation
	$[M + H]^+$	
	$[M + nH]^{n+}$	
	$[xM + H]^+$	
	$[xM + nH]^{n+}$	Desolvation and/or ion evaporation
	$[M + \text{alkali}]^+$	
	$[M + n \text{ alkali}]^{n+}$	
	$[xM + \text{alkali}]^+$	
	$[xM + n \text{ alkali}]^{n+}$	
$[M + yH + n \text{ alkali}]^{(n+y)+}$		
$C^+ A^-$ (organic or inorganic salt where C^+ = cation and A^- = anion)	$[C \cdot A]^+$	Field ionisation (electron tunnelling)
	C^+	Desolvation and/or ion evaporation or thermal ionisation
	$[C_{n+1}An]^+$	

1. Prokai, L., *Field Desorption Mass Spectrometry*. Practical Spectroscopy Series, ed. J.E.G. Brame. Vol. 9. 1990, New York: Marcel Dekker INC. 291.

Appendix 1b

Example of the simple code used to describe an Einzel lens.

```
; Einzel lens GEM File
;
; This GEM file creates a 2d cylindrically symmetrical array containing three
; fast adjustable electrodes describing an Einzel lens.
;
; This array is scaled at 0.1 mm/gu
;
; Array size = (320,245,1) in order to accomodate all electrodes
;
; The GEM file does NOT use a scaling factor which must be entered in the
; IOB
;
```

PA_Define(350,245,1,C,Y,E) ; Generates the array described above

Locate(0,0,0,1,0,0,0) { ; Locates at corner of array

Electrode(1) {Fill {Within {Corner_Box(50,50,50,230)}}} ; 1st
electrode

Electrode(2) {Fill {Within {Corner_Box(150,50,50,230)}}} ; 2nd electrode

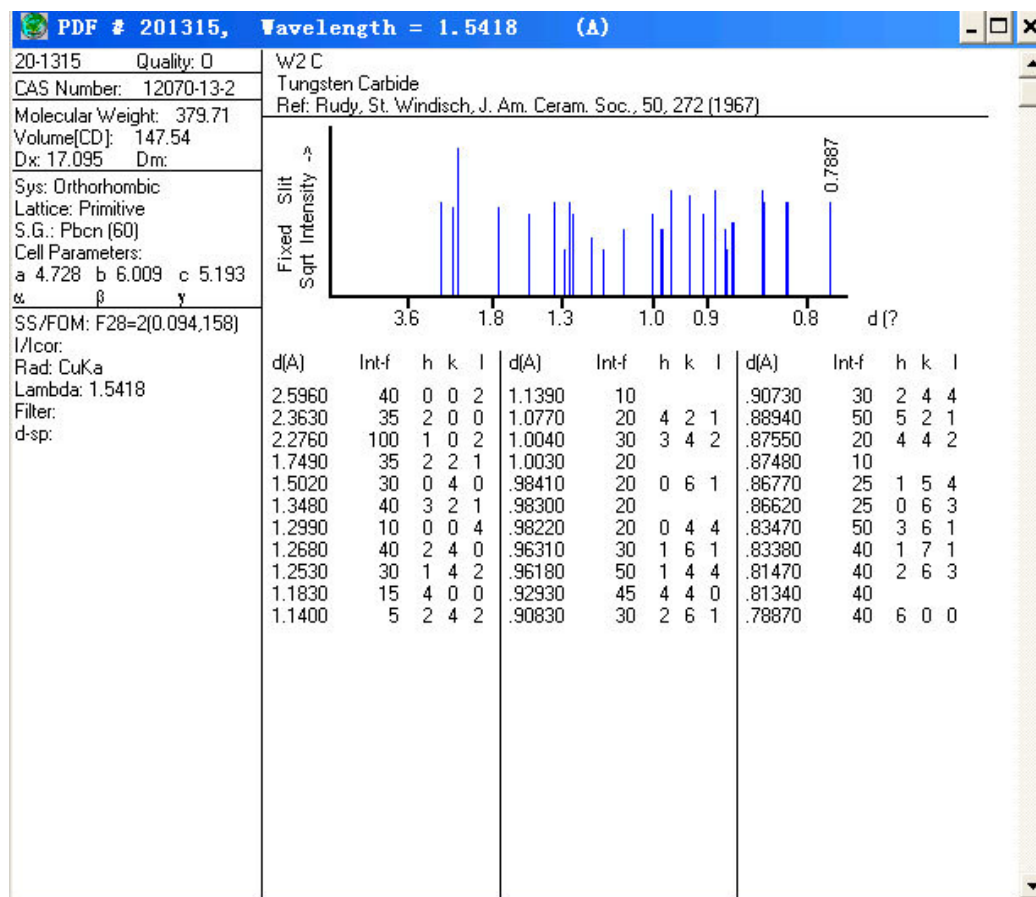
Electrode(3) {Fill {Within {Corner_Box(250,50,50,230)}}} ; 3rd electrode

} ; Closes locate

Chapter 3: Carbon nanotubes as field emitters

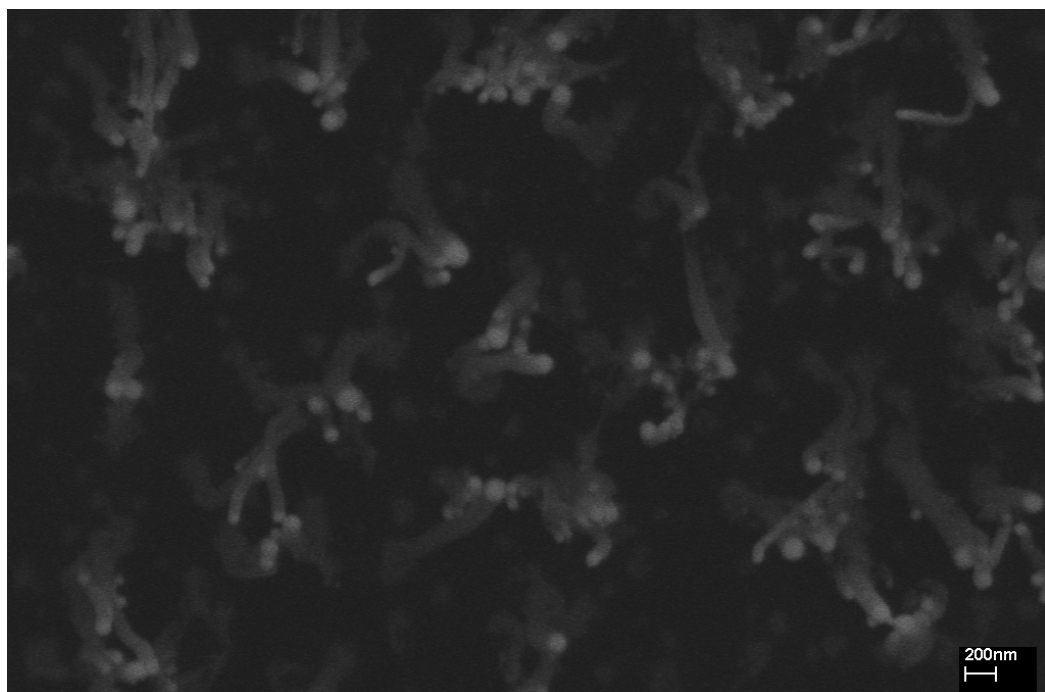
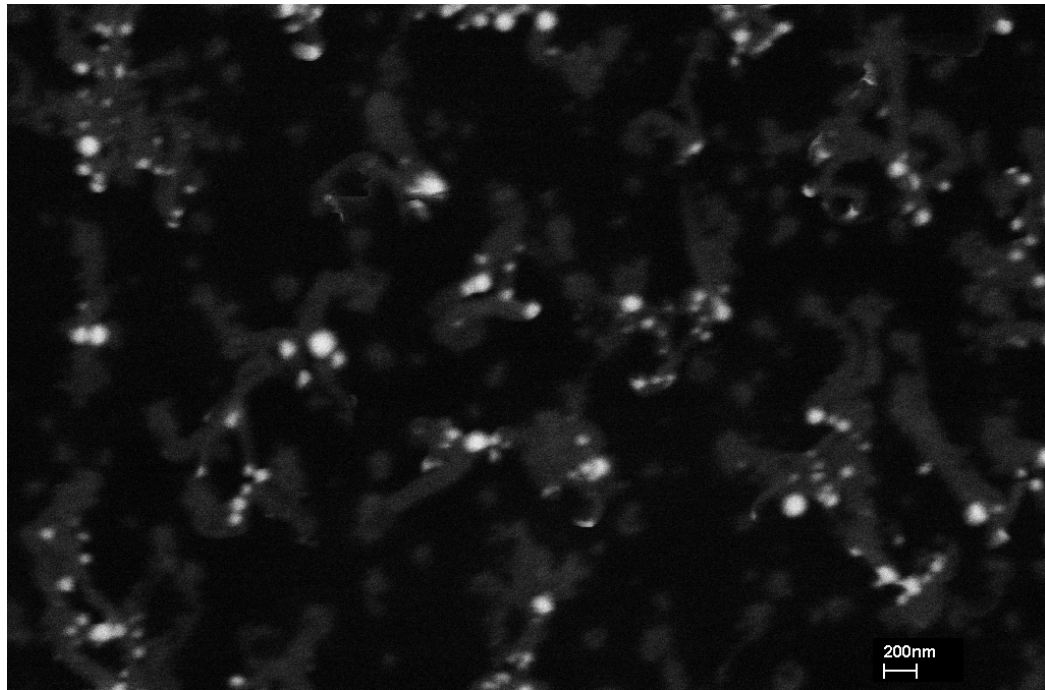
Appendix 3a

Powder diffraction file for W_2C which shows that a lattice spacing of 2.36 \AA is evident.



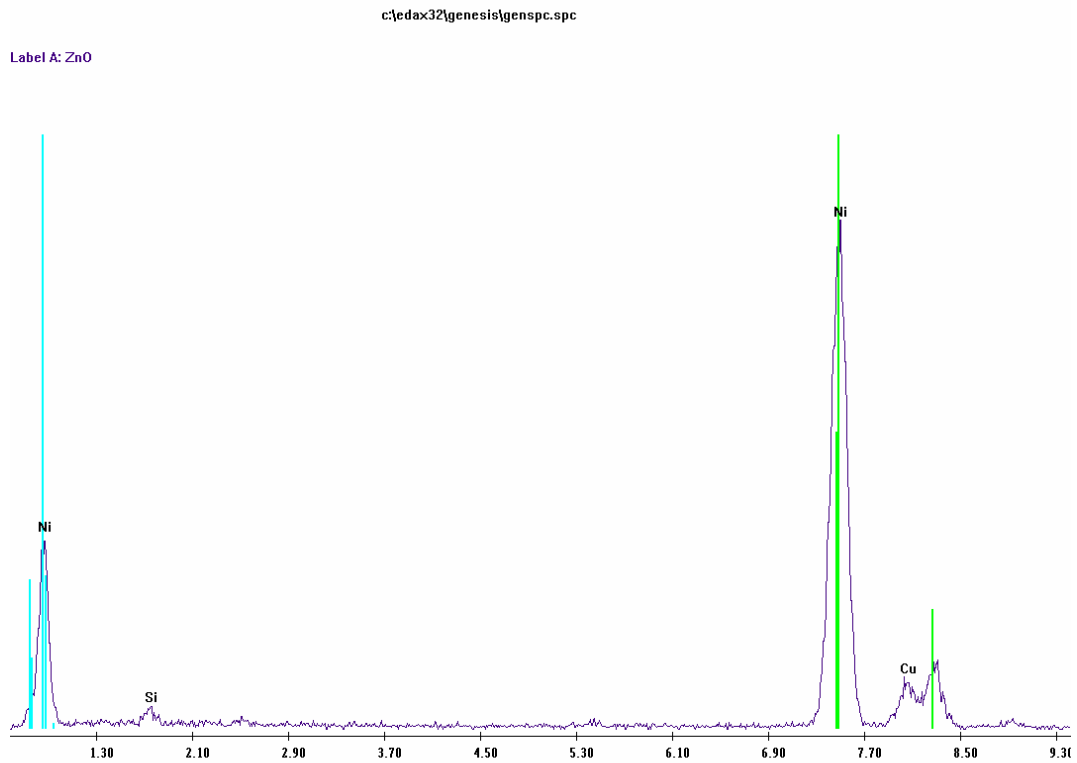
Appendix 3b

Comparison between the micrographs of an area of the dense nanotube array obtained using A, the QSMD and B, the SE2 detector.



Appendix 3c

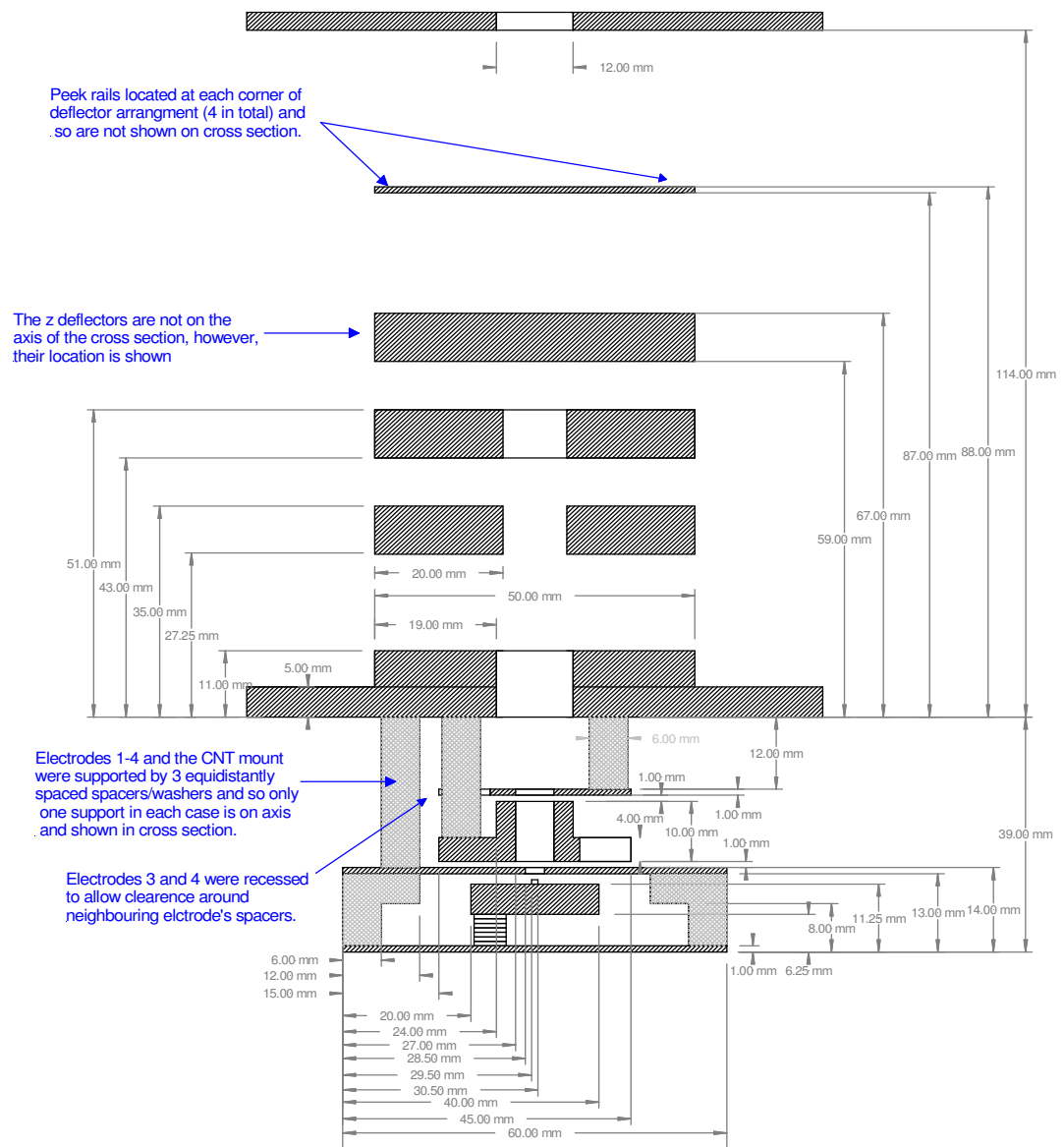
EDX spectrum of the catalyst particle at the tip of a carbon nanotube.

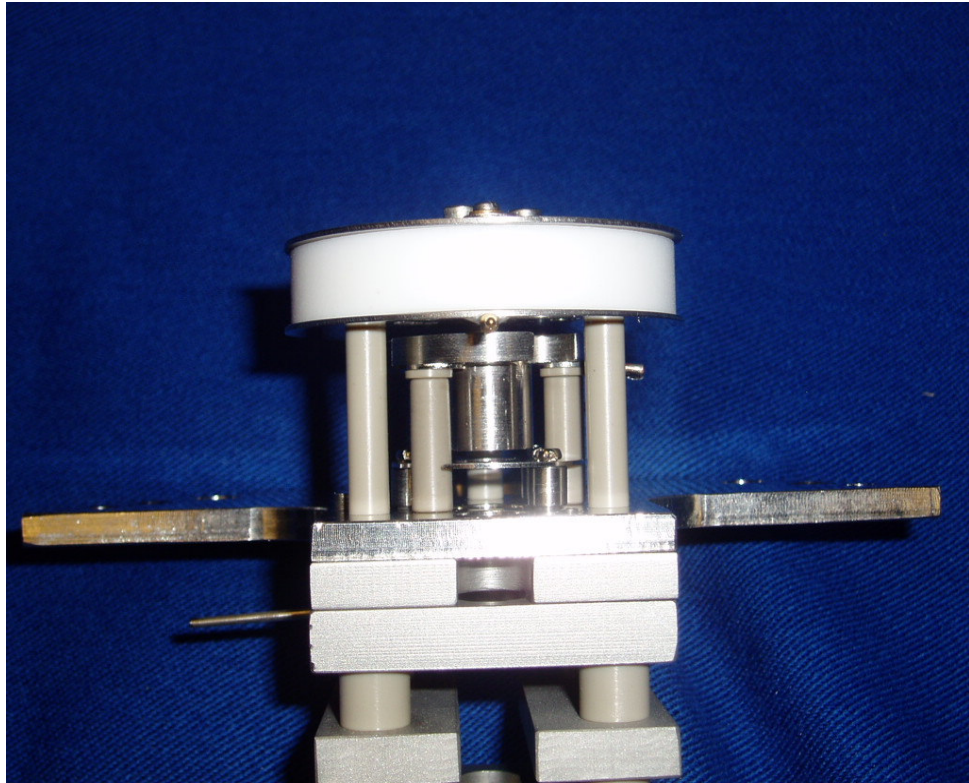
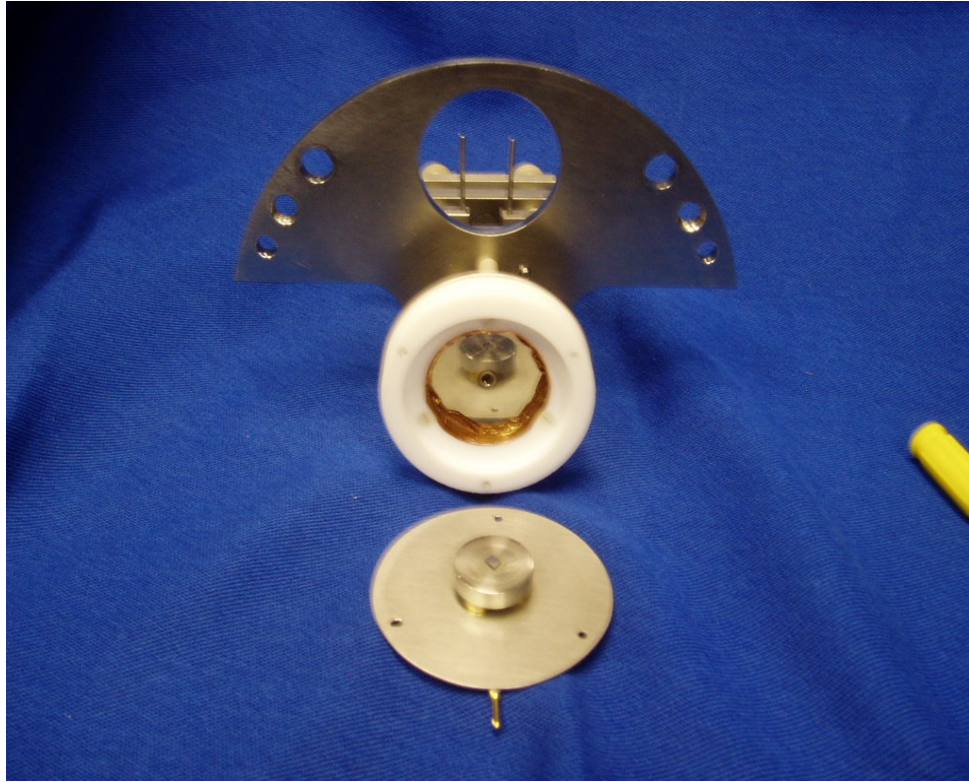


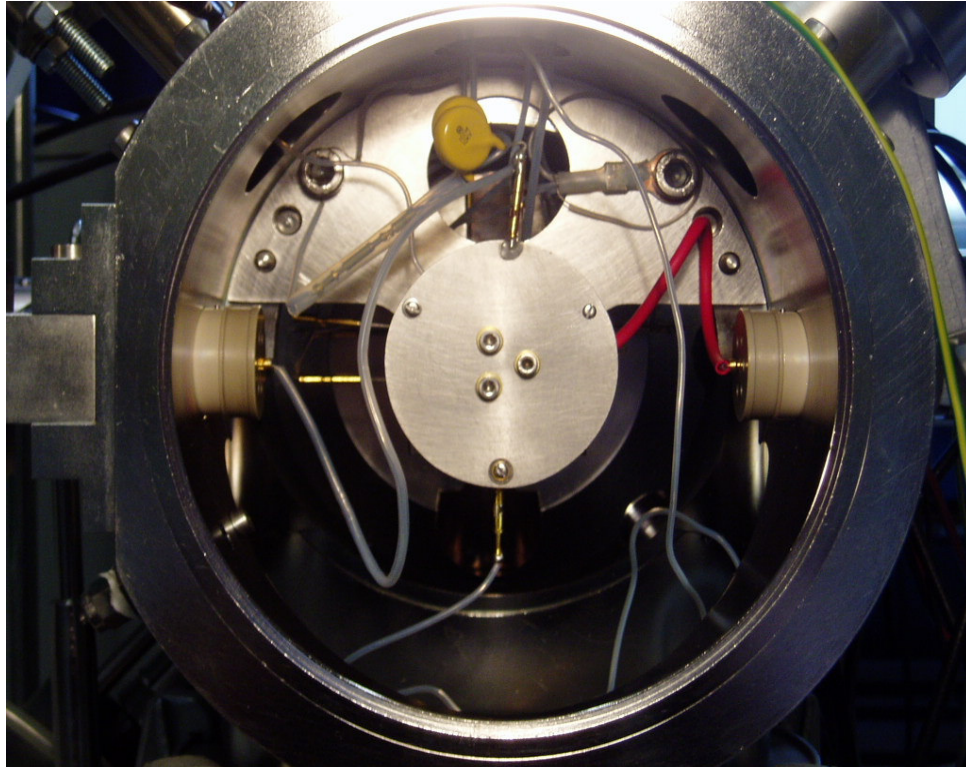
Chapter 4: Field Ionisation of gases using carbon nanotube

Appendix 4a

Schematic showing the design of the first generation source and photos illustrating parts of the source and where it sits in the vacuum chamber of the magTOF instrument





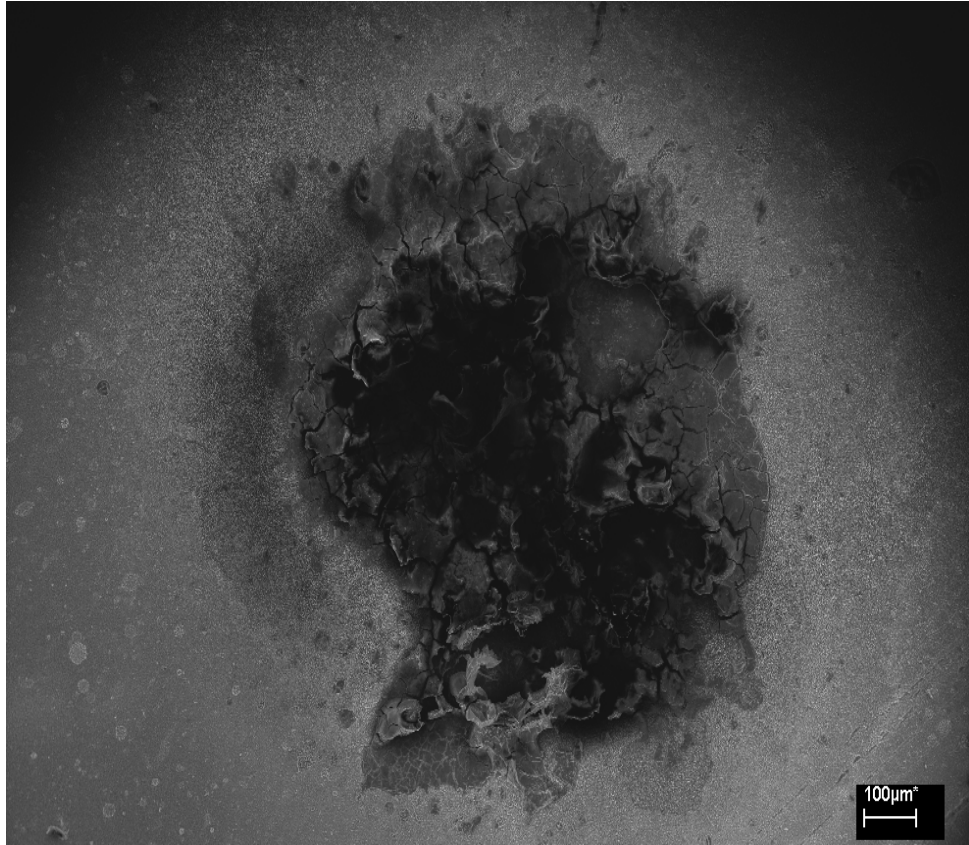


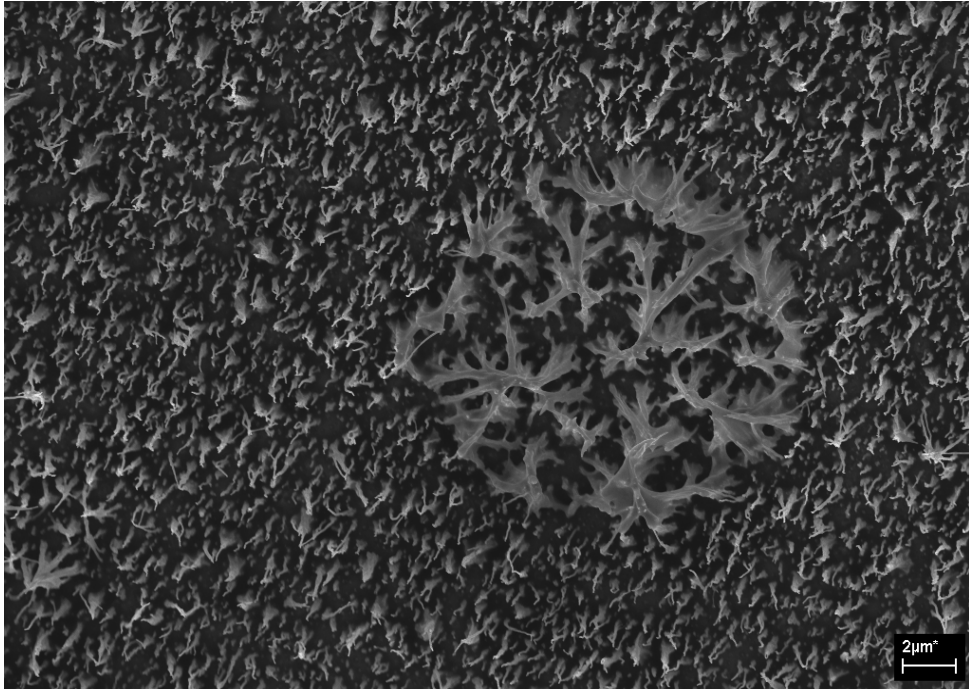
Chapter 5: Direct Introduction of Liquids into the Carbon Nanotube

Source

Appendix 5a

Micrographs illustrating the damage wrought on the nanotube array once an arc discharge had occurred. A, note that the position of the holes are completely obscured by the arc site. B and C show what appears to droplet like formations of amorphous carbon. This could be a result of plasma from the discharge dropping onto unaffected parts of the array

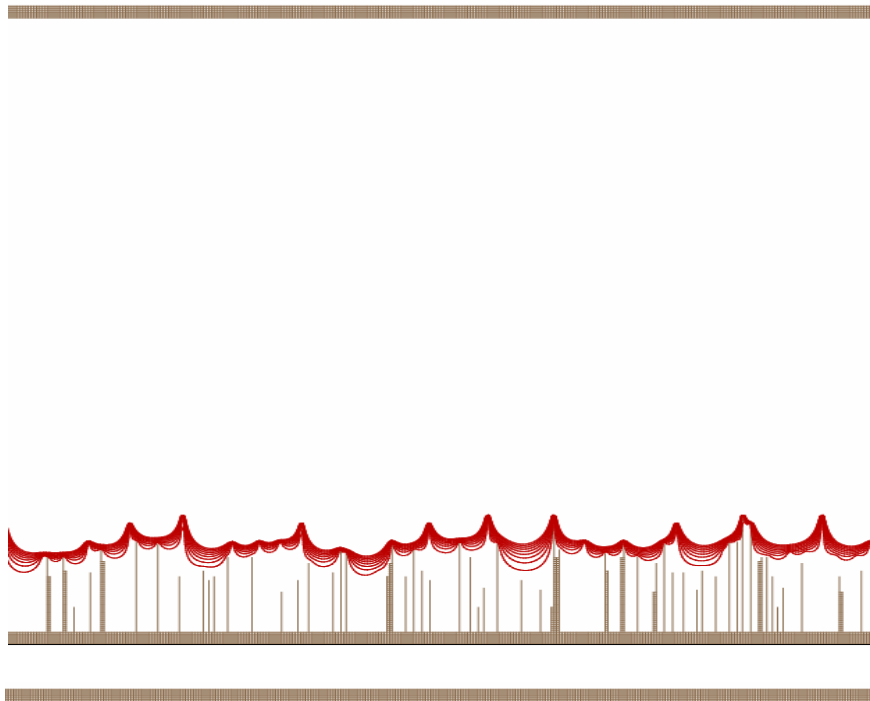




Appendix 5b

Pictures taken from the simulations of A, the nanotube array and B, the corresponding array when the nanotubes clump together

A



B

